Development of Novel Radiofrequency Coils for Hyperpolarized Magnetic Resonance Imaging

Tony Zhou

Department of Physiology, Anatomy and Genetics

Oxford Centre for Clinical Magnetic Resonance Research

Somerville College



University of Oxford

A thesis submitted in partial fulfilment of the requirements

for the degree of Doctor of Philosophy

Hilary Term 2022

Abstract

Magnetic Resonance Imaging (MRI) is the gold-standard diagnostic tool for cardiovascular conditions. However, this imaging technique is currently insensitive with a limited signal-to-noise ratio (SNR), leading to long acquisition times, poor spatial resolution and negatively impacts on the diagnostic quality of scans. These issues can be alleviated through improvements in hardware. The SNR is strongly determined by the performance of Radio-Frequency (RF) coils, devices that transmit and receive the electromagnetic (EM) fields which interact with the patient to generate the MR signal.

X-nuclear MRI, investigating non-proton 'X-' nuclei, provides unique metabolic information in vivo. Compared to conventional proton MRI scans, X-nuclei scans are performed at a different range of RF frequencies, therefore requiring special RF coils. However, due to limited wide-band power amplification at these frequencies and relatively low natural abundance of these X-nuclei in the body, this metabolic imaging heavily relies on efficient RF coils with strong local EM fields to achieve sufficient SNR. Conventionally, X-nuclei RF coils utilise a 'surface coil' design, comprising of one to several individual conducting loops positioned on the surface of the body. Using EM simulations, we show that for a given region of interest (ROI), surface coil designs inherently trade-off field homogeneity against field strength. In this work, methods were developed to compare and optimise coil design.

The main achievement of this project is the development of a novel class of RF coils, utilising a flexible multi-layer design that offers significantly improved transmit and receive sensitivity over that achieved by conventional surface elements. EM simulations of parameterized four- and six-layer multi-layer designs identified promising 3D conductor geometries that generated both a stronger and more uniform field profile than conventional circular conducting elements. Preclinical and clinical multi-layer coils were constructed for carbon (^{13}C) MRI at $7\,\mathrm{T}$ and $3\,\mathrm{T}$ respectively and compared to a range of conventional loop coils; improvements in transmit and receive field were consistent with simulation results. Subsequently, a two-fold increase in SNR was observed using a human multi-layer coil for cardiac phosphorus (^{31}P) spectroscopy on five human participants.

Commonly, cardiac RF receive coils comprise of several single elements partially overlapped in an array. These array elements are geometrically decoupled to allow good field coverage with the high sensitivity of small individual elements. This project proceeds to investigate the optimisation and decoupling ability of multi-layer elements to form multi-layer receive arrays, whilst preserving the increased sensitivity of the multi-layer design. This design offers a direct replacement to conventional loop elements in existing coil configurations, allowing increased SNR to be obtained at minimal additional cost beyond design and manufacturing complexity.

Acknowledgements

Table of Contents

1 Introduction **2**

1.1 Motivation . . . 2

1.1.1 Need for increased sensitivity through coil design . . . 3

1.1.2 Robust protocol for characterising and optimising surface RF coils . . . 4

1.1.3 Investigating array design using multiple optimised elements . . . 5

1.2 Objectives . . . 6

1.3 Outline of Chapters . . . 6

2 Background Theory **11**

2.1 Nuclear Magnetic Resonance: Physical Principles . . . 11

2.1.1 Electromagnetic Fields . . . 11

2.1.2 Nuclear Spin . . . 13

2.1.2.1 Quantum Mechanical Framework . . . 14

2.1.2.2 Classical Framework . . . 15

2.1.3 Image Reconstruction . . . 16

2.1.3.1 Bloch Equations and Magnetisation Relaxation . . . 17

2.1.3.2 Image Formation . . . 18

2.1.3.3 k-Space . . . 19

2.1.4 Noise . . . 20

2.1.4.1 SNR Definitions . . . 21

2.1.4.2 Measured Complex Noise . . . 22

2.1.4.3 Quality Factor in RLC circuits . . . 23

2.1.4.4 Sample and Coil Noise Contributions . . . 24

2.1.4.5 Scattering Matrix . . . 25

2.2 MRI Scanner Hardware . . . 27

2.2.1 Overview . . . 28

2.2.1.1 Main static field . . . 28

2.2.1.2 Gradient field . . . 28

2.2.2 Radiofrequency Hardware . . . 29

2.2.2.1 Coil Element . . . 29
2.2.2.2 Transmit Chain . . . 31
2.2.2.3 Receive Chain . . . 32
2.2.3 Minimising EM Coupling . . . 34
2.2.3.1 Coupling between Tx and Rx coils . . . 35
2.2.3.2 Coupling between proton and X-nuclei coils . . . 36
2.2.3.3 Coupling between neighbouring array elements . . . 37
2.3 Proton versus Non-Proton MRI . . . 37
2.3.1 Conventional MRI . . . 38
2.3.2 Multi-Nuclei Cardiac MRI . . . 39
2.3.2.1 13-Carbon MRS/I . . . 40
2.3.2.2 Sodium MRI . . . 41
2.3.2.3 Phosphorus MRS/I . . . 41
2.4 Summary . . . 42

3 Methodology **46**
3.1 Overview . . . 46
3.2 Computational Electromagnetics . . . 46
3.2.1 Time Domain and Frequency Domain . . . 47
3.2.1.1 Time Domain . . . 48
3.2.1.2 Frequency Domain . . . 49
3.2.2 Running EM simulations . . . 50
3.2.2.1 Accurate Human Voxel Model . . . 51
3.2.2.2 Co-simulation . . . 51
3.2.2.3 Quantification of Sample Noise . . . 52
3.2.2.4 Simulation Protocol . . . 52
3.3 Coil Construction and Bench-top Characterisation . . . 57
3.3.1 Characterisation Techniques . . . 58
3.3.1.1 Characteristic Impedance . . . 59
3.3.1.2 Resonance Frequency . . . 60
3.3.1.3 Measuring Scattering Parameters . . . 62
3.3.1.4 Measuring Quality Factor . . . 64

3.3.2 Isolation of Undesired Frequencies . . . 64
3.3.2.1 LC Traps on X-nuclei coils . . . 65
3.3.2.2 Baluns . . . 66
3.3.3 Resonance at desired frequency . . . 67
3.3.3.1 Capacitor Design Considerations . . . 68
3.3.3.2 Coil Tuning Protocol . . . 70
3.3.3.3 Coil Matching Protocol . . . 71
3.4 Scanner Coil Characterisation . . . 72
3.4.1 Experimental Setup . . . 73
3.4.2 Transmit Magnetic Field Protocol . . . 75
3.4.3 SNR Mapping Protocol . . . 81
3.4.4 Advantages and Disadvantages . . . 83
3.5 RF Coil Heating . . . 84
3.5.1 Localised Thermal Burns . . . 85
3.5.2 General Tissue Heating . . . 86
3.5.2.1 SAR from EM Simulations . . . 86
3.5.2.2 Tissue Temperature Measurements . . . 87
3.5.2.3 Safety Limits . . . 88
3.6 Summary . . . 90

4 Pre-clinical Multi-layer Design 93
4.1 Introduction . . . 93
4.1.1 Motivation for Novel Coil Design . . . 93
4.1.2 Chapter Overview . . . 94
4.2 Main Multi-layer Features . . . 94
4.2.1 Stacked Conductor Layers . . . 95
4.2.1.1 Increased Magnetic Flux Density . . . 95
4.2.1.2 Increased Q-value . . . 96
4.2.1.3 Proton Solenoid Prototype . . . 97
4.2.2 Offset Layers . . . 99
4.2.2.1 Skin and Proximity Effects . . . 99
4.2.2.2 Unwanted EM Shielding . . . 102

4.2.3 Star-Shaped Conductor Design . . . 104
4.3 Sodium Multi-layer Coil Development . . . 106
4.3.1 Sodium Multi-layer Prototype 1 . . . 106
4.3.1.1 Benchtop Results . . . 108
4.3.1.2 EM Simulation Setup . . . 109
4.3.1.3 Scanner Measurement Setup . . . 110
4.3.1.4 2D Field Map Results . . . 111
4.3.2 Sodium Multi-layer Prototype 2 . . . 112
4.3.2.1 B1 from EM Simulations . . . 113
4.3.2.2 SNR from EM Simulations . . . 116
4.3.2.3 Scanner Measured B1 . . . 117
4.3.2.4 Scanner Measured SNR . . . 118
4.4 Carbon Multi-layer Coil Development . . . 119
4.4.1 Prototype Construction . . . 119
4.4.2 Measured Receive Performance . . . 119
4.4.2.1 Non Localised Spectroscopy . . . 120
4.4.2.2 Chemical Shift Imaging . . . 121
4.5 Discussion . . . 122
4.5.1 Overview . . . 122
4.5.2 Petal, Spiral and Concentric Designs . . . 122
4.5.3 Impact of Multi-layer Design . . . 123
4.5.4 Further Work . . . 124

5 Human Multi-layer Coil Development 127
5.1 Introduction . . . 127
5.1.1 Human Multi-layer Coil . . . 127
5.1.2 Overview . . . 128
5.2 Further Multi-layer Design Improvements . . . 128
5.2.1 Curved Conductor Construction . . . 128
5.2.2 Peripheral Coil Region . . . 131
5.2.2.1 Boundary Region of Lower B-field . . . 132
5.2.2.2 Distributed Lumped Elements . . . 133

5.2.2.3 Decoupling of Neighbouring Elements . . . 134
5.2.3 Estimating Multi-layer Q-Value . . . 134
5.3 Multi-layer Optimisation . . . 135
5.3.1 EM Simulation Setup . . . 136
5.3.1.1 Field Uniformity versus Efficiency . . . 138
5.3.2 Parameter Sweep Results . . . 139
5.3.2.1 Transmit Optimisation . . . 140
5.3.2.2 Receive Optimisation . . . 142
5.3.3 Alternative Conductor Designs . . . 143
5.3.3.1 Tapered Conductor . . . 143
5.3.3.2 Cylindrical Conductor . . . 147
5.4 Human Multi-layer Prototype Coils . . . 154
5.4.1 Carbon Multi-layer . . . 155
5.4.1.1 Coil Construction . . . 157
5.4.1.2 Scanner and Simulation Setup . . . 159
5.4.1.3 B1 and SNR Results . . . 161
5.4.2 Phosphorous Multi-layer Coil . . . 164
5.4.2.1 Coil Construction . . . 165
5.4.2.2 B1 and SNR Values . . . 166
5.5 Multi-layer Heating Tests to Ensure Patient Safety . . . 168
5.5.1 SAR from EM Simulations . . . 169
5.5.2 Scanner Temperature Measurements . . . 172
5.5.2.1 Experimental Setup . . . 173
5.5.2.2 Power Absorbed Calculation . . . 177
5.5.3 Proposed Safety Limits in Coil Files . . . 180
5.5.3.1 Limiting SAR conversion (k-value) . . . 181
5.5.3.2 Minimising Proton Heating . . . 181
5.5.3.3 Limiting Maximum Voltage . . . 182
5.6 Multi-layer Acquired Human Data . . . 182
5.6.1 1D CSI Scan Setup . . . 183
5.6.2 Multi-Layer Coil Results . . . 185

5.6.2.1 Spectral SNR . . . 185
5.6.2.2 PCr/ATP Ratio and Variability . . . 186
5.7 Discussion . . . 188
5.7.1 Overview . . . 188
5.7.2 Further Work . . . 189

6 Multi-Element Arrays 192
6.1 Introduction . . . 192
6.1.1 Motivation For Multiple Elements . . . 192
6.1.2 Proton and X-nuclei Array Developments . . . 193
6.1.3 Tx and Rx Array Design Requirements . . . 194
6.1.4 Chapter Overview . . . 195
6.2 Characterising Multiple TxRx Elements . . . 195
6.2.1 Optimising 20 cm Loop Elements . . . 196
6.2.1.1 EM Simulation Setup . . . 196
6.2.1.2 Results: Elements, Position and Phase . . . 200
6.2.1.3 Four Element Example Field Profile . . . 203
6.2.2 Comparison against Existing Coil Designs . . . 205
6.2.2.1 Large Helmholtz Pair . . . 206
6.2.2.2 Quadrature Birdcage . . . 208
6.2.3 Overall Field Comparison . . . 210
6.3 Developing a Four Element Tx Array . . . 213
6.3.1 Simulating Tx Element Designs . . . 213
6.3.1.1 Optimising Dimension Parameters . . . 214
6.3.1.2 Optimising Overlap and Phase Shift . . . 217
6.3.2 Benchtop Measurements to Investigate Overlap . . . 220
6.3.2.1 Tx Array Construction . . . 222
6.3.2.2 Benchtop Setup and Method . . . 224
6.3.2.3 Field Maps Varying Overlap . . . 225
6.3.3 Scanner Measurements to Investigate Phase . . . 228
6.3.3.1 Scanner Experimental Setup . . . 229
6.3.3.2 Phase Shift Results . . . 230

6.3.3.3 Comparison with Helmholtz Coil . . . 234
6.3.4 Simulated Coil Comparison . . . 237
6.3.4.1 Overview B1 Efficiency Uniformity Within ROI . . . 238
6.4 Developing a Multi-layer Rx Array . . . 241
6.4.1 Geometric Decoupling . . . 241
6.4.1.1 Simulation and Benchtop Setup . . . 242
6.4.1.2 Two Multi-layer Element Decoupling . . . 245
6.4.1.3 Three Multi-layer Element Decoupling . . . 248
6.4.2 Multi-layer Phase and Overlap Angle . . . 251
6.4.2.1 EM Simulation Setup . . . 252
6.4.2.2 Two Multi-layer Phase Results . . . 254
6.4.3 Development of Multi-layer Array Prototype . . . 256
6.4.3.1 Receive Only Multi-layer Prototype . . . 258
6.5 Discussion . . . 259
6.5.1 Overview . . . 260

7 Conclusion and Further Work 264
7.1 Thesis Summary . . . 264
7.2 Multi-layer Coil design . . . 264
7.2.1 Applications . . . 265
7.2.2 Limitations and Further Work . . . 265
7.3 Coil Comparison using B1 and SNR mapping . . . 266
7.3.1 Applications . . . 266
7.4 Optimised Cardiac Array . . . 266
7.4.1 Applications . . . 267
7.4.2 Limitations and Further Work . . . 267

Appendix A Forms of Maxwell's Equations 268
A.1 Differential form in free space . . . 268
A.2 Integral form in free space . . . 268
A.3 Differential form in polarizable media . . . 268

Appendix B Combining Discrete Ports 270

Appendix C Scattering Parameters **272**

C.1 Quantifying S-parameters 272

C.2 Smith Chart 272

Appendix D Existing Scanner Field Mapping Methods **274**

D.1 Transmit Performance 274

D.1.1 The Double Angle Method 274

D.1.2 The Bloch-Siegert Method 275

D.2 Receive Performance 276

D.2.1 Non-localised Spectroscopy 276

D.2.2 Chemical Shift Imaging 277

Appendix E Multi-layer Coil Construction Protocol **279**

Appendix F Preclinical Multi-layer Circuit Simulation **280**

F.0.1 Circuit Simulation 280

Appendix G On-Axis B1 and SNR for Carbon Clinical Multi-layer Coils **281**

Appendix H Four Element Transmit Array Optimisation Data **283**

Appendix I Array Design Performance Across Frequencies **284**

List of Abbreviations

AM ..... Amplitude-Modulated

AMARES ..... Advanced Method of Accurate, Robust and Efficient Spectroscopic Fitting

ATP ..... Adenosine Triphosphate

BISTRO ..... B_1-Insensitive Train to Obliterate Signal

CAD ..... Computer Aided Design

CEM ..... Computational Electromagnetics

CK ..... Creatine Kinase

CNR ..... Contrast-to-Noise Ratio

CRLB ..... Cramer-Rao Lower Bounds

CSI ..... Chemical Shift Imaging

CV ..... Coefficient of Variation

DAM ..... Double Angle Method

DC ..... Direct Current

DICO ..... Directional Coupler

DNP ..... Dynamic Nuclear Polarization

EM ..... Electromagnetic

ESR ..... Effective Series Resistance

FDTD ..... Finite Difference Time Domain

FEM ..... Finite Element Methods

FFT ..... Fast Fourier Transform

FID ..... Free Induction Decay

FIT ..... Finite Integration Technique

FOV ..... Field of View

FPGA ..... Field-Programmable Gate Array

FWHM ..... Full Width at Half Maximum

IEC ..... International Electrotechnical Commission

IQR ..... Interquartile Range

IR ..... Infrared

LCP ..... Left-Handed Circularly Polarized

MRI ..... Magnetic Resonance Imaging

MOR ..... Model-Order Reduction

MRS ..... Magnetic Resonance Spectroscopy

MWS ..... Microwave Studio

NFC ..... Near-Field Communication

PA ..... Peak Amplitude

PCB ..... Printed Circuit Board

PCr ..... Phosphocreatine

PEC ..... Perfect Electrical Conductor

PERES ..... Petal Resonator Surface

PI ..... Parallel Imaging

PIN ..... Positive Intrinsic Negative

PM ..... Phase-Modulated

PPA ..... Phenylphosphonic Acid

PTFE ..... Polytetrafluoroethylene

pTx ..... Parallel Transmit

Q ..... Quality

$R1$ ..... Central Radius

$R2$ ..... Peripheral Radius

RCP ..... Right-Handed Circularly Polarized

RF ..... Radio-Frequency

RFID ..... Radiofrequency Identification

RLC ..... Resistor-Inductor-Capacitor

RMS ..... Root-Mean-Squared

Ro ..... Receive Only

ROI ..... Region of Interest

Rx ..... Receive

S ..... Scattering

SAR ..... Specific Absorption Rate

SNR ..... Signal-to-Noise Ratio

SVS ..... Single Voxel Spectroscopy

T_1 ..... Spin-Lattice Relaxation Time

T_2 ..... Spin-Spin Relaxation Time

TE ..... Echo Time

To ..... Transmit Only

TR ..... Repetition Time

Tx ..... Transmit

VNA ..... Vector Network Analyser

Publications

Patents

1. Zhou T, Lau JYC, Miller JJ, Tyler DJ, Randell C. “Radiofrequency coil.” (2019). US20220206090A1, United States. Also: EP3959526A1, European Patent Office; WO2020217069A1, WIPO (PCT).

Peer-Reviewed Journal Articles

1. Zhou T, Lau JYC, Chhina N, Randell C, Miller JJ, Tyler DJ. “Novel Multi-Layer RF Coil Design with 50% increased Signal-to-Noise”. Journal Article: In edit awaiting submission.
2. Tyler A, Lau JYC, Ball V, Timm K, Zhou T, Tyler DJ, Miller JJ. “A 3D-Hybrid-Shot Spiral Sequence for Hyperpolarized 13C Imaging”. Journal Article: Magnetic Resonance in Medicine, 85: 780-801 (2018).

Conference Abstracts

1. Zhou T, Lau JYC, Miller JJ, Chhina N, Randell C, Tyler DJ. “Multi-layer Radiofrequency Coils: A Novel Surface Coil Design for Improved B1+ Efficiency and Signal-to-Noise”. International Society for Magnetic Resonance in Medicine (April 2020, Sydney).
2. Zhou T, Lau JYC, Tyler A, Randell C, Miller JJ, Tyler DJ. “Multi-layered radiofrequency coil design for X-nuclei Imaging”. International Society for Magnetic Resonance in Medicine (May 2019, Montreal).
3. Zhou T, Lau JYC, Miller JJ, Tyler DJ. “‘Star-Shaped’ Multi Loop Radiofrequency Coil Design With Improved B1 Penetration for X-Nuclei Imaging”. British Chapter of the ISMRM Annual Meeting (2018, Oxford).

1 | Introduction

Magnetic Resonance Imaging (MRI) is a widely used non-invasive imaging modality offering excellent soft tissue contrast with widespread diagnostic value [1]. MRI offers detailed information about important tissue properties, including those reflective of common disease states [2, 3]. Conventional ^{1}H MRI is the gold-standard imaging modality for numerous conditions, with approximately $40\,000$ scanners in service worldwide, with this number growing at a rate of 2500 new scanners per year [4]. In addition, X-nuclear MRI and magnetic resonance spectroscopy (MRS) investigating non-proton 'X-' nuclei provides unique metabolic information *in vivo* (although significantly fewer MRI scanners are X-nuclei capable). Nevertheless, the diagnostic value of MRI/MRS scans is still restricted by an inherently low signal-to-noise ratio (SNR), often resulting in a compromise between image spatial resolution, scan time, and signal intensity. These issues are exacerbated in non-proton (X-nuclei) MRI, i.e. ^{31}P, ^{13}C, ^{23}Na (NMR active isotopes of phosphorous, carbon, and sodium respectively) etc., due to lower endogenous nuclei concentrations and lower gyromagnetic ratios which leads to lower polarization levels. As such, significant work has been done to increase the signal and contrast of MRI, as assessed by the SNR and contrast-to-noise ratio (CNR), through multiple mechanisms including increasing the static magnetic field strength of the MRI scanner, injection of contrast agents such as gadolinium [5], and artificially enhancing the polarization in the case of hyperpolarized non-proton MRI [6]. These methods, however, can be extremely costly; for example, increasing the field strength of an MRI scanner costs approximately £$1\,000\,000$ per tesla, T. Additionally, they may introduce additional complexities to the study; in the case of artificially enhanced polarization such as for hyperpolarized ^{13}C MRI, the total SNR is limited by the degree of hyperpolarization achieved, and the enhanced signal decays rapidly over the course of several minutes.

1.1 Motivation

The sensitivity of conventional magnetic resonance techniques are inherently restricted by low polarization obtained at achievable static magnetic field strengths and physiological body temperatures, resulting in compromises between spatial or spectral resolution, scan time, and signal intensity. This arguably forms the greatest limitation of the MRI technique. The MR signal is

measured through radiofrequency (RF) electromagnetic interactions with the sample (patient) under study. Interchangeable devices known as Radio-Frequency (RF) coils connect to the MR scanner to provide means to transmit and receive the electromagnetic signal at the resonant frequency of the nuclei of interest. The achievable SNR in any MRI experiment is strongly influenced by these RF coils used to acquire the MR signal through a two part process: the transmission of an oscillating magnetic field into the body (B_1^+), and the subsequent reception of signals emitted from the body in response.

Here, we discuss the motivation of this thesis from three aspects: firstly, a more efficient RF coil design for increased SNR; secondly, the need for an improved method of surface coil comparison and optimisation; and thirdly, the development of the novel design into an optimised RF array comprised of multiple elements for high sensitivity over a larger field of view.

1.1.1 Need for increased sensitivity through coil design

Individual coils are typically optimised for one of two tasks, namely RF transmission and reception. The role of the RF coil may be designated to transmit only (To), receive only (Ro), or operate transmit and subsequently receive (Tx-Rx). In the case where power delivery into the RF coil is not a limiting factor, as is typical for clinical proton MRI, the widely accepted paradigm consists of a volume transmit RF coil enclosing the patient for high transmit uniformity and a separate closely fitted surface receive coil array for high receive sensitivity [7]. However, in the case of X-nuclei MRI, RF power amplifiers are typically broad-banded to accommodate the range of frequencies required, which limits their maximum power output. Furthermore, whilst all clinical MR scanners contain a large, powerful, proton transmit 'body' coil, typically X-nuclei capable clinical MR scanners do not possess a multi-nuclear volume transmit coil. As such, surface coil elements are commonly used for both transmit and receive operations, both to achieve adequate transmit field strength and for optimal SNR.

Many approaches have been proposed to enhance sensitivity of *in vivo* MR over the last thirty years, such as increasing the main static magnetic field of the instrument, B_0 [8, 9]; cryogenically cooling coil circuitry to $77\,\mathrm{K}$ or below [10–12]; or exogenous nuclear hyperpolarization mechanisms that briefly circumvent the polarization limitation by imaging introduced non-equilibrium spin-labelled probes, revealing new information on disease [13–16]. However, all of these approaches come with significant associated disadvantages and greatly increased

cost: for example, increasing B_0 quickly becomes prohibitively expensive, relegating whole body human $>7\,\mathrm{T}$ scanners to under 100 worldwide (as of 2022) [17, 18]. Cryogenic RF coils inherently require rigid thermal insulation between conducting elements and the subject, are challenging to engineer, and furthermore can only provide benefit if the dominant noise sources is from coil circuitry, and therefore have only found niche application in small-animal pre-clinical MRI. As such, an efficient RF coil is needed to maximise available SNR. A novel highly B_1^+ and SNR efficient coil design would be beneficial for both ^{1}H and X-nuclei imaging, without the large costs associated with the alternatives.

1.1.2 Robust protocol for characterising and optimising surface RF coils

The EM field profile from an RF coil is determined by the design of the conductor in the coil. The field profile generated poses a trade-off between field uniformity and field strength, particularly in the case of surface coils where the field strength close to the coil centre can be orders of magnitude larger than the field strength at one coil diameter off-centre. Accurate B_1 and SNR field mapping of such an inhomogeneous profile proves challenging with commonly used techniques. Secondly, X-nuclei scans experience approximately 10^5 times lower SNR, therefore conventional ^{1}H mapping techniques require prohibitively long scan times for X-nuclei making them unsuitable for clinical use. A protocol is required that is able to produce accurate field maps with sufficient resolution using X-nuclei surface coils, that is robust to highly inhomogeneous field profiles and low SNR.

Optimisation of an RF coil design is unique to the coil design and highly dependent on the job and corresponding requirements of said coil. This motivates for a robust coil optimisation protocol to be developed to allow fair comparison between different coil designs, and to rapidly determine the best design for a given application. Comparison between coil designs is possible through EM simulations, which can determine field profiles without the need for construction of prototypes and subsequent testing. The accuracy of EM simulation results is dependent on the intricacy of the model and mesh density, and requires validation against known B_1 values through measured B_1 field maps. Due to the aforementioned field uniformity and strength trade-off that occurs across a range of dimensions, direct comparison and optimisation of a coil design is challenging; as such a method of characterising the trade off for a given range of dimensions within a coil design is required.

1.1.3 Investigating array design using multiple optimised elements

Lastly, owing to their fundamental requirements in all MRI experiments, much recent activity has focused on improving surface coil designs for MRI. Overall, the design philosophy of array coils has been to: simultaneously cover a large, anatomically appropriate field-of-view (FOV), conform to patient anatomy [19], be amenable to parallel imaging reconstruction methods, and be physically manufacturable. These constraints pose challenging engineering problems, but the fundamental physically-determined trade-off lies in the design of each element. With advancements in flexible PCB (printed circuit board) technology, more complex coil element designs with higher field efficiency can now be utilised as flexible RF coils. RF coil arrays consist of multiple individual loop elements, arranged for greater spatial coverage compared to a single element, whilst retaining the high sensitivity of smaller elements [20]. The most widely used array element is a single resonant loop formed from a circular or square conductor track. The field profiles of such loops are highly dependent on their dimensions, with smaller loops achieving higher magnetic field strengths close to the coil but with a steeper drop-off in magnetic field as distance from the coil increases. As such, the benefits of a higher density array is two fold: firstly allowing an increase in sensitivity closer to the coil over a large FOV (however not at depth). Secondly, the numerous coil elements permits the temporal acceleration of the MRI acquisition by the use of parallel imaging techniques [21–23] for reduced scan time [24]. However, the maximum depth sensitivity of an array is thus limited by the design of its elements, which in turn is limited by the anatomy of choice. Dense arrays have been particularly prominent in neuro-imaging due to the smaller distance to the centre of the head. For the imaging of thoracic organs, a coil with better depth penetration is required, typically at the cost of reduced sensitivity [25]. The ability for arrays to be constructed whilst preserving the high sensitivity of individual elements requires geometric decoupling of the individual elements. Investigation into the potential to construct arrays using a more efficient coil element design, will allow for an increased SNR over a greater depth of penetration, retaining the benefits of highly sensitive elements and array field coverage.

1.2 Objectives

With recent advancements in computational power, electromagnetic simulations allow us to rapidly test and identify novel valid RF coil designs, thereby bringing new opportunities to the field of RF coil development where commonly used surface coil element shapes have remained largely consistent over the last 30 years. This project develops and investigates a novel coil design, from developing a robust characterisation protocol and frameworks for design optimisation through to the performance of the coil in a clinical setting. The aims and objectives of this project are discussed below.

1. Developing a coil characterisation protocol that is robust, able to deal with high variation in field profile from surface coils, and accurate at low SNR.
2. Developing a framework for optimising transmit and receive surface coil element designs, through EM simulation.
3. Investigating a novel coil design for improved transmit field efficiency and receive sensitivity, verifying improvements through EM simulations and construction of a pre-clinical prototype.
4. Construction and human translation of a novel RF coil design, for human volunteer scans and comparison with existing clinical coils.

1.3 Outline of Chapters

The remainder of the thesis is organised as follows:

- Chapter 2 presents the theory of NMR, from both medical applications and engineering perspectives. With a focus on radiofrequency hardware, differences between transmit and receive operation as well as pre-clinical and clinical hardware are discussed.
- Chapter 3 provides a background review of X-nuclei RF coil design, construction and associated characterisation methods of surface coils. Three domains of measuring coil performance are discussed: benchtop measurements, EM simulations and phantom scans. A fully-sampled coil characterisation is implemented, allowing for both transmit and receive field mapping from a single scan, and is robust to high field variation and low SNR. Finally, methods for patient safety through verifying RF coil heating are presented.

- Chapter 4 presents a novel class of coil designs, 'multi-layer' RF coils, that utilise a 3D conductor geometry for increased SNR. A proof of concept multi-layer prototype is constructed for pre-clinical MRI. The multi-layer design requirements and current working theory are presented. Results from EM simulations and scanner measurements indicate improved transmit performance; however, further optimisation is necessary for receive sensitivity.

- Chapter 5 translates the multi-layer design presented in Chapter 4 into a suitable coil for human MRI. Optimisation of a parameterised multi-layer model is performed using EM simulations for four and six vertically-stacked layers, allowing simultaneously improved B_1 field uniformity and field efficiency. Several multi-layer RF coils were constructed for carbon and phosphorus MRI, where improvements in transmit and receive performance were recorded. Heating tests for human use and additional conductor designs were investigated. The most notable result was a two-fold increase in SNR across five human participants using the multi-layer coil when compared to a comparable commercially available coil.

- Chapter 6 investigates RF coils comprising of multiple elements, in two commonly used configurations: individual transmit-receive elements placed around the torso, and overlapped elements in array configurations. The performance of using one to four individual TxRx elements are characterised along with phase configurations, and compared to existing coil designs. An optimum four element transmit only array was constructed and tested on the scanner, to be used in conjunction with a multi-layer receive only array. A multi-layer array was developed which investigated the extent of geometric decoupling, phase shift and overlap angle using multi-layer elements which are four-fold rotationally symmetric. The multi-layer receive array allows for increased receive sensitivity over conventional arrays, over a larger FOV.

- Chapter 7 concludes this thesis by discussing the application, limitations and further work of the three achievements that stemmed from this project: a novel coil design with improved B_1 and SNR, a protocol for characterising and comparing RF coil performance, and the construction of an optimised cardiac array for ^{13}C MRI of the torso.

References

[1] Prince, J. L. and Links, J. *Medical Imaging Signals and Systems*. 2nd. Pearson, 2014. ISBN: 9780132145183.

[2] Vick, G. W. "The gold standard for noninvasive imaging in coronary heart disease: magnetic resonance imaging". In: *Current Opinion in Cardiology* 24 (6 Nov. 2009), pp. 567–579. ISSN: 0268-4705. DOI: 10.1097/HCO.0b013e3283315553.

[3] Ma, D. et al. "Magnetic resonance fingerprinting". In: *Nature* 495 (7440 Mar. 2013), pp. 187–192. ISSN: 0028-0836. DOI: 10.1038/nature11971.

[4] Ogbole, G. I. et al. "Survey of magnetic resonance imaging availability in West Africa". In: *Pan African Medical Journal* 30 (2018). ISSN: 19378688. DOI: 10.11604/pamj.2018.30.240.14000.

[5] Lohrke, J. et al. "25 Years of Contrast-Enhanced MRI: Developments, Current Challenges and Future Perspectives". In: *Advances in Therapy* 33 (1 Jan. 2016), pp. 1–28. ISSN: 0741-238X. DOI: 10.1007/s12325-015-0275-4.

[6] Ardenkjaer-Larsen, J. H. et al. "Increase in signal-to-noise ratio of $>$ 10,000 times in liquid-state NMR". In: *Proceedings of the National Academy of Sciences* 100 (18 Sept. 2003), pp. 10158–10163. ISSN: 0027-8424. DOI: 10.1073/pnas.1733835100.

[7] Bendall, M. R., Connelly, A., and McKendry, J. M. "Elimination of coupling between cylindrical transmit coils and surface-receive coils forin vivo NMR". In: *Magnetic Resonance in Medicine* 3 (1 Feb. 1986), pp. 157–163. ISSN: 07403194. DOI: 10.1002/mrm.1910030124.

[8] Schild, T. et al. "The Iseult/Inumac Whole Body 11.7 T MRI Magnet Design". In: *IEEE Transactions on Applied Superconductivity* 18 (2 June 2008), pp. 904–907. ISSN: 1051-8223. DOI: 10.1109/TASC.2008.921264.

[9] Sclocco, R. et al. "Challenges and opportunities for brainstem neuroimaging with ultrahigh field MRI". In: *NeuroImage* 168 (Mar. 2018), pp. 412–426. ISSN: 10538119. DOI: 10.1016/j.neuroimage.2017.02.052.

[10] Sanchez-Heredia, J. D. et al. "Low-Noise Active Decoupling Circuit and its Application to 13C Cryogenic RF Coils at 3 T". In: *Tomography* 3 (1 Mar. 2017), pp. 60–66. ISSN: 2379-139X. DOI: 10.18383/j.tom.2016.00280.

[11] Darrasse, L. "Perspectives with cryogenic RF probes in biomedical MRI". In: *Biochimie* 85 (9 Sept. 2003), pp. 915–937. ISSN: 03009084. DOI: 10.1016/j.biochi.2003.09.016.

[12] Wright, A. C., Song, H. K., and Wehrli, F. W. "In vivo MR micro imaging with conventional radiofrequency coils cooled to 77 K". In: *Magnetic Resonance in Medicine* 43 (2 Feb. 2000), pp. 163–169. ISSN: 0740-3194. DOI: 10.1002/(SICI)1522-2594(200002)43:2<163::AID-MRM1>3.0.CO;2-K.

[13] Ross, B. et al. "Hyperpolarized MR Imaging: Neurologic Applications of Hyperpolarized Metabolism". In: *American Journal of Neuroradiology* 31 (1 Jan. 2010), pp. 24–33. ISSN: 0195-6108. DOI: 10.3174/ajnr.A1790.

[14] Grist, J. T. et al. "Hyperpolarized 13C MRI: A novel approach for probing cerebral metabolism in health and neurological disease". In: *Journal of Cerebral Blood Flow & Metabolism* 40 (6 June 2020), pp. 1137–1147. ISSN: 0271-678X. DOI: 10.1177/0271678X20909045.

[15] Apps, A. et al. "Proof-of-Principle Demonstration of Direct Metabolic Imaging Following Myocardial Infarction Using Hyperpolarized 13C CMR". In: *JACC: Cardiovascular Imaging* 14 (6 June 2021), pp. 1285–1288. ISSN: 1936878X. DOI: 10.1016/j.jcmg.2020.12.023.

[16] Rider, O. J. et al. "Noninvasive In Vivo Assessment of Cardiac Metabolism in the Healthy and Diabetic Human Heart Using Hyperpolarized 13C MRI". In: *Circulation Research* 126 (6 Mar. 2020), pp. 725–736. ISSN: 0009-7330. DOI: 10.1161/CIRCRESAHA.119.316260.

[17] Clarke, W. T. et al. "Multi-site harmonization of 7 tesla MRI neuroimaging protocols". In: *NeuroImage* 206 (2020), p. 116335. ISSN: 1053-8119. DOI: https://doi.org/10.1016/j.neuroimage.2019.116335.

[18] Huber, L. *Ultra-High Field MRI scanners*. 2022. URL: https://drive.google.com/open?id=1dXG84OZIAOxjsqh3x2tGzWL1bNU (visited on 05/05/2022).

[19] Corea, J. R. et al. "Screen-printed flexible MRI receive coils". In: *Nature Communications* 7 (1 Apr. 2016), p. 10839. ISSN: 2041-1723. DOI: 10.1038/ncomms10839.

[20] Roemer, P. B. et al. "The NMR phased array". In: *Magnetic Resonance in Medicine* 16 (2 Nov. 1990), pp. 192–225. ISSN: 07403194. DOI: 10.1002/mrm.1910160203.

[21] Breuer, F. A. et al. “Controlled aliasing in volumetric parallel imaging (2D CAIPIRINHA)”. In: *Magnetic Resonance in Medicine* 55 (3 Mar. 2006), pp. 549–556. ISSN: 0740-3194. DOI: 10.1002/mrm.20787.

[22] Griswold, M. A. et al. “Generalized autocalibrating partially parallel acquisitions (GRAPPA)”. In: *Magnetic Resonance in Medicine* 47 (6 June 2002), pp. 1202–1210. ISSN: 0740-3194. DOI: 10.1002/mrm.10171.

[23] Shin, P. J. et al. “Calibrationless parallel imaging reconstruction based on structured low-rank matrix completion”. In: *Magnetic Resonance in Medicine* 72 (4 Oct. 2014), pp. 959–970. ISSN: 07403194. DOI: 10.1002/mrm.24997.

[24] Wiesinger, F., Boesiger, P., and Pruessmann, K. P. “Electrodynamics and ultimate SNR in parallel MR imaging”. In: *Magnetic Resonance in Medicine* 52 (2 Aug. 2004), pp. 376–390. ISSN: 0740-3194. DOI: 10.1002/mrm.20183.

[25] Baert, A. L. et al. *Parallel Imaging in Clinical MR Applications*. Springer, 2007. ISBN: 9783540688792.

2 | Background Theory

This chapter describes the background theory of MR imaging and spectroscopy as required for a full understanding of the materials covered in this thesis. This chapter is split into three sections: firstly, section 2.1 outlines the physical principles behind MRI, focusing on the electromagnetic fields used to detect the MR signal and the measurement of noise. Following on, section 2.2 discusses the engineering requirements for MR hardware, with a specific focus on radiofrequency related hardware. Lastly, section 2.3 provides a brief overview of the applications of MRI, distinguishing between conventional proton MRI and research-focused non-proton (X-nuclei), addressing in particular three primary nuclei investigated in this work: ^{13}C, ^{31}P, and ^{23}Na. Only brief discussion of image formation and pulse sequence design is included here as this work primarily focuses on hardware design and characterisation; extensive discussions of pulse sequence design and theory can be found elsewhere [1].

2.1 Nuclear Magnetic Resonance: Physical Principles

Broadly, the physics behind MR scanners can be described through both a classical and quantum mechanical framework. In this section, a brief overview of electromagnetism and the generation of EM fields is first described. This section then continues by presenting a quantum mechanical approach for describing magnetisation as the behaviour of individual nuclei. Subsequently, a classical approach is considered by describing the magnetisation as the net effect of an ensemble of nuclei. The discussions presented here are brief with minimal derivation, as more detailed descriptions of the underlying quantum mechanical principles are well understood, and can be found in textbooks [2].

2.1.1 Electromagnetic Fields

Electromagnetic (EM) fields are produced by accelerating electrical charges, described by the Lorentz force equation 2.1, with a force $\mathbf{F}$, from a charge, q, moving at velocity, $\mathbf{v}$, with an electric field, $\mathbf{E}$, and magnetic field, $\mathbf{B}$.

$$\mathbf{F} = q\mathbf{E} + q\mathbf{v} \times \mathbf{B} \tag{2.1}$$

In the case of MR, EM fields are generated by accelerating and decelerating electrons in the 'RF' coils used for the transmission and reception of signals, and, as such, a combination of both, time varying, electric and magnetic fields in 3D space is generated at the radio-frequency. Accurate determination of these EM fields is crucial to the design and characterisation of RF coils, to improve the strength of the magnetic fields generated and the quality (SNR) of MRI. These EM interactions (time evolution of E- and B-fields) can be fully described by a set of spatially and temporally varying differential equations, Maxwell's equations, in free space, described by equations 2.2 to 2.5 [3], with permittivity of free space, ϵ_0, permeability of free space, μ_0, charge density, ρ, and current density, $\mathbf{J}$. For simplicity, the Maxwell's equations presented here are of the differential form. In the case of MRI, the EM fields travel through a polarizable media; a brief summary of Maxwell's equations in polarizable media are presented in Appendix A. For completeness, the integral forms of Maxwell's equations are also shown in Appendix A, as both formulations are used by EM simulations as presented later in section 3.2.

$$\nabla \cdot \mathbf{E} = \frac{\rho}{\epsilon_0} \tag{2.2}$$

$$\nabla \cdot \mathbf{B} = 0 \tag{2.3}$$

$$\nabla \times \mathbf{E} = -\frac{\partial \mathbf{B}}{\partial t} \tag{2.4}$$

$$\nabla \times \mathbf{B} = \mu_0 \left(\mathbf{J} + \epsilon_0 \frac{\partial \mathbf{E}}{\partial t} \right) \tag{2.5}$$

For characterisation of the performance of RF coil designs, we seek solutions to the Maxwell equations for the E- and B-fields generated by the RF coil over typically a 3D region of interest (ROI). However, solutions to Maxwell's equations for EM systems with complex geometries and electromagnetic interactions (such as RF coils on the human body) are in general impossible to find analytically, and typically analytical solutions require either very highly constrained geometries or other simplifications to the equations. In an effort to simplify the field of electromagnetism, three branches of study exist with different assumptions that can approximate EM systems within their own regimes, their application to describe RF coil behaviour is discussed below:

- **Electrostatics** assumes that the electric charges ρ are at rest, and the time derivatives are zero. This is inappropriate for MRI as electrostatics only deals with electric fields.

- **Magnetostatics** assumes magnetic fields are generated by a constant electric current such that the charge is stationary or constant in velocity (and does not accumulate). This leads to the Biot-Savart equation 2.6, relating the magnetic field, $\mathbf{B}(\mathbf{r})$, at given point $\mathbf{r}$ from the axis, to the current, I, integrated over the path, C, of current flow [4]. The approximation of constant current is most valid for low frequency and direct currents (DC), but is less accurate for higher frequency oscillations. In the radiofrequency range, the Biot-Savart equation typically overestimates the B_1 field compared to measurements and full wave simulations. For the case of a circular RF coil of radius a, the Biot-Savart equation can be used to make useful initial approximations for the on-axis B_1 field strength, following equation 2.7.

$$\mathbf{B}(\mathbf{r}) = \frac{\mu_0}{4\pi} \int_C \frac{I d\mathbf{l} \times \mathbf{r'}}{|\mathbf{r'}|^{\mathbf{3}}} \tag{2.6}$$

$$B_{\text{On-axis}} = \frac{\mu_0 I a^2}{2(x^2 + a^2)^{3/2}} \tag{2.7}$$

- **Electrodynamics** allows for time varying currents, such that oscillating magnetic fields can be modelled. This is most valid for RF coils, as high frequency B-field oscillations can be accurately represented. However, Maxwell's equations cannot be solved analytically for 3D space and time for complex geometries. We are interested in the behaviour of EM fields, as they are generated by RF coils, which comprise of a fast (radio-frequency) time varying current. In this work, computational electromagnetic (EM) simulations are used extensively to approximate solutions to Maxwell's equations. Both theoretical simulations and experimental results are used to determine the EM field profile of an RF coil design.

2.1.2 Nuclear Spin

Atomic nuclei are comprised of protons and neutrons, and have an intrinsic 'spin' property. Spin, I, represents the intrinsic angular momentum, where both proton and neutrons have spin $I = 1/2$. Several different total spin states for the nuclei are possible: zero spin arises from an even number of protons and an even numbers of neutrons. Integer spins arise from an odd number of protons and an odd number of neutrons. Finally, half-integer spins arise from either odd protons and even neutrons, or even protons and odd neutrons. MRI can only observe nuclei with non-zero spins, mainly investigating half-integer spin nuclei - such as ^{1}H (primarily), ^{31}P,

^{13}C with spin $1/2$, or ^{23}Na with spin $3/2$, but also ^{2}H with spin 1, as a generalisation, termed NMR active isotopes.

2.1.2.1 Quantum Mechanical Framework

Within the main static magnetic field, B_0, the spins are polarized, creating magnetisation as described below. Outside of this magnetic field, there is no spin alignment, and thus no polarization or magnetisation. All MRI activities are performed within a homogeneous B_0 field. First, considering a spin $1/2$ nuclei, the quantum mechanical framework treats spins individually in two states: spin 'up' representing parallel orientation to B_0, and spin 'down' representing anti-parallel orientation to B_0 [2]. Two equations can be defined: firstly, the Larmor equation determining the Larmor frequency , ω_0, which is proportional to the energy difference, E, between the spin up and spin down states. This energy difference is determined by the gyromagnetic ratio, γ, and B_0 as shown in equation 2.8, where the γ is the ratio of the nuclei magnetic moment to its angular momentum.

$$\hbar\omega_0 = \Delta E = \gamma\hbar B_0 \tag{2.8}$$

It can be shown by considering the partition function, Z, for a spin-half (two level) system where $Z = 2\cosh\left(\frac{\beta\Delta E}{2}\right)$ that the nuclear polarization P at thermal equilibrium can be described by a Boltzmann distribution by equation 2.9, where $N_\uparrow$ is the population of up spins, and $N_\downarrow$ is the population of down spins at temperature T, and Boltzmann constant k_B.

$$P = \frac{N_\uparrow - N_\downarrow}{N_\uparrow + N_\downarrow} = \tanh\frac{\gamma\hbar B_0}{2k_B T} \approx \frac{\gamma\hbar B_0}{2k_B T} \tag{2.9}$$

The non-zero polarization gives rise to a magnetisation as each spin has a non-zero magnetic moment. As an example, at a field strength of $7\,\mathrm{T}$, out of one million proton nuclei, we expect approximately only six more spins in the up states compared to the down state. This low polarization is the primary reason for the intrinsically low sensitivity of MRI.

2.1.2.2 Classical Framework

Secondly, the classical framework can be considered following the discussion in [5], where an ensemble of nuclear spins are considered as a single net magnetisation vector, $\mathbf{M}$. Classically, $\mathbf{M}$ can be derived in terms of an applied magnetic field $\mathbf{B}$:

$$\frac{d\mathbf{M}}{dt} = \gamma(\mathbf{M} \times \mathbf{B}) \tag{2.10}$$

An oscillating radiofrequency field, B_1, oscillating at ω can be applied to the system in a direction that is perpendicular to the static B_0 field:

$$\mathbf{B_1} = B_1 \cos(\omega t)\hat{\mathbf{i}} - B_1 \sin(\omega t)\hat{\mathbf{j}} \tag{2.11}$$

The net magnetisation $\mathbf{M}$ is subsequently displaced (rotated) by the application of the B_1 field towards the transverse plane (i.e. perpendicular to the static magnetic field, B_0). This can be considered both in the static frame, an arbitrary coordinate system that is stationary, and consistent with the observer, or a rotating frame, with the z-axis aligned, and x, y-axes rotating at ω. Observing the excitation in a static frame of reference, the magnetisation vector $\mathbf{M}$ appears to spiral out of the alignment with B_0, as shown in Figure 2.1. Due to the rotating $\mathbf{M}$, it is simpler to describe the behaviour in the rotating frame of reference, where precession of the magnetisation is altered by both the B_0 (with precession at $\omega_0 = \gamma B_0$) and B_1 (with precession at $\omega_a = \gamma B_1$) according to equation 2.12 [6].

$$\frac{d\mathbf{M}}{dt} = \gamma(\mathbf{M} \times \mathbf{B_{eff}}) \tag{2.12}$$

where $\mathbf{B}_{\text{eff}}$ is:

$$\mathbf{B}_{\text{eff}} = \left(B_0 - \frac{\omega_a}{\gamma}\right)\hat{\mathbf{k}} + B_1\hat{\mathbf{i}}' \tag{2.13}$$

With the frame rotating counter-clockwise around the z-axis with an angular frequency ω, B_1 appears as a fixed magnetic field vector and the magnetisation $\mathbf{M}$ slowly tips into the transverse plane rotating at ω, as shown in Figure 2.1. The final tipped rotation position of the net magnetisation relative to the longitudinal axis depends on both the amplitude and duration of the applied B_1 field, if an RF pulse of amplitude B_1^+ with duration τ is applied, this rotates $\mathbf{M}$

by the flip angle α according to equation 2.14.

$$\alpha = \gamma \int_0^\tau B_1(t)dt \tag{2.14}$$

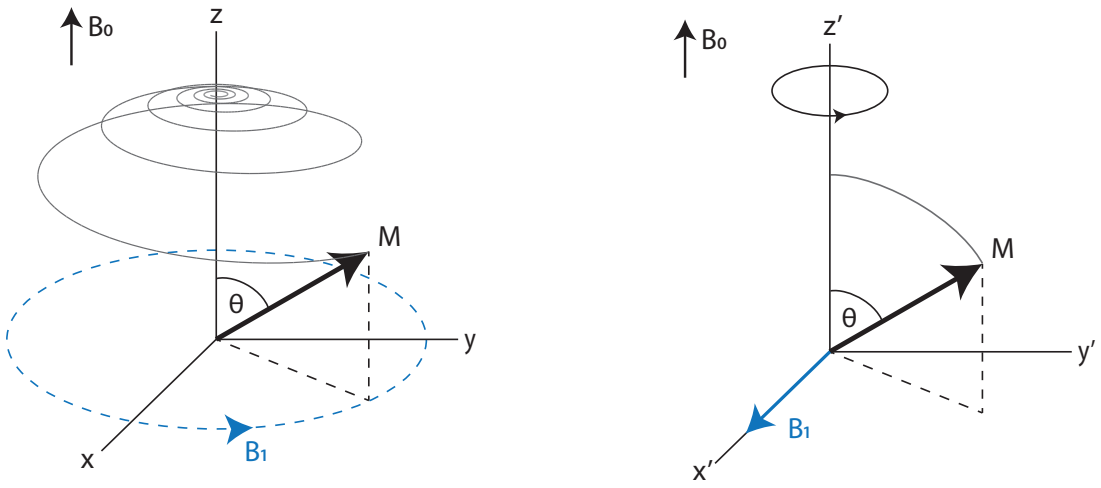

Figure 2.1: Diagram of magnetisation precession in (a) the static laboratory frame, where B_0 is aligned to the z-axis, both M and B_1 are precessing in the x-y plane at the frequency ω, (b) the rotating frame (counter-clockwise) around the z-axis at ω, where B_0 is still aligned to the z-axis, both M and B_1 tip towards the x-y plane.

2.1.3 Image Reconstruction

Unlike conventional NMR, MR imaging (and sometimes spectroscopy) utilises gradient magnetic fields to spatially encode the nuclei. The spatial encoding allows reconstruction of the original image from the measured signal of the receive coil. A brief overview of signal formation and image reconstruction is presented in this section.

The RF coil operates in a two step process, firstly, the coil transmits a B_1 field termed B_1^+ which is the right handed circularly polarized component of the B_1 field. This field interacts with the nucleus in the body as described above, and a subsequent B_1^- field (approximately of the opposite handedness to B_1^+, comprised the left handed circularly polarized component of the B_1 field) is received by the coil. When this receiver coil is brought close to the processing magnetisation, the time-varying B-field induces an electric current according to Faraday's law. The induced current generates a voltage which is measured through the magnitude and phase of

the signal, creating a complex MR signal. In addition to coil related factors discussed throughout this thesis, the signal is also proportional to external non coil-related factors: namely the B_0 and gyromagnetic ratio, γ defined above in section 2.1.2.1).

$$\text{signal} \propto \frac{\gamma^3 B_0^2}{T} \tag{2.15}$$

The final received signal magnitude to noise level is what determines the overall SNR.

2.1.3.1 Bloch Equations and Magnetisation Relaxation

The behaviour of the net magnetisation is governed by the Bloch equations 2.16 [7], expanding on 2.12, but including two relaxation time constants: T_1 (spin-lattice relaxation time constant) and T_2 (spin-spin relaxation time constant), and where $\mathbf{M}_0$ is the magnetisation at equilibrium along the static external magnetic field B_0.

$$\frac{d\mathbf{M}}{dt} = \mathbf{M} \times \gamma\mathbf{B} - \frac{\mathbf{M}_x\hat{l} + \mathbf{M}_y\hat{j}}{T_2} - \frac{(\mathbf{M}_z - \mathbf{M}_0)\hat{k}}{T_1} \tag{2.16}$$

Post application of the B_1^+ field (after transmission), the Bloch equation describes the trajectory of the magnetisation, M, during the RF pulse application at time, t, and as it spirals back to the equilibrium state, M_0. The process of relaxation (returning to equilibrium state) is determined by T_1 and T_2, described below. From equation 2.16, we can define the longitudinal (z) component of magnetisation, after an excitation flip angle of $90°$ as:

$$\mathbf{M}_z = \mathbf{M}_0 \left(1 - e^{-\frac{t}{T_1}}\right) \tag{2.17}$$

Here, the T_1 describes the rate of recovery of the longitudinal magnetisation towards equilibrium as it follows an exponential recovery path. A proportion of the increased high energy state will decrease to the low energy state, losing energy to the surrounding lattice. When the B_0 is aligned along z, the higher energy state will be the spin 'up' state.

Similarly, from the equation 2.16, we can define the transverse component (xy-plane) of the magnetisation, after an excitation flip angle of 90° as:

$$\mathbf{M}_{xy} = \mathbf{M}_0 e^{-\frac{t}{T_2}} \tag{2.18}$$

A simplified representation of the T_2, is as the decay in transverse magnetisation resulting from the dephasing (loss of phase coherence) of spins, that arises from local B_0 field inhomogeneities due to molecular tumbling. Both T_1 and T_2 are highly dependent on tissue type, allowing definition of soft tissue contrast.

Lastly, the time constant, ${T_2}^*$, is the combined effect from relaxation mechanisms from T_2 combined with inhomogeneities of the external B_0, which results in precession at frequencies around the Larmor frequency, and such that ${T_2}^* \leq T_2$. ${T_2}^*$ is related to T_2 and the field inhomogeneity ΔB_0 as described by equation 2.19 below.

$$\frac{1}{T_2^*} = \frac{1}{T_2} + \gamma \Delta \mathbf{B}_0 \tag{2.19}$$

2.1.3.2 Image Formation

This decaying signal is subsequently measured by the RF 'receive' coil, as the free induction decay (FID). However, for magnetic resonance imaging and spectroscopy, gradients are applied during the scan to allow spatial encoding of signal. To achieve this, MRI scanners contain three gradient coils, described below in section 2.2.1.2, which produce linear magnetic fields along the three Cartesian axis: x, y and z-directions. A linear ramping of the magnetic field strength, G allows the precession frequency ω of the nuclear spins to differ depending on their position, r such that:

$$\omega = \gamma(\mathbf{B}_0 + \mathbf{G} \cdot \mathbf{r}) \tag{2.20}$$

The subsequent total phase shift, ϕ for a given position is the time integral of ω:

$$\phi = \gamma \int_0^t \mathbf{G}(\tau) \cdot \mathbf{r} d\tau \tag{2.21}$$

The nuclear precession frequency and phase allows for spatial encoding, where sets of nuclei at each position in space will have a different spin property. For MRI, we commonly desire a stack of 2D images, and so perform three operations to the nuclei: spatial encoding in two directions, and the selection of a single slice. The slice selection, typically performed to acquire 2D images, uses a slice selective gradient in conjunction with an RF pulse. The slice selection varies the resonance frequency of the spins, such that the RF pulse applied will only excite a narrow

band (or slice) of nuclei. Following on from this, to achieve imaging in the other two dimensions, frequency and phase encoding are applied. The frequency encoding gradient, varies the precession frequency linearly in space during acquisition. Additionally, phase-encoding gradient is applied between the excitation and reception of the signal, commonly in the y-direction, always perpendicular to the frequency encoding direction, by applying a linear variation of phase to the image. This is a very brief description of imaging, and further details can be found in [1] and [2].

2.1.3.3 k-Space

The subsequent time dependent received signal, $s(t)$, is picked up by the RF coil and comprises of the magnetisation integrated over the imaging volume determined by the coil FOV. The signal, $s(t)$, possesses a complex phase component, ϕ, introduced by the gradients from equation 2.21, and magnetisation at given position, $M(r)$, introduced by the B_1 field, T_1 and T_2 values, described in the equations below:

$$s(t) = \int \mathbf{M}(\mathbf{r}) e^{i\gamma \int_0^t \mathbf{G}(\tau)\cdot\mathbf{r} d\tau} d\mathbf{r} \tag{2.22}$$

We can substitute for:

$$\mathbf{k}(t) = -\frac{\gamma}{2\pi} \int_0^t \mathbf{G}(\tau) d\tau \tag{2.23}$$

Such that:

$$s(t) = \int \mathbf{M}(\mathbf{r}) e^{-i2\pi\mathbf{k}(t)\mathbf{r}}\, d\mathbf{r} \tag{2.24}$$

Equation 2.24 for the received signal is the form of a Fourier transform for spatial magnetisation, where $k(t)$ is the k-space spatial frequency. In k-space, the image resolution and field of view (FOV) are reciprocal, such that high k-space values (on the edge of k-space) represents high frequencies relating to small details in image space, whilst small k-space values (at the centre of k-space) represents low frequencies relating to the FOV and structure. Reconstruction methods aim to efficiently acquire samples of k-space for conversion into an image. The FOV in image space is determined by the sampling density Δk of k-space for each dimension, such that FOV $= \frac{1}{\Delta k}$. An inverse Fourier transform can be applied to $s(t)$ to obtain the original magnetisation $M(r)$ at each voxel in real space. In this thesis, a Fast Fourier Transform (FFT) was applied over a Cartesian sampled grid, to obtain a final image of a map of magnetisation,

from the received MR signal. Further detail of reconstruction methods are elaborated upon in the Methods chapter, specifically in section 3.4.

2.1.4 Noise

Ultimately, the most useful metric of an MRI scan is the measured signal-to-noise (SNR). The final measured noise is dependent on multiple hardware design parameters, which are discussed in this chapter.

Typically, SNR is only determined after the image or spectra has been acquired and reconstructed. However, this overall SNR comprises of the sum of individual noise contributions from components up the imaging chain. As SNR is measured at the end of the image acquisition, it is difficult to monitor the relative contributions and effects of noise from each step in the overall scan. As a broad overview, two areas of SNR contribution from a typical scan are presented below: hardware, and imaging technique.

1. **Hardware.** The components of hardware that introduce noise consist of:
    - Inhomogeneities in, and the strength of, the main magnetic field B_0, leading to the decay of signal according to ${T_2}^*$, equation 2.19.
    - Resistance from inductive coupling of the RF coil to the sample, coil resistance and preamplifier resistance, the origins of which are discussed in section 2.1.4.4 below.
    - Contamination from external sources of noise, and noise from components further down the receive chain such as the mixer and analogue-to-digital converter (ADC).
2. **Imaging Sequence and Reconstruction.** Parameters of the imaging sequence also determine the overall signal level, such as:
    - Image resolution and additional scan parameters.
    - The addition of contrast agents (enhancement techniques e.g. Gadolinium).
    - k-space sampling strategies (e.g. non-uniform sampling schemes).
    - The reconstruction method, such as accelerated (parallel) imaging techniques and the method of combining multiple coils (e.g. sum-of-squares).

In the field of MRI technical development, significant work is being done in developing more efficient imaging sequences and reconstruction techniques. This work primarily focuses on hardware improvements, specifically exploring the RF coil and sample noise.

2.1.4.1 SNR Definitions

SNR calculations can be somewhat subjective, however work has been done towards quantification of SNR [8], and common definitions are used among the MR community. There are generally two common SNR definitions, both are used throughout this project:

1. SNR can be defined as the ratio of signal power, P_{Signal}, to background noise power, P_{Noise}, of the measurement. An equivalent alternative formulation is the root-mean-squared (RMS) signal amplitude, A_{signal}, divided by the RMS noise amplitude, A_{Noise}, where A represents the induced current or voltage [9]. Both descriptions are presented below, in equation 2.25.
$$\text{SNR} = \frac{P_{\text{signal}}}{P_{\text{noise}}} = \left(\frac{A_{\text{signal}}}{A_{\text{noise}}}\right)^2 \tag{2.25}$$
2. In the case of a uniform phantom (with no variation in composition across the phantom) an alternative definition of SNR is the reciprocal of the coefficient of variation (CV), calculated as the mean of signal magnitude divided by the standard deviation of signal noise magnitude. This is typically used to determine the SNR of a measured image. Within a region of interest (ROI), the SNR is the mean pixel value of signal divided by the standard deviation pixel value of noise. In MRI, a two or three-dimensional ROI is typically defined that encapsulates the observed region to calculate the mean signal, whilst noise is typically calculated on images absent of signal signal. In X-nuclei MRS, the signal is typically determined in the FID readout as the first point (or few points) of the FID over the standard deviation of the last few points.

$$\text{SNR} = \frac{\text{Mean of signal region}}{\text{Standard deviation of noise region}} \tag{2.26}$$

Additionally, instead of the empirical measurements presented above, an analytical equation can be used to approximately determine SNR through the scan and hardware parameters. The power spectral density (or voltage variance) can be calculated via Equation 2.27, where R is the resistance, T is the temperature, k_B is the Boltzmann constant, and BW is the bandwidth.

$$\overline{v_n^2} = 4k_BTR\,\text{BW} \tag{2.27}$$

The theoretical SNR can then be calculated taking into account the scan parameters, where V_0

is voxel volume, M_T is magnetisation, F is the noise figure measuring the degradation of SNR of a component, t_0 is sampling window, t_R is repetition time, t_{scan} is scan time [10]:

$$\text{SNR} \approx F^{-\frac{1}{2}} \frac{\omega(B_1/I)}{\sqrt{4k_B RT}} V_0 M_T \sqrt{\frac{t_0}{t_R} t_{\text{scan}}} \tag{2.28}$$

Equation 2.28 shows that SNR $\propto 1/\sqrt{R}$, which is extensively used in this work to compare SNR from simulated and measured coil resistances.

2.1.4.2 Measured Complex Noise

Pixels in the reconstructed MRI image have complex values comprising of a real and imaginary component with a Gaussian distribution each. The Gaussian probability density, $p_{\text{Gaussian}}(x)$, can be determined using the mean, m, and variance, σ [11], as shown in equation 2.29 below.

$$p_{\text{Gaussian}}(x) = \frac{1}{\sigma\sqrt{2\pi}} e^{-\frac{(x-m)^2}{2\sigma^2}} \tag{2.29}$$

Commonly, magnitude images are used for B_1^+ and SNR maps, this skews the noise distribution such that it is no longer Gaussian, and instead can be considered to follow a Rician distribution. The Rician distribution follows from both the real and imaginary components forming a bi-variate normal distribution, such that they are both independent (with zero correlation) and normally distributed (individually Gaussian). In the case of MRI, the distribution of both real and imaginary components are equal in magnitude, leading to the following probability density function, $p_{\text{Rician}}(x)$, where I_0 is the modified Bessel function of the first kind with order zero [12], as shown in equation 2.30 below.

$$p_{\text{Rician}}(x) = \frac{x}{\sigma^2} e^{-\frac{(x^2-m^2)}{2\sigma^2}} I_0\left(\frac{mx}{\sigma^2}\right) \tag{2.30}$$

The exact noise probability density distribution is used to fit noise characteristics for accurate coil comparison, as described in Methods section 3.4. However, two simplifications can be made:

- At the phantom centre (or in general at regions of high SNR ≥ 5), the magnitude noise can be considered a Gaussian distribution.

- Outside the phantom, the magnitude noise can be considered a Rayleigh distribution in the approximation that $I_0(mx/\sigma^2) = 1$.

2.1.4.3 Quality Factor in RLC circuits

Whilst the SNR can be measured through the acquired image, a method of measuring the individual contributions of resistance, particularly from the RF coil, can be used to predict SNR, through Equation 2.28. The resistance, R, can be approximated through monitoring the Quality (Q) factor, without scanner measurements. The Q factor is a dimensionless metric, commonly used in RF engineering to characterise the efficiency of RLC circuit resonators (any electrical circuit consisting of a resistor (R), an inductor (L), and a capacitor (C) component, forming a harmonic oscillator) [13]. The Q-factor is defined as the peak energy stored in the circuit, divided by the average energy dissipated per cycle. This is summarised in equation 2.31, which can be measured using the fractional bandwidth, B_f. This fractional bandwidth is related to the peak bandwidth $\Delta\omega$, or the full width at half maximum (FWHM) which is the bandwidth over which the power of vibration is greater than half the power at the resonant frequency, defined as $\Delta\omega/\omega_0$. The FWHM is measured between two cutoff frequencies ω_1 and ω_2 of the frequency response such that: $\Delta\omega = \omega_2 - \omega_1$, where the cut-off is at $-3\,\mathrm{dB}$ from the peak resonance frequency ω_0 representing the max frequency response.

$$Q = \frac{\text{Maximum energy stored}}{\text{Energy dissipated per cycle}} = \frac{1}{B_f} = \frac{\omega_0}{\Delta\omega} \tag{2.31}$$

Conventional RF coils (the best example being a simple loop of conductor) are well approximated as series RLC circuits, but such a simplification is less accurate for the more complex conductor designs proposed in this thesis. The Q-value for a series RLC circuit, equation 2.32 differs from a parallel RLC circuit, equation 2.33. These conditions arise from determining the complex impedance, Z, and setting the imaginary component to zero, as discussed in section 3.3.1.1.

$$Q_{\text{Series}} = \frac{1}{R}\sqrt{\frac{L}{C}} = \frac{\omega_0 L}{R} \tag{2.32}$$

$$Q_{\text{Parallel}} = R\sqrt{\frac{C}{L}} = \frac{R}{\omega_0 L} \tag{2.33}$$

The aim of this work is to maximise resonance efficiency; from equation 2.32, we can see this

can be achieved either through maximising L or minimising R. For RF coils, the loss in RF coils, which is often presented as a series of resistive components, R, is inherent to the coil and sample properties, and cannot be easily minimised. Therefore maximising total inductance, L, is investigated in this project, whilst minimising additional resistances introduced by the design.

2.1.4.4 Sample and Coil Noise Contributions

The origin of resistance experienced by an RF coil system arise from random fluctuations in a resistor which are thermally activated in a dissipative medium (fluctuation-dissipation theorem) [14]. When considering the overall total noise from RF coils, we can consider two primary dissipative elements: the coil resistance and the sample resistance, with the relative weighting of both determined by sample dimensions, frequency and other scan parameters. As a side note, a source of loss to consider is the radiative losses that arise from lost EM signal through far field radiation, however the magnitude of such losses are small, and negligible at these frequencies. For higher frequencies ($500\,\mathrm{MHz}$ and up), radiation damping can play a significant part [15]. The relative contributions of the two primary sources of RF noise: coil and sample resistance as described below, are important in this work for identifying efficient coil designs:

1. Receive coil resistance, R_{Coil}: This is from a combination of conductive losses of the wire and solder, effective series resistance of lumped element components (such as typically $0.3\,\Omega$ quoted by manufactures for capacitors), high frequency losses from eddy currents such as skin effects and proximity effects (described in detail in section 4.2.2.1). Within the conductor, thermal energy of electrons give rise to a noise power which can be described as the Johnson-Nyquist noise, generated by the thermal agitation of the electrons from an applied voltage [16]. Coil resistance approximately scales with resonance frequency, ω_0 as: $R_{\text{Coil}} \propto \omega_0^{\frac{1}{2}}$, [10].
2. Sample resistance, R_{Sample}: This arises from magnetically induced eddy current losses within a conductive sample (such as the human body). Sample resistance is intrinsic from the inductive coupling between the coil and sample, and scales with resonance frequency and size of sample, r: $R_{\text{Sample}} \propto \omega_0^2 r^5$, [10].

Following equation 2.28 and removing scan dependent parameters, we can approximate SNR in terms of coil and sample resistance using the relation $R = R_{\text{Coil}} + R_{\text{Sample}}$ (ignoring radiative

losses):

$$\text{SNR} \propto (\omega^2 B_1)/\sqrt{R_{\text{Coil}} + R_{\text{Sample}}} \tag{2.34}$$

Practically, the Q-factor can be measured to determine the relative size of individual noise contributions. We can modify Equation 2.32 into two forms: Q_{Loaded}, where the coil is placed on a loading sample, such that the overall resistance contains both sample and coil resistance, Equation 2.35, and Q_{Unloaded} where the coil is not placed on any loading, such that the overall resistance only contains coil resistance, Equation 2.36.

$$Q_{\text{Loaded}} = \frac{\omega L}{R_{\text{Coil}} + R_{\text{Sample}}} \tag{2.35}$$

$$Q_{\text{Unloaded}} = \frac{\omega L}{R_{\text{Coil}}} \tag{2.36}$$

Both Q-value metrics can be measured using a network analyzer, allowing the contributions of coil and sample noise to be determined individually for a given RF coil. Finally, the Q-ratio, defined in Equation 2.37 can be used as an indicator of coil sensitivity. Improving coil designs allows for $R_{\text{Sample}} \gg R_{\text{Coil}}$, such that the Q-ratio is maximised:

$$Q_{\text{ratio}} = \frac{Q_{\text{Unloaded}}}{Q_{\text{Loaded}}} = 1 + \frac{R_{\text{Sample}}}{R_{\text{Coil}}} \tag{2.37}$$

The individual contributions of noise are widely measured in coil characterisation, and described in more detail in section 3.3.1.

Following from equation 2.34 and equation 2.35, the SNR can be determined from both B_1 and Q-values according to the following equation:

$$\text{SNR} \propto (\omega^2 B_1)/\sqrt{Q_{\text{Loaded}}} \tag{2.38}$$

2.1.4.5 Scattering Matrix

Scattering (S)-parameters are used to describe the electrical behaviour of linear electrical networks, and are used extensively in antenna design. S-parameters are dependent on three factors: the frequency (e.g. $30\,\text{MHz}$), the characteristic impedance of the system (e.g. $50\,\Omega$), and the

number of ports (e.g. 2 ports) [17]. The definition of the S-parameter matrix for a two port network between incident (a_i) and reflected power waves (b_i) is given by equation 2.39.

$$\begin{pmatrix} b1 \\ b2 \end{pmatrix} = \begin{pmatrix} S_{11} & S_{12} \\ S_{21} & S_{22} \end{pmatrix} \begin{pmatrix} a_1 \\ a_2 \end{pmatrix} \tag{2.39}$$

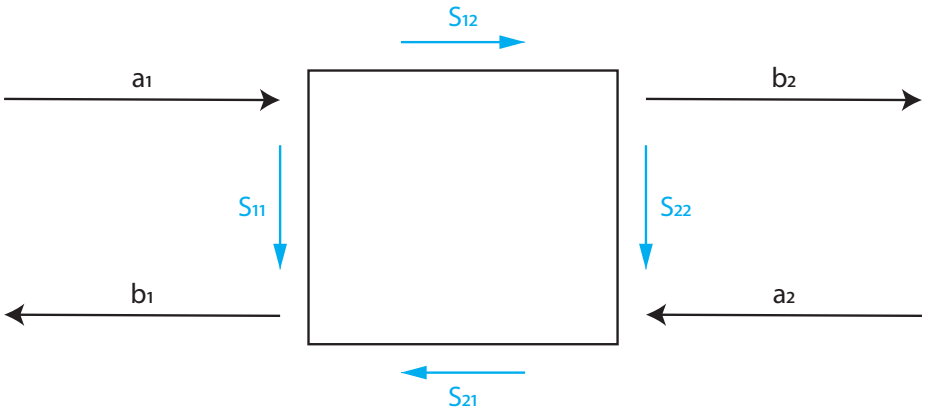

Figure 2.2: Two port system showing incident, a_1 and a_2, power waves and reflected, b_1 and b_2, power waves from each port. The direction of S-parameters are shown with input reflection coefficient as S_{11}, output reflection coefficient as S_{22}, forward transmission coefficient as S_{21}, and reverse transmission coefficient as S_{12}.

If we assume that a two-port system, as shown in Figure 2.2, is terminated with a load that is the characteristic impedance, then to obtain the maximum external power from a source, the impedance of the load must equal the impedance of the source, which follows that $a_2 = 0$. Here, S_{11} is the input port voltage reflection coefficient:

$$S_{11} = \frac{b_1}{a_1} \tag{2.40}$$

And S_{21} is the forward voltage gain (transmission from port 1 to port 2):

$$S_{21} = \frac{b_2}{a_1} \tag{2.41}$$

Similarly, if port 1 was terminated with a load of the characteristic impedance, then $a_1 = 0$.

Here, S_{22} is the output port voltage reflection coefficient:

$$S_{22} = \frac{b_2}{a_2} \tag{2.42}$$

And S_{12} is the reverse voltage gain (transmission from port 2 to port 1):

$$S_{12} = \frac{b_1}{a_2} \tag{2.43}$$

The above can be generalised for a system with N ports, where S is the scattering matrix, according to equation 2.45.

$$\mathbf{b} = \mathbf{S}\mathbf{a} \tag{2.44}$$

$$\begin{pmatrix} b_1 \\ \vdots \\ b_N \end{pmatrix} = \begin{pmatrix} S_{11} & \dots & S_{1N} \\ \vdots & \ddots & \vdots \\ S_{N1} & \dots & S_{NN} \end{pmatrix} \begin{pmatrix} a_1 \\ \vdots \\ a_N \end{pmatrix} \tag{2.45}$$

Such formalism is commonly used to monitor coupling across arrays of RF coils (with multiple identical elements). The diagonal of the S-matrix, S_{ii}, represents the reflection for each RF coil, and the off-diagonal elements, S_{ij}, represent the mutual inductance between RF coil elements. As such, the S-matrix and scattering coefficients are complex, frequency dependent, and Hermitian. S-parameters of RF coils are used in this project to describe the power reflection of a single element (S_{ii}) or the power transmission between a pair of elements (S_{ij}) described in Methods, section 3.3.1.3. For efficient RF coil design, impedance matching is typically utilised, where the source impedance and load impedance are matched, to maximise transmitted power in the circuit.

2.2 MRI Scanner Hardware

This section briefly discusses the main components of MRI scanners, with an initial overview of the scanner magnetic fields. Following this, the RF specific hardware is discussed in greater detail. A general overview of RF coils can be found in [13], whilst more detailed discussions of RF coils can be taken from [18].

2.2.1 Overview

MRI systems are often described as 'a coil within a coil within a coil...', such that there are four 'layers' of coils nested inside one another. Starting from the outer layer and proceeding towards the centre of the scanner, there are: main static field coils, shim coils, gradient coils and finally RF coils. These four coil systems operate broadly at three magnetic field frequency regimes, in order of increasing frequency: static field, gradient field oscillating on the order of ms and radiofrequency field oscillating on the order of ns. The radiofrequency (RF) fields are generated by RF coils, as discussed below in section 2.2.2.

2.2.1.1 Main static field

In the case of full body clinical MR scanners, the main static magnetic field, B_0, is typically generated by a cryogenically cooled superconducting electromagnet. For clinical MRI, B_0 is typically around $1.5 - 3\,\mathrm{T}$, and pre-clinical MRI systems operate at $7\,\mathrm{T}$ or higher. Additionally, modern MRI scanners have excellent B_0 homogeneity, such that the presence of a sample with different dielectric properties will negatively impact the field homogeneity. Additional fine tuning to the homogeneity is achieved through the use of shim coils generating small perturbing spatially varying magnetic fields. Active shimming involves using current directed through shim coils to generate corrective magnetic fields; unwanted spherical harmonic components of the uncorrected magnetic field are combined with a supplemental magnetic field with the same spatial distribution, but equal and opposite magnitude to the unwanted field. The superposition cancels the magnetic field inhomogeneity.

2.2.1.2 Gradient field

The gradient magnetic field, G is generated by gradient coils. The purpose of gradient fields are to distort the B_0 field, causing the resonance frequency of nuclei to vary as a function of position, to allow for spatial encoding of the MR signal. Three sets of orthogonal gradient coils are generally used: the x-, y-, and z-gradients, with each coil set driven by an independent gradient power amplifier. Gradient field frequencies are in the kHz range (dependent on pulse sequence), and ideally instantly switch on and off. However, this is not physically possible, gradients are limited by their maximum strength G_{max} and the time taken to reach this maximum strength – also known as the rise time. One measurement used to compare gradients is the slew

rate: $S_{\max}$, which is $G_{\max}/(\text{rise time})$.

2.2.2 Radiofrequency Hardware

The role of the entire RF hardware chain is to transmit and receive RF signal in the MHz range, as efficiently and uniformly as possible. RF coils can be differentiated by three mode of operation: Transmit-Only (To), Receive-Only (Ro) and Transmit-Receive (TxRx). Presented here in order of a typical MRI operation: a signal is generated in the transmit chain, then transmitted and received through RF coils, and finally processed through the receive chain [19]. The component overview is shown in Figure 2.3.

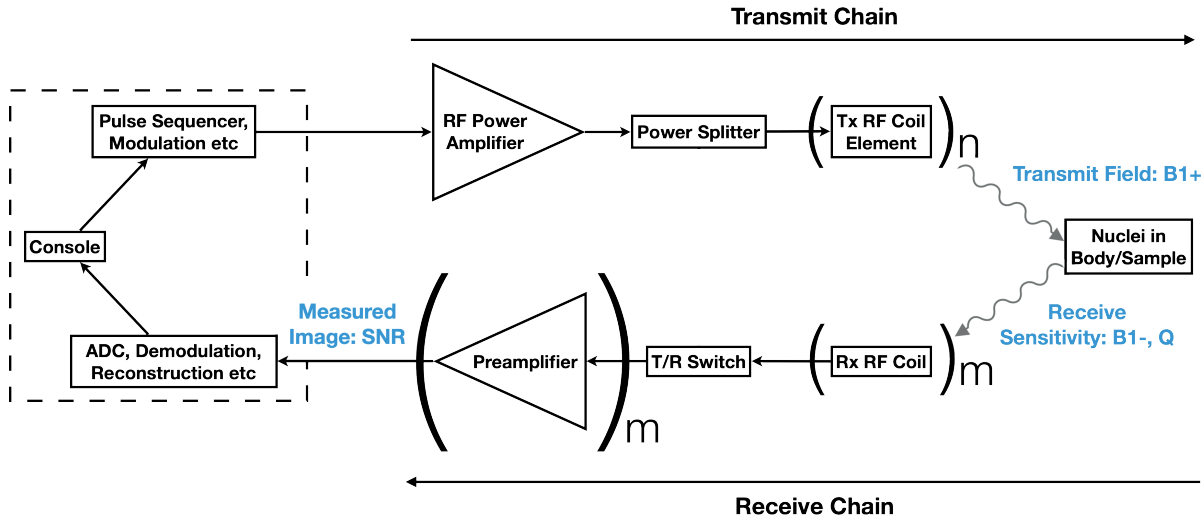

Figure 2.3: Diagram of RF hardware. Components on the top row show the transmit chain for an 'n-element' TX coil to generate a B_1^+ field. Components on the bottom row show the receive chain for an 'm-element' RX coil to receive a B_1^- field and measure SNR.

2.2.2.1 Coil Element

Hoult (1976) was the first to discuss the SNR of a single element NMR receiver [20], with a focus on the Helmholtz configuration. Subsequent discussion of multiple individual RF elements with overlapping fields of view led to the development of RF arrays [21]. From here, it was recognised that a small ROI could be imaged with higher sensitivity by a closely fitted coil, to increase the SNR [22], i.e. by placing a small coil on the surface of the sample, close to the ROI. The design of RF coil elements is discussed in detail throughout this thesis, however a brief summary of the electrical properties and physical properties are presented here to facilitate discussion in this chapter.

Electrical Properties:

RF coil elements comprise of a RLC circuit (made up of electrically inductive, capacitive and resistive components). Both Tx and Rx elements are designed to inductively couple to the sample, and generate a magnetic flux density B_1^+ and B_1^- respectively, as described previously in section 2.1.2.2.

The coil is both 'tuned' and 'matched' by adjusting lumped element values, represented here as discrete capacitors for capacitance and discrete inductors for inductance. The tuning of the coil adjusts the resonance frequency to match the Larmor frequency determined by the nuclei from equation 2.8. Similarly, the coil is impedance matched to minimise reflected power with the sequence of components in the transmit and chains at the resonance frequency. A more detailed discussion of the protocol for coil tuning and matching can be found in the Methods chapter, section 3.3.3. With correct tuning and matching, the small external perturbation at resonance from the precessing magnetisation in the body will induce a larger response from the coil which is detected as signal.

Physical Properties:

There are numerous distinct physical RF coil designs, one common way of categorising the designs is to split them between 'surface coils' and 'volume coils'. Surface coils are typically shaped such that the coil element(s) can be placed close to the anatomy being imaged, crucially the FOV of the coil is designed to be localised to the ROI. Volume coils typically enclose the entire patient/sample within the coil FOV, including the anatomy being imaged. Note there is a difference between the imaging FOV, which is determined by the pulse sequence and scan parameters, and the coil FOV which is determined by the region of coil sensitivity determined by coil design. The B_1 field profiles and within the coil FOV are highly dependent on the coil dimension. This holds true for all coil designs, from surface coils to volume coils. Specifically for surface loops, a smaller loop diameter will achieve higher magnetic field strengths close to the coil but with a steeper drop-off in magnetic field away from the coil centre, and a smaller coil field of view, as shown from the Biot-Savart equation, equation 2.7. Conversely, a larger loop diameter will achieve a lower peak magnetic field strength but with a shallow profile off-centre and correspondingly larger field of view. There is a balance between field uniformity and field efficiency for both Tx and Rx coils which manifest in the B_1^+ (for Tx) and SNR values (for Rx).

In discussion of surface RF coil dimensions, RF coils comprising of more than one element should be included. RF arrays which are comprised of more than one element that is overlapped in close proximity can be constructed similarly from large individual elements or small individual elements. Smaller individual elements will similarly allow for increased sensitivity closer to the coil, but not at depth. Thus the maximum depth sensitivity of an array is limited by the design and dimension of its elements similarly to single elements coils. The trade off between field uniformity and field efficiency holds for arrays, where dense arrays with smaller elements achieve higher sensitivity close to the coil, whilst less dense arrays with larger elements achieve better sensitivity at depth.

2.2.2.2 Transmit Chain

The transmit and receive components of an RF coil can be separated. On transmit, the electronic 'RF-front end' is responsible for generating, shaping, and amplifying the electrical currents required to produce the B_1^+ field. The exact components and functions differ across vendors and how modern the scanner is; an example of basic RF-transmit chain components are presented here:

Frequency Synthesiser →Modulator →Amplifier →Directional Coupler (DICO) →Phase Shift (→T/R Switch) →Coil

- **Frequency synthesiser:** This generates a continuous sinusoidal carrier wave at (or near) the desired Larmor frequency. The output from the synthesizer is sent to two places: (1) further down the RF-transmitter chain to the pulse modulator for shaping; and (2) into the RF-receiver chain where it will be used as a reference for demodulating/decoding the MR signal in the receive chain.
- **Pulse Modulator:** The continuous carrier wave from the frequency synthesizer is shaped (modulated, e.g. with a Gaussian/Sinc envelope applied), as required by the pulse sequence. Overall the signal is comprised of a high frequency carrier wave (MHz range) modulated by a low frequency envelope (dependent on pulse duration, around ms duration, equivalent to kHz). For modern scanners, these first two steps may be achieved by a field-programmable gate array (FPGA) which synthesises the RF waveform at the right frequency with phase and amplitude control.

- **High Power RF Amplifier:** The RF waveform passes through the RF amplifier that generates the large currents required to drive the RF coils and achieve adequate B_1. As discussed below, ^{1}H and X-nuclei amplifiers typically differ in both frequency and peak power. The RF power amplifier is an integral component of Tx coil performance, as the B_1^+ is directly proportional to the voltage supplied by the amplifier.
- **DICO:** In most clinical scanners, DICOs are implemented as an additional safety measure, built into the transmission line of each transmit channel. The DICO measures the forward and reflected RF waveforms, ensuring the RF coil is well matched, to prevent excessive reflected power back into the RF amplifier.
- **Phase shift/Power splitter:** The amplified waveform is then sent to the Tx RF coil. Here, the current is divided (typically evenly) amongst the number of transmit elements using a power splitter. Additionally, desired relative phase shifts between elements are applied using a phase shifter. Commonly, for ^{1}H MRI a quadrature hybrid coupler is present, and in-phase ($0°$ offset between two channels) or quadrature ($90°$ offset) phase can be applied to optimally drive quadrature body coils.
- **Transmit-Receive Switch:** Electronic switching circuitry is necessary to ensure that current is delivered to the transmit coil at the time requirements set by the pulse sequence, and prevent transmission into the receive coil. This is achieved commonly through a DC bias line, and inbuilt logic on the scanner, such that the receive coil is detuned when the transmit coil is transmitting. This is required to isolate the transmit and receive functions, and prevent the large electric currents present during transmission from entering and overloading the sensitive receiver circuitry.

2.2.2.3 Receive Chain

The key requirement of the receive chain is to achieve the maximum SNR, in order to obtain the best possible image quality. The SNR represents the statistical confidence in the robustness of features of the image in MRI (or spectrum, in the case of MRS). A high SNR means the signal is substantially stronger than the random variations in the intensity due to noise, and therefore we have high confidence that the apparent features in the image reflect the physical characteristics of the sample.

The receive chain is comprised of the following components:

Coil Decoupling →Pre-amplification →Demodulation →ADC →Image Processing

- **Coil Decoupling:** The RF receiver coils and associated circuitry that will detect the emitted MR signal are tuned to this same frequency. To prevent the coil components (namely capacitors with insufficient voltage ratings), and the preamplifier from being burned out by high currents induced, the receive coil is electronically 'detuned' such that the transmit and receive coils are 'decoupled' briefly during RF transmission, as described in section 2.2.3.1.

- **Low Noise Pre-amplifier:** The induced current on the coil is extremely weak (on the order of mV for $^{1}\mathrm{H}$ and $\mu\mathrm{V}$ for X-nuclei); as such, it may be easily contaminated when travelling through the coaxial cable from the coil. To minimise contamination by external noise, a low noise preamp is used to amplify the signal. Ideally, the preamp is placed as close to the coil element as possible to minimise noise contamination from the cables. Additionally a second high/low gain amplification stage can follow (such as on the Agilent/Varian pre-clincal $7\,\mathrm{T}$ scanner).

- **Demodulation** From the transmit modulation step, the waveform is both amplitude-modulated (AM) and phase-modulated (PM). Signal intensity and spatial location information are extracted through demodulation, by comparing the received signal to the carrier wave from the RF synthesizer.

- **Analogue to Digital Conversion:** As the name suggests, the ADC digitises the analogue signal at an intermediate frequency. Improvements in ADC performance have been achieved over the last 10 years, in part thanks to mobile phone development. Specifically compact ADCs are available allowing direct sampling of signals in the higher frequency ranges ($\sim 100\,\mathrm{MHz}$) with large dynamic range.

- **Image Processing** Commonly the image is processed using vendor specific integrated methods, such that the scanner shows the final image. Specifically for the work presented in this thesis, the raw signal data was reconstructed and analysed offline using Siemens' TWIX data files in the MATLAB programming environment (MATLAB R2019-R2022, Mathworks, MA).

2.2.3 Minimising EM Coupling

Electromagnetic coupling is a phenomenon where the EM field from one source/coil results in the generation of current in another source/coil through the mutual inductance across two coils. In the case of RF coil interactions, the oscillating B-field from coil one induces an oscillating current in coil two at the resonance frequency, ω, determined by Lenz's law, causing energy transfer through the inductive coupling [23]. This transfer of energy may be desired or undesired.

In MRI, two examples of desired inductive coupling are: between the sample and the coil, allowing the receive coil to pick up the resultant magnetisation from the sample nuclei, and secondly the use of pick-up probes which are inductively coupled to the main coil for benchtop coil characterisation, as discussed in the methods chapter (section 3.3). However, additional inductive coupling is generally undesired, and given the vast number of coils and conductive loops present in MR scanners, numerous possible couplings across components can be anticipated. Arguably, the greatest hurdle faced in the design and construction of efficient RF coils is to minimise these unwanted couplings through design. These couplings are undesirable as they result in the current flowing around a coupled loop, dissipating energy into the coil instead of into the sample, and can overload lumped elements with excess voltage. Broadly, there are three categories of undesired EM coupling: in the case of separate transmit and receive coils, coupling may occur between them, for multi-nuclear MRI, coupling between ^{1}H and X-nuclei coils can occur, and thirdly in arrays of multiple elements, coupling can occur between neighbouring elements. These three cases are shown in Figure 2.4, and presented individually below.

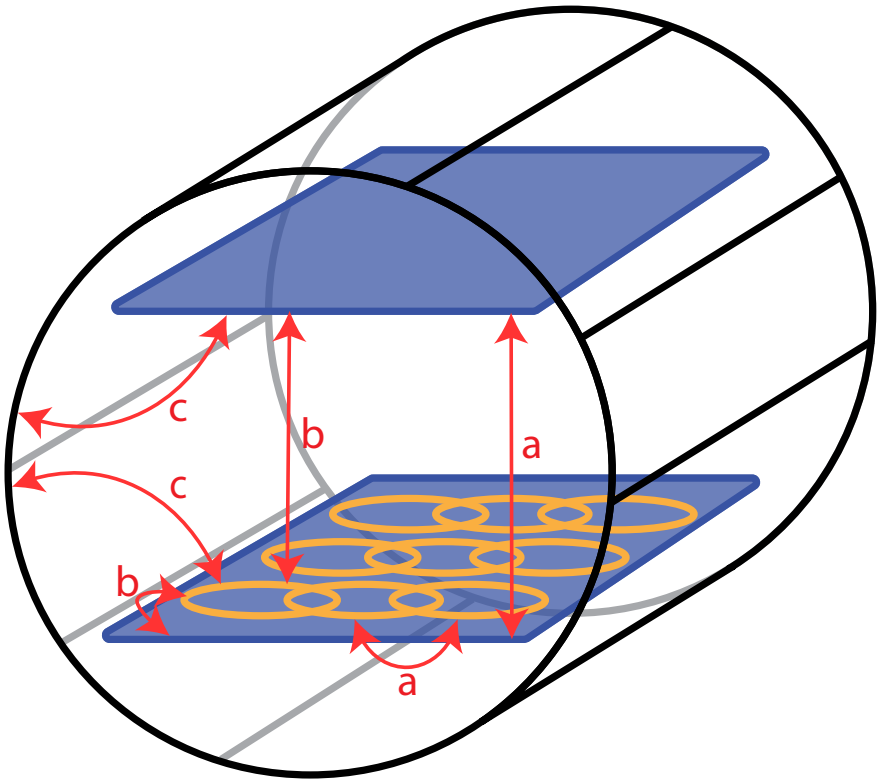

Figure 2.4: Simplified diagram showing a ^{13}C RF coil configuration consisting of a transmit Helmholtz pair loop and a receive arrays, with ^{1}H body coil consisting of a birdcage design. The design is consistent with the constructed novel ^{13}C array described in Chapter 6. The three aspects of EM coupling can be shown here: (a) coupling between neighbouring (in this case, identical) coil elements tuned to the same frequency; this coupling can be minimised through geometric overlap (as seen from the receive arrays), increased separation (as seen from the transmit elements), discussed in section 2.2.3.3. (b) Describes coupling between the transmit and receive ^{13}C coils in close proximity; this coupling can be minimised through active and passive detuning circuitry (not shown in figure), discussed in section 2.2.3.1. (c) coupling between ^{1}H body coil and ^{13}C coils sitting within proton coil FOV; this coupling can be minimised through ^{1}H traps and baluns (not shown in figure), discussed in section 2.2.3.2.

2.2.3.1 Coupling between Tx and Rx coils

For most MRI applications using surface RF coils, the optimum transmit coil dimension differs from the optimum receive coil dimension. Maximising receive sensitivity whilst requiring uniform transmit means using separate Tx and Rx coils. As the transmit power is many orders of magnitude stronger than the expected received signal, the preamplifier after the Rx coil needs to be isolated from the high power to prevent damage to the sensitive circuitry. To prevent this mishap, when the Tx coil is active (i.e. transmitting power), the Rx must be tuned off-resonance to minimise distortions to the Tx field and excess power delivery into the Rx

chain. This isolation is commonly achieved by 'detuning' the receive coil such that the receive coil is temporarily made no longer resonant at the resonant frequency ω when the Tx coil is transmitting. Both active and passive detuning are commonly implemented on clinical coils: the passive detuning circuitry comprises of a capacitor with crossed diodes which conducts if the voltage greater than their reverse breakdown voltage is applied, and adds capacitance into the circuit, changing the resonance frequency, detuning the circuit in the event of active detuning failure. The active detuning circuit comprises of a PIN (positive intrinsic negative) diode and lumped elements in a parallel circuit such that when a forward DC bias is applied to the PIN diode, the parallel circuit inserts a high impedance, blocking current flow at the resonant frequency during the transmit phase. An alternative is to naturally ensure the Rx coil is detuned, and only resonant when a forward DC bias is applied, this ensures the Rx coil is 'safe' even when the DC bias is not applied as expected during transmission.

2.2.3.2 Coupling between proton and X-nuclei coils

In multi-nuclear MRI, a ^{1}H coil (typically the body coil) is used to run a ^{1}H localisation scan, and a single resonance X-nuclei coil (typically a surface coil) is used to acquire X-nuclei data[18]. In this setup, the EM field at the ^{1}H frequency is transmitted through the X-nuclei coil, which is commonly positioned closer and on the patient. Due to resonant loops generated from the coil structure, the entire X-nuclei coil or sections of the coil may resonate at the transmitted ^{1}H frequency, as seen in the novel coil design presented in section 4.2.2. This may lead to loss of B_1 field uniformity, unexpected local heating from unexpected resonant loops that exceeds safety limits, or generates local hot-spots of E-field, both of which are a concern for patient safety. To minimise unexpected resonances, 'RF traps' are placed at intervals along the conductor path to minimise sections of unwanted resonances. RF traps typically consist of an inductor and capacitor, forming a small LC circuit (commonly around $1\,\mathrm{cm} \times 1\,\mathrm{cm}$ diameter), positioned in series to the coil element, tuned to the resonant frequency of the ^{1}H Larmor frequency. During ^{1}H transmission, the ^{1}H EM field that couples to the X-nuclei coil is resonant within the ^{1}H traps locally through induced eddy currents, absorbing the energy within the trap, and preventing the coil being resonant or re-transmitting the EM field. To be effective, ^{1}H traps need to be placed at regular intervals along the coil conductor path and minimise phase shifts along the cable. However there are two drawbacks: firstly, proton traps inherently increase the

resistance of the coil system through an effective series resistance (ESR) and secondly, create localised distortions to the ^{1}H B_1^+ field due to the resonance of the LC circuit, which will distort commonly used localisation scans near the coil. A similar coupling may occur between the coaxial cables of the X-nuclei RF coil and the ^{1}H transmitted field, where the EM field may induce unwanted currents on the surface of the outer shield of the coaxial cable. In this case, a similar technique is applied where ^{1}H cable baluns (balancing units) block any ^{1}H EM fields from being generated in the cable. The isolation of undesired frequencies is described in greater detail in section 3.3.2.

2.2.3.3 Coupling between neighbouring array elements

Arrays provide the benefit of an increased FOV when compared to a single individual coil element. Arrays still retain the high sensitivity of small surface elements provided no coupling occurs between array elements. Naturally, bringing two loops resonant at the same frequency in close proximity, such that the region of coil sensitivity of both coils overlap, strong inductive mutual coupling will typically occur. This causes the field profile from one element to be skewed across neighbouring elements, and as such will reduce the depth penetration and receive sensitivity within ROI of individual elements.

To counter this, a method of geometric decoupling [23] can be used, where elements are isolated from each other by partially overlapping adjacent loops such that the mutual inductance is zero. This leads to zero magnetic flux linkage between adjacent pairs of loops and hence zero interaction. Complete elimination of coupling between all neighbouring elements is practically impossible to achieve, however, the loss of sensitivity can be minimised further down the receive chain. Further isolation can be achieved using decoupled low input impedance preamplifiers that reduce interference amongst nearest and more distant neighbours. Both methods are used in Chapter 6 to develop a novel array design.

2.3 Proton versus Non-Proton MRI

Whilst conventional ^{1}H MRI is the gold standard clinical diagnostic tool for non-invasive, non-radioactive medical imaging, with extensive applications in for example cardiovascular, neuro, and musculoskeletal areas, X-nuclei MRI is still actively researched and developed, and seldom

used in a clinical setting. Additional metabolic information can be obtained through multi-nuclear imaging, and promising results from several nuclei are driving a revised interest in routine clinical X-nuclei imaging. However, X-nuclei MRI faces several challenges largely due to physical limitations, primarily in limited SNR, lower gyromagnetic ratio, lower natural abundance in the body, all compounded by less powerful RF hardware. This final section discusses the challenges of X-nuclei, and the differences in hardware compared to proton MRI.

2.3.1 Conventional MRI

^{1}H is comparatively abundant in the human body, which has over $60\,\%$ water by mass, and an approximate ^{1}H concentration of $110\,\mathrm{M}$ (pure water contains $110\,\mathrm{M}$, humans will have a slightly lower ^{1}H concentration). As such, sufficient signal is available to acquire high resolution images within several seconds, or within a single breath-hold, at clinical scanner field strengths. When considering transmission of the RF energy for ^{1}H applications, the primary RF power amplifier (as described in section 2.2.2) is narrow-band, only requiring delivery at a specific range of frequencies matching that of the ^{1}H resonance. This specific requirement therefore allows the power amplifier to generate upwards of $40\,\mathrm{kW}$ RF power, or equivalently $1.5\,\mathrm{kV}$ delivery using the equation: $P = V^2/R$ with a $50\,\Omega$ impedance, assuming that the phase angle between current and voltage is zero (such that the reactive load of the RF coil is approximately resistive to $50\,\Omega$). This high power delivery allows for the generation of high B_1^+ fields which can achieve desired flip angles (α) following equation 2.14.

The consequence of this is that ^{1}H transmit performance is practically not limited by power or B_1^+ strength, but rather by the specific absorption rate SAR (discussed in greater detail in section 3.5), whilst ^{1}H receive performance is still limited by the sensitivity of signal reception. This influences the RF coil choice; the common ^{1}H RF coil paradigm is to use a volume coil for transmitting, and small surface coil elements for receive. A volume coil exhibits high field uniformity but is limited (as is the case with all larger coils) by its B_1 efficiency, which requires high RF power to drive and additionally poor receive sensitivity. On the other hand, the small surface elements commonly form a surface array which allows the high sensitivity of small individual coil elements to be retained, but over a larger field of view (FOV). This is preferable in terms of SNR compared to one large loop, although lacks the depth of field penetration into the sample.

2.3.2 Multi-Nuclei Cardiac MRI

The limitations of X-nuclei MRI is significantly greater than that of ^{1}H MRI, as both transmit B_1^+ and receive sensitivity are orders of magnitude lower. As the secondary X-nuclei RF power amplifier commonly exhibit broadband power amplification (over a wide range of frequencies covering all commonly used X-nuclei), the power delivery is typically significantly lower than for ^{1}H, at approximately $8\,\mathrm{kW}$ (system dependent, and attenuated to approximately $4\,\mathrm{kW}$ at the coil plug); the equivalent of approximately $400\,\mathrm{V}$ is delivered to the RF coil. This could result in insufficient B_1^+ generated from a volume coil; as such, more efficient surface elements are used for transmit (either as a single element or limited in number, to maintain sufficient power to each element). For all nuclei, receive sensitivity is inherently limited; however, this is an even greater limitation for X-nuclei, with it being difficult to distinguish the recorded signal above the noise floor. Three factors that differ between X-nuclei and ^{1}H MRI in limiting the receive sensitivity are:

1. **Natural abundance:** For ^{1}H, ^{31}P, ^{23}Na, all three NMR active isotopes are found to be $100\,\%$ abundance in the body. For ^{13}C, only $1\,\%$ of carbon in the body is ^{13}C, and most carbon is not in the metabolite of interest, leading to weak signal in thermal equilibrium (and thus the need for hyperpolarization).
2. **Relative sensitivity:** The sensitivity is proportional to gyromagnetic ratio: γ^3, following equation 2.15. As all three X-nuclei have significantly lower γ than proton, listed in Table 2.1, the relative sensitivity is approximately $1\,\%$ that of the ^{1}H nuclei.
3. **Quadrupolar relaxation:** For nuclei with spins >$1/2$, in this case ^{23}Na with $\mathrm{I} = 3/2$, a non-spherical charge distribution leads to shorter T_2, as described in section 2.1.3.1.

Table 2.1: Summary of gyromagnetic ratio, relative sensitivity compared to ^{1}H, resonance frequency at $3\,\mathrm{T}$, and resonance frequency at $7\,\mathrm{T}$ for the nuclei ^{1}H, ^{13}C, ^{31}P and ^{23}Na.

Nuclei	Gyro. Ratio	Rel. Sens ^{1}H: $(\gamma_X/\gamma_H)^3$	ω at $3\,\mathrm{T}$ /MHz	ω at $7\,\mathrm{T}$ /MHz
^{1}H	42.57	1.000	123.03	300.5
^{13}C	10.71	0.016	30.98	75.6
^{31}P	17.23	0.066	49.80	121.6
^{23}Na	11.26	0.019	32.54	79.5

Whilst this project was initially focused on RF coil design for ^{13}C MRI, RF coils for two

additional X-nuclei were tested. The construction of the ^{23}Na coils allows for coil phantom testing at a nearby resonance frequency to ^{13}C, with cheaper and readily available ^{23}Na phantoms (compared to the costly alternative of ^{13}C powder additional loading). The construction of coils for the ^{31}P nuclei allows for human scans with a coil design, without the challenges surrounding ^{13}C clinical scans discussed below.

2.3.2.1 13-Carbon MRS/I

^{13}C signal is the most challenging out of the 'common' X-nuclei to acquire due to the low SNR that arises from the shared challenge of lower gyromagnetic ratio (Table 2.1), and in addition ^{13}C has a low natural abundance in the body of approximately $1\,\%$ which is evenly dispersed around the body, not localised in the imaging regions. Early ^{13}C MRS involved ^{13}C enriched intravenous glucose infusion to increase measured SNR [24]. More recently, a technique of artificially and temporarily increasing the polarization, P, beyond the limits dictated by the Boltzmann equation 2.9, is possible via dynamic nuclear polarization (DNP). DNP involves the addition of free radicals at temperatures below $1.4\,\mathrm{K}$, the high polarization of electrons at this temperature can then be transferred to the ^{13}C nuclei through microwave irradiation by predominantly a process of thermal mixing [25]. Thermal mixing describes a complex set of processes, where ensembles of electrons spin exchange energy with ensembles of nuclear spin, particularly relevant to liquids DNP. *In vivo* ^{13}C MRI/MRS was made feasible by the method of dissolution-Dynamic Nuclear polarization which produces a room temperature solution quoted to achieve up to $10\,000\times$ increased polarization [26]. This hyperpolarized ^{13}C MRI allows for real-time *in vivo* investigations of metabolism in a variety of diseases, including cancer, cardiovascular disease, and metabolic diseases of the liver and kidney [27, 28]. [1-^{13}C]Pyruvic acid was used in first-in-man trials for prostate cancer imaging [29]; the goal of this technique is to increase capacity and to move towards routine clinical applications.

However, from a detection standpoint, two significant challenges are still present: firstly, the short spin-lattice (T_1) relaxation time post-dissolution leads to a fast exponential decay of signal with a half-life less than a minute (in the absence of metabolism). Secondly, the total signal is determined from the hyperpolarisation step, such that the signal is finite (not proportional to B_0) and does not replenish but rather created by the hyperpolarisation process. The finite and fast decaying signal leads to limited SNR, and requires custom pulse sequences and extremely

efficient RF coils to both capture the data in the short scan window and detect the signal at a high sensitivity for maximum SNR (where typically increased scan duration by increasing the number of repeats and duty cycle can alleviate SNR limitations).

2.3.2.2 Sodium MRI

^{23}Na imaging has the highest signal level after ^{1}H in-vivo, with $100\,\%$ natural abundance (virtually all sodium in the body exists as the ^{23}Na isotope and is NMR-active), and is highly concentrated within structure of typical interest. However, ^{23}Na has no natural chemical shift dispersion and is not suited for spectroscopy, but can be used for MR imaging. ^{23}Na imaging shows potential value in several aspects: musculoskeletal, where the ^{23}Na level in cartilage can serve as an index of cartilage and tendon health. For cardiovascular, the total ^{23}Na concentration increases by up to $50\,\%$ in stroke and by over $200\,\%$ in cardiac ischaemia with reperfusion. In oncology, malignant tumours exhibit increased intracellular and extracellular concentrations [30], and finally kidneys to monitor renal function [31].

However, the challenge ^{23}Na MRI faces is the quadrupolar relaxation that arises from the spin $3/2$ nucleus, which leads to a very short T_1 and T_2 decay time. Whilst short T_1 allows short scan TR, the short T_2 requires short scan TE. On the other hand, from an RF coil development perspective, as ^{23}Na imaging is straightforward to develop, possessing high signal levels from aqueous sodium chloride and allowing high number of averages without necessary RF spoiling thanks to the short TR. The relatively high X-nuclei signal and short TR makes ^{23}Na an easy platform to test RF coil designs through phantom MRI scans. Additionally, the resonance frequency of ^{23}Na is close to that of ^{13}C (Table 2.1), such that the performance of a coil tuned to ^{23}Na are expected to be consistent for a similar coil tuned to ^{13}C.

2.3.2.3 Phosphorus MRS/I

^{31}P MR imaging and spectroscopy additionally provides information relating to energy metabolism in tissues. This is, for example in the heart, achieved through monitoring the ratio of phosphocreatine (PCr) and adenosine triphosphate (ATP) [32]. An additional ^{31}P MRS technique is saturation transfer, where narrow bandwidth RF-pulses can be applied to selectively saturate specific peaks in the ^{31}P spectrum. If the ^{31}P nucleus in the saturated metabolite goes through a chemical exchange with another metabolite, the saturated nucleus retains and transfers its

magnetisation state to the exchange partner. This technique is commonly used to monitor the creatine kinase (CK) reaction PCr + ADP $\leftrightarrow$ ATP + Cr, where the magnetisation in the γ-ATP peak is depleted by selective RF irradiation and causes a drop in PCr signal through the CK reaction. However, *in vivo* signal from ^{31}P in organs such as the heart, is limited leading to limited peak identification beyond the noise floor. For human ^{31}P MRS and MRI benefits from both a higher field strength (at $7\,\mathrm{T}$) and high RF coil B_1^+ uniformity, allowing for increased separation between metabolites. However, the trade-off between B_1 uniformity and B_1 efficiency places an upper bound on the ability of conventional ^{31}P RF coils to alleviate the linewidth and sensitivity issues. RF coils with novel conductor designs that improve on the B_1 uniformity and efficiency trade off can be developed with the aim to alleviate these issues, (there is a greater need for improved RF coil design in ^{31}P beyond that of ^{23}Na) whilst ^{31}P human scans are comparatively simple to run compared to hyperpolarized ^{13}C [33].

2.4 Summary

This chapter presents an overview of the physics and engineering theory behind the MRI technique. First, the resonance frequency and magnetisation are determined from a quantum mechanics approach. The evolution of the magnetisation by a B_1 field, however, is best described through a classical mechanics approach. A brief summary of image reconstruction through the Bloch equations and signal generation through k-space Fourier transform was presented. Following this, SNR and individual noise contributions were defined. The engineering background of MRI was subsequently described, focusing on the transmit and receive RF chains. An overview of the biggest challenge in RF coil construction; minimising the EM coupling was discussed. Finally a comparison between X-nuclei and ^{1}H MRI is made. X-nuclei MRI is commonly limited by the B_1 power delivery on transmit, whereas ^{1}H MRI is to a lesser extent limited by B_1 but often by the absorption of energy into the sample: the specific absorption rate (SAR). On receive, all nuclei are limited by receive sensitivity, and thus SNR.

The next chapter discusses the methods for coil characterisation, split into transmit and receive performance metrics for obtaining B_1 and SNR maps respectively. Here, a more extensive characterisation protocol is developed for X-nuclei RF coils.

References

[1] Bernstein, M. A., King, K. F., and Zhou, X. J. *Handbook of MRI Pulse Sequences*. 1st. Elsevier Academic Press, 2004. ISBN: 9780120928613.

[2] Levitt, M. H. *Spin Dynamics: Basics of Nuclear Magnetic Resonance*. 2nd. Wiley, 2008. ISBN: 978-0-470-51117-6.

[3] Griffiths, D. J. *Electrodynamics*. 2013.

[4] Jackson, J. D. *Magnetostatics, Faraday's Law, Quasi-Static Fields*. 1998.

[5] Mabuchi, H. "Derivation of Maxwell-Bloch-type equations by projection of quantum models". In: *Physical Review A* 78 (1 July 2008), p. 015801. ISSN: 1050-2947. DOI: 10.1103/PhysRevA.78.015801.

[6] Miller, J. J. J. J. "Dynamic Nuclear Polarisation as a Probe of Metabolism in Pathophysiology". DPhil thesis. Oxford: The University of Oxford, 2015.

[7] Bloch, F. "Nuclear Induction". In: *Physical Review* 70 (7-8 Oct. 1946), pp. 460–474. ISSN: 0031-899X. DOI: 10.1103/PhysRev.70.460.

[8] Wang, J., Reykowski, A., and Dickas, J. "Calculation of the signal-to-noise ratio for simple surface coils and arrays of coils [magnetic resonance imaging]". In: *IEEE Transactions on Biomedical Engineering* 42 (9 1995), pp. 908–917. ISSN: 00189294. DOI: 10.1109/10.412657.

[9] Kumar, A., Edelstein, W. A., and Bottomley, P. A. "Noise figure limits for circular loop MR coils". In: *Magnetic Resonance in Medicine* 61 (5 May 2009), pp. 1201–1209. ISSN: 07403194. DOI: 10.1002/mrm.21948.

[10] Hayes, C. E. et al. "An efficient, highly homogeneous radiofrequency coil for whole-body NMR imaging at 1.5 T". In: *Journal of Magnetic Resonance (1969)* 63 (3 July 1985), pp. 622–628. ISSN: 00222364. DOI: 10.1016/0022-2364(85)90257-4.

[11] Macovski, A. "Noise in MRI". In: *Magnetic Resonance in Medicine* 36 (3 Sept. 1996), pp. 494–497. ISSN: 07403194. DOI: 10.1002/mrm.1910360327.

[12] Gudbjartsson, H. and Patz, S. "The rician distribution of noisy mri data". In: *Magnetic Resonance in Medicine* 34 (6 Dec. 1995), pp. 910–914. ISSN: 07403194. DOI: 10.1002/mrm.1910340618.

[13] Gruber, B. et al. “RF coils: A practical guide for nonphysicists”. In: *Journal of Magnetic Resonance Imaging* 48 (3 Sept. 2018), pp. 590–604. ISSN: 10531807. DOI: 10.1002/jmri.26187.

[14] Hoult, D. and Lauterbur, P. C. “The sensitivity of the zeugmatographic experiment involving human samples”. In: *Journal of Magnetic Resonance (1969)* 34 (2 May 1979), pp. 425–433. ISSN: 00222364. DOI: 10.1016/0022-2364(79)90019-2.

[15] Bloembergen, N. and Pound, R. V. “Radiation Damping in Magnetic Resonance Experiments”. In: *Phys. Rev.* 95 (1 1954), pp. 8–12. DOI: 10.1103/PhysRev.95.8.

[16] Landauer, R. “Johnson-Nyquist noise derived from quantum mechanical transmission”. In: *Physica D: Nonlinear Phenomena* 38 (1-3 1989). ISSN: 01672789. DOI: 10.1016/0167-2789(89)90197-8.

[17] Kurokawa, K. “Power Waves and the Scattering Matrix”. In: *IEEE Transactions on Microwave Theory and Techniques* 13 (2 Mar. 1965), pp. 194–202. ISSN: 0018-9480. DOI: 10.1109/TMTT.1965.1125964.

[18] Vaughan, J. T. and Griffiths, J. R., eds. *RF Coils for MRI*. Wiley, 2012.

[19] Hoult, D. “The NMR receiver: A description and analysis of design”. In: *Progress in Nuclear Magnetic Resonance Spectroscopy* 12 (1 Jan. 1978), pp. 41–77. ISSN: 00796565. DOI: 10.1016/0079-6565(78)80002-8.

[20] Hoult, D. and Richards, R. “The signal-to-noise ratio of the nuclear magnetic resonance experiment”. In: *Journal of Magnetic Resonance (1969)* 24 (1 Oct. 1976), pp. 71–85. ISSN: 00222364. DOI: 10.1016/0022-2364(76)90233-X.

[21] Kaufman, L. et al. “Switchable MRI RF coil array with individual coils having different and overlapping fields of view”. US4881034A. California, U. of. 1989.

[22] Ackerman, J. J. H. et al. “Mapping of metabolites in whole animals by 31P NMR using surface coils”. In: *Nature* 283 (5743 Jan. 1980), pp. 167–170. ISSN: 0028-0836. DOI: 10.1038/283167a0.

[23] Roemer, P. B. et al. “The NMR phased array”. In: *Magnetic Resonance in Medicine* 16 (2 Nov. 1990), pp. 192–225. ISSN: 07403194. DOI: 10.1002/mrm.1910160203.

[24] Ross, B. et al. “Clinical experience with 13C MRS in vivo”. In: *NMR in Biomedicine* 16 (6-7 2003), pp. 358–69. DOI: 10.1002/nbm.852.

[25] Wind, R. et al. “Experimental setup for enhanced 13C NMR spectroscopy in solids using dynamic nuclear polarization”. In: *Journal of Magnetic Resonance (1969)* 52.3 (1983), pp. 424–434. ISSN: 0022-2364. DOI: 10.1016/0022-2364(83)90168-3.

[26] Ardenkjaer-Larsen, J. H. et al. “Increase in signal-to-noise ratio of $>$ 10,000 times in liquid-state NMR”. In: *Proceedings of the National Academy of Sciences* 100 (18 Sept. 2003), pp. 10158–10163. ISSN: 0027-8424. DOI: 10.1073/pnas.1733835100.

[27] Rider, O. J. and Tyler, D. J. “Clinical Implications of Cardiac Hyperpolarized Magnetic Resonance Imaging”. In: *Journal of Cardiovascular Magnetic Resonance* 15 (1 Dec. 2013), p. 93. ISSN: 1532-429X. DOI: 10.1186/1532-429X-15-93.

[28] Rider, O. J. et al. “Noninvasive In Vivo Assessment of Cardiac Metabolism in the Healthy and Diabetic Human Heart Using Hyperpolarized 13C MRI”. In: *Circulation Research* 126 (6 Mar. 2020), pp. 725–736. ISSN: 0009-7330. DOI: 10.1161/CIRCRESAHA.119.316260.

[29] Nelson, S. J. et al. “Metabolic Imaging of Patients with Prostate Cancer Using Hyperpolarized [1-^{13}C]Pyruvate”. In: *Science Translational Medicine* 5 (198 Aug. 2013). ISSN: 1946-6234. DOI: 10.1126/scitranslmed.3006070.

[30] Madelin, G. et al. “Sodium MRI: Methods and applications”. In: *Progress in Nuclear Magnetic Resonance Spectroscopy* 79 (May 2014), pp. 14–47. ISSN: 00796565. DOI: 10.1016/j.pnmrs.2014.02.001.

[31] Maril, N. et al. “Sodium MRI of the human kidney at 3 tesla”. In: *Magnetic Resonance in Medicine* 56 (6 2006). ISSN: 15222594. DOI: 10.1002/mrm.21031.

[32] Watson, W. D. et al. “Use of cardiac magnetic resonance to detect changes in metabolism in heart failure”. In: *Cardiovascular Diagnosis and Therapy* 10 (3 June 2020), pp. 583–597. ISSN: 22233652. DOI: 10.21037/cdt.2019.12.13.

[33] Neubauer, S. “The Failing Heart - An Engine Out of Fuel”. In: *New England Journal of Medicine* 356 (11 Mar. 2007), pp. 1140–1151. ISSN: 0028-4793. DOI: 10.1056/NEJMra063052.

3 | Methodology

3.1 Overview

This chapter describes the methods used to design, construct and test novel RF coil designs. This chapter builds on the existing work on RF coil characterisation, and adapts the methods used to tackle the challenges of characterising non-proton surface coils, and in particular addresses the issues arising from the significantly lower SNR and field profile non-uniformity. The structure of this chapter follows RF coil development stages in chronological order. Firstly, electromagnetic (EM) simulations (computational electromagnetics), section 3.2, are used to determine the feasibility of the coil design and provide an initial approximation of coil performance. With a valid coil design, the next step involves the construction of a coil element and associated components. Here, bench-top measurements are used to monitor the coil performance throughout the construction process, as described in section 3.3. The next step is on-scanner characterisation of the coil, using phantoms that mimic the dielectric properties and signal of a human body. A modified, fully-sampled method is described in section 3.4, which was robust against high field variations, as well as able to separate transmit and receive performance. Finally, section 3.5 describes the characterisation of tissue heating from electromagnetic simulations, ensuring the specific absorption rate (SAR) will fall within safety guidelines.

3.2 Computational Electromagnetics

Computational Electromagnetics (CEM) is the process of simulating the interactions of electromagnetic fields with objects [1]. As discussed in the Theory chapter, section 2.1.1, Maxwell's equations cannot be solved analytically for the complex geometries found in RF coil design. Modern EM simulation packages can overcome this by either iterating through the fields in both time and 3D space, or formulating an eigenvalue problem to calculate the steady state, producing efficient and accurate solutions to Maxwell's equations. The propagation of the electromagnetic wave in time can be determined, allowing for computation of the E-, H-, and other associated fields over the system. For MRI applications, EM simulations are used to

achieve field maps of three primary metrics: B_1^+, SNR, and SAR. Further, additional metrics are determined using EM simulation to characterise and optimise coil designs. Below, a complete list of metrics for RF coil characterisation available from EM simulations is presented, and is split into three categories: transmit, receive and coil feasibility.

1. Transmit performance quantification
    - B_1^+ field profile in 2D plane
    - B_1^+ strength and B_1^+ uniformity in specific ROI/voxels
    - Current and voltage through capacitors
2. Receive performance quantification
    - SNR field profile in 2D plane
    - Mean SNR in specific ROI/voxels
    - Q-values: Q_{Loaded} and Q_{Unloaded} (discussed previously in section 2.1.4.3)
    - Resistance contributions: coil and sample resistances (discussed previously in section 2.1.4.4)
3. Coil feasibility
    - Scattering parameters: S_{11} and S_{21} (discussed previously in section 2.1.4.5); used to determine lumped element layout, capacitance values and decoupling
    - SAR heating map in an anatomical human model, and max SAR heating values averaged over $10\,\text{g}$ tissue mass (discussed later in section 3.5)

Many of the above metrics are used together to determine the optimum coil design and to optimise the chosen coil design throughout this thesis. Examples include deciding between surface coil single elements, surface coil arrays and volume coil designs, and altering the number of conductor layers, dielectric layer thickness, conductor width, and conductor shape. The following sections briefly discuss the EM simulation methods used in this work.

3.2.1 Time Domain and Frequency Domain

CEM typically computes the E- (electric) and H- (magnetic) fields across the problem domain with boundary conditions determined by the object dielectric properties. Looking at the overall picture, there are several regimes of calculating EM fields. In fully time-varying 3D space, analytical solutions are impossible, and as such, approximate solutions to Maxwell's equations are computed through electrodynamics. Maxwell's equations can be written in two forms, as

an integral equation or differential equation, as shown in Appendix A. Similarly, methods to solve them can be in the time domain or frequency domain. The methods applied, through CST STUDIO SUITE® [2], use the differential equation, and consist of two solvers: (1) Finite-Difference Time-Domain (FDTD), and (2) Finite Element Methods (FEM), both with their own advantages and limitations. Whilst the exact algorithms used by commercial solvers are not publicly available, the following section aims to highlight the general principles of the two solvers and to provide an overview of their benefits and drawbacks.

3.2.1.1 Time Domain

Time domain computation primarily utilises a commonly used numerical analysis technique, the FDTD method, by discretising Maxwell's equations in both time and space. The space is split using a hexahedral mesh/grid, commonly referred to as a 'Yee cell' [3]. A 'leapfrog' manner is used where the electric field is solved at a point in an instant in time. The magnetic field is then solved at the same point in the next instant of time, and the process is repeated. Three properties follow from this method. Firstly, a dense mesh structure is necessary to capture RF coils which are typically curved in nature, which leads to high computational power requirements. Secondly, the leapfrog method can deal with the time dependence of transient and driven sources, such that the system is continuously shifting between two states; in the case of RF coils, the system responds to the source being the RF coil. Thirdly, the Yee cell discretisation requires hexahedral meshing, which is poor at capturing curved structures, and requires high mesh cell density, but has the benefit of utilising human voxel models. An example of the meshing structure is shown in Figure 3.1.

Advantages of Time Domain:

- FDTD allows more accurate and efficient modelling of transient responses between sample and coil (suited for planar RF coils).
- Human voxel models can be used for more representative EM interactions.
- Straightforward to implement adequate meshing; as all intricate coil designs can be captured by increasing mesh density.
- More robust compared to FEM, as it is possible to brute force a problem with enough time/computational power; the solutions do not need to 'converge' as is the case with frequency methods.

Disadvantages of Time Domain:

- Computational time and power scales with the simulation mesh density.
- Computational time scales linearly with the number of ports (e.g. the number of capacitor elements), so larger coils are significantly slower to simulate.
- A significantly larger number of mesh cells are required for a given wavelength, leading to long simulation times (although this issue could be alleviated using parallel computing).

3.2.1.2 Frequency Domain

Frequency domain simulations can be used as an alternative numerical analysis technique: using the FEM method. Here, the system is broken into finite elements, the 3D space is discretised, and the differential form of Maxwell's equations is solved with Dirichlet boundary conditions. As the method requires solutions of minimising energy to converge, this method suits systems with no time dependence (i.e. reaching steady state), or harmonic time dependence (switching between two frequencies). The boundary conditions do not need to be orthogonal, and as such both tetrahedral meshing and hexahedral meshing can be used. An example of the tetrahedral meshing structure is shown in Figure 3.1.

Advantages of Frequency Domain:

- Both tetrahedral and hexahedral meshes can be used, with tetrahedral meshing more accurately capturing curved geometrical surfaces, and as a result can better estimate the field profile, inductance and capacitance of resonant structures.
- Additionally, EM simulations can rapidly determine the resonance frequency of RF coils (in the case of a steady state field).
- Fewer mesh cells are required to capture the curvature of the coil structure [4], leading to reduced simulation times.
- FEM is able to capture the field from all discrete ports simultaneously through one simulation round, reducing the simulation time of complex coils with multiple capacitors.

Disadvantages of Frequency Domain:

- Solutions are required to converge (i.e. reach steady state or harmonic state). Careful implementation of meshing is required to ensure solution convergence.

- Vacuum meshes (meshes with no object, outside of coil and sample objects) are large, which leads to less accurate field profiles near coil boundaries.
- Scales poorly with the number of monitor frequencies, such that investigation over a series of frequencies requires recalculation (such as tuning a coil for ^{13}C and ^{31}P at approximately 30 and 50 MHz respectively), leading to longer simulation times.

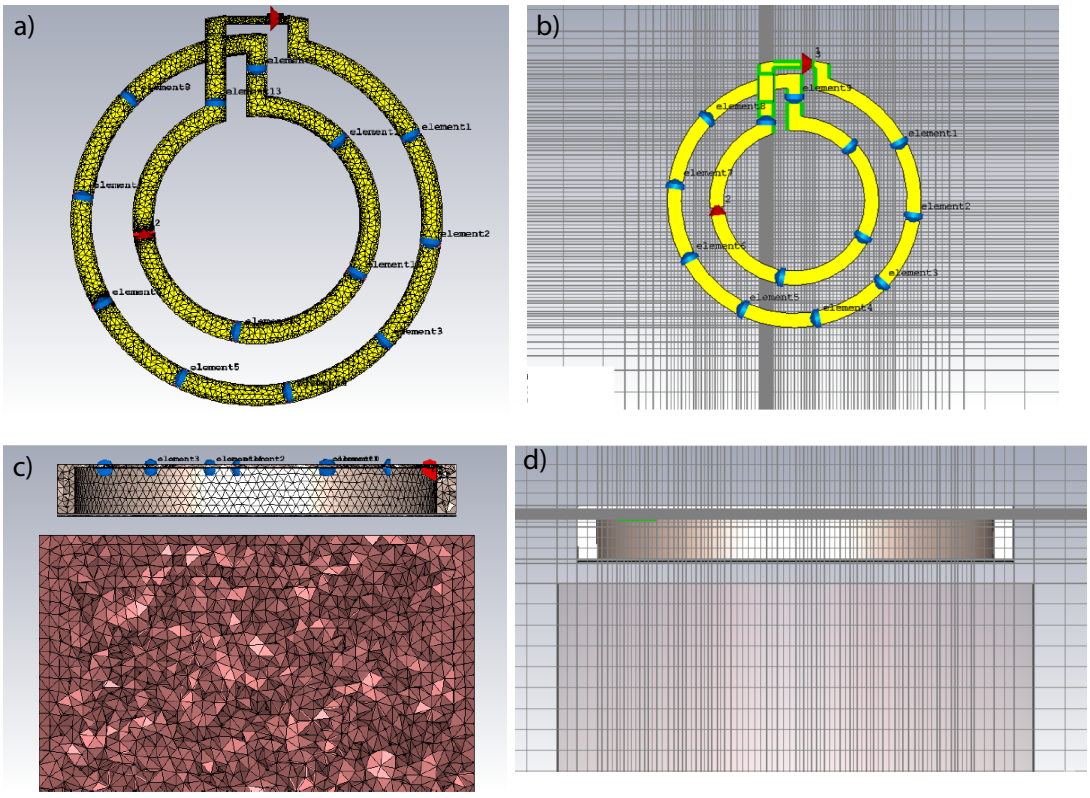

Figure 3.1: Two meshing methods shown on an example of a concentric loop RF coil. (a) Top view showing tetrahedral meshing of coil, (b) top view showing hexahedral meshing of coil, (c) cross-sectional side view showing tetrahedral meshing of coil housing and phantom, (d) cross-sectional side view showing hexahedral meshing of coil housing and phantom.

3.2.2 Running EM simulations

The CST Microwave studio package used in this thesis offers both time and frequency domain simulations. CST uses a specific time domain implementation: FIT (finite integration technique), which is similar to the standard FDTD method described above in section 3.2.1.1. The solver allows for broadband simulations in a single run (to achieve the coil responses over a wide range of frequencies), without requiring individual simulations at each frequency. For frequency domain simulation, an FEM method variant is implemented, with an additional

model-order reduction (MOR) feature that aims to speed up the simulation of resonant structures (in this case RF coils). Two simulation package-specific aspects were implemented for this work: the accurate human voxel model and the co-simulation method. Both aspects are discussed below in sections 3.2.2.1 and 3.2.2.2.

3.2.2.1 Accurate Human Voxel Model

There are several commercially available human models for electromagnetic simulations within CST. The two models primarily used are Hugo [5] and Virtual Family models from the Visible Human Project [6], used to serve as common reference points for human anatomy. All anatomical models were imported at a $2\,\mathrm{mm}$ isotropic resolution into the simulation space, with dielectric properties loaded corresponding to the tissue type and property at every voxel. The models were meshed using a hexahedral meshing structure, and simulated using the time domain algorithm. This work assumes that the models were accurate and representative, and that the dielectric properties at the simulation frequency ranges of approximately $20 – 120\,\mathrm{MHz}$ were valid.

3.2.2.2 Co-simulation

The primary benefit of the CST EM simulation package over other commercial EM solvers is the 'co-simulation' capability, which allows adjustment of lumped element capacitors without re-simulation. CST considers the simulated environment as a Microwave Studio (MWS) block, with discrete ports that allow the placement of lumped elements. The results from the EM simulation block are fed through the circuit simulation and combined, allowing coil tuning, and matching of discrete ports (lumped element capacitors) in the coil post-simulation. Using lumped element values defined in the circuit, the simulated result from each port is subsequently combined to tune and match the coil. The significant advantage of this approach is that the system does not need to be re-simulated for every change in capacitor value; this is particularly important for modelling RF coils, as this significantly reduces the time required to tune and match RF coils as well as allowing the EM field to be investigated at several resonance frequencies (by using only one set of simulated results). Due to this feature, EM simulations can be used to determine approximate capacitor values for coil construction, and verify coil feasibility across frequencies. The co-simulation technique introduces additional steps over

conventional EM simulations, requiring the combination of individual ports from the MWS block using the circuit elements. Unfortunately, the exact method used for EM calculations and combination used by the MWS package is not publicly known. However, tables provided in Appendix B show the effects of B_1^+ and SAR from different options in combining individual ports.

3.2.2.3 Quantification of Sample Noise

For an indication of achievable SNR, EM simulations can be used to determine the B_1^+ and Q_{Loaded} for coil comparison, through equation 2.38. Absolute quantification of the individual components of SNR can be further achieved by calculating the sample noise. Subsequently, the relative contributions of sample and coil noise (as presented in section 2.1.4.4) can be determined using the Q_{ratio}, equation 2.37. The sample resistance can be calculated from the integral of the E-field for $1\,\text{A}$ current. The assumption is made that the body (sample) does not contain any lossy magnetic material, which is a valid approximation for living tissue (particularly in an MRI scan). The total sample resistance can be determined by the electric field at point $\mathbf{r}$, $\mathbf{E}(\mathbf{r})$, and tissue conductivity, σ, from Equation 3.1 below [7]. Practically, the E-field is sampled at $2\,\text{mm}$ isotropic resolution over the body voxel model, and exported and summed in MATLAB® [8] to produce a single value representing sample resistance at $1\,\text{W}$.

$$R_{\text{Sample}} = \int_{\text{Sample}} |\mathbf{E}(\mathbf{r})|^2 \sigma dv \tag{3.1}$$

3.2.2.4 Simulation Protocol

The full protocol for EM simulation to obtain B_1 field maps, SNR estimates from Q-values, and SAR values is presented here. A flow chart showing the main steps for calculating B_1 and SNR are shown in Figure 3.2.

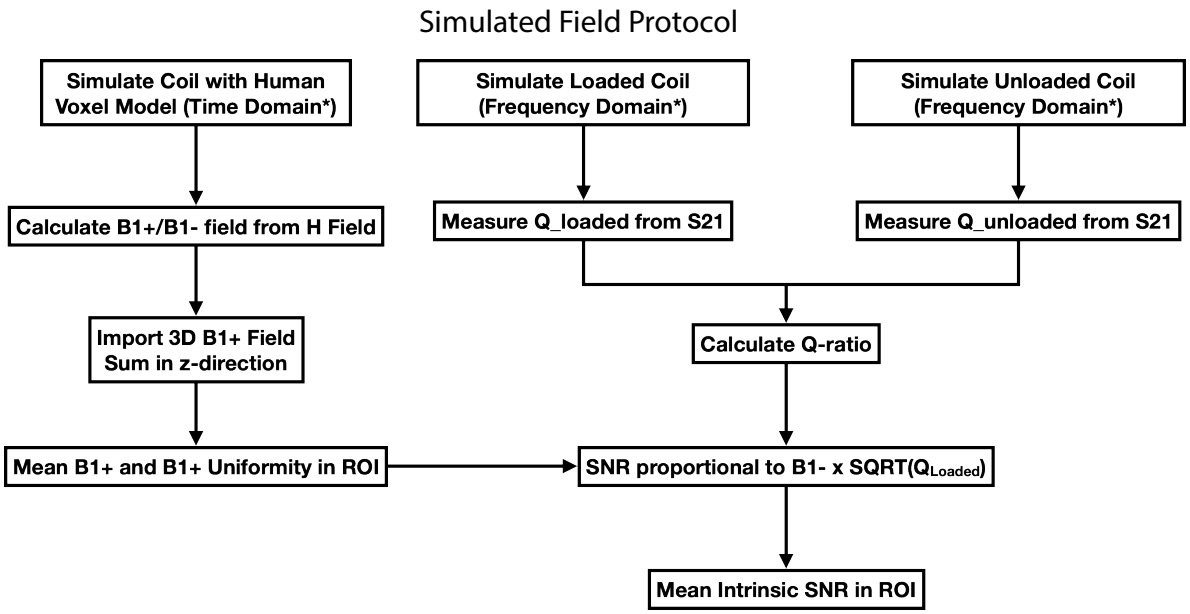

Figure 3.2: Protocol for obtaining simulated B_1^+ and SNR fields.

1. Setting up the simulation environment:
   (a) **Simulation Frequency Range:** Sufficiently large to capture coil resonance response and multiple peaks; however, the range is limited by computational power (e.g. 10 – $50\,\mathrm{MHz}$, for $^{13}\mathrm{C}$ at $3\,\mathrm{T}$ with $30.98\,\mathrm{MHz}$ central frequency).
   (b) **Boundary Conditions:** Determines the properties of $\mathbf{E}(\mathbf{r})$ and $\mathbf{B}(\mathbf{r})$ fields at edge of simulation space; examples include (1) normal conditions representing free space, where $\mathbf{E}(\mathbf{r})$ and $\mathbf{B}(\mathbf{r})$ tend to zero as $\mathbf{r}$ tends to infinity, (2) periodic conditions which approximates large systems using a single unit cell, and (3) mirror conditions where $\mathbf{E}(\mathbf{r})$ and $\mathbf{B}(\mathbf{r})$ are reflected. Typically for RF coils, the simulation space is much larger than the coil diameter given the wavelength is in the order of meters, and the RF coil is typically tens of centimetres. At this scale, normal boundary conditions are used, which is sufficiently far to prevent contamination of EM field into the body or coil.
   (c) **Reduction of Simulation Complexity:** Symmetry planes which reduce the number of calculations and save computational time.
   (d) **Excitation Port:** The method of driving the simulation, either using discrete ports, which mimic circuit input and output into the RF coil, or plane waves of uniform circular polarization at the $^1\mathrm{H}$ frequency to investigate the B_1^+ field from a $^1\mathrm{H}$ vol-

ume coil.

(e) **Type of Simulation:** Time domain versus frequency domain, discussed above in section 3.2.1.

2. Creating the objects for simulation:

(a) **Modelled Objects:** Both dielectric and conductive objects such as RF coils, phantoms and human voxel models are included, discussed in section 3.2.2.1. These models were created either on the native 3D software modeller, or imported as 3D models from external CAD modelling software. In this work, the more complex conductor designs were created using the SolidWorks® CAD modelling software [9] and imported into CST as a .sat file which stores the 3D geometry information as a text file.

(b) **Material Dielectric Properties:** The correct dielectric properties at the simulation frequency range must be assigned. Examples include the dielectric constant, conductivity, permeability, and permittivity. The important materials requiring the correct assignment are the annealed copper for the coil conductor, polyimide for the insulator, and perfect electrical conductor (PEC) for pickup probes.

(c) **Discrete Ports:** The discrete (signal) ports must be set for lumped elements with values that need to be changed, such as for tuning and matching the coil element post simulation, and fixed ports for lumped elements that are fixed in value post simulation, such as ^{1}H traps, ^{1}H baluns, and X-nuclei baluns (these components are presented in more detail in section 3.3.2).

(d) **Field Alignment:** The simulated coil and model is aligned such that the expected B_0 field is in the +z direction of simulation space. This allows the B_1^+ and B_1^- circular polarization directions to be calculated correctly.

3. Setting up the simulation parameters:

(a) **Field Monitors:** Monitors record the 3D field at a specific frequency, for RF coil applications; this includes the E-field (to calculate sample resistance), H-field (to calculate B_1) and power loss field (to calculate SAR).

(b) **Mesh Cells:** The simulation space can be divided into discrete points, represented by mesh cells. Different levels of control can be implemented for more critical components, for example local mesh control for fine meshing on critical components,

global mesh cells for general mesh control, and mesh cell type of either hexahedral or tetrahedral, which is dependent on the simulation type.

(c) **Sweeping Parameters:** Multiple simulations can be queued that take one Microwave Studio (MWS) block, such as with and without a phantom for Q_{Loaded} and Q_{Unloaded} measurements respectively, or sweeping through a coil parameter (e.g. coil radius) for optimisation of the coil design.

4. Running the EM Simulation:
   (a) **Acceleration:** The simulation time can be shortened by multiple threaded CPU cores and/or setting up parallel processing with GPU acceleration, significantly shortening FDTD simulation method times.
   (b) **Running Simulation:** For a single simulation, the simulation can be run on CST MWS, whilst to set up multiple simulations of different models the 'Job Control Centre' can be used to create a queue which will be run in sequence automatically.
5. Co-simulation (discussed above in section 3.2.2.2):
   (a) **Schematic Circuit Simulation:** Simulated results from the MWS block for each port can be combined in the circuit simulation, by adding capacitors and inductors on the discrete ports, and a power source to the input discrete port. This step allows for coil tuning and matching post-simulation.
   (b) **Effective Series Resistance (ESR):** Resistors are added in series to mimic the ESR of lumped element components; as an example, a $0.03\,\Omega$ resistor was added in series alongside each capacitor group. The ESR is obtained from Passive Plus Inc.® 1111C/P capacitor data sheet [10] for 30 MHz.
   (c) **S-parameter Combined Ports:** The overall response of the coil from the input ports can be calculated by combining the individual response from each of the discrete ports, connected using circuit simulation elements. For a single element RF coil, the S_{11} is monitored to tune and match the coil with a set characteristic impedance, typically $50\,\Omega$.
   (d) **Overall Field Profiles**: The overall E-, H- and power loss fields from the input port can be calculated by combining individual fields from each of the discrete ports, using the response/circuit simulation calculated in the previous step. This is implemented using the 'AC combine' function, which combines the signals as

presented in Appendix B.

(e) **Parameter Tuner:** The schematic components such as the capacitor and inductor values are adjusted post-simulation using the 'tuner', described in section 3.2.2.2. By monitoring the S-parameters, the coil can be tuned and matched accordingly.

6. Results processing:

(a) **Q-Value Measurement**: The Q-value of the coil element is determined through the S_{21} measurements from the circuit simulation, between the coil element and a pick-up probe. S_{21} values are exported offline into MATLAB®; the resonance frequency and bandwidth are determined using equation 2.31, from section 2.1.4.3, to calculate Q_{Loaded} and Q_{Unloaded}.

(b) B_1^+ **Field:** This is calculated from the right-handed circularly polarized (RCP) component of H-field directly on CST. Two ROIs of the B_1 values are measured:

- B_1^+ in human voxels are assigned to the organ of interest (e.g. heart/kidneys), with the mean and standard deviation sampled at $2\,\mathrm{mm}$ resolution to give the overall mean field strength and field uniformity value.
- B_1^+ is measured in a cross sectional plane; for example, at a $100\,\mathrm{mm} \times 100\,\mathrm{mm}$ FOV, with slice thickness of $5\,\mathrm{mm}$ exported into MATLAB®, again sampled at $2\,\mathrm{mm}$ isotropic resolution.

(c) **Sensitivity (SNR) Field:** The relative SNR is calculated from the B_1^-, as the left-handed circularly polarized (LCP) component of the H-field, and the Q_{Loaded} values according to equation 2.38. The data can be presented similarly as the B_1^+, either in the form of a single mean and uniformity value over a region of interest, or as a 2D cross-sectional plane.

(d) **Absolute SNR Quantification**: This can be achieved by measuring the total E-field integrated over the sample, using equation 3.1, as presented in section 3.2.2.3.

(e) **SAR Map and Peak SAR:** The SAR is calculated from the E-field, or equivalently the power loss, according to equation 3.15 over a $10\,\mathrm{g}$ tissue mass average, following the IEEE/IEC 62704-1 standard, as discussed later in section 3.5.2.

An example of an EM model created for ^{13}C MRI is a 'conventional' 20 cm diameter loop coil, using PulseTeq's design, which can be found in Figure 3.3.

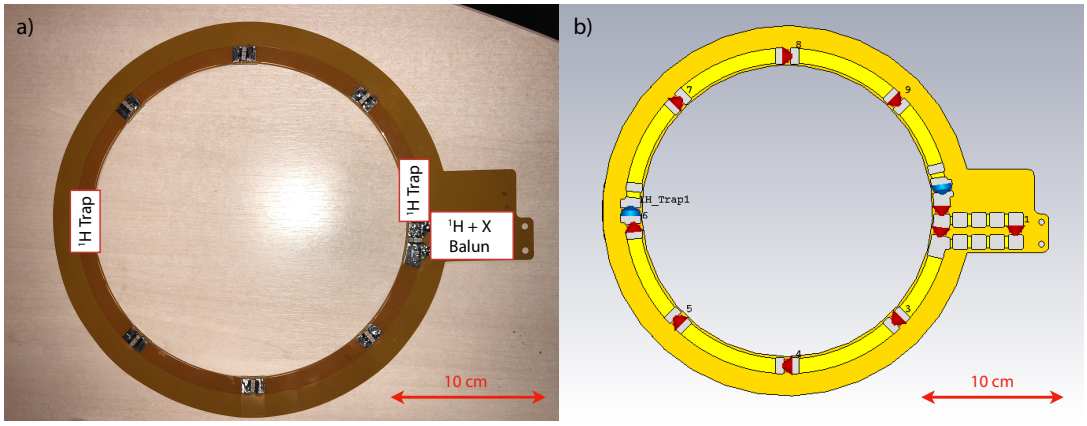

Figure 3.3: ^{13}C transmit receive surface RF coil built onto flexible PCB. (a) Photo of Coil, and (b) Model on CST for EM Simulation.

3.3 Coil Construction and Bench-top Characterisation

Construction of conventional RF coil designs is well-developed, largely driven by the MRI industry, whilst more niche coil designs are being developed by universities and academia. Construction of an X-nuclei coil is largely similar to that of a ^{1}H coil. As such, this section takes a high-level overview of the aims of RF coil construction, particularly focusing on the additional components of X-nuclei coils. The reasoning behind any deviations to conventional coil construction is also discussed here. For a more complete guide on RF coil construction, the steps in building a typical array design for ^{1}H MRI can be found from several sources, such as in [11].

The basic overall aim of RF coil construction is to achieve two basic functions:

1. Maximised transmission and/or subsequent reception of EM fields at the desired nuclear Larmor frequency. This is achieved through tuning and matching the coil to be resonant at the desired frequency. The method of achieving this is discussed below in section 3.3.3.
2. Minimised transmission and subsequent reception of EM fields at undesired nuclei Larmor frequencies. This is achieved by isolating the coil from undesired frequencies. The method of achieving this is discussed below in section 3.3.2.

Despite the clear cut and simple aims, RF coil construction can be complicated due to multiple coil resonances and unexpected EM coupling interactions that arise from other coils. The

primary challenge associated with constructing a 'good' coil, i.e. with high sensitivity, is the often unpredictable nature of coil response when tuning and matching the coil. As an example, altering the electrical property of the coil, i.e. altering the capacitors, inductors and conductor tracks, has an effect on the resonance frequency, impedance matching of the coil, and decoupling of the coil. The complexity is additionally increased by the numerous possible circuit designs for impedance matching, ^{1}H traps, baluns, and detuning, where the addition of one component changes the properties of other components. This section aims to discuss the methods and benchtop tests used in constructing and characterising the in-house RF coils described in this thesis, through a more systematic approach to surface coil construction. Here, the scope of discussion is limited to the construction of a single element; later chapters in this thesis expand the work around multiple elements, where there are EM interactions across more than one element. This is discussed in section 6.4.1.1 through decoupling of multiple elements.

3.3.1 Characterisation Techniques

RF coils can be represented as RLC (resistor-inductor-capacitor) circuits, with a complex electrical impedance, Z, comprised of both a real component representing resistance, R, and an imaginary component representing reactance, X. Under an excitation source (such as alternating current), RLC circuits form harmonic oscillators, similarly to LC circuits; however, the resistor creates a dampening effect on these oscillations and determines the energy loss, as shown in section 3.3.1.4. The total resistance is the sum of the sample and coil resistances. Here, a 'well-built' RF coil firstly aims to minimise the resistance, which allows the minimum energy to be lost per oscillation and provides the highest sensitivity. Secondly, the natural resonant frequency of the coil circuit harmonic oscillations should match the Larmor frequency determined by the nuclear rotation in the magnetic field. Thirdly, the coil should be impedance matched to minimised reflected power in both directions; for example transmit RF coils are commonly impedance matched to $50\,\Omega$ resistance and zero reactance; this value is determined by the RF power amplifier.

In this section, benchtop measurements are used to characterise the coil with regard to the three above requirements, using Q-values (described initially in section 2.1.4.3), and S-parameters (described initially in section 2.1.4.5). These benchtop coil characterisations were performed with two pieces of equipment: a network analyzer and a pick-up probe (or alternatively termed

a sniffer probe). The S-parameters were measured using a vector network analyzer (VNA; Rhode and Schwarz, ZNLE3 $1\,\mathrm{MHz}$ – $3\,\mathrm{GHz}$) that measures both amplitude and phase properties, widely used to characterise two-port RF systems. An RF pick-up probe is a simple loop forming a connection between the coaxial shield and coaxial core that allows the electronic test equipment (in this work, the network analyzer and oscilloscope) to measure the RF signal. Below, the methods used in the construction of a single coil element are presented; the specific details regarding the design of coil components are not discussed here due to proprietary IP belonging to PulseTeq Ltd.

3.3.1.1 Characteristic Impedance

When starting coil construction, the most important metric of RF coil performance is the electrical impedance, Z, which opposes an AC current similarly to how resistance, R, opposes a DC current. Impedance can be represented in polar form: $Z = |Z|e^{j\ \arg(Z)}$, where $|Z|$ is the ratio of voltage amplitude to current amplitude and $\arg(Z)$ is the phase difference between voltage and current. Alternatively, impedance is defined in Cartesian form as $Z = R + jX$, combining the effects of the resistance, R, and reactance, X. With AC current, sinusoidal voltage and current waves can be represented as complex functions denoted by voltage, V, and current, I, respectively.

$$\begin{aligned} V &= |V| \exp j(\omega t + \phi_V) \\ I &= |I| \exp j(\omega t + \phi_I) \end{aligned} \tag{3.2}$$

Following this, the impedance is defined as $Z = V/I$:

$$Z = \frac{|V|}{|I|} \exp j(\phi_V - \phi_I) \tag{3.3}$$

Hence, we can determine the impedance for each of the three components of the RLC circuit:

- For a resistor, using Ohms law: $v_R(t) = I_{R(t)}R$:

$$Z_R = R \tag{3.4}$$

- For a capacitor, using the relation: $I_C(t) = C\frac{dv_{C(t)}}{dt}$:

$$Z_C = \frac{1}{j\omega C} \tag{3.5}$$

- For an inductor, using Faraday's law: $v_L(t) = L\frac{dI_L(t)}{dt}$:

$$Z_L = j\omega L \tag{3.6}$$

Using the combined impedance of the individual components of an RLC circuit, we can arrive at the equations that must be satisfied for both tuning and matching the circuit. The total impedance of RLC circuits (from all individual lumped components) differs between series and parallel circuits due to the equations for combining impedance. For series circuits, $Z_{total} = Z_1 + Z_2 + ... + Z_n$, whilst for parallel circuits, $\frac{1}{Z_{\text{total}}} = \frac{1}{Z_1} + \frac{1}{Z_2} + ... + \frac{1}{Z_n}$. In both cases, two equations govern the construction of RF coils: the real part of Z gives equation 3.7 which describes the matching criteria of the coil typically matched to $50\,\Omega$, and the imaginary part of Z gives equation 3.8 which describes the tuning criteria of the coil. When rearranged according to section 3.3.1.2, this gives equation 3.10 below.

$$R = \mathrm{Re}(Z_R) = 50\,\Omega \tag{3.7}$$

$$X_{\text{Total}} = \mathrm{Im}(Z_{\text{C}}) + \mathrm{Im}(Z_{\text{L}}) = \frac{1}{\omega C} + \omega L = 0\,\Omega \tag{3.8}$$

3.3.1.2 Resonance Frequency

The resonance frequency of a coil element is obtained from rearranging equation 3.8 for ω which must equal the Larmor frequency, ω_0, as determined by the nuclei, presented previously in equation 2.8. This gives equation 3.10, which is the tuning criteria for the RF coil.

$$\omega_0 = \frac{1}{\sqrt{L_{\text{Total}} C_{\text{Total}}}} \tag{3.9}$$

$$\omega_0 = \gamma B_0 \tag{3.10}$$

The above equation is valid for LC and RLC circuits including series, parallel circuits with finite L and C. Typically, RF coils are considered series RLC circuits where L is the total inductance (comprising of the self inductance and mutual inductance) and C is the total capacitance (comprising of self capacitance and stray capacitance). For a simple coil design, as is the case with the coil presented in Figure 3.4, the self capacitance can be calculated as: $\frac{1}{C_{\text{Self}}} = \frac{1}{C_{\text{Match}}} + \frac{3}{C_{\text{Tune}}}$. Given the single conductor layer, we make the approximation that the stray capacitance is small, and the only contribution is from coupling to the dielectric sample,

such that $C_{\text{Total}} = C_{\text{Self}}$. Practically, the resonance frequency is determined as the frequency corresponding to the minimum S_{11} value, or the maximum S_{21} value from Figure 3.4.

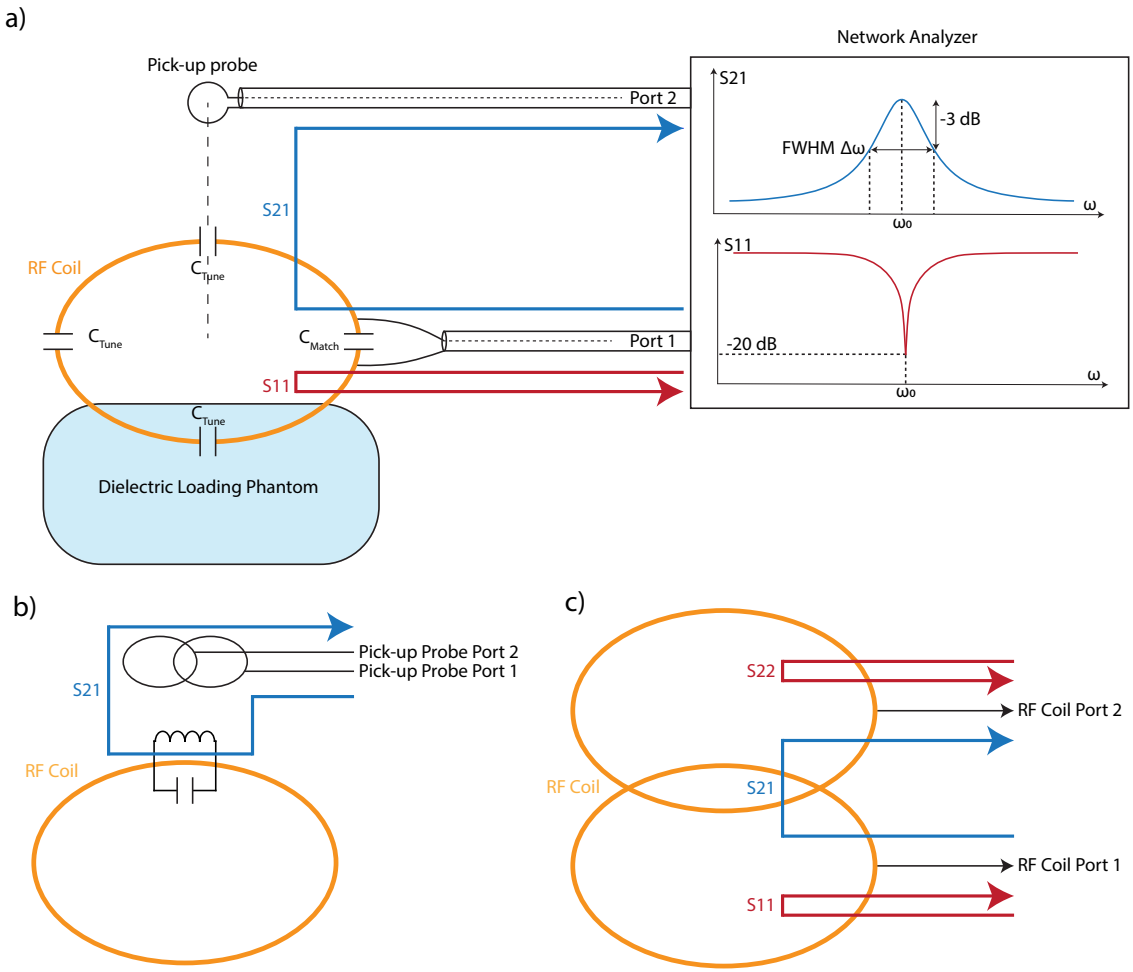

Figure 3.4: Diagram of example benchtop S-parameter measurements using a two-port network analyzer and pick-up probes. (a) An RF coil and pick-up probe connected to network analyzer, vertically separated by approximately 1 coil diameter, with the coil loaded by dielectric loading phantom or sample. Example S_{11} measurement (in red) showing $-20\,\text{dB}$ reflection at the resonance frequency from the coil. Example S_{21} measurement (in blue) showing transmission to measure Q-values using resonance frequency and FWHM at $-3\,\text{dB}$ from the peak. (b) Two decoupled pick-up probes connected to network analyzer, positioned above the coil to measure local resonances, in this case a ^{1}H trap using S_{21} Q-values. (c) Two RF coil elements connected to the network analyzer, to measure the overlap for geometric decoupling through S_{21} transmission, and individual S_{11} and S_{22} reflection coefficients.

The total inductance is calculated by inserting known values for total capacitance and frequency into equation 3.10. Whilst these discussions treat the RF coil as an RLC series circuit, more complex conductor designs, such as those developed in Chapter 4, entail stronger mutual capac-

itance and mutual inductance, which may not necessarily be in series. Therefore, the Q-factor relations discussed in section 2.1.4.3 may not be the ideal approximation. Additionally, it is important to note that even with this simple circuit design, changing both the matching and tuning capacitors changes the coil S_{11} and S_{21}; these coupled effects complicate coil construction. Therefore, the protocol for tuning and matching the coil is an iterative step, which is described later in section 3.3.3.

3.3.1.3 Measuring Scattering Parameters

Building on from the discussion of S-parameters in the Theory chapter, section 2.1.4.5, we next discuss methods for measuring the two S-parameters: S_{11} and S_{21} in a two-port RF system using the network analyzer and pick-up probes. Discussion of the quantification of the S_{11} and S_{21} metrics can be found in Appendix C. The following section is kept short, and only discusses the practical method of measuring S-parameters, and the advantages of S_{21} versus S_{11}.

For an S_{11} measurement, a range of frequencies are monitored, with the marker at the desired Larmor resonance frequency. We can lower the minimum in the S_{11} curve by decreasing the matching capacitance, or raise the minimum in the S_{11} curve by increasing the matching capacitance. The aim of coil tuning and matching is to adjust the capacitance such that the S_{11} curve intersects the normalised impedance point $z = 1$, discussed in greater detail below in section 3.3.3. This is achieved, more specifically, by changing the tune capacitance of the coil, which will firstly shift the marker along the curve (higher capacitance shifts to lower frequency), and secondly have a coupled effect on the impedance matching, as well as the match capacitance of the coil, as shown in Figure 3.4 a.

The x-axis value of the peak $S_{21}(\mathrm{dB})$ represents the resonance frequency of the RF coil, and the y-value peak represents a relative $S_{21}(\mathrm{dB})$ value for a given separation between the pick-up probes and coil. The peak and FWHM value is subsequently used to calculate the Q-factor in the following section 3.3.1.4. Measuring S_{21} is more difficult, with one or two pick-up probes required. The pick-up probe is placed at a minimum of 1 coil diameter away from the test coil, with the centres coinciding and the plane of both loops parallel. This allows for measurement of the test loop properties without excessive coupling to the pick-up loop, and a symmetric S_{21} curve as rotating the pick-up loop alters the symmetry of the S_{21} curve. In the case of measuring a small resonant loop which cannot be connected to the network analyzer directly, two pick-

up probes are used; one pick-up probe is connected to port 1 of the network analyzer and the second probe is connected to port 2 of the network analyzer as shown in Figure 3.4 b. The two pick-up loops are overlapped such that they are geometrically decoupled, and invisible to each other. This allows for the resonance of only the RF coil to be detected without contamination from the coupling of the pick-up probes.

Whilst S_{21} and S_{11} measurements of coil elements provide the same information, there are situations where the use of S_{21} versus S_{11} measurements is advantageous. A brief discussion of the advantages of using S_{11} and the advantages of using S_{21} are discussed below so as to illustrate which method was chosen at a given coil construction step.

Advantages of using S_{21} over S_{11}:

- The RF coil does not need to be connected to the network analyzer. This is useful for measuring LC traps, baluns, or small elements where large inductance changes occur when connected with additional conductor tracks. In these cases, the test coil is inductively coupled to two pick-up loops.
- For observing the resonance frequency of the test coil, the coil does not need to be matched to the characteristic impedance. This is useful for LC loops as part of a coil, or for example 'high impedance' coils.

Disadvantages of using S_{21} over S_{11}:

- Lower ESR pick-up probes are used to minimise resistance measurements of the test coil. However, the mutual inductance of the probes are picked up via inductive coupling to the coil and cannot be eliminated. The undesired additional inductance is minimised by the use of small probes (approximately $1\,\mathrm{cm}$ in diameter) and placed far from the test coil (more than 1 test coil diameter).
- Poor reproducibility of S_{21} measurements are seen, as the relative position between the test coil and probes need to be fixed. As the surrounding area of the coil must be free from any conductive material, no metal clamps can be placed on the coil, and so creating a test rig to keep the coil in place is tricky.
- Detected S_{21} signal is weak and noisy, due to the large separation necessary between test coil and pickup loop, as discussed above. To counteract this, the S_{21} spectrum is averaged, over typically 8 or 16 times, requiring measurements with the coil in place for

around 20 seconds (depending on resolution and bandwidth).

3.3.1.4 Measuring Quality Factor

This section builds upon the discussion of Q-factors from the Theory chapter, section 2.1.4.3. Starting with the RF coil tuned and matched at resonance, the Q-value is calculated using a network analyzer. Two S_{21} methods are used to determine Q: either port 1 connected to the coil and port 2 connected to a pick-up probe, or port 1 and port 2 connected to two decoupled pick-up probes. These methods are shown in Figure 3.4 a and b respectively. Both methods calculate the S_{21} by measuring the FWHM, at $-3\,\mathrm{dB}$ from the peak, using the equations described in section 2.1.4.3. The advantage of the first Q-value method is that the position of the pick-up probe and the S_{21} magnitude gives information on the field profile of the entire coil element. However, the magnitude is relative to the distance between the coil and probe, and so absolute quantification is challenging. Additionally, as the Q-value is measured from the coil to the probe, this measured value must be doubled. The advantage of the second Q-value method is the ability to determine the effects of localised resonant loops, however, this requires careful decoupling of both coils by changing the overlap.

3.3.2 Isolation of Undesired Frequencies

RF coil construction typically requires ensuring resonance at desired frequencies, and the isolation of undesired frequencies. Typically, when building a coil element, the isolation elements are constructed before the coil is made to be resonant. This section discusses the method of building LC traps and baluns for decoupling to the ^{1}H coils.

Starting with an empty PCB, or a base copper conductor track, the isolation component is usually constructed and placed before the capacitors for tune and match, as the LC traps and baluns will alter the resonance frequency of the coil. Decoupling of neighbouring elements is not discussed here, however decoupling components (such as PIN-diodes for active detuning) will be affixed at this stage. This subsection describes the method of constructing components on a coil element that prevent the resonance at undesired frequencies. The most important frequency to avoid, in the case of non-proton RF coils on clinical systems with an integrated ^{1}H body coil, is naturally the ^{1}H frequency. This is particularly challenging for ^{13}C, as the ^{1}H frequency is approximately four times the ^{13}C frequency, which may coincide with higher

order resonances. Resonance at the ^{1}H frequency must be avoided for three reasons, firstly to minimise damage into the receive preamplifier (particularly for a receive coil), secondly, to minimise the EM coupling between the coils to preserve the field profile and sensitivity of the non proton coil, and thirdly for patient safety by removing potentially unexpected E-field hot-spots.

3.3.2.1 LC Traps on X-nuclei coils

Whilst an RF coil can be considered a resonant RLC circuit with an unwanted damping caused by the resistive component, an RF trap can similarly be considered a resonant RLC component, but with a wanted damping frequency. The fundamental difference is that whilst the RF coil is designed to be resonant and transmit/receive the B_1 field over a larger FOV at the X-nuclei frequency, the opposite is desired of the ^{1}H RF trap; to minimise any transmitted/received fields (to minimise field distortions) at the ^{1}H frequency. Practically, the three components (R, L, and C) must be designed to set two constraints: the bandwidth (determined by R) and the resonant frequency (determined by L and C). The final degree of freedom left determines the type of filter circuit by the position of L and C in parallel or series. Typically, ^{1}H traps comprise of an L and C lumped element component, with additional resistor component arising from the ESR from both the inductor and capacitor element. This LC circuit is placed in series to the coil circuit, and acts as a band stop filter across the RF coil. A band stop filter is a frequency selective circuit, which allows all frequencies to pass except within a specific band. Effectively, the ^{1}H trap is tuned to ^{1}H resonance frequency, and dissipates oscillations within the proton frequency range, but allows circuit resonance at other frequencies. The size of the resistor determines the Q-values (as shown previously in equation 2.32), thus a smaller R leads to a larger Q, or smaller bandwidth on the band stop filter. For the case of ^{1}H traps the bandwidth of the filter can be narrow, as to only cover the specific ^{1}H frequency, and so no additional resistance needs to be included beyond the ESR.

During a ^{1}H scan, the ^{1}H EM fields incident into the coil is absorbed by the ^{1}H traps locally, and prevents the coil being resonant or absorbing the field. ^{1}H traps need to be placed at regular intervals along the coil conductor path to be effective, however they come with several drawbacks that must be mitigated. Firstly, RF traps inherently increase the resistance of the coil system, secondly the RF traps take up space and create local E- and H-field hot-spots (the pen-

etration is observed to be approximately $1\,\mathrm{cm}$ into the patient), and thirdly, they make tuning and matching coils more challenging as the RF traps contribute to the overall capacitance and inductance. Safety requirements on clinical coils commonly require ^{1}H traps and cable baluns to be placed at specific maximum separation distances as determined by Siemens documentation. The filter performance of ^{1}H traps can be fine tuned locally (individually) by the S_{21} using two pick-up probes as shown in Figure 3.4 b, and the overall filtering can be verified looking at the S_{11} of the overall coil at the ^{1}H frequency. The resistive contributions that degrade the coil performance can be measured by the Q-value of the coil.

Construction of ^{1}H LC traps are fairly straightforward and well known, a brief summary of the protocol used in this work is presented below:

1. Select an initial capacitance based on factors such as high voltage requirements, high Q (low ESR) and spatial constraints for counterpart inductor component. Typically, approximately a $50\,\mathrm{pF}$ capacitor was used for $120\,\mathrm{MHz}$ RF traps.
2. Determine the design of LC circuit and construct onto RF coil. A smaller loop diameter limits B_1^+ field distortions from ^{1}H localiser scans with X-nuclei coil. Typically, the dimension of the LC trap is kept as small as possible, around $1\,\mathrm{cm} \times 1\,\mathrm{cm}$ footprint.
3. The resonance of the LC traps are determined using the aforementioned methods. Whilst the capacitance value is known, the inductance of a given inductor is frequency dependent, and not easily determined. Here, using equation 3.10, for $120\,\mathrm{MHz}$, and fixed C-value, we can determine an approximate L-value.
4. Adjust or change the inductor according to the previously determined L value, such that the resonance is at $120\,\mathrm{MHz}$.
5. Measure S-parameters of the overall coil, ensuring isolation at the ^{1}H frequency, and secondly the 'high' Q-value has not been diminished by the addition of the RF traps.
6. Repeat steps and implement sufficient RF traps until current blocking is achieved for sufficient ^{1}H coil decoupling, verified through scanner tests and EM simulations.

3.3.2.2 Baluns

Baluns are commonly found on the cabling of RF coils, or at the connection point between the coil element and cabling. Typically, a coaxial cable (RG223/U) is used to deliver the RF signal to and from the coil element, designed to carry high frequency signals with low losses.

Coaxial cables consisting of a inner conductor (the core, typically solid copper or silver) and an outer concentric conducting shield (typically woven copper or silver), separated by a dielectric insulator. Typically the cable shield is connected to the coil ground and the cable core is connected to the coil input. For a well matched RF coil, at any point along the cable, the current flowing on the inner core is equal to, but opposite to the current on the outer shield, this is the desired differential mode of current flow. However, at the ends of the cables (connection to coil), if the coil is not perfectly matched, a reverse current may be generated on the shield, which is in the direction of the core, and thus common mode. This common mode current leads to external fields generated from the RF shield that will radiate outwards, with the undesired effect of coupling to conductors in close proximity and generating noise. Over great distances, this will reduce the sensitivity of receive coils, reduce the power of the transmit coil, and may even alter the tuning.

This issue is alleviated by RF baluns, derived from 'balanced - unbalanced unit', which allow the core and shield lines to be balanced by eliminating common mode signal. Many balun designs exist and are widely used in RF coil cable current suppression; the coils constructed in this thesis specifically utilise two types of balun designs taken from PulseTeq: 'bazooka' baluns and coil baluns. On almost all X-nuclei RF coils, ^{1}H cable baluns are typically required to be placed at less than quarter wavelength intervals (for $120\,\mathrm{MHz}$, this equates to approximately $50\,\mathrm{cm}$) along all cables. Bazooka baluns are designed with a conductor sleeve encapsulating the coax cable, such that it is a quarter wavelength, and so the impedance is infinite. The infinite impedance on the outer shield of the cable ensures the current on the inner conductor equals current on outer conductor, balancing the current flow. The second type of balun used is on the coil element, to balance the current before reaching the coil from the cable. For X-nuclei coils, two baluns are needed: firstly a ^{1}H balun, and secondly an X-nucleus balun. These types form an approximate LC design, however the theory is not covered in detail due to PulseTeq IP. Several bazooka baluns (also known as transmission line baluns) [12] and coil baluns were constructed and tested, and placed into the RF coils described in this thesis.

3.3.3 Resonance at desired frequency

Once isolation elements are in place, the next step is to place tuning and matching capacitors onto the coil element to ensure resonance at the desired frequency. Coil tuning and matching

is performed iteratively, such that an approximate tuning is implemented, following this, the coil is approximately matched, which will cause the resonance tune to be out of the desired range and require subsequent re-tuning. This time consuming process is repeated until both the coil tune and match are at acceptable levels. The process is facilitated by a good initial approximation of capacitance determined from EM simulations software and circuit simulators, as described in section 3.2.

Previously, section 3.3.1.2 described the ideal conventional single loops as an RLC series circuit, with a resistive component (representing both coil and sample resistance), an inductance component (representing the intrinsic inductance of the coil, determined by the design of the conductor parts), and a capacitive component (determined by discrete capacitors), positioned in series. In actuality, RF coils also experience parasitic (unwanted) resistance, inductance and capacitance. Parasitic resistance is obtained from imperfect soldering, and the effective series resistance (ESR, approx $0.03\,\Omega$) of capacitors and fuses. Both additional inductance and stray capacitance may arise from imperfect solder and excess conductor track. These 'parasitic' inductances and capacitances do not diminish the Q-factor of the coil (thus parasitic might not be the right term), however they may hinder the tuning and matching of the coil. This additional capacitance or inductance may not be in series, as shown by the novel coil design described in Chapters 4 and 5, which leads to complications when tuning and matching the coil, and cannot be easily achieved simultaneously. Therefore, this section describes the iterative process of tuning, in section 3.3.3.2, followed by matching in section 3.3.3.3.

3.3.3.1 Capacitor Design Considerations

Following on from the discussion above, a coil may be 'tuned' by either adjusting the capacitance or inductance. There are several factors to consider when placing capacitors, namely the phase of the field in the coil, and the voltage. The phase difference $\Delta\phi$ between two points of a conductor is determined by the length of the electrical path, Δx and the wavelength, λ in equation 3.11:

$$\Delta\phi = 2\pi\Delta x/\lambda \tag{3.11}$$

For coils, at a relatively high example frequency of $300\,\mathrm{MHz}$, the quarter-wavelength is approx-

imately $25\,\mathrm{cm}$. To ensure a coherent phase across the coil, capacitors are split and evenly distributed along a conductor track at intervals significantly smaller than $25\,\mathrm{cm}$. This was evident with the novel preclinical coil design, where distributed capacitors showed better B_1 uniformity compared to a single capacitor, section 4.4. Here, as an initial approximation, the total capacitance can be calculated from the reciprocal of capacitors in series, simply from equation 3.12, when ignoring any capacitance in parallel (discussed below). The second factor to consider is the voltage; each capacitor has a voltage rating determined by the manufacturer. For RF coils built in this work, non-magnetic, ceramic high Q-factors (>$10\,000$ at $1\,\mathrm{MHz}$) capacitors were acquired from Passive Plus Inc [10]. The maximum voltage rating was limited by the physical size of the ceramic chip and capacitance. As an example, larger 0.22" by 0.25" capacitors tolerated a voltage of approximately 2.5 – $3\,\mathrm{kV}$ and can be used for ^{1}H volume coils, with an ESR of approximately $0.1\,\Omega$. A smaller capacitor of dimensions 0.11" by 0.11" tolerated a voltage of 1 – $1.5\,\mathrm{kV}$ suitable and typically used for receive coils and X-nuclei transmit coils, and an ESR of approximately 0.02 – $0.05\,\Omega$. The smaller capacitors take up less space, and have a three times lower ESR, which is important in a power limited case, or in receive. For transmit X-nuclei coils for the Siemens MRI system, a potential difference of approximately $400\,\mathrm{V}$ is expected across the capacitors at max power of $4\,\mathrm{kW}$ (section 2.3.2), so the voltage rating of 1 – $1.5\,\mathrm{kV}$ of the smaller capacitors are suitable. Generally three capacitors or more are used in parallel (to the conductor), to allow for a reduced ESR (the resistance in parallel is reduced), whilst the total capacitance is determined as the sum of capacitance in parallel. Typically the ESR increases as capacitance increases, so groups of three capacitors allow for both a higher total capacitance achieved with minimum ESR, and higher voltage rating (Kirchhoff's voltage law), whilst simultaneously minimising resistance, as shown in Figure 3.5.

For single loop coils, the total capacitance C_{Total} calculated from N individual tune C_{T_i} capacitors and one match C_{M} capacitor in series is as follows:

$$\frac{1}{C_{\text{Total}}} = \frac{1}{C_{T_1}} + ... + \frac{1}{C_{T_N}} + \frac{1}{C_{\text{M}}} \tag{3.12}$$

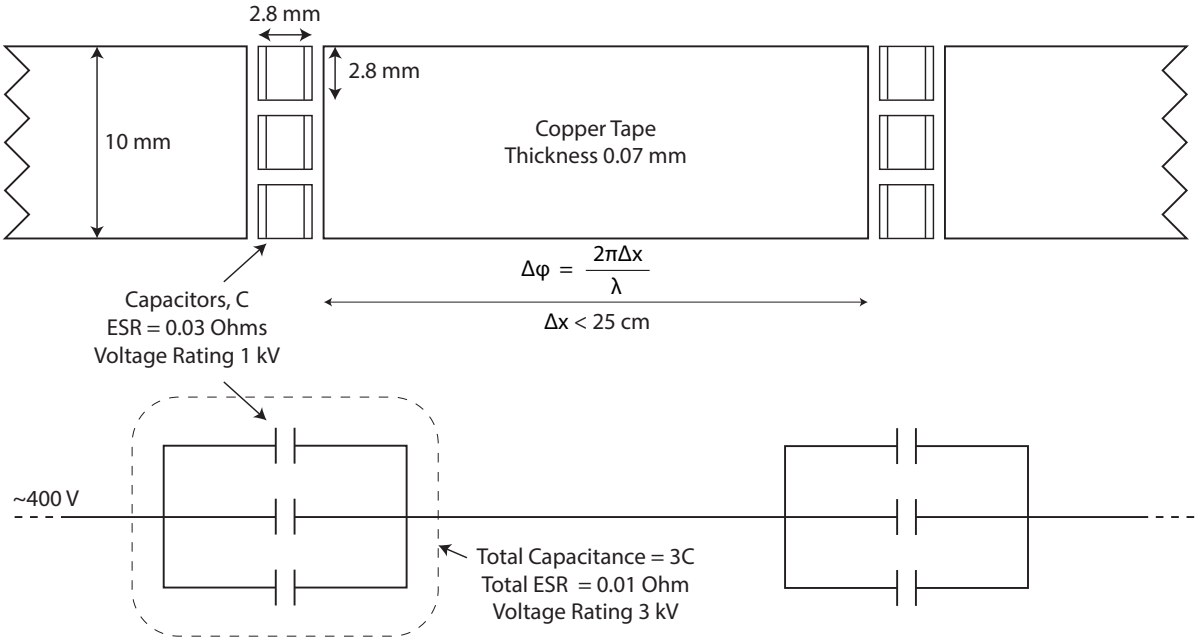

Figure 3.5: To scale diagram of capacitor connections on the copper conductor to tune and match the RF coil. The above figure shows the capacitance, ESR, and voltage rating of individual capacitors. Three capacitors are grouped together to achieve the desired resonance, lower ESR and higher voltage rating across a gap. Additionally the phase shift, $\Delta\phi$ is shown with a copper length, Δx of less than $25\,\mathrm{cm}$ at $300\,\mathrm{MHz}$. The corresponding circuit diagram is shown below.

3.3.3.2 Coil Tuning Protocol

For this work, taking into account the discussion above, the tuning circuit comprises of uniformly distributed lumped capacitors in series along the conductor at approximately $10\,\mathrm{cm}$ intervals, with each lumped capacitor consisting of three individual discrete capacitors in parallel, combined to achieve the desired total capacitance to tune the coil, as shown in Figure 3.5. The protocol used for tuning the coil is as follows:

1. Starting with a PCB or copper track with only isolation elements (from above), ensure gaps in the conductor allow capacitor distributed in series along the coil, to minimise phase shifts along the coil, and ensure within each lumped element group, sufficient capacitors in parallel for acceptable voltage rating, and minimised ESR.
2. Solder initial estimate of capacitor onto coil PCB, and connect coaxial connector, typically BNC (Bayonet Neill-Concelman) or SMA (SubMiniature version A), and determine total capacitance of coil, according to equation 3.12.
3. Calibrate cable effects on network analyzer with S_{11} using three calibration points con-

nected to port 1, and S_{21} using through cable between port 1 and port 2 [13]

4. The RF coil is plugged into port 1 of the network analyzer, and the pick-up probe is plugged into port 2, as shown in Figure 3.4. S_{11} measurement determines coil resonance frequency and match, whilst S_{21} measurement determines Q-value, and ESR of components placed.
5. Measure resonance frequency, to determine coil inductance, L, using equation 3.10 and total capacitance of coil measured previously. With L_{Coil}, calculate expected capacitance needed to achieve desired resonance, adjust capacitance correspondingly, (if ω is higher than ω_0 then increase capacitance and vice-versa).

3.3.3.3 Coil Matching Protocol

A matching circuit must be used to 'match' the coil to the expected impedance of the power supply: commonly the transmit coil is matched to $50\,\Omega$ as determined by the RF power amplifier, whilst receive coils are $50\,\Omega$ or higher impedance determined by the low noise preamplifier. Several matching circuits exist, commonly L, T and π-circuits [14]. The circuit chosen will require feasible capacitance and inductance values: typically range of approx 1.5 – $300\,\mathrm{pF}$ and 50 – $1000\,\mathrm{nH}$ both limited by stability of the value at the lower bound and ESR at the upper bound. Additionally the bandwidth of the matching circuit (range of frequencies which the matching is suitable for) is an important consideration. The simplest case is the L matching circuit, with one single match capacitor in parallel to the coil itself, and appropriate for most coils (of reasonable inductance and capacitance). The protocol for coil matching is as follows:

1. Starting from an approximately tuned coil from above, but with poor matching, the coil can be plugged into port 1 for S_{11} measurements.
2. The impedance, Z, is measured at the desired resonance frequency. Depending on different contributions of resistance and reactance, an appropriate matching circuit should be selected or adjusted.
3. Manual impedance matching or automated using circuit simulators can be used to determine the necessary match capacitance for impedance matching. As a standard rule, if the S_{21} curve does not reach the characteristic impedance of $50\,\Omega$, the match capacitance needs to be reduced, and if the S_{21} curve is exceeds the characteristic impedance, the match capacitance needs to be increased.

4. S_{11} of the new match measured, with Q-values monitored using S_{21} from a pick-up loop. The resonance frequency most likely will have been altered, and requires subsequent tuning, following the protocol from the above section.

3.4 Scanner Coil Characterisation

Following benchtop characterisation of the RF coil prototype, B_1^+ and SNR maps are acquired on the scanner using phantoms that mimic the sample dielectric properties of the sample to be studied. The B_1^+ and SNR maps allow visualisation of the field strength and uniformity of the transmit and receive field profiles, to allow comparison of surface coils, and determining the optimum coil dimension for a given design. There are several common approaches to X-nuclei RF coil field mapping on the scanner, these methods and their associated advantages and disadvantages are discussed in Appendix D. However, these common transmit methods (double angle method, DAM, and Bloch-Siegert method) are susceptible to the challenges of X-nuclei imaging, namely the noisy scans from low SNR and the high RF inhomogeneities of surface coils. Additionally, this inhomogeneous transmit leads to the measured SNR on receive SNR being strongly influenced by the achieved flip angle on transmit. These coupled transmit-receive field effects from the Tx-Rx coil requires transmit calibration to isolate the transmit performance on a single voxel, for B_1^+ indications. For subsequent SNR indications, the noise within a single voxel is measured at voltage required for a $90°$ flip angle, obtained from the transmit calibration. This can be achieved typically using either a single voxel spectroscopy (SVS) method or and chemical shift imaging, both are discussed in Appendix D.

In this section, a protocol is described that fully samples the voltage-signal relationship, which deals with the high variability in field strength from surface coils, the low SNR that arises from X-nuclei imaging, and further allows mapping of the receive sensitivity profile without transmit field profile influences, from the same scan. Whilst this method of field characterisation is well understood, it is typically not implemented or published due to long scan durations, and limited use outside of accurate coil characterisation. The experimental setup for reproducible coil characterisation and comparison across different coil designs is described in section 3.4.1, the transmit and receive protocol and analysis of acquired data in section 3.4.2 and 3.4.3 respectively, and finally the advantages and disadvantages of this method compared to existing

characterisation methods is discussed in section 3.4.4.

3.4.1 Experimental Setup

This section focuses on the approach taken for assessment of clinical coils but a similar approach was taken for the development and testing of pre-clinical coils, just on a smaller scale. Fair performance comparison between different RF coil designs is challenging, due to two factors. Firstly the high field inhomogeneity from the sharp transmit and receive field drop off (approximately $1/r^3$), such that the field strength and coil sensitivity becomes highly dependent on the distance from the coil. This requires consistent placements of the coil on the phantom and relative to the selected ROI. Secondly, the coil loading must be consistent with surface coils of different coil FOVs, where too much or too little dielectric loading will negatively affect the magnitude of B1 and SNR, and therefore the coil performance. Additionally, if conductivity and permittivity of the dielectric within the coil FOV is significantly different, the field profile (notably the depth penetration of the field) will differ. As such, a reproducible and consistent experimental setup was necessary for consistent loading of RF coils, to ensure consistency across scans and coil placements. This section describes the steps taken to ensure a fair comparison across different coil designs

The strength of dielectric loading experienced by the coil is dependent on the phantom shape and position (specifically the filling factor of the coil FOV) such that a larger phantom will more heavily load a larger coil, whilst a smaller phantom will load a smaller coil more. This comes from the fact that as larger coils are more sensitive at far greater depths, and smaller coils are more sensitive closer towards the coil centre. To ensure consistent loading, the conductor of the coil was ensured to be separated from the surface of the phantom by $1\,\mathrm{cm}$. As different coil and phantom pairs will lead to different loading, consistent loading was ensured by monitoring the S_{11} reflection with a network analyzer. Additionally, the nature of flexible coils constructed in this project, whilst allowing the coil to conform to the patient, will alter the inductance (bending the coil will increase the inductance), and consequently change the resonance frequency 'tuning'. As such, a general framework was developed to allow different coils to be compared fairly, with the overall experimental setup shown in Figure 3.6 a.

1. A signal phantom is used that represents the size of anatomy, placed on the scanner table (e.g. ethylene glycol, torso sized for ^{13}C)

2. The coil is placed on the phantom, such that the conductor is $1\,\mathrm{cm}$ from the surface of the phantom and the ROI is within the phantom at the target depth (e.g. from $8\,\mathrm{cm}$ to $12\,\mathrm{cm}$ for the heart)
3. A loading phantom (typically saline bag) is placed next to the coil. For single element Tx/Rx coils, the saline bag is positioned above the coil, this positioning allows fine adjustment of loading by moving the saline bag towards or away from the coil centre. This offers more reproducible and consistent loading than human participants.
4. The network analyzer is connected to coil individual elements, with the coil positioned inside the scanner, to measure S-parameters to determine coil matching and loading.
5. Long cables are run between the coil in the scan room and the network analyzer in the (via wave guides). The long cables strongly affected the S-parameter measurements of the coil, and calibration was required to negate these, as described in section 3.3.3
6. The position of the loading phantom (and strength) was adjusted to change the matching, as well as the shaping of the coil for flexible PCB designs, until a $-20\,\mathrm{dB}$ or better reflection coefficient was measured.

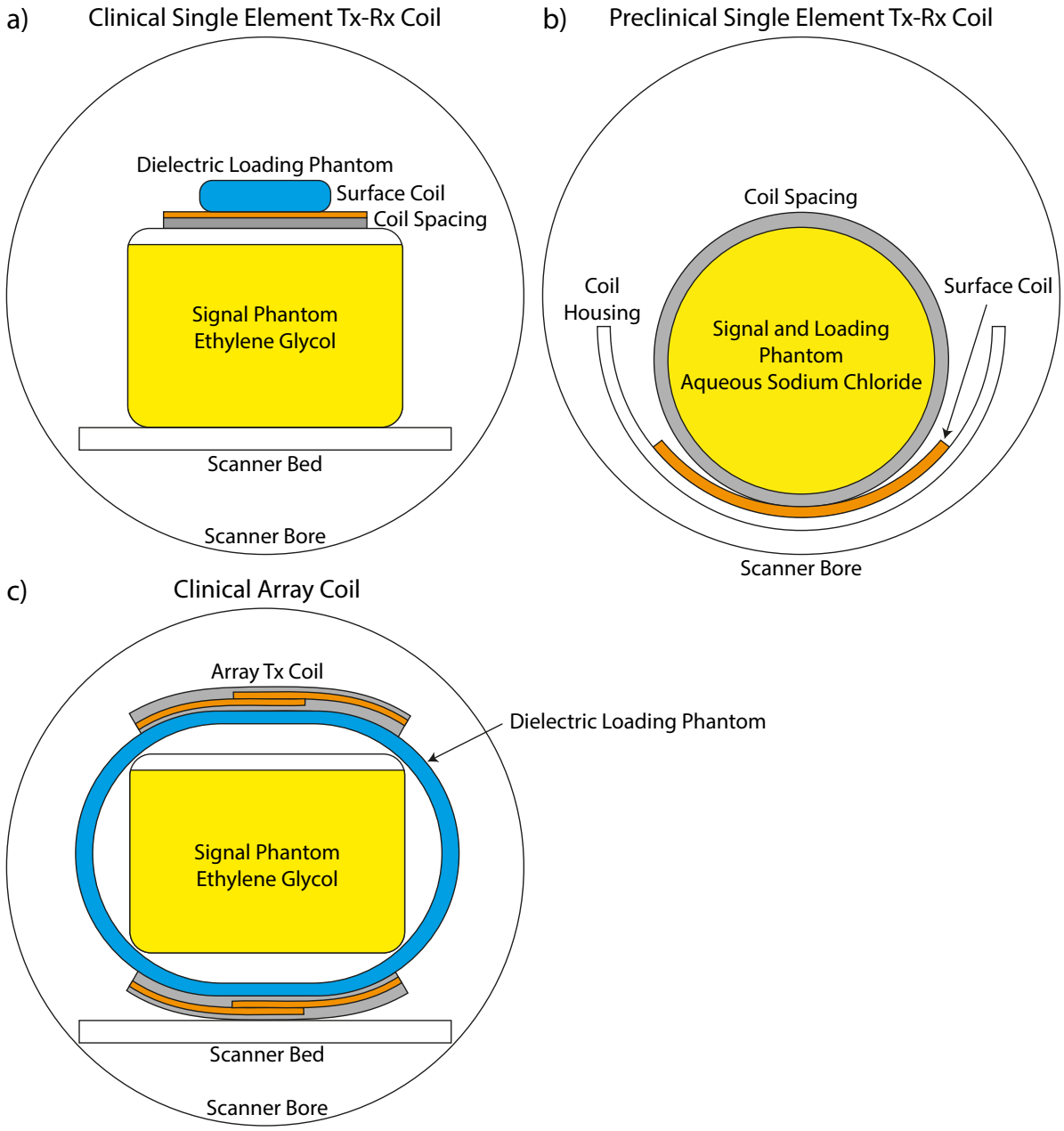

Figure 3.6: On-scanner experimental setup with phantoms. (a) Clinical MRI single element coil setup with saline bag for dielectric loading and ethylene glycol tub for signal. (b) Preclinical MRI single element coil setup with Signal and loading phantom (e.g. aqueous sodium chloride). (c) Clinical MRI array coil setup with hollow cylindrical body loading phantom and ethylene glycol tub for signal.

3.4.2 Transmit Magnetic Field Protocol

The basis of this field mapping method is that a sinusoidal relationship exists between voltage supplied, V, and signal, S. We can form an equation to determine the coefficients of the sinusoid using the normalised peak signal, S_{peak}, and the voltage required for a $90°$ flip, $V_{90°}$,

such that $\frac{V_{90^\circ}}{\xi} = 90^\circ$, as in Equation 3.13.

$$\frac{S}{S_{\text{peak}}} = \sin\left(\frac{V}{\xi}\right) \tag{3.13}$$

This equation is commonly used for the 'power calibration' of the RF coil, however despite the name, the power scales with the voltage^2, and the B_1 linearly with voltage. Here, ξ is a measure of coil efficiency, such that a smaller ξ represents less voltage required to achieve a given signal. Typically, in magnitude encoded B_1^+ mapping protocols (as discussed in Appendix D), images are acquired at distinct voltages, $V_1, \ldots, V_n$, to allow a sinusoidal fit of equation 3.13 at each voxel to obtain the two coefficients, S_{peak} and ξ, as shown in Figure 3.7. Typically, the next step is to re-scale ξ to produce a flip angle map for a given input power or voltage, then convert to B_1^+ using the relation between flip angle and B_1 given in equation 2.14, section 2.1.2.2. To fully sample the sinusoidal curve, the minimum sampling frequency is determined using the Nyquist-Shannon sampling theorem. In the case of the expected sine curve of frequency $1/\xi$, equation 3.13, can be fully sampled at twice the frequency at $2/\xi$. The main challenge with surface coil field mapping is the high variation in flip angle across the coil FOV, by several orders of magnitude. The flip angle is proportional to the reciprocal of the frequency $1/\xi$, as such, to satisfy the sampling theorem at regions close to the coil, a high sampling density must be used (e.g. at every $5\,\text{V}$). However, voxels far from the coil centre coincide with noisy scans from typically low signal regions. Due to the low coil sensitivity far from the coil centre, only low flip angles can be sampled. Thus it would be challenging to fully capture the sinusoidal curve through extrapolation of the low voltage signal data points. Improved curve fitting can be achieved by increasing the voltage sampling range. As such, scans up to the max allowed voltage should be run, so as to measure signal and fully sample the sinusoidal curve as far from the coil as possible, for accurate and comprehensive field mapping. To simultaneously satisfy the requirements of high sampling density and a wide range of voltages, a variable density voltage sampling scheme was proposed. By varying the sampling density across all voxels, we are able to fully sample the sinusoidal curve close to the coil with signal flipping at high frequency, and fully capture the sine curve as far form the coil as possible, shown in Figure 3.7. An example of the sampling scheme is to run images at voltage steps of $5\,\text{V}$ from zero to $20\,\text{V}$, then steps of $10\,\text{V}$ until $60\,\text{V}$, then steps of $20\,\text{V}$ until $100\,\text{V}$, then steps of $40\,\text{V}$ until max

voltage.

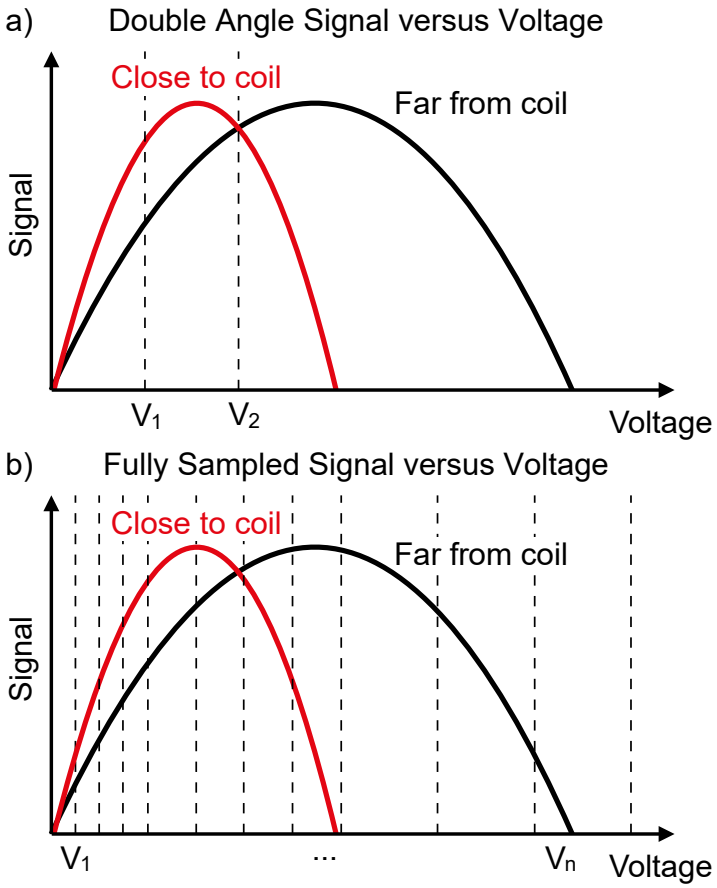

Figure 3.7: Comparison of B_1 mapping methods used in thesis. (a) Signal versus Voltage relationship showing double angle method at captured voltages V_1 and V_2, (b) Signal versus Voltage relationship showing fully sampled method which captures a series of voltages $V_1, \ldots, V_n$.

A further challenge was encountered when attempting the sinusoidal curve-fit specifically at regions close to the coil. At these regions, across the full range of voltages up to the maximum supplied to the coil, the nuclei is flipped several revolutions. Each subsequent 'sinusoidal peak' or revolution, causing the signal to digress from a sinusoid, but rather with an envelope of exponential decay and small changes in oscillation frequency. As a rough generalisation, these deviations are primarily due to T_1 and T_2 decay constants, field inhomogeneities and partial volume effects. In these cases, the signal data points captured at the lower voltages are more representative of the coil performance and so preferentially the first sine peak should be used for calculating the flip angle. As such, the voltage - signal data was truncated independently for each voxel, at the voltage value which was twice the voltage required to achieve a $90°$ flip, $V_{90°}$, or equivalently at approximately at the voltage required to achieve a $180°$ flip, $V_{180°}$. For

particularly inefficient coil designs, with the limited power of the X-nuclei amplifier, V_{180° may not be able to be measured at the largest voltage supplied to the coil. To sample a further point along the sinusoidal curve, the total voltage $\times$ RF pulse duration metric can be increased. Therefore when the max voltage is reached, increasing the RF pulse duration can sample further along the sinusoidal curve.

The accuracy and success of curve fitting of the truncated values above was quantified using the coefficient of determination metric, R^2 ranging from 0 to 1 (where zero represents zero determination, and one represents full determination). This R^2 evaluates the 'goodness-of-fit; of the predicted signal values, f_i, compared against the measured signal values, y_i. The R^2 can be calculated according to equation 3.14 below, with $\bar{y}$ representing the mean of the y_i data set.

$$R^2 = 1 - \frac{\sum_i (y_i - f_i)^2}{\sum_i (y_i - \bar{y})^2} \tag{3.14}$$

Using this single peak truncation, characterising the first peak sinusoid is straight forward and achieved with high accuracy (high R^2) close to the coil. However whilst slightly worse R^2 values are expected for regions far from the coil due to decreased SNR, identification of the correct peak for truncation was challenging. Random peaks in signal that arise from the noise were often selected for truncation and distorted the curve fit, as such the 'findpeaks' function was used which identified peaks of a given peak prominence, which is a measure of how much the peak stands out against neighbouring peaks from the intrinsic height and relative location. The MATLAB® function 'lsqcurvefit' is a non-linear least-squares solver, of the two possible algorithms, empirically it was determined the Levenberg-Marquardt Algorithm [15] was more robust against the high noise compared to the Trust-Region-Reflective Algorithm [16].

This protocol was implemented for field mapping of all the X-nuclei RF coils built in this work, as presented in Chapters 4, 5 and 6. The method was found to be more robust when dealing with low SNR from natural abundance ^{13}C scans and high field inhomogeneities of surface coils compared to the other commonly used methods for X-nuclei coil mapping, as discussed in Appendix D. The exact B_1^+ protocol is presented below, and summarised visually in Figure 3.8.

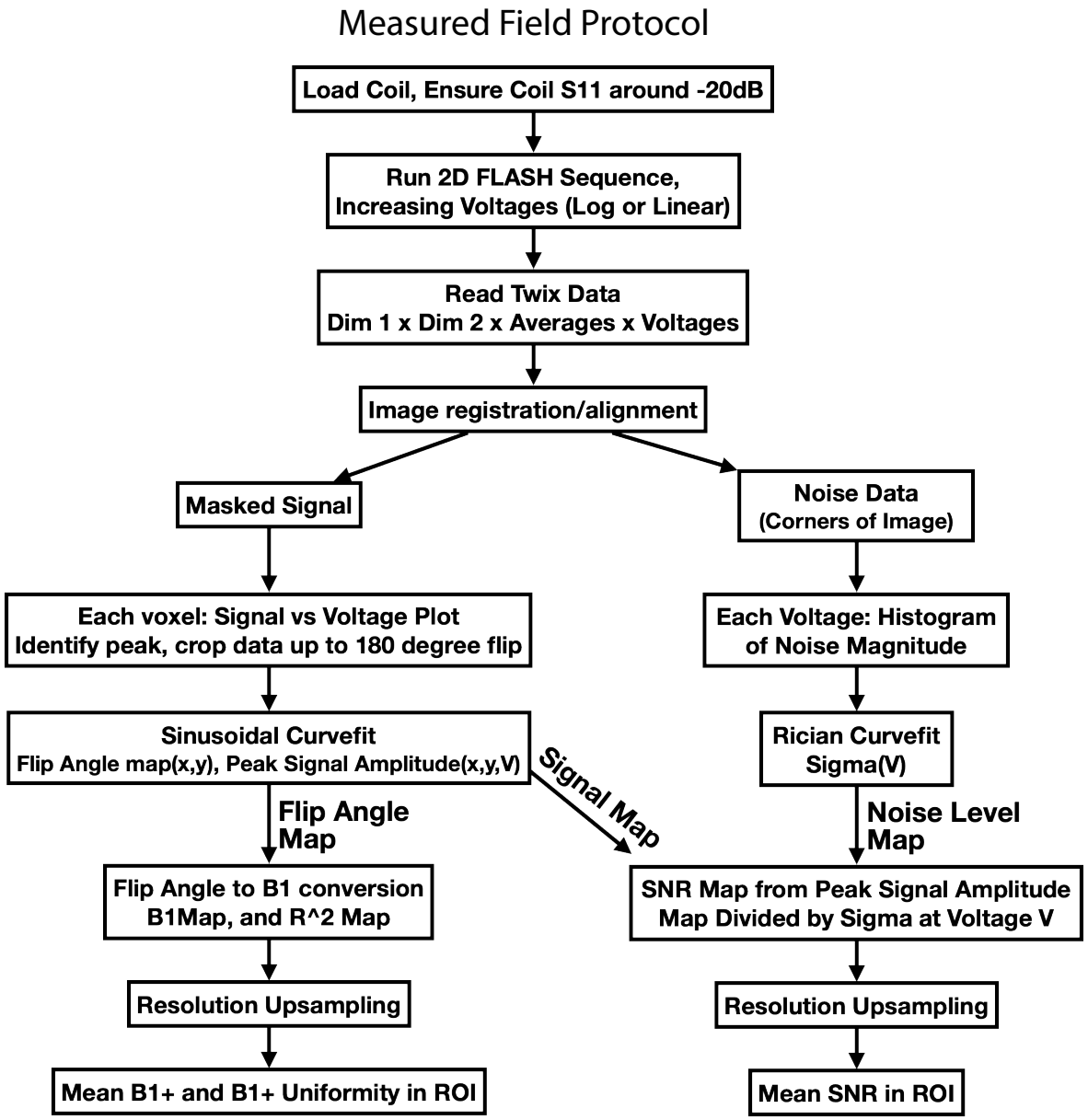

Figure 3.8: Protocol to obtain measured on-scanner B_1 and SNR maps by fully sampling the power curve. Noise and signal data are treated separately, and combined in the end for SNR.

- Coil placed on phantom with reproducible coil loading, such that the $S_{11} \leq -20\,\mathrm{dB}$ measured on the network analyzer as discussed above in section 3.4.1.
- A series of 2D gradient echo scans (Siemens: FLASH, GE: GRE) are performed over the same voxels over the full voltage range of the scanner, with higher sampling rate at the lower voltages. Typical scan parameters used are: long TR (fully relaxed $7.5\,\mathrm{s}$) short TE ($\sim 8\,\mathrm{ms}$), low resolution ($16\,\mathrm{voxels} \times 16\,\mathrm{voxels}$), high averages (32-64 averages), large

FOV ($640\,\mathrm{mm} \times 640\,\mathrm{mm}$), slice thickness $2\,\mathrm{cm}$, resulting in $2\,\mathrm{cm}$ isotropic voxels, 'sinc' RF pulses, with long pulse durations (1 – $2\,\mathrm{ms}$, longer pulse duration was used when insufficient voltage).

- The scanner raw data file (Siemens 'TWIX') is exported into MATLAB® and restructured into a 4D array of dimensions representing: x-direction voxel, y-direction voxel, averages, voltages.
- Image registration and alignment of data (x- and y-direction voxel shifts) for consistent ROI and coil positioning across different coils.
- Binary signal and noise mask generated using threshold determined by MATLAB® function 'greythresh'. Signal data extracted and processed in protocol below, noise data extracted and processed in section 3.4.3.
- At each voxel:
  - A mean signal versus voltage plot is generated over the averages (64), V_{90° is identified using MATLAB® function 'findpeak' by minimum peak prominence, peak height and peak width as expected from the data and position from coil.
  - Truncation of the sinusoid plot is performed at the expected V_{180°, which is two times V_{90°, to minimise deviations from the sinusoid due to T_2 decay, and partial volume from B_1 inhomogeneities at voltages causing over-tipping (nuclei revolution of greater than one).
  - The sinusoidal curve fit is performed using MATLAB® function 'lsqcurvefit' with the Levenberg-Marquardt algorithm for $y = A|\sin(Bx)|$. Here, the A coefficient represents the peak amplitude to be used in SNR calculations in section 3.4.3, and the B coefficient represents the flip angle map, as the voltage required to achieve a given flip angle. Both peak amplitude and flip angle stored in a 2D array representing x- and y- direction voxels.
  - The flip angle map converted to a B_1^+ map using equation 2.14. Additionally, the R^2 map is obtained using equation 3.14.
- The resolution of both B_1^+ and R^2 maps are up-sampled by a factor of 2, using zero padding (such that a 16×16 resolution is up-sampled to 32×32).
- Desired metrics are extracted such as the mean B_1^+ and B_1^+ uniformity in the ROI (for example defined as a 2D circle of radius 6, with the centre positioned $10\,\mathrm{cm}$ from the coil

centre).

3.4.3 SNR Mapping Protocol

The SNR can be extracted from the same set of B_1 mapping scans. By fully sampling the signal versus voltage relationship across every voxel, the transmit and receive field profiles can be decoupled from the final image. SNR is calculated and defined previously in section 2.1.4.1 as the mean of signal divided by standard deviation of noise, equation 2.26. At each 2D gradient echo image, (for a given voltage), the signal is extracted from the A coefficient of the sinusoidal curve fit at voxels within the masked magnitude image, as described above in section 3.4.2. This signal value is effectively the peak signal, obtained at V_{90°. The mean signal used in equation 2.26 is the signal averaged over the ROI. On the other hand, the noise is extracted from the four corners of the magnitude image, as an example a resolution of 32×32 will combine the noise from four corners of 5×5, giving $100\,\text{voxels}$ to sample. These corners are chosen to be far away from the regions of signal to minimise signal contamination for all coil designs; typically the scan is positioned such that the ROI is in the centre of the FOV. If any signal is contaminated into the noise corners, this would show from the curve fit in Figure 3.9.

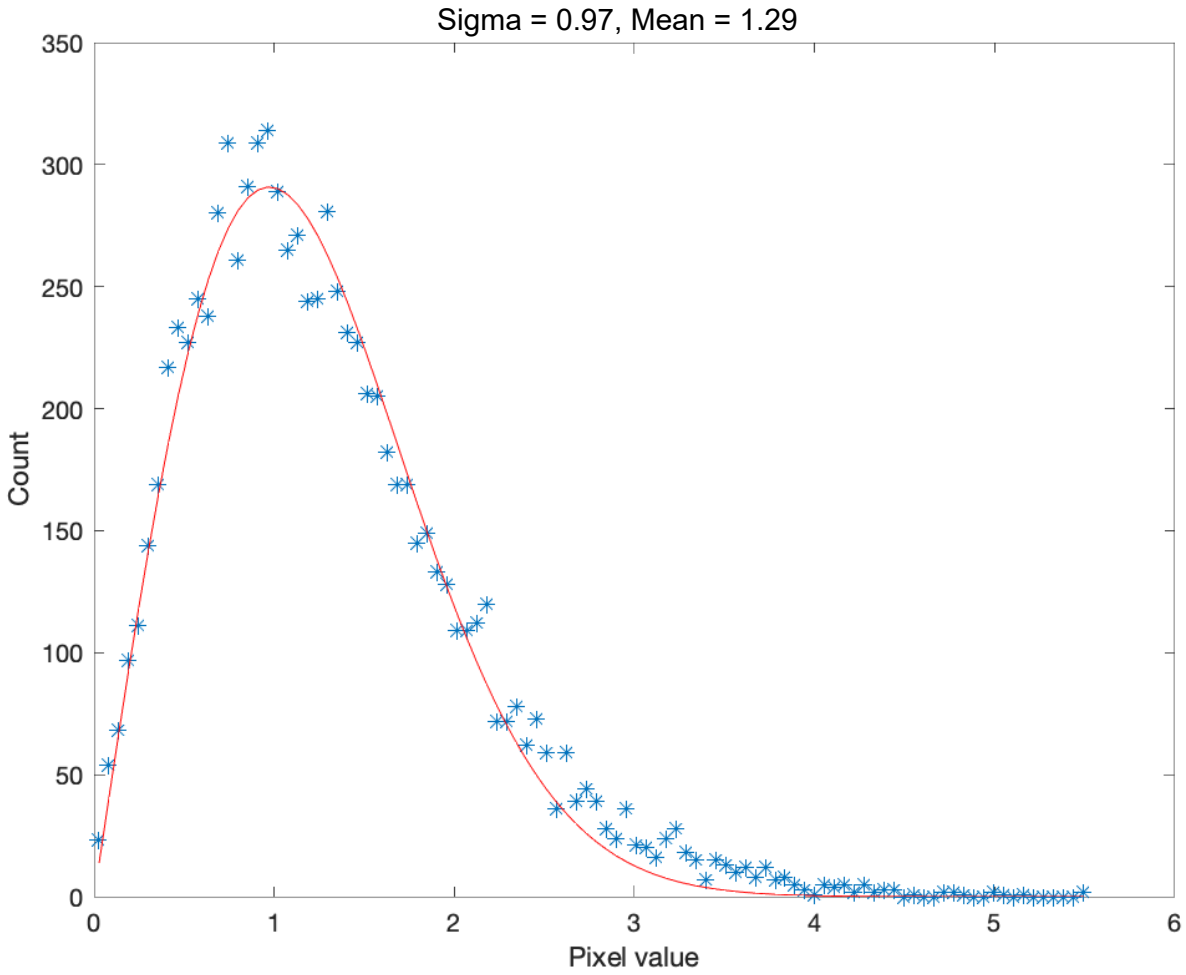

Figure 3.9: Example noise histogram with Rician curve fit showing mean and sigma at one single voltage with data points obtained from each voxel.

The noise is extracted from the acquired magnitude images, and as presented in section 2.1.4.2, this noise follows a Rician distribution. The Rician distribution follows from both the real and imaginary components forming a bi-variate normal distribution, leading to the Rician probability distribution function, $p_{Rician}(x)$, as shown in equation 2.29, where I_0 is the modified Bessel function with order zero [17], as described previously in equation 2.30. For curve fitting to extract the variation, σ, the noise is plotted on a histogram. For sufficient data points, the noise values are taken from each scan before averaging, which leads to 64 averages over 100 voxels, for a total of 6400 points for each voltage. We expected this fitted noise variation, σ, to be constant across voltages; however, this was often not the case, possibly due to scanner preamplifier gain rescaling or variations in number of averages. These small variations in σ were plotted across voltages, and the noise value at each voxel was chosen that corresponded to the peak signal voltage (or equivalently V_{90°). The division of coefficient A by σ on a voxel

by voxel basis finally produces a 2D SNR map independent of transmit field profile. The exact SNR protocol is presented below, and summarised visually in Figure 3.8.

- Continuing from the masked image in section 3.4.2, for each voxel: coefficient A is extracted as peak signal for each voxel.
- Noise corner extracted from the data set, for each individual image at each voltage (e.g. 5×5 voxels for each corner over 64 averages, combined to $20 \times 5 \times 64$ data set).
- At each voltage:
  - Histogram of noise magnitude plotted, taking the noise voxels from individual averages.
  - Rician distribution curve fit to noise data, to determine noise variation, σ for each voltage.
  - Signal map from peak amplitude coefficient A (above) is divided by the noise level map from σ, to determine SNR at each voltage. Here, σ is expected to be independent of V.
- σ plotted against voltage, and the σ at the voltage required to achieve the corresponding peak signal, A is recorded.
- SNR calculated as A/σ at each voxel to form SNR map.
- Using zero-filling, the resolution of the SNR map is up-sampled by a factor of 2.
- Desired metrics are extracted such as the mean SNR in the ROI (for example defined as a 2D circle of radius 6, with the centre positioned $10\,\mathrm{cm}$ from the coil centre).

3.4.4 Advantages and Disadvantages

This section summaries the advantages and disadvantages of this fully sampled coil characterisation method compared to existing methods presented in Appendix D. The three primary advantages of this method are:

- **Robust against low SNR scans.** This is ideally suited to X-nuclei MRI, as both sinusoidal curve fitting for signal and Rician curve fitting for noise improve 'smoothness' of B_1^+ and SNR maps from otherwise noisy images.
- **Mapping of highly non uniform field profiles.** Small surface coils and array elements produce highly non-uniform field profiles, the fully sampled signal versus voltage relationship with variable voltage sample rate captures a wide range of flip angles for a large

inhomogeneous field maps.

- **Separate Tx and Rx field profiles**. The B_1^+ and SNR field maps can be obtained from the same set of scans, such that the receive profile has no transmit field effects. Reproducible coil loading was achieved with a network analyzer, allowing the coil to be well 'matched' with the optimum transmit field and highest receive sensitivity.

The primary disadvantage of this method of coil characterisation is the long acquisition times and technicalities in setting up the scan. The long duration arises from a combination of: high number of averages (typically 64 to 128), long TR time ($7.5\,\mathrm{s}$ in ^{23}Na and ^{13}C) to minimise T_1 effects without RF spoiling, and the numerous and wide range of voltages that were sampled (although somewhat reduced by the variable density sampling). This method of coil characterisation on phantoms was typically performed overnight, for one coil, to produce very high quality field maps, as used to characterise coils developed in chapters 4, 5 and 6.

3.5 RF Coil Heating

This section discusses only the EM heating considerations of coil safety, that are associated with a novel RF coil design. Whilst other potential sources of hazards can occur, they typically arise from the larger static magnetic field [18, 19], and are of no concern to RF coil design.

From Maxwell's equations, a changing B-field is accompanied by a changing E-field. Therefore in MRI, the transmitted B_1^+ will cause a corresponding E-field in to the patient. The strength of any interaction is therefore determined by the inductive coupling between the RF coil and the patient. We expect a wide range of RF effects to be present during B_1^+ transmission. However we only need to consider a small subset of effects, i.e. the ones that cause heating, or thermal effects. Typically much of the RF power transmitted does not cause heating, only less than $2\,\%$ of the RF power is actually absorbed by the nuclei [20]. These effects arise from the E-field (not B-field). The E-field deposits energy into the tissue through resistive heating, where charge carriers are accelerated by the E-field imparting them with kinetic energy, and dielectric heating, where polar molecules (primarily water) align with the oscillating E-field, causing rotating dipoles to collide with other molecules. The relative contribution of both are difficult to separate out; generally we attribute both processes towards E-field heating.

Broadly, there are two types of EM heating that are of concern, the first is localised heating

causing thermal burns, in small hot-spots, and the second is E-field heating from energy deposition into the body across the larger coil FOV. Localised hot spots can be avoided through coil design and RF traps that resonate and absorb EM fields at specific frequencies. However, the second form of EM heating arises from the E-field that is the counterpart of the B_1^+ field in EM oscillations. This form of heating cannot be minimised, without deteriorating the B_1^+ field. This section describes the sources of both types of heating and the efforts in minimising local hot-spots, whilst measuring and limiting the general energy deposition levels.

3.5.1 Localised Thermal Burns

Thermal burns account for nearly two-thirds of injuries in clinical MRI, and as such are an important health consideration. An accurate knowledge of the EM field interactions of a given RF coil design is crucial to minimise thermal injuries. There are three underlying physical mechanisms that lead to RF induced burns [21]. The first type is inductive heating, where eddy currents are induced between the metal and skin (which is a reasonable conductor), the high resistance of the metal-skin boundary generates heat. The second effect is heating from a resonant loop, this is the most common heating and generates the highest amount of heating. The resonant circuits absorb and release energy at the resonant frequency causing a significant amount of burns in the FOV of the resonant loop. Lastly, heating from the antenna effect, where wires may act as antennas, producing standing current waves concentrated at the tips, causing localised heating.

An accurate knowledge of the EM field interactions of an RF coil is required to minimise thermal injuries. Inductive heating is minimised in this work by ensuring adequate separation between the coil conductors and skin, typically $1\,\mathrm{cm}$, as is the case with the clinical translation of novel coils designed in this work, section 5.2. Heating from the resonant loop is minimised through ^{1}H RF traps that absorb oscillations induced in the coil conductor from eddy currents, and prevents the main loop from resonating. This is typically the method for decoupling X-nuclei and ^{1}H RF coils, as described previously in section 2.2.3.2. This may not be sufficient, as additional resonant loops may form from overlapping conductor designs, as is the case with the novel coil presented in section 4.2.2. Here, blocking each resonant loop formed using a ^{1}H trap is unfeasible due to the increase in ESR of each additional ^{1}H trap as well as spatial constraints, so careful monitoring of the heating must be performed through EM simulations

and heating tests. Finally, the antenna effect is minimised by cable baluns and coil design to prevent unexpected standing waves in the cable shield.

3.5.2 General Tissue Heating

General tissue heating from the E-field of the coil can be measured through the specific absorption rate, SAR, which determines the amount of power deposited by the RF field over a certain mass of tissue, typically W/kg. SAR limits are determined by international safety bodies, and may differ depending on documentation. This work uses the standard SAR limits described in IEC 60601-2-33 [22]. The amount of heating, and thus SAR is highly dependent on the RF coil setup, and patient, as such it differs significantly between scans. Methods have been developed to estimate SAR on modern MR scanners, and in addition, RF coil SAR values are calculated for approval for patient scanning. The exact algorithm for SAR calculation during an MR scan is vendor specific, and will not be discussed here. Instead, first, the methods of EM simulation to determine SAR from an RF coil are presented, and subsequently, the measured temperature changes on the scanner are used to calculate the SAR scaling of the RF coil. Ultimately, the aim is to determine whether the two methods agree, and ensure that the maximum allowed voltage supplied to the Tx RF coil is within standard safety limits.

3.5.2.1 SAR from EM Simulations

The method of obtaining the SAR values follows from the EM simulation protocol discussed above in section 3.2.2. The SAR is calculated from the E-field within the tissue according to equation 3.15 below, where σ is the electrical conductivity, E is the RMS E-field, ρ is the sample density and V is the volume of sample. This equation ignores perfusion effects and best approximates inanimate matter.

$$\text{SAR} = \frac{1}{V}\int_{\text{Sample}} \frac{\sigma(\mathbf{r})|\mathbf{E}(\mathbf{r})|^{\mathbf{2}}}{\rho(\mathbf{r})} d\mathbf{r} \tag{3.15}$$

As an example, for surface coils placed on a human voxel model, the SAR is determined from time domain simulations performed with approximately $3\,000\,000$ hexahedral mesh cells. The $10\,\mathrm{g}$ averaged SAR values were calculated directly on CST according to the IEEE/IEC 62704-1 standard. SAR simulations are normalised by input power, as such the SAR values shown

below are for $1\,\mathrm{W}$ of input power. The results of the SAR simulation can be used to generate a map of SAR values on the human voxel model, the individual SAR values can then be sampled (e.g. at $1\,\mathrm{mm}$ isotropic resolution) to be plotted into a cumulative histogram, as shown in section 5.5.3. In this work, we are generally interested in three SAR metrics on the torso, all of which are calculated for a specific coil design and specific human voxel combination:

1. Max SAR ($10\,\mathrm{g}$ average), for surface cardiac coils is typically around $0.5\,\mathrm{W\,kg^{-1}}$ or lower
2. The 95th percentile SAR, for surface cardiac coils is typically around $0.1\,\mathrm{W\,kg^{-1}}$ or lower
3. Mean SAR averaged, for surface cardiac coils is typically around $0.02\,\mathrm{W\,kg^{-1}}$ or lower

3.5.2.2 Tissue Temperature Measurements

The simulated SAR overestimates the temperature change, as typically blood perfusion will reduce the heating effects which has been modelled using the Bioheat equation [23]. As such, verification of SAR heating values were obtained using on-scanner measurements, to compare against the simulated SAR values. High energy deposition on the sample was achieved using sequences with high duty cycles. The coil was positioned on $2\,\mathrm{kg}$ of pork mince ($8\,\%$ fat), inside a thin plastic refuse bag. An initial scan was performed to determine the location of the temperature hot spots, as identified using both temperature sensitive paper, and an IR (infrared) camera. Once the hot spots were verified to be consistent with the expected regions from EM simulations, two temperature probes were positioned at the hot spots. Both temperature probes are accurate to $0.1\,^{\circ}\mathrm{C}$, with a measurement rate of $1\,\mathrm{Hz}$. Typically, one probe was positioned on the surface of the pork, and the second probe was positioned $1\,\mathrm{cm}$ directly below the first probe to measure below surface energy deposition. Both ^{1}H and the X-nuclei heating scans were performed at $200\,\%$ SAR by running on the 1st level as described in the IEC documentation [22], as a safety margin.

Temperature recordings were carried out, however rapid temperature fluctuations resulting from the $0.1\,^{\circ}\mathrm{C}$ measurement accuracy of the measurement probe were seen. The fluctuations were smoothed out using a $60\,\mathrm{s}$ rolling mean. Due to heat dissipation in the pork, the measured temperature increases non-linearly over time. As such, a 'worst case' k-value was calculated by determining the maximum temperature gradients over a $5\,\mathrm{min}$ period sampled at $1\,\mathrm{s}$ intervals. Using both input power and temperature change, the average power from equation 3.17, and

power absorbed can be calculated from equation 3.18. This leads to the measured k-value from absorbed power divided by average power. The SAR and associated measured k-value was calculated from the measured data using the equations 3.16 to 3.19. The variables are listed below:

- P_{Peak} is the peak input power delivered during the RF pulse in W
- V_{Input} is the voltage of the RF pulse delivered to the coil in V
- R is the intrinsic real impedance of the system set to $50\,\Omega$
- P_{Average} is the average input power delivered over a TR in W
- P_{Absorbed} is the power absorbed by the tissue during heating in W
- C is the specific heat capacity taken as $2500\,\mathrm{J\,{}^{\circ}C^{-1}\,kg^{-1}}$ of pork mince [24]
- ΔT is the temperature change during RF heating in $^{\circ}\mathrm{C}$
- t is the duration of heating in s
- k_{Measured} is the measured SAR conversion factor for $1\,\mathrm{W}$ in $\mathrm{kg^{-1}}$

$$P_{\text{Peak}} = \frac{V_{\text{input}}^2}{R} \tag{3.16}$$

$$P_{\text{Average}} = P_{\text{Peak}} \times \frac{t}{TR} \tag{3.17}$$

$$P_{\text{Absorbed}} = \frac{C\Delta T}{t} \tag{3.18}$$

$$\mathrm{k}_{\text{Measured}} = \frac{P_{\text{Absorbed}}}{P_{\text{Average}}} \tag{3.19}$$

3.5.2.3 Safety Limits

Safety limits on the scanner depend on factors such as patient size, coil position and coil type. The limits on maximum power are referred as SAR limits, and make the distinction between global (or whole body) SAR applicable for a body volume coil, local (or partial body SAR) applicable for either small surface coils or a volume coil placed on the extremities, and head SAR. An additional factor that substantially affects the local SAR is the coil FOV, where the exposed patient mass to total patient mass ratio is considered, such that a larger coil will have more stringent SAR limits approaching that of the global SAR.

Historically all transmit coils using a port other than the body port used head coil safety limits.

Table 3.1: SAR values in $\mathrm{W\,kg^{-1}}$ of body sections imaged for normal and 1st level controlled operation modes. The SAR limit is further dependent on the part of body, with whole body having the lowest limit, followed by head, then partial body and local SAR limits. Imaging of local extremities allows for the highest SAR limit.

SAR Operating Mode /$\mathrm{W\,kg^{-1}}$	**Whole: Body**	**Partial: Body**	**Head**	**Local: Head**	**Local: Trunk**	**Local: Extremities**
Normal	2	2-10	3.2	10	10	20
1st Level	4	4-10	3.2	20	20	40

Such limits are safe, but may unnecessarily limit performance. Modern safety limits allow for tailored SAR limits dependent on the body part to be scanned, and the range of coil FOV is reflected by the partial body SAR, as shown in Table 3.1. The partial body SAR limit scale with the ratio of 'exposed patient mass'/'total patient mass', in normal operating mode, the partial body SAR is calculated according to equation 3.20.

$$\text{Partial Body SAR} = 10\,\mathrm{W\,kg^{-1}} - (8\,\mathrm{W\,kg^{-1}} \times \text{Exposed Mass/Total Mass}) \tag{3.20}$$

As such, a coil with large FOV over a significant region of the torso will have a more restrictive SAR limit than a more localised coil. Additionally, in the case of imaging of localised regions and extremities, a second limit should be taken to ensure the temperature rise is limited to $1\,^{\circ}\mathrm{C}$.

Practically, due to the smaller maximum power of most X-nuclei RF power amplifiers, in conjunction with the small diameter of surface loops covering a limited portion of the body, the $2\,\mathrm{W\,kg^{-1}}$ SAR limit is rarely exceeded when running the common suite of X-nuclei imaging protocols. As such, the primary aspect of concern with X-nuclei coils is the coupling to the body coil. Changes to the coil design were made in this work to alleviate this coupling, such as to increase the separation between the coil and patient using foam in order to minimise hot spots from the RF trap, and implementing RF traps to suppress specific resonant frequencies. With regards to coil and scanner interfacing, we used two parameters which ensure patient safety: firstly the maximum SAR scaling allowed by the scanner internal SAR measuring system, and the maximum voltage input from RF amplifiers.

3.6 Summary

This chapter follows the protocols used in RF coil development approximately chronologically. First, electromagnetic simulations are used to determine the validity of the design in terms of: practicality of construction, the simulated B_1^+, and SAR. Following this, the methods for coil construction and benchmark characterisation are presented, and the S parameters and Q-values are used to monitor the performance of the overall coil and individual components, such as RF traps. A fully-sampled B_1^+ and SNR mapping protocol is presented which was robust against low SNR and highly inhomogeneous B_1^+ fields, as is the case with X-nuclei surface coils, and the protocol to determine both transmit and receive performance from a single set of measurements. Lastly, the methods of characterising tissue heating through energy deposition from the RF coil and presented. Finally, the methods for obtaining measured and simulated SAR are discussed, used to determine the corresponding safety limits imposed on the coil.

References

[1] Davidson, D. B. *Computational Electromagnetics for RF and Microwave Engineering*. 2nd. Cambridge University Press, 2010. ISBN: 9780511778117. DOI: 10.1017/CBO9780511778117.

[2] *CST STUDIO SUITE*. Dassault Systèmes Simulia Corp. URL: https://www.3ds.com/products-services/simulia/products/cst-studio-suite/.

[3] Kunz, K. S. and Simpson, L. "A Technique for Increasing the Resolution of Finite-Difference Solutions of the Maxwell Equation". In: *IEEE Transactions on Electromagnetic Compatibility* EMC-23 (4 1981). ISSN: 1558187X. DOI: 10.1109/TEMC.1981.303984.

[4] Shewchuk, J. R. "Tetrahedral mesh generation by Delaunay refinement". In: 1998. DOI: 10.1145/276884.276894.

[5] Nikolovski, M. "Detailed Modeling of the Human Body in Motion to Investigate the Electromagnetic Influence of Fields in a Realistic Environment". In: 2018.

[6] Ackerman, M. J. "The visible human project". In: *Proceedings of the IEEE* 86 (3 1998). ISSN: 00189219. DOI: 10.1109/5.662875.

[7] Ocali, O. and Atalar, E. “Ultimate intrinsic signal-to-noise ratio in MRI”. In: *Magnetic Resonance in Medicine* 39 (3 Mar. 1998), pp. 462–473. ISSN: 07403194. DOI: 10.1002/mrm.1910390317.

[8] *MATLAB*. MathWorks. URL: https://uk.mathworks.com/products/matlab.html.

[9] *SOLIDWORKS*. Dassault Systèmes. URL: https://www.solidworks.com/.

[10] Data Sheet. PPI1111CPDATA11521RevA. URL: https://www.passiveplus.com/pdf/PPI-1111CP.DATASHEET.pdf.

[11] Fujita, H. et al. “RF Surface Receive Array Coils: The Art of an LC Circuit”. In: *Journal of Magnetic Resonance Imaging* 38 (1 July 2013), pp. 12–25. ISSN: 10531807. DOI: 10.1002/jmri.24159.

[12] Roberts, W. “A New Wide-Band Balun”. In: *Proceedings of the IRE* 45.12 (1957), pp. 1628–1631. DOI: 10.1109/JRPROC.1957.278293.

[13] Silvonen, K. “A general approach to network analyzer calibration”. In: *IEEE Transactions on Microwave Theory and Techniques* 40 (4 Apr. 1992), pp. 754–759. ISSN: 00189480. DOI: 10.1109/22.127526.

[14] Sohn, S.-M. et al. “(Pi)-matching technique for RF coil of MRI systems”. In: IEEE, June 2012, pp. 1–3. ISBN: 978-1-4673-1088-8. DOI: 10.1109/MWSYM.2012.6259772.

[15] Moré, J. J. *The Levenberg-Marquardt algorithm: Implementation and theory*. 1978. DOI: 10.1007/bfb0067700.

[16] Coleman, T. F. and Li, Y. “An interior trust region approach for nonlinear minimization subject to bounds”. In: *SIAM Journal on Optimization* 6 (2 1996). ISSN: 10526234. DOI: 10.1137/0806023.

[17] Gudbjartsson, H. and Patz, S. “The rician distribution of noisy mri data”. In: *Magnetic Resonance in Medicine* 34 (6 Dec. 1995), pp. 910–914. ISSN: 07403194. DOI: 10.1002/mrm.1910340618.

[18] *RCE-7: Protection of Patients and Volunteers Undergoing MRI Procedures*. Guidance. Health Protection Agency. 2008. ISBN: 978-0-85951-623-5. URL: https://www.gov.uk/government/publications/magnetic-resonance-imaging-mri-procedures-protection-of-patients-and-volunteers-from-exposure.

[19] *Safety Guidelines for Magnetic Resonance Imaging Equipment in Clinical Use*. Guidance. Medicines and Healthcare products Regulatory Agency. 2021. URL: https://www.gov.uk/government/publications/safety-guidelines-for-magnetic-resonance-imaging-equipment-in-clinical-use.

[20] Gabriel, C., Gabriel, S., and Corthout, E. "The dielectric properties of biological tissues: I. Literature survey". In: *Physics in Medicine and Biology* 41 (11 Nov. 1996), pp. 2231–2249. ISSN: 0031-9155. DOI: 10.1088/0031-9155/41/11/001.

[21] Dempsey, M. F., Condon, B., and Hadley, D. M. "Investigation of the factors responsible for burns during MRI". In: *Journal of Magnetic Resonance Imaging* 13 (4 Apr. 2001), pp. 627–631. ISSN: 1053-1807. DOI: 10.1002/jmri.1088.

[22] *IEC SAR Documentation*. Safety and Performance Requirements. International Electrotechnical Commission. 2010. URL: https://webstore.iec.ch/publication/2647.

[23] Weinbaum, S. and Jiji, L. M. "A new simplified bioheat equation for the effect of blood flow on local average tissue temperature". In: *Journal of Biomechanical Engineering* 107 (2 1985). ISSN: 15288951. DOI: 10.1115/1.3138533.

[24] Tavman, S., Kumcuoglu, S., and Gaukel, V. "Apparent Specific Heat Capacity of Chilled and Frozen Meat Products". In: *International Journal of Food Properties* 10 (1 Jan. 2007), pp. 103–112. ISSN: 1094-2912. DOI: 10.1080/10942910600755151.

4 | Pre-clinical Multi-layer Design

4.1 Introduction

4.1.1 Motivation for Novel Coil Design

Recent clinical ^{1}H RF coil developments have been typically focused on two aspects: firstly, towards increasing the flexibility and conformity of coil elements, such as GE Air^{TM} coils [1], stretchable liquid coils [2], and screen printed arrays [3, 4]. These designs allow improved patient comfort and reduced separation between coil and patient, however this is at the expense of lower Q-values and loss of coil sensitivity. Secondly, work has been focused on increasing the number and density of array coil elements [5], for example 64 elements for brain MRI [6] and 128 elements for cardiac MRI [7]. These designs retain the high sensitivity of small individual elements close to the coil, and allow for accelerated parallel imaging [8]. However, numerous small elements lack depth penetration into the sample, which in turn, limits the choice of anatomy that can be imaged. As such, dense arrays have been particularly prominent in neuroimaging where the distance between the centre of the brain and the coil is small. However, for the imaging of thoracic organs, larger coils with better depth penetration are required, typically at the cost of reduced sensitivity. In most cases, array elements are comprised of 2D planar circular closed conductor loops, and are constrained by the inherent trade-off between coil uniformity (and depth penetration) and coil sensitivity, as determined by the individual element diameters.

For MRI on all nuclei (both ^{1}H and non-proton), an improved coil sensitivity will directly lead to improved diagnostic capabilities, as previously discussed in Chapter 1, section 1.1.1. This need has partly driven some development towards more efficient coil designs, notably the petal resonator [9] and multi-turn elements [10]. These planar surface coil designs, however, are limited by high frequency current losses (as discussed later in section 4.2.2.1) with non-optimised EM field profiles. Advances in EM simulations have allowed for rapid prototyping and testing of more complex coil designs. This chapter explores the potential for improved RF coil sensitivity through the development of 'multi-layer' coils. The multi-layer design utilises multiple layers of stacked conductors which are offset and separated by insulator layers, to allow for in-

creased magnetic flux density and resonance efficiency. As part of this, we use EM simulations to determine and subsequently construct valid 'multi-layer' RF coil prototypes that improve on the field uniformity-sensitivity trade-off held by conventional square and circular loop designs. The proposed multi-layer design utilises a novel set of conductor geometries that vary in 3D space to minimise high frequency current losses, and provide increased transmit field efficiency and receive sensitivity, consequently improving the achievable SNR over conventional loop elements.

4.1.2 Chapter Overview

This chapter is comprised of four sections that chronologically follow the development of a single element multi-layer prototype. Initial prototyping was performed on a $7\,\mathrm{T}$ pre-clinical MRI scanner for ease of development. Section 4.2, describes the theory behind the multi-layer pre-clinical prototype. Section 4.3, describes the construction, simulation and on-scanner measurements of two ^{23}Na multi-layer prototypes. Following the successful development of the ^{23}Na coils, section 4.4, describes a ^{13}C multi-layer coil which was developed and tested for further improved receive sensitivity. Finally, section 4.5, provides a discussion of the work in this chapter, which is limited to simple pre-clinical prototypes. The following chapter, Chapter 5, presents the work undertaken in translating the multi-layer design into a clinical RF coil for human research studies.

4.2 Main Multi-layer Features

Throughout this project, a range of multi-layer coil designs using different conductor layering structures were constructed and tested. For clarity and conciseness, two final designs are discussed in this thesis: a simpler design using straight conductors for the pre-clinical coils discussed in this chapter, and a more complex design using curved conductors for the clinical coils discussed in the following chapter, Chapter 5. Design aspects that improve coil performance can be grouped into two key areas which are presented below: firstly, stacking conductor layers such that the field is superimposed over a central region (presented in section 4.2.1), and secondly, offsetting neighbouring layers so as to minimise conductor overlap (presented in section 4.2.2). Finally, the pre-clinical conductor design of a star shape was determined to satisfy the

design aspects, and the layering structure for such a coil is presented in section 4.2.3. The detailed protocol for construction of the coils can be found in Appendix E, with instructions on the design, rotation angle and offset of each conductor layer. Additionally, an overarching summary of the multi-layer RF coil design, can be found in the in the claims of the multi-layer patent [11].

4.2.1 Stacked Conductor Layers

In this chapter, the multi-layer design comprises of four to six stacked 'conductor layers' sandwiched by electrically insulating 'dielectric layers'. The most basic form of a stacked conductor design would be a solenoid, comprising of multiple stacked loops formed from a continuous spiral. The benefits of a solenoid, such as the increased magnetic flux density (section 4.2.1.1) and increased Q-values (section 4.2.1.2) are only valid in the case of DC or low frequency currents respectively. The limitation of a solenoid design at RF frequencies is shown in section 4.2.1.3, through the construction and simulation of a ^{1}H solenoid RF coil.

4.2.1.1 Increased Magnetic Flux Density

Following from the discussion in section 2.1.1, moving charges along a straight path create circular magnetic fields in the plane perpendicular to the path. In the case of a surface RF coil positioned on a body, oriented such that the coil central axis is aligned with the y-axis (with the B_0 aligned along the z-axis), the electrons oscillate along a closed loop in the x-z plane. For the multi-layer design, if designed to minimise loss, the magnetic flux density of multiple stacked layers should be increased proportionally by the number of layers. This increase is best illustrated by quantifying the B-field magnitude improvements when applying a steady current using the Biot-Savart equation (2.7), which serves as an approximation for radio-frequencies.

In the case of a steady current, I, through a long solenoid, the B_1^+ within the enclosed volume of the solenoid can be considered to be proportional to the number of turns N, and the material dependent permeability, μ, in equation 4.1 below.

$$B_1^+ = \mu N I \tag{4.1}$$

In the early days of MRI, solenoid RF coils utilising the increased magnetic flux density of

multiple turns in the central volume by fully enclosing the ROI, much in the same way as a modern birdcage design, were constructed [12]. However, with modern MRI scanners, the static magnetic field B_0 is in the z-axis, requiring the B_1^+ to be circularly polarized in the x-y plane. As such, the central axis of a solenoid can only be placed perpendicularly to the z-direction, and is subsequently spatially constrained to be no more than several centimetres vertically. With a short solenoid geometrically confined as a surface coil on the body (i.e. flattened into a plane), the above approximation is an overestimation of the B-field, as the B-field would decrease with distance away from the centre of the solenoid. We can approximate this on-axis field, for n turn per unit length of a circular solenoid, of length $-\zeta$ to ζ along the z-axis, with radius a, current density I, at a distance z from the solenoid centre, according to equation 4.2 [13].

$$B_z = \frac{\mu n I}{2}\left[\frac{\zeta}{\sqrt{\zeta^2 + a^2}}\right]_{-\zeta}^{\zeta} \tag{4.2}$$

Naively at this point of the discussion, ignoring high frequency effects, we would expect the on-axis B-field away from the centre of the solenoid to scale proportionally to the number of turns. This would in theory translate to an n-fold increase in transmit B_1^+ efficiency of a surface solenoid over conventional single loops.

4.2.1.2 Increased Q-value

From section 2.1.4.4 equation 2.38, SNR is proportional to B_1^-, and $\sqrt{Q}$, where B_1^- is the LCP component of the B_1 and approximate in magnitude to the B_1^+, and Q-loaded represents the resonance efficiency of the coil, described in methods section 3.3.1.4. With the multi-layer design, we expect improvements in B_1^- efficiency arising from the increased central flux density. Taking the assumption that the loaded RF coil is an RLC circuit, with R_{Total} as the sum of resistive losses (from the coil and coupling to sample), and L_{Total} representing the total inductance, the Q_{Loaded} (coil loaded by a sample so as to mimic a real scan) is determined at the resonance frequency ω by equation 4.3:

$$Q_{\text{Loaded}} = \frac{\omega L_{\text{Total}}}{R_{\text{Total}}} \tag{4.3}$$

Therefore, to maximise Q_{Loaded}, L_{Total} should be maximised, and simultaneously R_{Total} should

be minimised.

Again, looking at the case of a solenoid with a steady state current of I and loop area A, the inductance is proportional to the number of turns, N, squared, equation 4.4.

$$L_{\text{Solenoid}} = \mu_0 \frac{N^2 A}{l} \tag{4.4}$$

Assuming the RMS currents are the same between the solenoid and a single loop: $I_{\text{Solenoid}} = I_{\text{Loop}}$ then we expect $L_{\text{Solenoid}} = N^2 \times L_{\text{Loop}}$ (valid in the case that a consistent power, P is supplied, and both coils are matched to impedance Z).

Without taking into account high frequency losses, we expect R to scale with the conductor track length, and as such scale linearly with N. Overall, Q_{Solenoid} scales linearly with N (with an $\approx N^2$ contribution from L_{Total} divided by an $\approx N$ contribution from R_{Total}), which leads to a $\sqrt{N}$ scaling in SNR from the $\sqrt{Q}$ term in equation 2.38. This combined with improvements in the solenoid B_1^- should theoretically significantly increase SNR.

4.2.1.3 Proton Solenoid Prototype

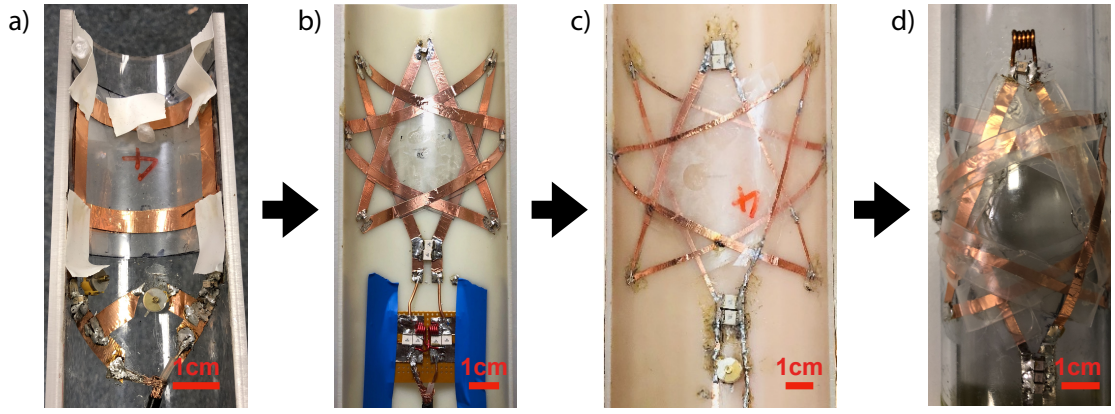

Figure 4.1: Evolution of multi-layer prototype coil designs. Left to Right: Photos of (a) ^{1}H 'Solenoid' Coil, (b) and (c) ^{23}Na Multi-Layer coil with ^{23}Na Balun, and (d) ^{13}C Multi-Layer coil with ^{1}H Trap.

In an attempt to utilise the theoretical increases in magnetic flux density and coil Q-value from stacked conductor layers, an initial square solenoid prototype was constructed for ^{1}H at $\omega = 300.3\,\mathrm{MHz}$ for a $7\,\mathrm{T}$ Varian pre-clinical scanner. The rudimentary Tx-Rx coil comprised of four square conductor layers, sandwiched by acetate dielectric layers. The proof of concept coil was constructed quickly and not optimally designed, and as such only featured a single tuning capacitor, a single matching capacitor and no additional decoupling or detuning circuitry. A photo of this solenoid coil can be found in Figure 4.1a), documenting the progression of the multi-layer prototypes. Coil construction of a solenoid was particularly challenging; following the protocol set out in section 3.3.3.2, given that the high total inductance of the solenoid design, equation 3.10, dictates that a small total capacitance (of approximately $1 - 2\,\mathrm{pF}$ total) must be used. Scanner B_1^+ maps of the ^{1}H solenoid coil were obtained using the Double Angle Method (described in Appendix D, section D.1.1). However, no appreciable gain in B_1^+ strength was observed compared to a single square loop of the same dimensions. Additionally, EM simulations were performed showing that the top and bottom surfaces of the solenoid coil exhibited the expected current density, but zero current density on the surfaces in between the conductor layers. This outcome is due to high resistance and EM shielding experienced by these layers. As an example, Figure 4.2 a and b shows no field improvements when using a four layer stacked solenoid compared to a single loop of the same diameter (with circular elements to allow distributed capacitors).

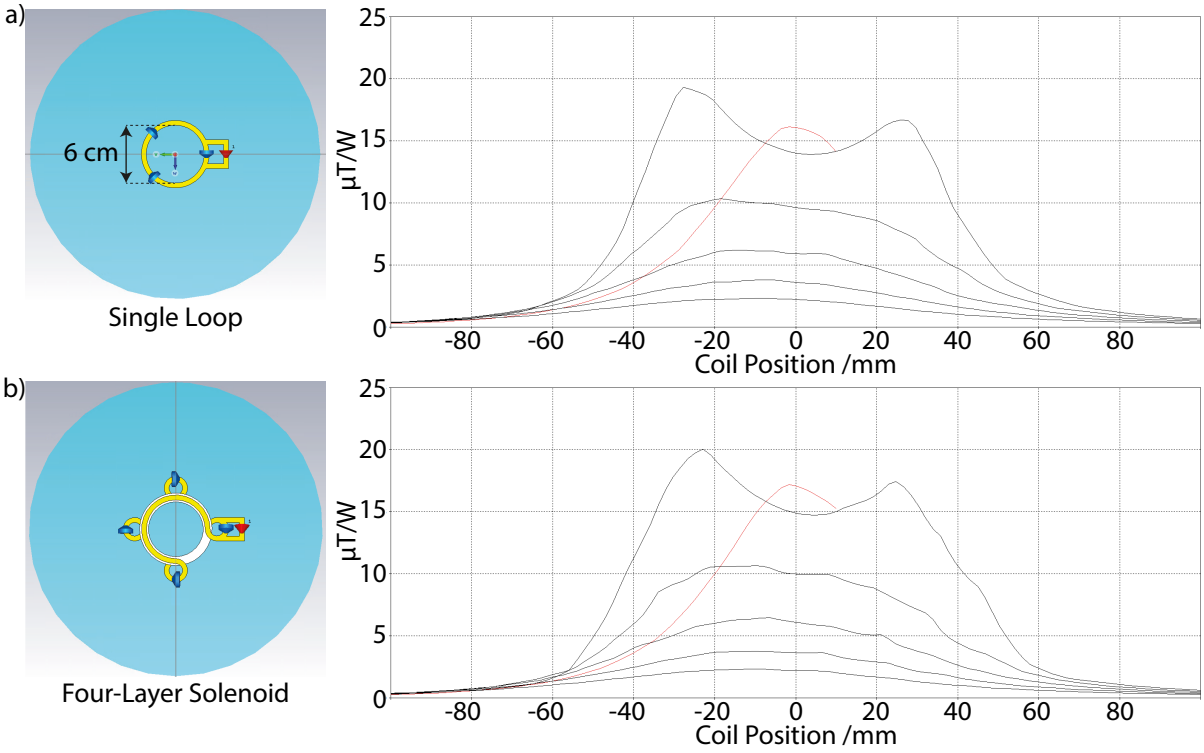

Figure 4.2: EM models and 1D plots for four stacked conductor pre-clinical coil examples, with a central overlapping region of 6 cm diameter. Red line represents the on-axis plot of B_1^+ for 1 W power through the coil centre (along the coil y-axis). Black lines represent the horizontal plot of B_1^+ for 1 W power horizontally at 2 cm depths (along the coil x-axis) for: (a) single loop coil, (b) four layer solenoid coil with periphery loops for distributed tuning conductors.

4.2.2 Offset Layers

At high frequencies of current oscillation, the entire conductor structure resonates, which consequently leads to two downsides: resistive losses from skin and proximity effects, section 4.2.2.1, and shielding of the EM field from neighbouring conductors, section 4.2.2.2. These high frequency effects are unwanted, as their combined effects increase the coil resistance, reduce the Q-loaded value and overall reduce the transmit and receive performance of a stacked solenoid coil design.

4.2.2.1 Skin and Proximity Effects

The deviation of current flow from a steady state to that of high frequency oscillations in the RF range has profound effects on the B-field of the coil, leading to a phenomenon known as the 'skin effect' [14]. The skin effect describes the tendency for alternating current at high frequencies to be distributed along the surface of the conductor, such that the current density is

the highest at the conductor surface, and exponentially decreases towards the conductor centre, as shown in Figure 4.3 a. This effect arises from eddy currents created in the conductor by the changing magnetic field which constrain the electrons to travel on the surface 'skin', the depth of which is described by equation 4.5 below. Here, ρ is the resistivity of the conductor, ω is the frequency of current oscillations, μ is the permeability of the conductor, and ϵ is the permittivity of the conductor. In the case that $\omega \ll 1/\rho\epsilon$, simplifications can be made to calculate the skin depth according to equation 4.6:

$$\delta = \sqrt{\frac{2\rho}{\omega\mu}}\sqrt{\sqrt{1+(\rho\omega\epsilon)^2}+\rho\omega\epsilon} \tag{4.5}$$

$$\approx \sqrt{\frac{2\rho}{\omega\mu}} \tag{4.6}$$

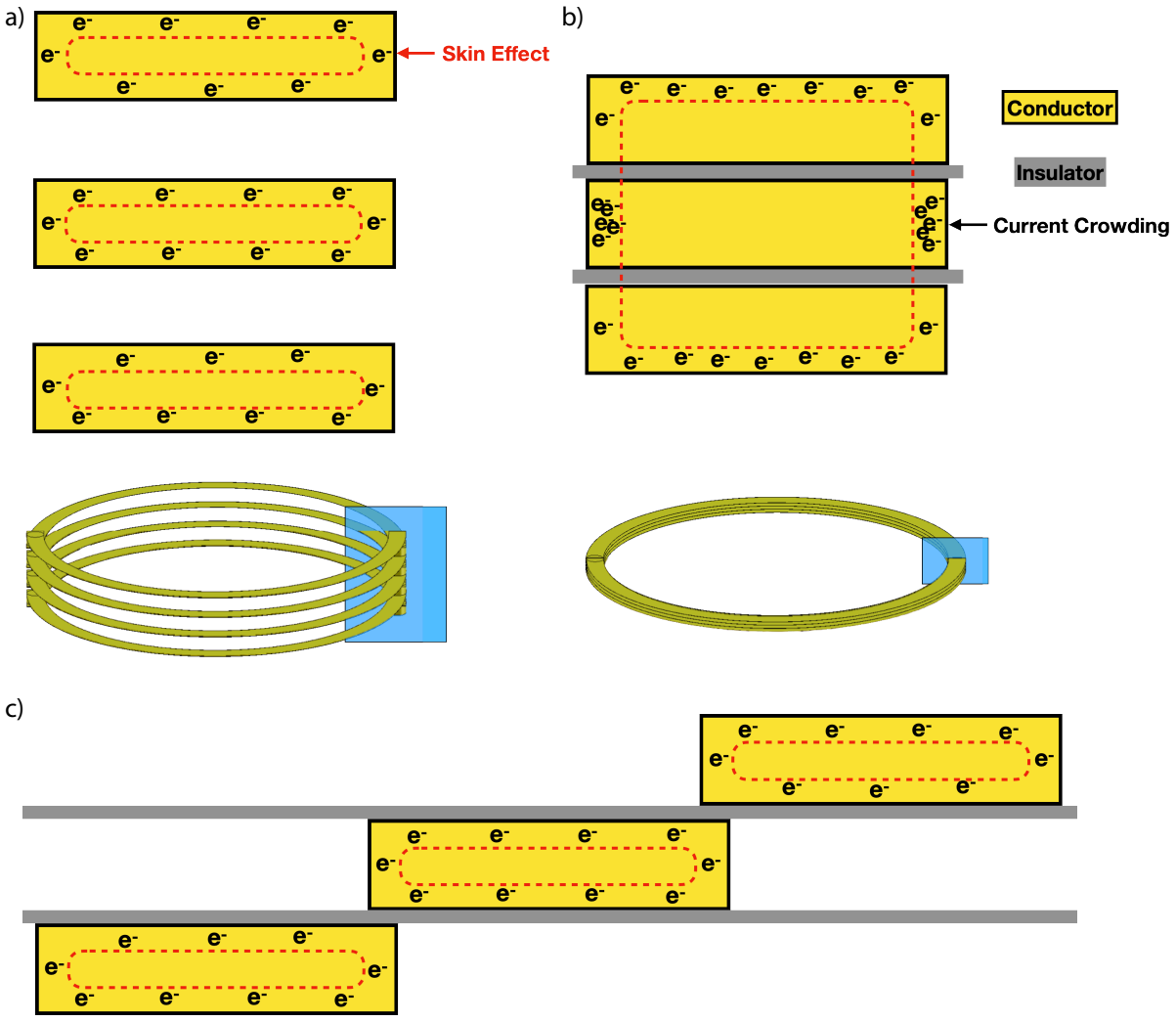

Figure 4.3: Diagram (not to scale) illustrating conductor layering structure and possible electron distribution. (a) A layered solenoid with conductors vertically separated (as is the case with a volume solenoid coil) showing electrons in skin effect. (b) A stacked solenoid with alternating dielectric and conductor layers (as is the case with a surface solenoid coil), showing electron current crowding. (c) A multi-layer offset conductor design which reduces current crowding and EM shielding.

Conventional copper used for the conductor of RF coils has a resistivity of $1.72 \times 10^{-8}\,\Omega\,\mathrm{m}$ [$100\,\%$ International Annealed Copper Standard], and a permeability of approximately $1\mu_0$ (where μ_0 is the permeability of free space $= 4\pi \times 10 \times 10^{-7}\,\mathrm{H\,m^{-1}}$), so the skin depth can be calculated from Equation 4.6, to be $11.90\,\mu\mathrm{m}$ at $30\,\mathrm{MHz}$ (^{13}C Larmor frequency at $3\,\mathrm{T}$), and $5.952\,\mu\mathrm{m}$ at $120\,\mathrm{MHz}$ (^{1}H Larmor frequency at $3\,\mathrm{T}$). In the case of a typical PCB (printed circuit board) using '$2\,\mathrm{oz}$' copper (historically referring to a conductor track thickness of $70\,\mu\mathrm{m}$), the flowing current is confined to around $10\,\%$ of the conductor volume. However, despite the skin effect leading to additional AC resistances for all coils, the skin effect alone is not responsible

for the under-performance of the initial solenoid design described in the previous section, and additional effects are to blame.

In the case of two neighbouring conductors with parallel current flows, the distribution of current within the first conductor will be constrained to a smaller region that is farthest away from the second conductors, and vice versa. This inhomogeneous distribution of current density across the surface of the conductor is an effect known as 'current crowding'. Current crowding leads to unwanted localised heating and thermal hotspots, as well as the 'proximity' effect [15]. The increased resistance arises from the alternating magnetic field inducing eddy currents in the neighbouring conductors, where the neighbouring electrons are repelled into a more confined area. Importantly, the proximity effect increases with frequency, and the effective resistance of the conductor is subsequently increased due to this confinement. The RF coil community is aware of the proximity effect, and the magnitude has been quantified previously in small spiral NMR coils, [16], however this resistive effect is not typically encountered in the larger MRI coils of single loops. In the case of stacked conductor layers, the conductor layers are at very close proximity (only separated by a thin dielectric, e.g 50 μm separation), with current flow being parallel between the two layers; this leads to strong proximity effects. We believe that with a simple solenoid design, high resistances are experienced by currents flowing on the conductor surfaces which are adjacent to another conductor surface (i.e. all faces except the top- and bottom-most), as illustrated in Figure 4.3 b. This diminishes the benefits of a stacked solenoid with multiple layers, and is the primary reason for the absence of any B_1^+ field improvements in the initial prototype design.

4.2.2.2 Unwanted EM Shielding

A further aspect to consider is the shielding of the B-field by the upper and lower conductor layers, blocking the RF field produced by the central conductor layers from reaching the sample. EM waves mostly reflect off conductors, so EM waves generated from inner layers of a stack get reflected backwards towards the middle of the stack instead of propagating outwards from the stack (towards the sample). In the case of an oscillating current, time-varying EM fields generate eddy currents which act to cancel that EM field. In the case of RF coils, the time-varying EM field is reflected from the surface of the conductor such that the B_1 field cannot penetrate a conductor, and gets shielded. The majority of RF shielding in MRI is beneficial,

two examples of its applications are: shielding of the ^{1}H body coil from the gradient coils, and secondly, shielding of the scan room to minimise signal contamination from external RF signals from being erroneously detected. However, RF shielding is unwanted for a stacked conductor coil design, as in regions where the conductors directly overlap (which is $100\,\%$ of the conductor area for a solenoid). The conductor closer to the sample shields the varying magnetic field generated from the layers further away. For the multi-layer design, only the outermost layers can emit EM waves without reflection loss.

In this work, we show the loss of B_1 field from EM shielding and proximity effects can be minimised by offsetting each conductor layer in-plane to reduce the overlap and proximity of neighbouring conductor tracks. Single conductor layers can be specifically designed for a complete current path when tessellated, so as to minimise conductor overlap whilst preserving a central overlapping region and high inductance allowing for increased magnetic flux density and coil sensitivity. This is the core concept of the multi-layer coil design. The process to construct such a coil is described in Appendix E. In this design, the in plane offset distance between the neighbouring layers as well as the conductor shape within each layer determines the balance between the field loss from the proximity and shielding effects against the field gain from high magnetic flux in the central region and high Q-values due to the multiple layers. This work primarily investigated two multi-layer designs: firstly, a star-shaped coil comprised of straight conductors where each layer formed an approximate Λ shape for the pre-clinical prototypes, as discussed below in section 4.2.3, and secondly, a curved coil comprised of curved conductors where each layer formed an approximate Ω shape for clinical prototypes. Examples of the offset layering structure are shown in Figure 4.4 for both straight and curved conductors.

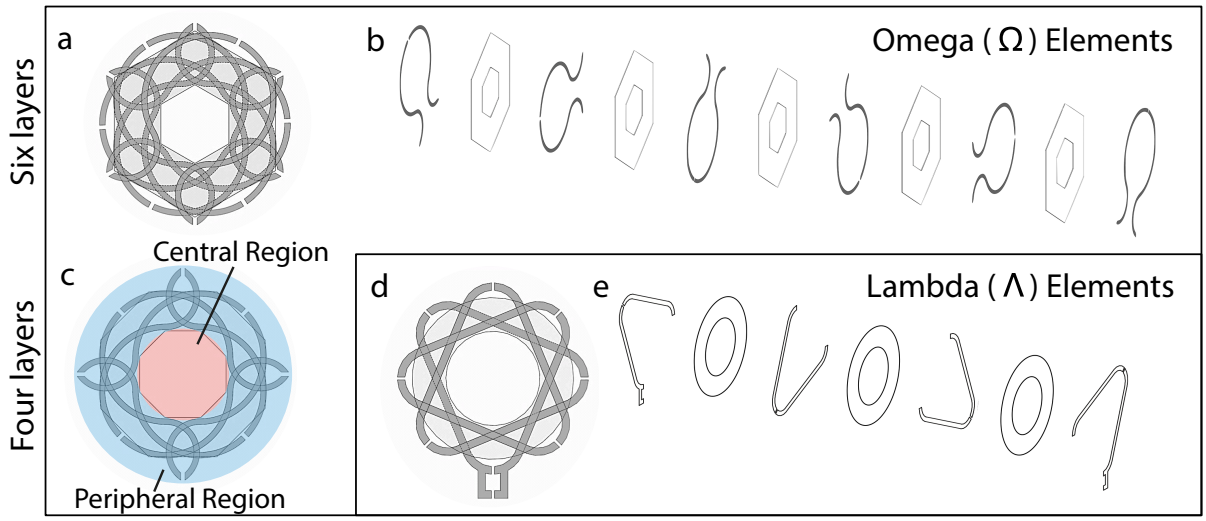

Figure 4.4: Differences in layering structure for straight and curved conductor with four and six layers. (a) six-layer curved conductor top view, (b) six-layer curved conductor exploded view, (c) four-layer curved conductor top down view, (d) four-layer straight conductor top down view, (e) four-layer straight conductor exploded view.

Taking a single multi-layer coil element, we can divide the coil into two regions: a central overlapping region, which is placed over the ROI for increased sensitivity and flux density, and a peripheral region at the edge of the coil formed from the vertices of the star shape, as shown above in Figure 4.4. At this stage of development, the aim was to maximise the central overlapping region, whilst simultaneously minimising the peripheral region.

4.2.3 Star-Shaped Conductor Design

At this early stage of the multi-layer concept, we sought the simplest design that may be constructed, primarily as a proof of concept. The constraints of rotational symmetry and straight tracks formed from a single conducting path, are satisfied by the group of regular star polygons. This group can be represented by 'Schlafli symbol' notation, $\{n/m\}$, where n represents the number of vertices of the polygon and m represents the density or 'starrines' with every m^{th} vertex connected, such that if $m = 2$ then every second point is joined. The diagrams for each of the shapes discussed below are presented in Figure 4.5.

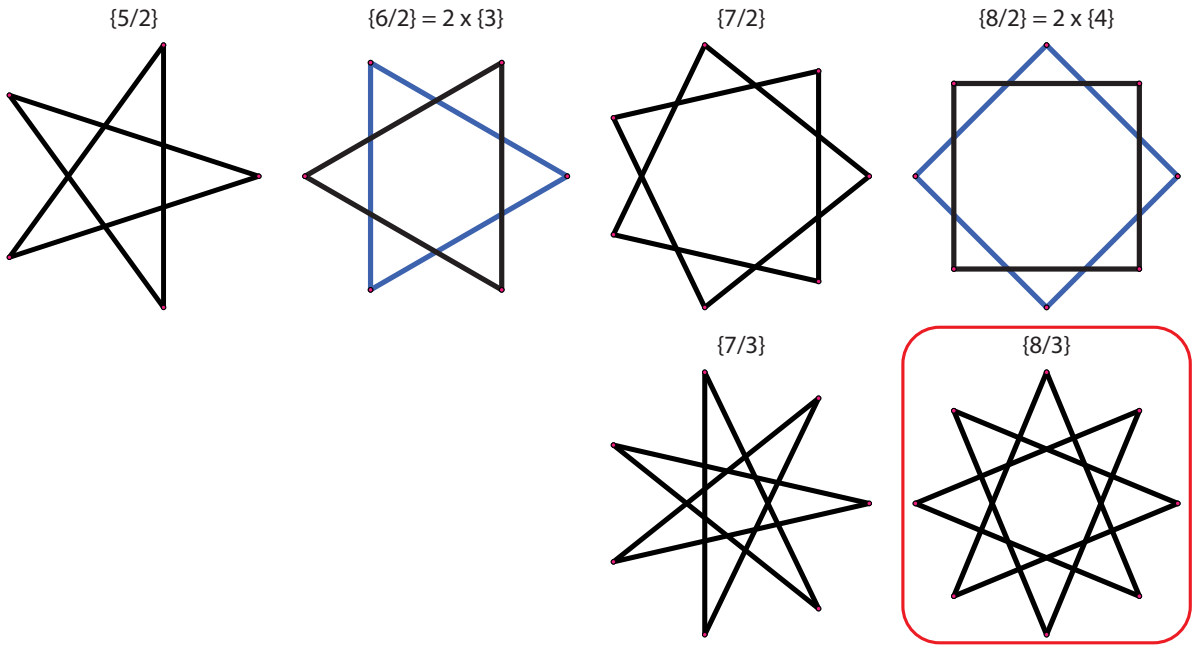

Figure 4.5: Diagrams showing layout of straight conductors forming regular star polygons shapes from five to eight vertices. Single continuous conductor tracks shown in black, and degenerate shapes comprised of two conductors shown in blue and black. The first viable option for the multi-layer coil design with the minimum number of vertices is eight, with the $\{8/3\}$ design identified by the red square.

- The minimum number of vertices required to form an overlapping structure with straight sides is five, as both three and four vertices form a triangle and square respectively, and cannot overlap into a continuous structure.
- With fives vertices, a pentagram of $\{5/2\}$ represents the simplest coil design with two fully enclosed conductor layers. However, the central overlapping region of this shape is small in area (less than $50\,\%$ of the total coil area), and the increase in magnetic flux density and Q-value is minimal from only two fully enclosed layers. When taking into account losses from the proximity effects, EM shielding, and wasted B-field in the peripheral region, this does not offer significant improvements over conventional coils.
- With six vertices, a regular star representing a hexagram of $\{6/2\}$ can be formed, which is degenerate such that it cannot be formed from a single continuous conductor path. The hexagram comprises of two equilateral triangles such that $\{6/2\} = 2 \times \{3\}$.
- With seven vertices, two possible hexagrams can be formed, $\{7/2\}$ and $\{7/3\}$:
  - With the $\{7/2\}$ geometry, the central overlapping region is larger (significantly more than $50\,\%$ of the total coil area). However, only two fully enclosed conductor layers are formed, giving an insufficient increase to flux density and Q-value.

  - With the $\{7/3\}$ geometry, three fully enclosed conductor layers are formed with higher magnetic flux density, however the central overlapping region is significantly smaller than $50\,\%$ of the total coil area. Therefore, much of the EM field generated by coil is positioned over the peripheral region and the field generated is inefficient at reaching the ROI.
- With eight vertices, two possible octagrams can be formed: $\{8/2\}$ and $\{8/3\}$:
  - The $\{8/2\}$ geometry is degenerate and cannot be formed from a single continuous path. The octagram comprises of two squares such that $\{8/2\} = 2 \times \{4\}$.
  - The $\{8/3\}$ geometry allows for three fully enclosed conductor layers in the central region, and for that region to be reasonably large compared to the total surface area (approx $50\,\%$). This design was chosen for the pre-clinical prototype coil as this presented a balance of maximising central overlapping region and increased magnetic flux density.

A series of eight-sided star shaped pre-clinical coil prototypes were constructed for testing, primarily two nuclei were investigated: ^{23}Na and ^{13}C. This chosen layering structure was selected from the possible shapes in Figure 4.5, and illustrated in Figure 4.4 d showing the top down view and 4.4 e showing the exploded view.

4.3 Sodium Multi-layer Coil Development

The aim at this stage of the multi-layer prototype testing was to construct a home-built multi-layer coil that could be compared against conventional loop coils through phantom imaging scans. The construction and initial benchtop testing is presented in section 4.3.1. Two ^{23}Na pre-clinical multi-layer prototypes were constructed for a $7\,\mathrm{T}$ Varian pre-clinical scanner, equating to a resonance frequency of $79.8\,\mathrm{MHz}$. Further improvements on both coil construction and scanner measurements were made to the pre-clinical multi-layer design. Section 4.3.2 presents the second prototype and associated improvements.

4.3.1 Sodium Multi-layer Prototype 1

The number and complexity of lumped element components was limited, such that the coil was constructed with the minimum number of lumped elements to reduce any additional parameters.

The coil featured only one tuning capacitor, one matching capacitor, one balun (for common mode current suppression on the cable, described in section 3.3.2.2), and no ^{1}H traps as the coil was used without a volume coil. This allowed the subsequent coil characterisation to focus on the coil conductor design. The 8-sided star Tx-Rx multi-layer coil was constructed for ^{23}Na, chosen due to readily available sodium chloride that possess relatively high SNR and adjustable coil loading through concentration, as well as a resonance frequency that is close in proximity to other X-nuclei (^{13}C, ^{31}P, ^{129}Xe etc.).

This first prototype iteration was constructed simply with $2\,\mathrm{oz}$ copper tape of $10\,\mathrm{mm}$ width and $70\,\mu\mathrm{m}$ thickness adhered directly onto the inner surface of a nylon tube cut in half along the diameter forming a half-pipe shape. A photograph of this first sodium coil with $10\,\mathrm{mm}$ width conductor track can be found in Figure 4.1 b. An electrically insulating layer of acetate was placed between regions where the conductor overlapped. All subsequent layers of conductors were applied on top of the dielectric layer and half pipe. As alluded to above, the coil was designed to be used in the absence of a ^{1}H volume coil.

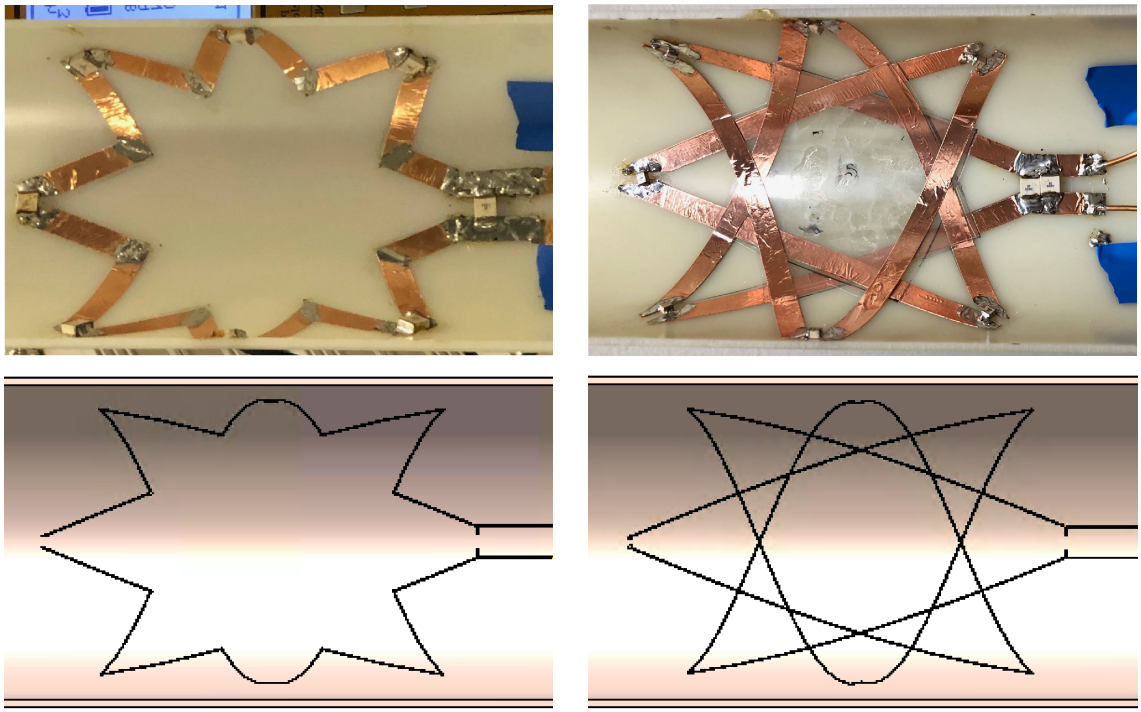

Figure 4.6: Photographs (top row) and simulated models (bottom row) of example single loop coil and star shaped multi-layer coil. These coils are part of the first sodium pre-clinical prototype.

As the field profile is highly dependent on the coil diameter, two custom single layer coils with the representative dimensions were constructed to ensure fair comparison across coil designs. In total, three pre-clinical coils were constructed: the star-shaped multi-layer design as described in section 4.2.3, a large single loop congruent to the outer track of the multi-layer coil (with the aim of achieving a similar coil FOV to the multi-layer), and a small single loop congruent to the central overlapping region of the multi-layer coil (with the aim of achieving a similar field profile). The flexible structure was placed on a $80\,\mathrm{mm}$ half pipe pull-wound nylon tube. The photos and models of the multi-layer and large single loop coil are shown above in Figure 4.6.

4.3.1.1 Benchtop Results

The multi-layer coil and single loop coils were constructed and subsequently tuned and matched for ^{23}Na at $7\,\mathrm{T}$, according to the protocol described in Appendix E. S-parameter and Q-values were characterised using a vector network analyser and pick-up probes, as described in the Methods chapter, section 3.3. S-parameters were measured for all three coils, and ensured to be $-20\,\mathrm{dB}$ or lower, which equates to less than $1\,\%$ reflected power. Due to the multiple resonances of the multi-layer design, a pickup probe was used to identify the correct resonance that represented the EM field from the collective coil central region. Following this, the Q-values and ratio of contributions of resistance were measured, with a probe positioned near (but not close enough to influence the inductance of) the RF coil, through both EM simulations and bench-top measurements of the same setup. The coil was shielded from the rest of the scanner, such that the coil was only coupled to the sample not the scanner integral structure [17]. A layer of copper was wrapped around the outer surface of the half-pipe structure for consistent shielding. An EM shield comprised of a copper sheet that covered the bottom face of the half pipe was included to minimise inductive coupling to the scanner bore and other objects in the absence of a volume coil, and obtain higher Q-values as shown in Table 4.1. Q-values were calculated for the loaded case, unloaded case, and unloaded without EM shield for the three coils using benchtop measurements, as shown in Table 4.1.

Whilst benchtop measurements were used here to record Q-values during the coil construction process, benchtop measurements cannot obtain an indication of B_1^+, SNR, or relative contributions of coil and sample resistances. As such, circuit simulators were used to investigate obtain-

Table 4.1: Benchtop measured Q-values for the three ^{23}Na coils in the loaded and unloaded case. Q-values were calculated as the resonance frequency, ω, divided by the fractional bandwidth, $\Delta\omega$. Additionally, the effects of the copper shield placed on the outer surface of the coil on the Q-value were characterised.

Coil Configuration	Parameters	Small Single Loop	Large Single Loop	Multi-layer
Unloaded, No Shield	ω /MHz	77.62	77.62	77.94
	$\Delta\omega$ /MHz	3.184	3.395	5.240
	Q_{Unloaded}	24.38	22.86	14.87
Unloaded, With Shield	ω /MHz	79.19	79.95	80.57
	$\Delta\omega$ /MHz	2.952	2.931	3.963
	Q_{Unloaded}	26.83	27.28	20.33
Loaded, With Shield	ω /MHz	79.15	79.39	80.08
	$\Delta\omega$ /MHz	3.394	3.753	5.082
	Q_{Loaded}	23.32	21.23	15.76
$Q_{\text{Unloaded}}/Q_{\text{Loaded}}$		1.15	1.28	1.29

ing the relative contributions of coil and sample resistances, performed in LT-SPICE (Linear Technology, California, US) and presented in Appendix F. However, we were not confident with the circuit simulator results obtained as this does not take into account coil interactions, and more inclined to trust the full wave simulation results in the following sections.

4.3.1.2 EM Simulation Setup

EM simulations were used to determine the feasibility of the pre-clinical eight-sided star prototype and to give an indication of field improvements over conventional loops. The coil EM models were created on CST Microwave Studio. At this stage of development, the conductor was modelled as a thin wire, as the wire could be easily curved along the surface of the cylinder, although this inaccurately represented the actual conductor width of $10\,\mathrm{mm}$. For ^{23}Na at $7\,\mathrm{T}$, EM simulations were performed over the frequency range of $70\,\mathrm{MHz}$ to $90\,\mathrm{MHz}$, with both E and H monitors at $79.8\,\mathrm{MHz}$, following the protocol described in section 3.2.2. The standard 'normal boundary conditions' were used which add free space around the model edge that attenuate the EM field. Regarding the choice of simulation type, the curved geometry was better captured using tetrahedral meshing using frequency domain, FEM simulations. Hexahedral meshing would require exceptionally high mesh density, which leads to long computational times, and poor accuracy of curves. Standard materials belonging to the CST 'materials library' were assigned to components of the coil: 'annealed copper' was used as the coil conductor,

'polyimide' was used for the coil dielectric (to represent acrylic and polytetrafluoroethylene, PTFE later on), and a PEC (with zero resistivity) was used to model pick-up probes and the EM shield. Discrete ports were used to model capacitor positions to utilise the co-simulation function for coil tuning and matching post simulation. Transmit performance was characterised by the time averaged magnitude of B_1^+ in a predefined ROI for an input of $1\,\mathrm{V}$ into the coil. A circular ROI with a $10\,\mathrm{mm}$ radius, positioned $30\,\mathrm{mm}$ above the coil centre was used to quantify the field profile, consistent with the ROI defined previously for EM simulations.

4.3.1.3 Scanner Measurement Setup

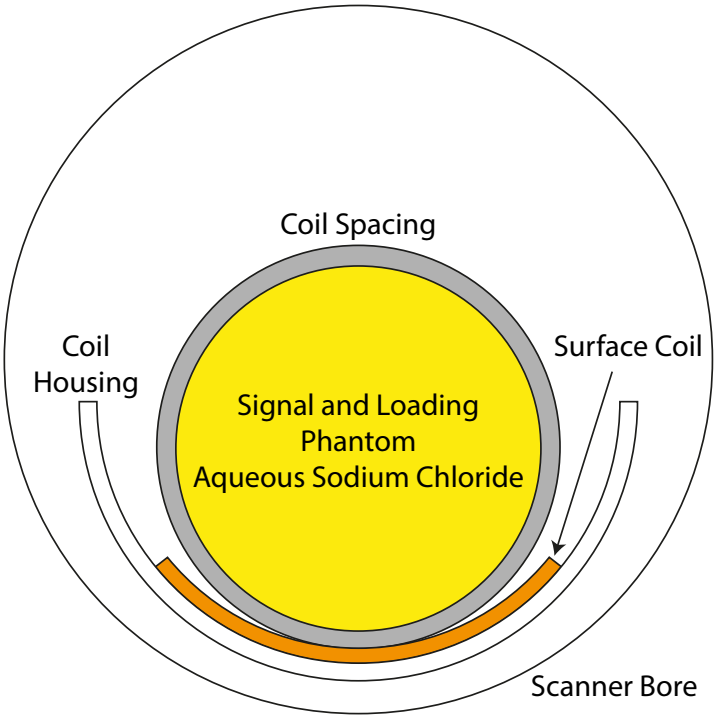

Figure 4.7: Preclinical MRI single element coil setup with signal and loading phantom (of aqueous sodium chloride).

The multi-layer design B_1^+ and SNR field maps were obtained on the scanner and compared with the two custom built single layer loop coils. All three RF coils were run in transmit-receive mode; 2D gradient echo axial images (GRE, $160\,\mathrm{ms}$ TR, $1.9\,\mathrm{ms}$ TE, $0.78 \times 0.78 \times 100\,\mathrm{mm}^3$ voxel size, $1\,\mathrm{ms}$ Gaussian pulse, 1024 averages) of an aqueous NaCl phantom were performed at increasing transmit power supplied by the RF amplifier, from $0\,\mathrm{W}$ to $9\,\mathrm{W}$ in steps of $10\,\mathrm{W}$. At this stage, the large slice thickness of $100\,\mathrm{mm}$ was initially chosen to maximise signal. 2D flip-angle projection maps were scaled for $1\,\mathrm{V}$ through the coil, allowing the 2D B_1^+ field

profile to be calculated from equation 3.13. ^{1}H scans were not needed due to reasonably fast ^{23}Na images for coil localisation, allowing the complexity of the coil to be kept at a minimum, omitting circuit elements such as ^{1}H traps, ^{1}H baluns and other decoupling circuitry. The experimental setup is shown in Figure 4.7. 2D cross-sectional (axial) maps of B_1^+ for transmit and SNR for receive performance were obtained using the protocol described in the Methods chapter, section 3.4.

4.3.1.4 2D Field Map Results

The B_1^+ 2D maps obtained from these scanner measurements are shown in Figure 4.8 and indicate significant transmit improvements of around $50\,\%$, however the field profiles do not follow the expected on-axis drop off away from the coil centre, and a large disparity was found between EM simulated and measured results.

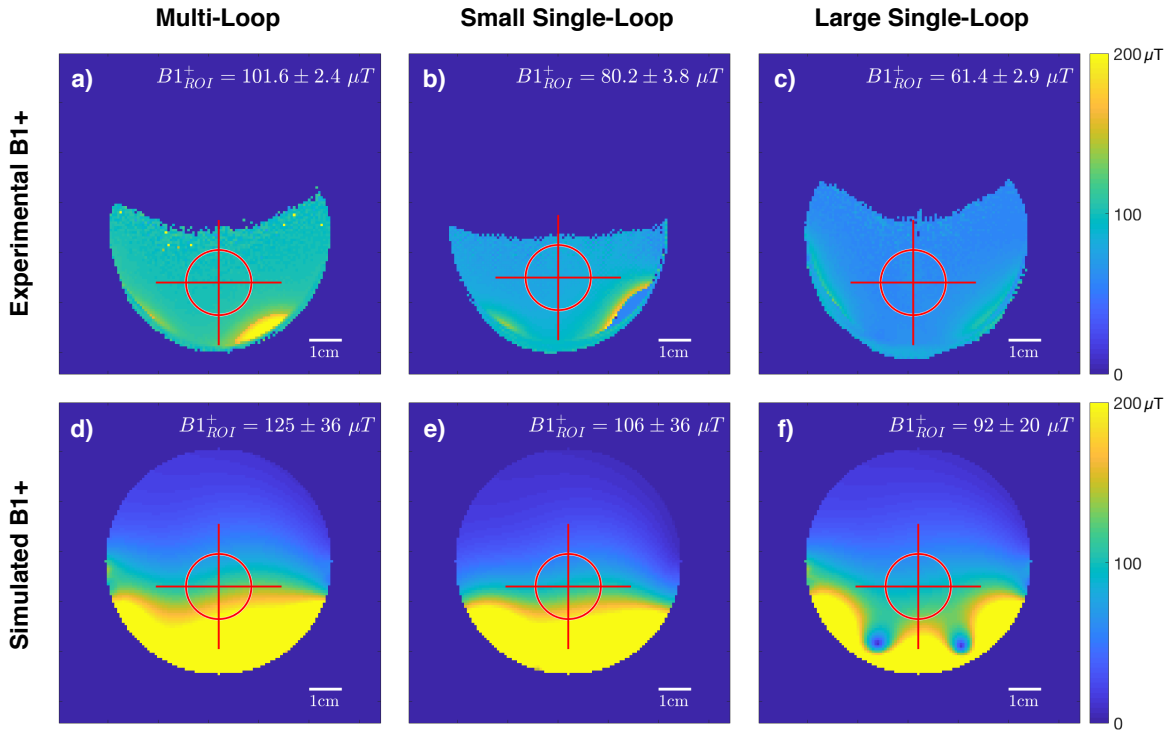

Figure 4.8: 2D simulated and measured B_1^+ for $100\,\mathrm{V}$ excitation, with ^{23}Na pre-clinical coils, with slice thickness of $100\,\mathrm{mm}$. Top row: measured B_1^+ maps, (a) Multi-layer coil B_1^+ of $101.6 \pm 2.4\,\mu\mathrm{T}$, b) Small single loop coil B_1^+ of $80.2 \pm 3.8\,\mu\mathrm{T}$, (c) Large single loop B_1^+ of $61.4 \pm 2.9\,\mu\mathrm{T}$. Poor agreement is seen when comparing experimental and simulated B_1^+ maps. Bottom row: simulated B_1^+ maps, (d) Multi-layer coil B_1^+ of $125 \pm 36\,\mu\mathrm{T}$, (e) Small single loop coil B_1^+ of $106 \pm 36\,\mu\mathrm{T}$, (f) Large single loop coil B_1^+ of $92 \pm 20\,\mu\mathrm{T}$

Several issues were identified with the experimental setup at this stage of prototype testing:

- A high concentration of NaCl was used for high signal, however the strong conductivity of the phantom led to a disparity in the on-axis drop off of the B_1^+ compared to simulated biological tissue loading.
- A high slices thickness of $100\,\mathrm{mm}$ was used, which has the effect of averaging the field profile in the z-direction.
- Large voxel slices lead to partial volume effects on the B_1^+ and SNR field in the x and y-direction.
- An inconsistent conductor width was used between the simulated model (where the conductor was comprised of a thin wire) and the constructed coil (where the conductor was $10\,\mathrm{mm}$ wide).

Whilst the above results give an indication of the increased B_1^+ efficiency of the multi-layer design, the results do not represent correctly the expected on-axis field profile.

4.3.2 Sodium Multi-layer Prototype 2

A second ^{23}Na pre-clinical multi-layer prototype was constructed to minimise the discrepancy between the simulated and measured B_1^+ values from the previous prototype. This multi-layer coil was constructed for ^{23}Na ($\omega = 79.5\,\mathrm{MHz}$, $Q_{\text{Unloaded}}/Q_{\text{Loaded}} = 1.18$ from benchtop measurements), of the same octagram conductor design. The coil was matched to a lower concentration of aqueous sodium chloride ($0.15\,\mathrm{M}$), consistent with the dielectric properties from EM simulation and biological tissue. Similarly to the previous iteration, this RF coil was run in transmit-receive mode, and compared against two custom built single-layer ^{23}Na coils of comparable size: firstly, a smaller single layer loop with a B_1^+ field profile congruent to the multi-layer coil central overlapping region ($Q_{\text{Unloaded}}/Q_{\text{Loaded}} = 1.07$), and secondly, a larger single layer loop tracing the outer track of the multi-layer coil ($Q_{\text{Unloaded}}/Q_{\text{Loaded}} = 1.13$). The photo and EM models of the three coils are shown in Figure 4.9.

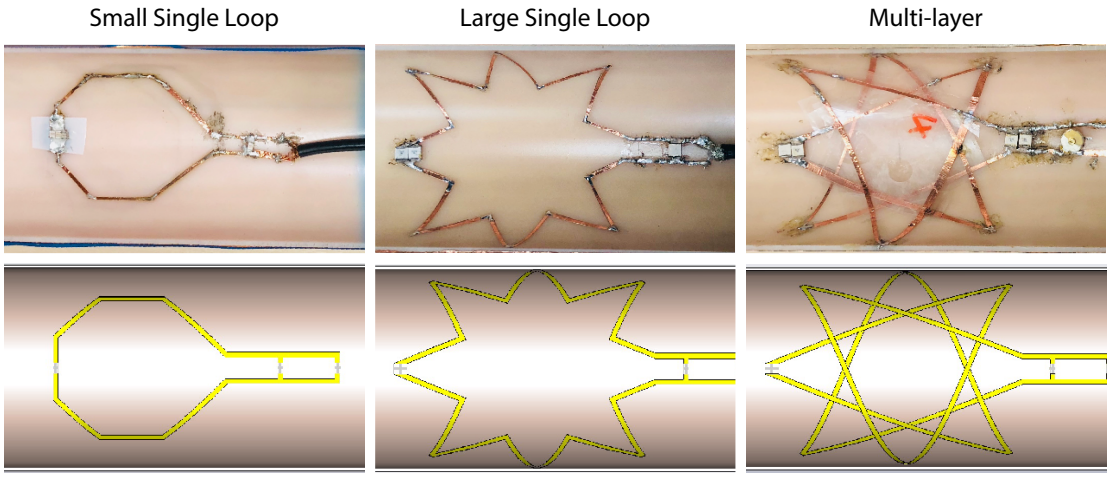

Figure 4.9: Photographs (top row) and simulated models (bottom row) of small single loop, large single loop and multi-layer coils. These coils are belong to the second sodium pre-clinical prototypes.

Several improvements were made in this second iteration, both in terms of coil design but also experimental field mapping protocol. With regards to coil design, there were four notable improvements over the previous iteration:

1. Thinner conductor tracks ($2\,\mathrm{mm}$ compared to the previous $10\,\mathrm{mm}$ width) were used for improve field uniformity and reduced EM shielding effects.
2. On the previous prototype, charred (burnt) regions were observed on the acrylic sheets, which acted as the dielectric layers to prevent current arcing in regions of direct conductor overlap. The previous material acetate had an insufficient dielectric breakdown voltage of $8\,\mathrm{kV\,mm^{-1}}$ [18]. In the second iteration, PTFE sheets of $1\,\mathrm{mm}$ thickness were used to separate regions of direct conductor overlap, allowing the dielectric breakdown voltage to be substantially increased to $17\,\mathrm{kV\,mm^{-1}}$ [18] and ensure the current is confined along the conductor tracks.
3. A ^{23}Na balun (balancing unit) was placed between the coil element and coaxial cables, to reduce unwanted currents induced on the coaxial cable.

4.3.2.1 B1 from EM Simulations

EM simulations were performed with an accurately modelled coil with a $2\,\mathrm{mm}$ conductor width matching the exact shape of the constructed prototypes. From the EM simulation results in the

previous section, it was deemed that accurate conductor geometry was necessary for more comparable simulated and measured results. The multi-layer design was initially created on a 2D flat surface, and then uniformly deformed onto the cylindrical surface using Solidworks (Dassault Systèmes, Vélizy-Villacoublay, France). Consistent with EM simulations of the first ^{23}Na prototype, 2D axial cross-sectional B_1^+ maps were generated, with an identical circular ROI with the centre $30\,\mathrm{mm}$ on-axis from the coil centre and with a radius of $10\,\mathrm{mm}$. The transmit B_1^+ efficiency and B_1^+ uniformity results are, summarised in Table 4.2 with B_1^+ efficiency as $\mu\mathrm{T\,V^{-1}}$ and B_1^+ uniformity as a percentage from one minus the coefficient of variation.

Similarly, this second ^{23}Na multi-layer prototype shows significantly increased B_1^+ strength compared to the two single loops. The simulated multi-layer coil achieved a B_1^+ efficiency of $0.732\,\mu\mathrm{T\,V^{-1}}$ compared to the small loop of $0.401\,\mu\mathrm{T\,V^{-1}}$ and large loop of $0.317\,\mu\mathrm{T\,V^{-1}}$. Significant improvement in the transmit efficiency was seen with the multi-layer compared to single loops: the multi-layer coil has $78\,\%$ higher mean B_1^+ than the smaller loop coil, and $129\,\%$ higher mean B_1^+ than the larger loop coil. These large transmit efficiency improvements are shown through the 2D simulated B_1^+ maps averaged over $5\,\mathrm{mm}$ thick slices, as shown in Figure 4.10. Additionally, the multi-layer design achieved comparable B_1^+ uniformity to the small coil: $71.7\,\%$ versus $74.9\,\%$. However, the multi-layer design achieved significantly worse B_1^+ uniformity when compared to the large loop coil ($71.7\,\%$ versus $90.0\,\%$). Improved agreement was seen between simulated and measured values, however simulated values still overestimated the multi-layer and small loops.

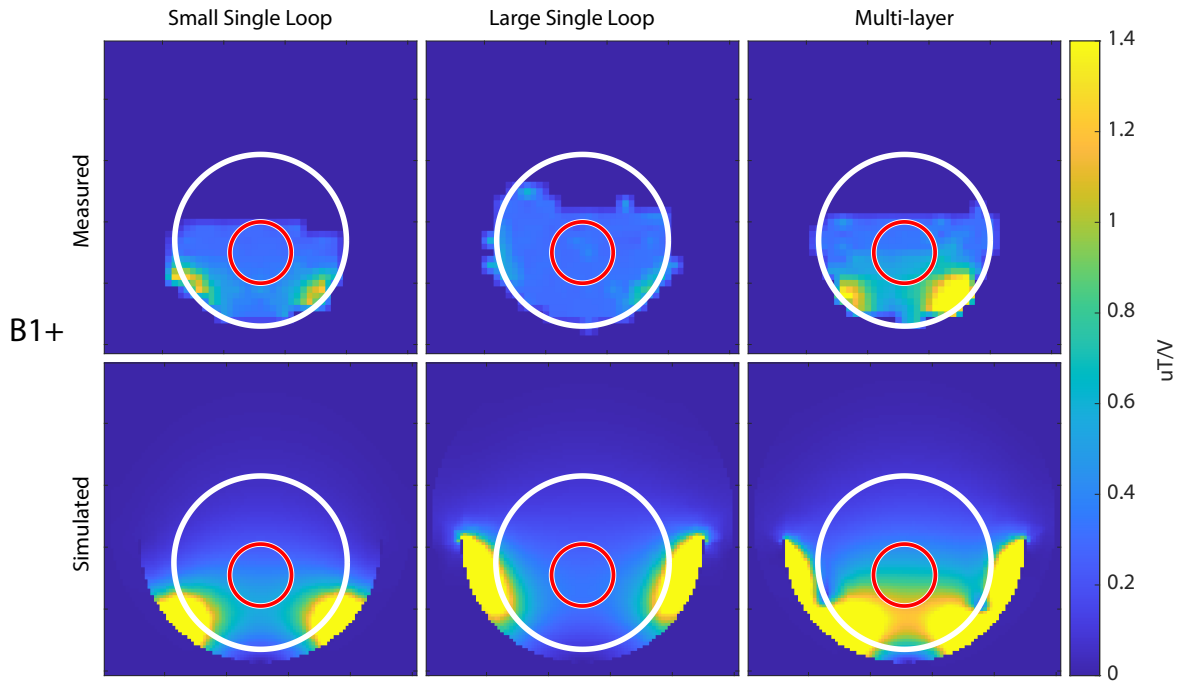

Figure 4.10: Measured and simulated 2D B_1^+ maps for ^{23}Na pre-clinical MRI, with slice thickness $5\,\mathrm{mm}$, showing that the multi-layer coil has increased B_1^+ compared to both the small and large single loops.

From Figure 4.10, the smaller loop coil tracing the overlapping region, achieves approximately comparable field profiles and field uniformity to the multi-layer coil. As such, the dimension of the smaller loop offers a fair comparison against the multi-layer design. On the other hand, the large single loop is too large to compare to the multi-layer design. Nevertheless, the significant observation is that the multi-layer coil offers improved field efficiency relative to a single layer coil of comparable size to the central overlapping region of the multi-layer coil. The increased B_1^+ efficiency indicates that an increase in magnetic flux density within the central overlapping region was achieved by the multi-layer design. However, additional field efficiency may be due to the curved conductor design, which brings the effective centre of the coil closer to the ROI, and disproportionately benefits the multi-layer design with an increased B_1^+ field at the centre of the coil and a steep drop-off. The decrease in field uniformity when compared to the large single loop can be attributed to the peripheral regions of the star-shape coil, where the B_1^+ field originating from the peripheral region destructively interferes with the field from the central region, thus creating a ring of lower field in the boundary between the two regions.

Table 4.2: Measured and simulated coil performance in ROI for three pre-clinical ^{23}Na RF coils: small loop, large loop and multi-layer. On transmit, the B_1^+ efficiency and B_1^+ uniformity are recorded. On receive, the mean SNR is recorded.

	Single Layer		
Measured ROI	Small Loop	Large Loop	Multi-layer
Mean B_1^+ /μT V^{-1}	0.317	0.316	0.456
B_1^+ Uniformity	89.2 %	93.1 %	74.0 %
Mean SNR	1.000	0.327	0.808
Simulated ROI	Small Loop	Large Loop	Multi-layer
Mean B_1^+ /μT V^{-1}	0.410	0.320	0.732
B_1^+ Uniformity	74.9 %	90.0 %	71.7 %
Mean SNR	0.575	0.479	1.000

4.3.2.2 SNR from EM Simulations

Table 4.3: EM Simulated Q-values in the loaded and unloaded case for all three coils. Sample losses are determined from EM simulations, with coil and total losses calculated from the sample loss and Q-values.

	Small Single Loop	Large Single Loop	Multi-layer
Q_{Unloaded}	157.38	185.66	217.62
Q_{Loaded}	140.4	159.5	133.7
Q-Ratio	1.12	1.16	1.63

Receive performance is commonly characterised as the SNR measured by the coil during receive operation, and represents the sensitivity of the coil to magnetisation from nuclei precession. We can determine relative coil sensitivity using Q-values which represent the resonance efficiency of a coil, at the specified Larmor frequency described in section 2.1.4.3. The method used for simulating SNR follows the EM simulation protocol, described in section 3.2.2.3, taking into account Q-loaded values and the magnitude of B_1^-. Following equation 2.38, B_1^- scaled by the square root of Q-loaded is used to give an indication of relative SNR. Whilst typically SNR is dependent on scan parameters, the relative SNR can be determined, normalised across the three coils. Q-values were simulated for both the loaded case (with a loading phantom representative of a sample) and the unloaded case (without any loading), which can be

used to determine both the Q-ratio and the breakdown of coil and sample losses, as shown in Table 4.3. 2D axial cross-sectional SNR maps with the same ROI positioning as the B_1^+ maps discussed above, were obtained for all three coils. The relative SNR maps were normalised by the highest mean ROI, shown in Figure 4.11, and summarised in Table 4.2. Comparing the two conventional loops, the smaller single loop, with a relative SNR of 0.576, has a higher SNR from the large single loop, with an SNR of 0.45. Here, the smaller coil experiences both less coil and sample resistance, therefore a lower loaded Q-value, and a stronger B_1^- field. The relative SNR of 1.0 from the multi-layer coil is significantly higher than the SNR than from the small single loop of 0.58. Overall, EM simulation has shown this initial pre-clinical multi-layer prototype has improved transmit and receive performance over both single loops of approximately $50\,\%$ or more.

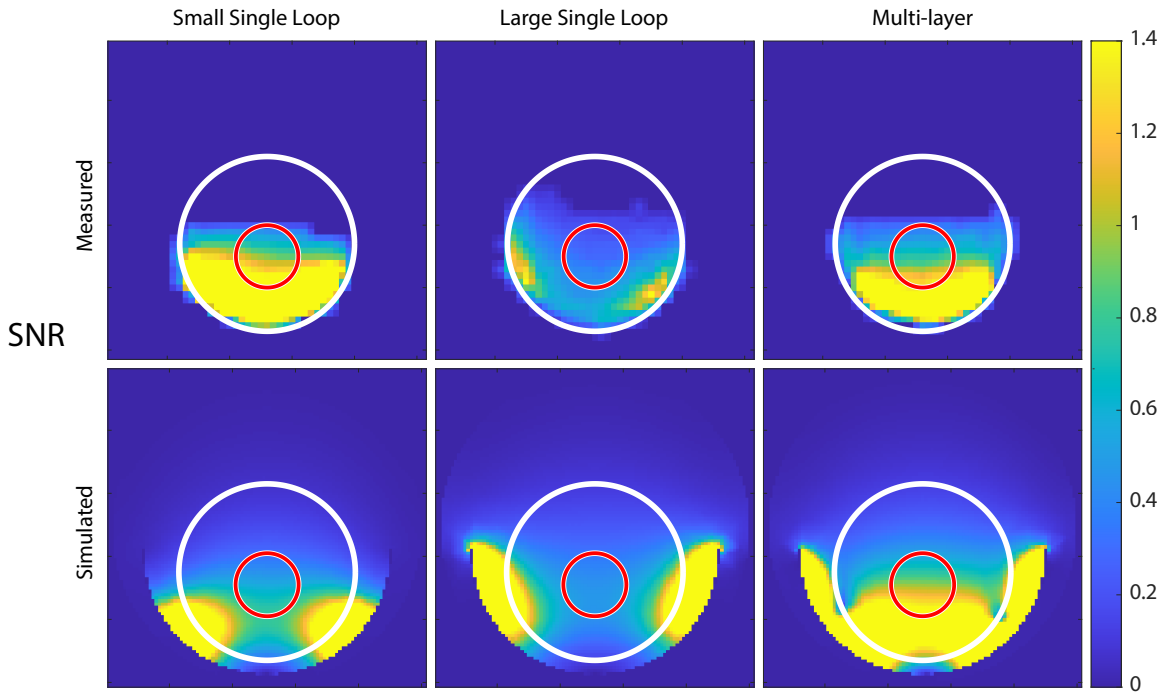

Figure 4.11: Measured and simulated 2D SNR maps for ^{23}Na pre-clinical MRI, with slice thickness $5\,\mathrm{mm}$, showing that the multi-layer coil has lower receive sensitivity than the small single loop but greater than the large single loop.

4.3.2.3 Scanner Measured B1

2D cross-sectional (axial) maps of B_1^+ for transmit and SNR for receive performance were obtained at a resolution of 32×32, with $5\,\mathrm{mm}$ isotropic voxels, which represents a significantly thinner slice over the previous iteration of $100\,\mathrm{mm}$ thickness. For comparison with

EM simulated values, the simulated B_1^+ field profiles were exported at $1\,\mathrm{mm}$ resolution and summed over 5 slices in MATLAB. Within the similar ROI defined as above, the multi-layer field maps are shown in Figure 4.10 and summarised in Table 4.2. The multi-layer design achieved a measured field efficiency of $0.456\,\mu\mathrm{T\,V^{-1}}$ and a substantially higher simulated field efficiency of $0.732\,\mu\mathrm{T\,V^{-1}}$. The smaller single loop achieved a field efficiency of $0.317\,\mu\mathrm{T\,V^{-1}}$ measured and $0.410\,\mu\mathrm{T\,V^{-1}}$ simulated. Compared to the smaller single layer loop, the multi-layer coil achieved $43.8\,\%$ and $78.5\,\%$ increased measured and simulated field efficiency respectively. The larger single layer loop achieved a field efficiency of $0.316\,\mu\mathrm{T\,V^{-1}}$ measured and $0.320\,\mu\mathrm{T\,V^{-1}}$ simulated; compared to the larger single loop, the multi-layer coil achieved $45.2\,\%$ and $128.8\,\%$ increased measured and simulated field efficiency respectively. The multi-layer coil design, however, achieved worse field uniformity on transmit compared to the two single loop coils.

4.3.2.4 Scanner Measured SNR

The relative SNR of the multi-layer coil was $19.6\,\%$ lower than the small single loop but significantly higher than the large single loop. The reduced measured B_1 field uniformity and SNR of the constructed multi-layer coil can be attributed to two design aspects: firstly, the straight conductor of the simple star shaped multi-layer design formed sharp corners within layers causing electric, E-field, hot-spots. Secondly, a region of reduced B_1 field was formed around the boundary between the central overlapping region and peripheral region of the coil, which negatively impacted the field uniformity.

Better agreement was found between the simulated and measured B_1^+ field profiles in this second ^{23}Na prototype. Nevertheless, a discrepancy was still evident between simulated and measured values within the ROI. We attribute this discrepancy to two factors: firstly differences in dielectric constant and conductivity of the simulated saline water compared to aqueous NaCl phantom, and secondly to the poor manual construction of the coil prototypes. The Q-values of the constructed coils were reduced from the theoretical values achievable from EM simulations, suggesting additional losses from the coil construction.

4.4 Carbon Multi-layer Coil Development

Following the successes of the ^{23}Na prototypes, a final ^{13}C pre-clinical prototype was constructed with the intended purpose of testing the design for hyperpolarized ^{13}C imaging in vivo. The coil was smaller, with distributed capacitors on the points of the star edges, for improved receive sensitivity. The ^{13}C pre-clinical multi-layer coil capable of mouse and rat scanning was constructed and tested, and compared to a commercially available pre-clinical coil.

4.4.1 Prototype Construction

This Tx-Rx pre-clinical coil was constructed to be smaller than the previous ^{23}Na prototype (with a flattened approximate diameter of $5\,\mathrm{cm}$) suitable for rat and mouse imaging. The coil featured distributed capacitors, ^{1}H traps, and other components for the coil to be placed inside a ^{1}H volume coil (Rapid Biomedical, Rimpar, Germany) with an inner bore of $72\,\mathrm{mm}$ diameter. The star-shaped design was constructed on the outside of an acrylic tube for the separation between the coil and animal to be sufficient (of approximately $1\,\mathrm{cm}$). ^{1}H LC traps were constructed along the coil for the suppression of resonant currents at the ^{1}H frequency, which would have been induced by the ^{1}H volume coil during localisation scans. A photo of the ^{13}C prototype can be found as the third and final pre-clinical prototype in Figure 4.1. The carbon prototype was constructed such that $\omega = 75.9\,\mathrm{MHz}$, and $Q_{\text{Unloaded}}/Q_{\text{Loaded}} = 1.38$.

4.4.2 Measured Receive Performance

The ^{13}C multi-layer coil was compared to a commercially available quadrature surface coil (Rapid Biomedical) with two $90°$ offset loops of approximately $3\,\mathrm{cm}$ diameter. The multi-layer coil has a central region diameter of approximately $5\,\mathrm{cm}$, hence the fields of view of these two coils were comparable. However, even slight differences in the coil FOV can drastically change the field profile, and therefore fair comparison of SNR was challenging. This ^{13}C coil comparison serves more as a proof of concept than direct comparison of multi-layer performance. Two experiments were performed: a non-localised peak SNR measurements of a small fiducial, followed by chemical shift imaging (CSI, discussed in Appendix D) to obtain a 2D spectral SNR map on discrete voxels.

4.4.2.1 Non Localised Spectroscopy

A small ^{13}C Urea fiducial ($10\,\mathrm{mm}$ diameter, $9\,\mathrm{M}$) was placed in a central region of interest that represents the position of a rat's heart on both coils. Non-localised pulse-acquire spectroscopy was run at increasing power as a 'power calibration' as described in section D.2.1, to determine the voltage required to achieve $90°$ nuclei excitation over the fiducial. Due to the inhomogeneity in B_1^+ field of surface coils, a small high concentration fiducial was chosen to allow for a relatively uniform B_1^+ field within the fiducial volume, for a sinusoidal relationship between signal versus voltage. The multi-layer coil achieved a $90°$ flip angle on the urea fiducial at $35\,\mathrm{dB}$ RF transmit power (as indicated on the $7\,\mathrm{T}$ pre-clinical scanner), with the quadrature coil requiring $41\,\mathrm{dB}$ transmit power. The $6\,\mathrm{dB}$ difference indicated the multi-layer design requires approximately half the power to that of a quadrature coil to achieve the $90°$ flip angle.

4.4.2.2 Chemical Shift Imaging

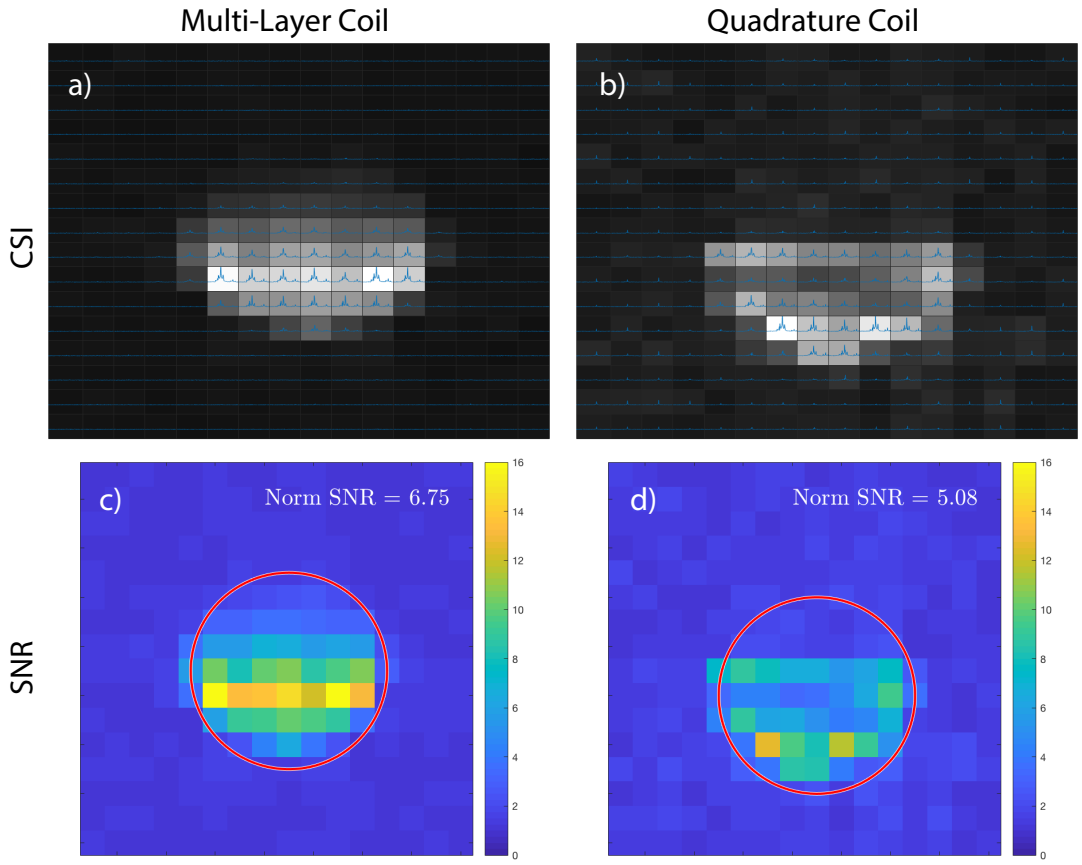

Figure 4.12: SNR of the ^{13}C multi-layer coil versus commercially available quadrature coil (Rapid Biomedical) on ethylene glycol phantom. Top row: 2D CSI using calibrated power from ^{13}C Urea fiducial, (a) Multi-layer coil, (b) Quadrature coil. Bottom row: 2D SNR map calculated from CSI voxels, averaged over coil FOV (total sensitivity), (c) Multi-layer coil SNR (normalised by peak voxel) of 6.75, (d) Quadrature coil SNR (same normalisation) of 5.08.

Next, the receive sensitivity of each coil was characterised by 2D CSI (as presented in Appendix D, section D.2.2) performed on the cylindrical phantom of natural abundance ethylene glycol, using the required input power to supply V_{90° at the ^{13}C Urea fiducial. At every voxel, CSI obtains a chemical shift spectrum, where the SNR can be calculated as the peak signal divided by the standard deviation of noise, from equation 2.26, section 2.1.4.1.

The axial CSI data for the multi-layer and quadrature coils were converted into SNR maps, as shown in Figure 4.12. Over the ROI, the multi-layer coil achieved an SNR of 6.75 whilst the quadrature coil achieved an SNR of 5.08. As such, the multi-layer coil shows $33\,\%$ higher SNR compared to the quadrature coil. However, taking into account that quadrature coil designs theoretically improve SNR up to $\sqrt{2} = 41.4\,\%$ over a single element, this translates to the

multi-layer coil achieving theoretically up to $88\,\%$ higher SNR over a single element.

4.5 Discussion

In summary, this chapter developed the theory and initial prototypes for the multi-layer design. The multi-layer design consistently achieves improved transmit efficiency compared to conventional loop coils, as quantified through EM simulations, benchtop measurements and scanner measurements. Receive SNR improvements were seen with the EM simulations and the ^{13}C multi-layer prototype, however no receive improvements were seen with the ^{23}Na multi-layer prototype. This was primarily due to the limitations of the straight conductor design, undistributed lumped elements, and losses from construction quality.

4.5.1 Overview

Overall, the multi-layer coil showed improved B_1 strength and adequate B_1 uniformity. However, the B_1 field uniformity was not as high as in conventional coils, primarily due to a ring of null (zero) field between the peripheral and central regions. This arises from the parallel direction of current flow in the central overlapping region and the peripheral region and is addressed in the subsequent chapter. The field mapping of the pre-clinical star shaped prototype led to two design improvements for the clinical multi-layer prototypes, implemented in Chapter 5:

- Curved conductors were implemented, which allows reversed current flow in the peripheral region, such that the field from the peripheral region is in phase with the field from the coil centre, and the region of lowered field is eliminated. This allows for improved B_1^+ uniformity, as discussed later in section 5.2.2.
- Flexible conductor tracks were implemented, by using flexible PCBs to wrap around the torso. The curved coil brings the effective coil centre, where the improvement in magnetic flux density is greatest, closer towards the ROI.

4.5.2 Petal, Spiral and Concentric Designs

There are alternative high Q designs, found typically outside of the field of RF coils. In these designs, high Q is achieved through planar concentric rings and spiral designs, where each turn of the spiral increases the coil inductance, L_{Coil}. Each turn of the conductor is separated

(in plane), so as to minimise the coil resistance from proximity effects, R_{Coil}, as described in section 4.2.2.1. Outside of RF coil technologies, planar spiral and concentric antennas are used in wireless charging applications [19] and radiofrequency identification (RFID), particularly near-field communication (NFC), applications [20, 21]. In these cases, a strong and efficient EM field is crucial for efficient data and energy transfer. Specifically, concentric ring designs have been implemented as RF coils [10, 22, 23]. From a theoretical standpoint, the concentric ring design has four limitations when compared to the multi-layer design:

1. The maximum number of turns is spatially constrained by the coil outer geometry, as each turn requires a certain width and separation between neighbouring turns. This imposes a limit on the maximum inductance of the coil, and thus limits the maximum Q of the coil.
2. As each turn has different radius, the magnetic flux density is most concentrated within the smallest central loop, and decreases in strength with each subsequent turn. This leads to a less-than-optimal 'central overlapping region'. Due to the trade-off that exists between field uniformity (and conversely depth penetration) and field efficiency, an optimum radius exists for maximum field strength within an ROI. However, the strongest flux from the inner turn is non-optimal.
3. Lumped elements are ideally evenly distributed along the coil for coil uniformity. However, element components themselves create localised regions of E-field hotspots and B-field distortions. Whilst the multi-layer design allows the lumped elements to be evenly distributed on the peripheral region, the concentric design places lumped elements in the central region.
4. The concentric design lacks a peripheral region, which is formed from a multi-layer design, the benefits of which are described above.

One such high Q design implemented as a novel RF coil is the petal resonator surface (PERES) coil [24], which comprises of a central circular loop with peripheral loops distributed around this central loop. This design has been shown to offer $26\,\%$ and $35\,\%$ SNR improvements over corresponding circular coils and phased-array coils respectively at $1.5\,\mathrm{T}$ [9].

4.5.3 Impact of Multi-layer Design

The results presented show the multi-layer design as a promising avenue for improved B_1 efficiency and SNR across two nuclei: ^{13}C and ^{23}Na. B_1^+ strength increases of $50\,\%$ are seen,

which correspond (approximately) to the improvements in using quadrature coil designs, or approximately requires half the power with the multi-layer coil to achieve the same flip angles. This increase in transmit performance is achieved without significant loss of field uniformity, for single element Tx-Rx coil designs.

4.5.4 Further Work

So far, the novel coil design has been limited to pre-clinical prototype constructions, where the copper and insulator layered structure has been constructed in an electronics workshop in-house. However, an increase in the complexity of the multi-layer design is required to achieve higher constructed Q-values (with increased inductance and minimised resistance) for improved SNR, beyond that which can be achieved by building in-house. Further additional investigations into the design, such as: clinical translation towards a human sized coil and lower frequencies, replacing elements in common coil paradigms, such as multiple elements/array configurations, decoupling with ^{1}H volume coils, and heating safety tests (SAR measurements) are discussed in the following chapters of this thesis. No further work was done on the pre-clinical multi-layer coils due to the time limits of this project, however more optimised prototypes could be constructed for improved animal imaging. The decision to focus on clinical coils was made as a result of the design being easier to construct at lower frequencies, as is the case with clinical MRI at typically lower field strengths, and coil performance sitting further towards the sample-noise-dominated regime.

References

[1] *AIR^{TM}*. GE Healthcare. URL: https://www.gehealthcare.com/products/magnetic-resonance-imaging/air-technology.

[2] Motovilova, E. et al. “Stretchable self-tuning MRI receive coils based on liquid metal technology (LiquiTune)”. In: *Scientific Reports* 11 (1 Dec. 2021), p. 16228. ISSN: 2045-2322. DOI: 10.1038/s41598-021-95335-6.

[3] Corea, J. R. et al. “Screen-printed flexible MRI receive coils”. In: *Nature Communications* 7 (1 Apr. 2016), p. 10839. ISSN: 2041-1723. DOI: 10.1038/ncomms10839.

[4] Winkler, S. A. et al. “Evaluation of a Flexible 12-Channel Screen-printed Pediatric MRI Coil”. In: *Radiology* 291 (1 Apr. 2019), pp. 180–185. ISSN: 0033-8419. DOI: 10.1148/radiol.2019181883.

[5] Keil, B. and Wald, L. L. “Massively parallel MRI detector arrays”. In: *Journal of Magnetic Resonance* 229 (Apr. 2013), pp. 75–89. ISSN: 10907807. DOI: 10.1016/j.jmr.2013.02.001.

[6] Keil, B. et al. “A 64-channel 3T array coil for accelerated brain MRI”. In: *Magnetic Resonance in Medicine* 70 (1 July 2013), pp. 248–258. ISSN: 07403194. DOI: 10.1002/mrm.24427.

[7] Schmitt, M. et al. “A 128-channel receive-only cardiac coil for highly accelerated cardiac MRI at 3 Tesla”. In: *Magnetic Resonance in Medicine* 59 (6 June 2008), pp. 1431–1439. ISSN: 07403194. DOI: 10.1002/mrm.21598.

[8] Deshmane, A. et al. “Parallel MR imaging”. In: *Journal of Magnetic Resonance Imaging* 36 (1 July 2012), pp. 55–72. ISSN: 10531807. DOI: 10.1002/jmri.23639.

[9] Rodríguez, A. O. et al. “Experimental development of a petal resonator surface coil”. In: *Magnetic Resonance Imaging* 23.10 (2005), pp. 1027–1033. ISSN: 0730-725X. DOI: https://doi.org/10.1016/j.mri.2005.09.001. URL: https://www.sciencedirect.com/science/article/pii/S0730725X05002559.

[10] Giaquinto, R. O. J. et al. “Multi-turn element RF coil array for multiple channel MRI”. US7282915B2. Co, G. E. and University, J. H. 2004.

[11] Zhou, T. et al. “Radiofrequency coil”. WO2020217069A1. Limited, O. U. I. 2019.

[12] Lufkin, R. et al. “Solenoid surface coils in magnetic resonance imaging”. In: *American Journal of Roentgenology* 146 (2 Feb. 1986), pp. 409–412. ISSN: 0361-803X. DOI: 10.2214/ajr.146.2.409.

[13] Callaghan, E. E. and Maslen, S. H. *The Magnetic Field of a Finite Solenoid*. NASA-TN-D-465. Technical Report. Cleveland, OH United States, 1960.

[14] Wheeler, H. “Formulas for the Skin Effect”. In: *Proceedings of the IRE* 30 (9 Sept. 1942), pp. 412–424. ISSN: 0096-8390. DOI: 10.1109/JRPROC.1942.232015.

[15] Smith, G. S. “Proximity Effect in Systems of Parallel Conductors”. In: *Journal of Applied Physics* 43 (5 May 1972), pp. 2196–2203. ISSN: 0021-8979. DOI: 10.1063/1.1661474.

[16] Eroglu, S., Friedman, G., and Magin, R. “Estimate of losses and signal-to-noise ratio in planar inductive micro-coil detectors used for NMR”. In: *IEEE Transactions on Magnetics* 37 (4 July 2001), pp. 2787–2789. ISSN: 00189464. DOI: 10.1109/20.951307.

[17] Doty, F. D. et al. “Radio frequency coil technology for small-animal MRI”. In: *NMR in Biomedicine* 20 (3 May 2007), pp. 304–325. ISSN: 09523480. DOI: 10.1002/nbm.1149.

[18] *Dielectric Strength*. URL: https://omnexus.specialchem.com/polymer-properties/properties/dielectric-strength.

[19] Lu, X. et al. “Wireless Charging Technologies: Fundamentals, Standards, and Network Applications”. In: *IEEE Communications Surveys & Tutorials* 18.2 (2016), pp. 1413–1452. DOI: 10.1109/COMST.2015.2499783.

[20] Mohan, S. et al. “Simple accurate expressions for planar spiral inductances”. In: *IEEE Journal of Solid-State Circuits* 34 (10 1999), pp. 1419–1424. ISSN: 00189200. DOI: 10.1109/4.792620.

[21] Konanur, A. S., Karacaoglu, U., and Yang, S. “Spiral near field communication (NFC) antenna coil”. US10325708B2. Corp, I. 2012.

[22] Uesaka, K. “Antenna-coil design apparatus and design method”. US7334736B2. Ltd, H. 2004.

[23] Rowell, C. R., Lai, H.-W., and Mak, C.-L. “Miniature and multi-band RF coil design”. US8056819B2. Science, H. K. A. and Institute, T. R. 2008.

[24] Mansfield, P. “The petal resonator: a new approach to surface coil design for NMR imaging and spectroscopy”. In: *Journal of Physics D: Applied Physics* 21.11 (Nov. 1988), pp. 1643–1644. DOI: 10.1088/0022-3727/21/11/015.

5 | Human Multi-layer Coil Development

5.1 Introduction

5.1.1 Human Multi-layer Coil

The theory of the multi-layer RF coil design was established in Chapter 4, followed by the construction of several simple pre-clinical multi-layer prototypes. Experimentally, the pre-clinical coil achieved significant transmit improvements compared to single-layer conventional loop coils, although the coil underachieved in both field uniformity and receive sensitivity (on the ^{23}Na prototype only). The limitations imposed by straight conductors created regions of lower B-fields, out of phase B-fields in the peripheral region, and E-field hotspots at the edge of the coil. These factors combined led to wasted EM fields at the peripheral regions of the coils, limiting both field uniformity and receive sensitivity. The aim of this chapter was to develop a clinical system MR coil using the multi-layer design for improved B_1^+ efficiency as well as SNR without the loss of field uniformity. Potential improvements in SNR are more significant than B_1^+, as this coil design could be used to improve clinical ^{1}H studies in addition to X-nuclei research studies. To utilise the improvements in transmit and receive, the multi-layer coil elements are required to both be able to directly replace conventional loop coils, and also to integrate with existing coils such as ^{1}H volume coils.

Starting from the pre-clinical development in the previous chapter, two main challenges are encountered in the clinical translation: first, understanding the effects of the EM field when altering the multi-layer design, and second, ensuring the safety of the proposed coils for human applications. However, presently we do not have a systematic approach to optimise or tailor the EM fields from the multi-layer coil design. As such, efforts were made to parameterise the multi-layer design and sweep through the parameter values to map out optimum designs. Extensive coil characterisation and safety measurements were then conducted. This chapter highlights the significant aspects of work undertaken in the development of a human version of the multi-layer coil.

5.1.2 Overview

Broadly, this chapter is split into two halves. The first half highlights further multi-layer design improvements brought about by an optimised curved conductor shape. Section 5.2 discusses the construction of the curved conductor, the benefits of the peripheral coil region, and compares the multi-layer design against spiral and concentric planar coils. Section 5.3 documents the EM field profile when sweeping through different parameters of the multi-layer design through EM simulations, allowing for the identification of the individual multi-layer designs with optimum transmit and receive performances. The second half of this chapter focuses on the characterisation and implementation of a human multi-layer coil. Section 5.4 characterises the multi-layer coil through measured and simulated phantom field maps, with section 5.4.1 showing two ^{13}C multi-layer coils compared to three commercially available loop coils (PulseTeq Ltd), and section 5.4.2 showing one ^{31}P multi-layer coil compared to one commercially available loop coil (PulseTeq Ltd). Section 5.5 shows the RF heating measurements, and coil development undertaken to ensure safety for the ^{31}P coil on humans. Finally, section 5.6 characterises the improvements of the multi-layer design on five human volunteers with the ^{31}P multi-layer coil compared to a commercially available loop coil (PulseTeq Ltd) of comparable size.

5.2 Further Multi-layer Design Improvements

The conductor geometry for the pre-clinical coils described in Chapter 4 were built in-house and necessitated simple, straight conductor tracks, which imposed limitations on the EM field. For clinical coils, flexible PCB technology allowed for quadruple layered PCB designs, of any conductor and dielectric shape. This section describes two main benefits of a multi-layer coil with curved conductors: firstly further improvements to the Q-value in section 5.2.1, and secondly improvements to the field uniformity, particularly between the central and peripheral regions in section 5.2.2.

5.2.1 Curved Conductor Construction

Four Ω-shaped conductor layers are tessellated to form the next multi-layer prototype construction. These complex conductors were achieved through flexible PCBs (supplied by FlexibleTechnology Ltd, Isle of Bute UK). The Ω element design was chosen as minimal parameters

(five in total, as described below) were needed to characterise the design. Here, we present a procedure for modelling the Ω conductor shape and tessellating the elements into a multi-layer coil. This 3D CAD (computer aided design) model was created on SolidWorks, and was then used for both EM simulations in CST and exported as Gerber files using Eagle (Autodesk, California, US) for PCB design. The multi-layer PCB constructed from curved conductors in this work was comprised of four conductor layers separated by four dielectric layers. The simplest curved conductor layer design consists of a central circular segment (formed from $3/4$ of a circle), connected at each end by two smaller peripheral circular segments (formed from $1/2$ of a circle). The steps in generating such a curved multi-layer design, as shown in Figure 5.1, are presented below.

1. A large loop forms the central overlapping region, of radius, $R1$ (e.g. $100\,\mathrm{mm}$) and conductor width, W (e.g. $10\,\mathrm{mm}$).
   (a) A segment of the loop is removed, with the number of layers, N (e.g. 4 or 6), such that the angle of the removed segment is $360/N°$ (i.e. 4 layers requires $90°$, 6 layers requires $60°$).
   (b) Equivalently, the loop sweeps an angle of $(N-1) \times 360/N°$, (i.e. 4 layers requires $270°$, 6 layers requires $300°$)
   (c) The centre of the loop is positioned at polar coordinates $(0, 0)$.
2. Two smaller peripheral loops attached at both 'ends' of the cut central loop, this forms the peripheral region, of radius, $R2$ (e.g. $50\,\mathrm{mm}$), width W (e.g. $10\,\mathrm{mm}$).
   (a) The peripheral loop is formed from half of the conductor ring (e.g. angle of removed segment is $180°$).
   (b) One loop positioned at polar coordinates $(R1, 0)$, and the other loop positioned at $(R1, (N-1) \times 360/N°)$.
3. The three loops consisting of the central loop with two peripheral loops (one at each end) are joined together for a single conductor layer. Each subsequent conductor layer, i, is vertically separated by a dielectric layer.
   (a) Each subsequent layer, i, is rotated by $(i-1) \times 360/N°$ (i.e. 4 layers requires rotations of $0°$, $90°$, $180°$, $270°$), at the centre of the central loop $(0, 0)$.
   (b) Each layer, i, is shifted by an offset, O (e.g. $25\,\mathrm{mm}$), which determines the ratio of central overlapping area and peripheral area. The offset shift vector is different for

each layer, and determined by the vector $(O, (i-1) \times 360/N°)$.

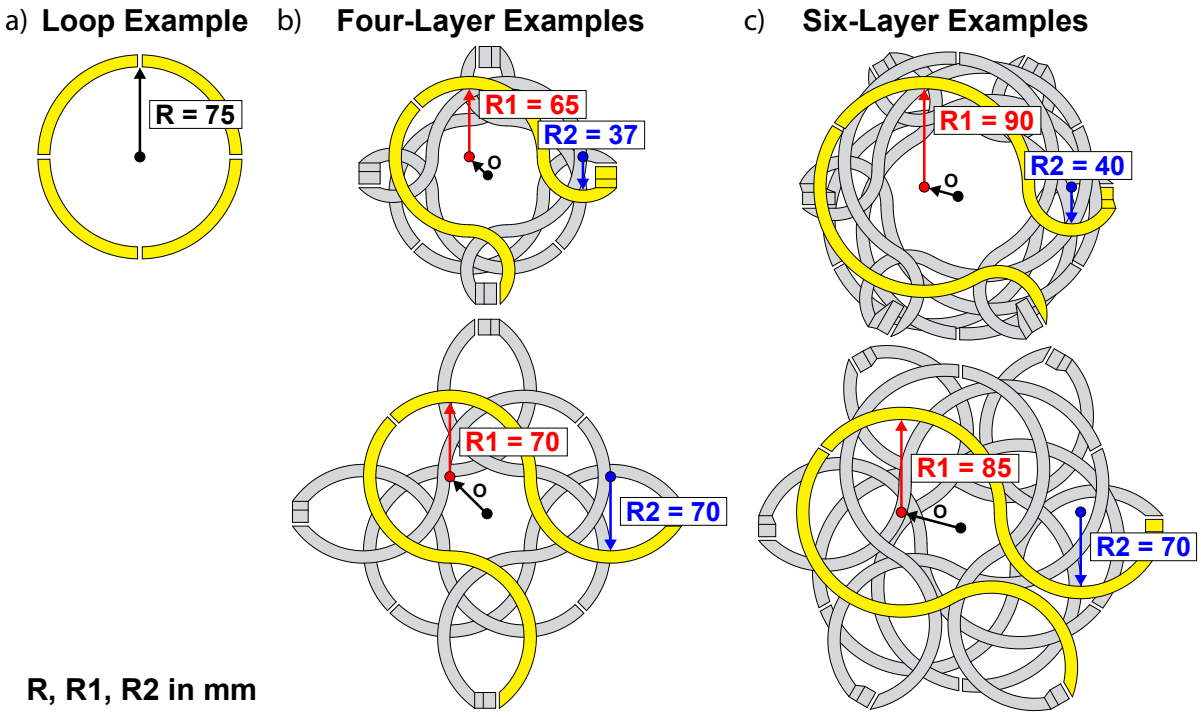

Figure 5.1: Parameterised multi-layer designs. (a) Conventional loop with R (radius) parameter, with example of $R = 75\,\text{mm}$. (b) Four-layer multi-layer designs with $R1$ (central radius) and $R2$ (peripheral radius), with examples of $R1 = 65\,\text{mm}$, $R2 = 37\,\text{mm}$ (constructed 'small multi-layer' coil) and $R1 = 70\,\text{mm}$, $R2 = 70\,\text{mm}$. (c) Six-layer multi-layer designs with $R1$ and $R2$, with examples of $R1 = 90\,\text{mm}$, $R2 = 40\,\text{mm}$, and $R1 = 85\,\text{mm}$, $R2 = 70\,\text{mm}$.

Overall, we identified five parameters which are required for the construction of the coil: (1) radius of central region, $R1$, (2) radius of peripheral region, $R2$, (3) offset, O, (4) conductor width, W, and (5) number of layers, N. As the multi-layer design is one single continuous structure, the currents must be bridged across the layers. Typically, 'vias' are used in PCBs to conduct current between layers. However, vias are typically lossy at high frequencies and undesired in RF coils [1, 2]. Instead, the multi-layer design used lumped elements such as capacitors and ^{1}H traps to conduct the alternating current across neighbouring layers, to form a single continuous conducting path as shown in Figure 5.2 b. The dielectric layer design also requires some thought; the exact shape does not substantially affect the magnitude of the EM fields, beyond minor changes to refractive index, separation distance of conductor layers and electric isolation between conductor layers. However, each dielectric layer requires specific cut-outs to allow lumped elements to connect each of the conductor layers when the layers are stacked on top of one another. As each subsequent layer covers the layer beneath, for lumped

elements to be placed on a given conductor layer, all dielectric layers above the given conductor layer require sections cut out around the position of the lumped element gap. This design of the conductor layers are shown most clearly in Figure 5.2; the exact design of the dielectric can vary between coils, but must be cut out at specific regions to allow lumped elements to be distributed along the coil conductor and bridge conductor layers.

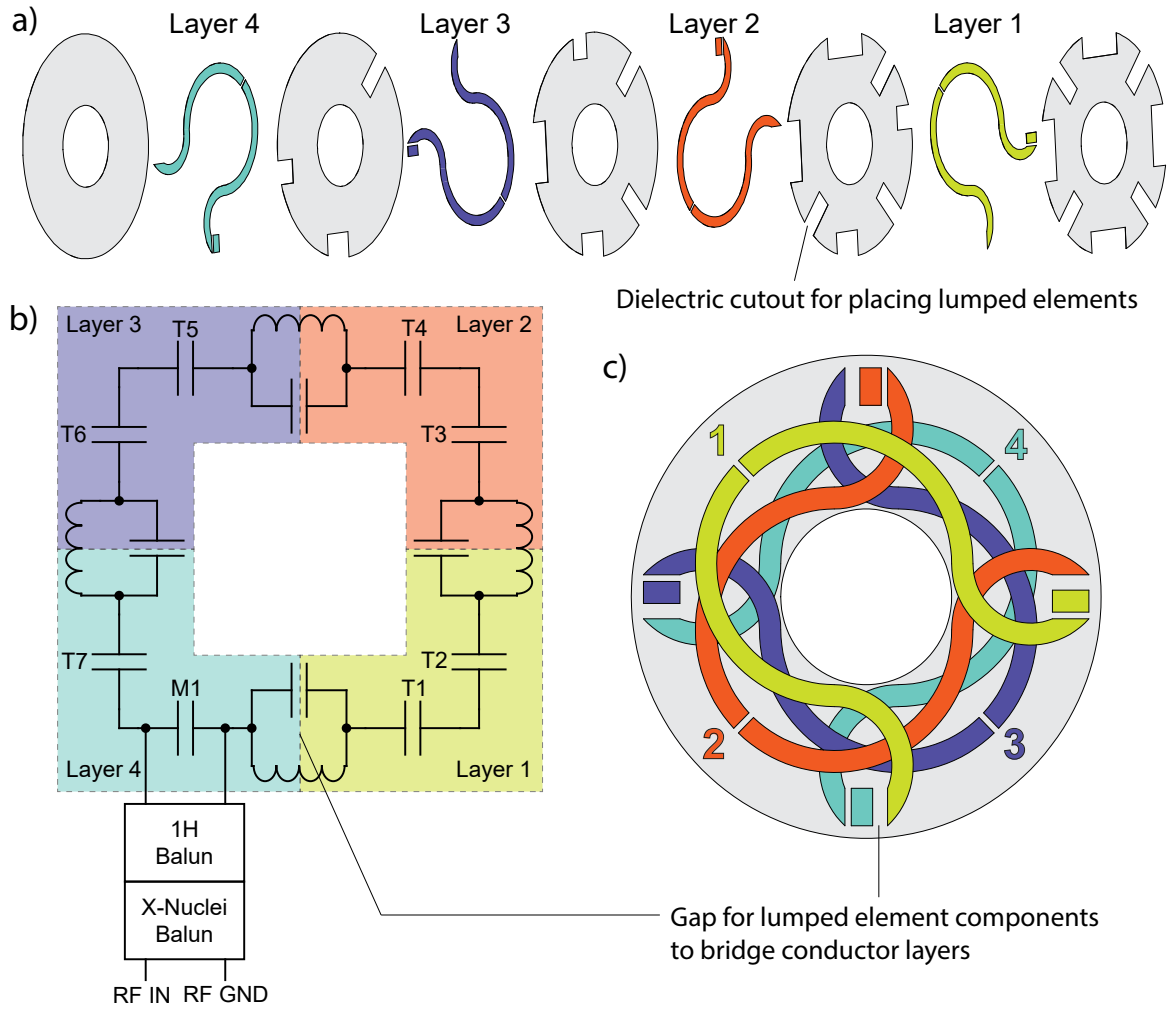

Figure 5.2: Example multi-layer stacked conductor design. (a) Expanded layer structure showing alternating conductive and dielectric layers. (b) Schematic diagram of discrete lumped elements, using ^{1}H LC traps and capacitors to bridge across conductor layers. (c) Diagram showing stacked conductor layers and regions of overlap with gaps for lumped element components.

5.2.2 Peripheral Coil Region

We found empirically that four- and six-layer designs provided a good balance between increased coil sensitivity and complexity of construction for human cardiac applications. Two

regions of the coil are formed: a central overlapping region, and a peripheral region. The central overlapping region is designed for increased magnetic flux density and Q-value, whilst the peripheral region can be designed for improved field uniformity from three aspects: (1) eliminating the region of lower field between central and peripheral region, (2) distributing lumped elements along the conductor track, and (3) decoupling of neighbouring coil elements in an array. The curved conductor design allows the three design aspects to be achieved.

5.2.2.1 Boundary Region of Lower B-field

The curved conductor design reverses the direction of current flow in the peripheral region of the loop compared with the straight conductor designs used in the previous chapter. This allows the EM fields from the peripheral regions to be in-phase with the EM field from the central region. This eliminates the ring of lower field observed in the star-shaped pre-clinical design that was created by the parallel current between the central and peripheral regions. An example of the field improvements is shown in Figure 5.3, with EM simulations of a parallel peripheral region design (much like the design of the pre-clinical star shaped coils scaled up to human sizes) and a reversed peripheral region design, which is of approximate dimensions to the star shaped design but with reversed direction peripheral loops to minimise regions of lower B-field. Despite the non-optimal reversed peripheral region design (when compared to the more optimal coil designs such as in Figure 5.1), an increase of the on-axis B_1^+ through the coil centre (red line) is seen. Additionally, greater uniformity is seen across the coil plane at all depths (black lines) by eliminating dips in the B_1^+ at the peripheral region boundary with the reversed current design.

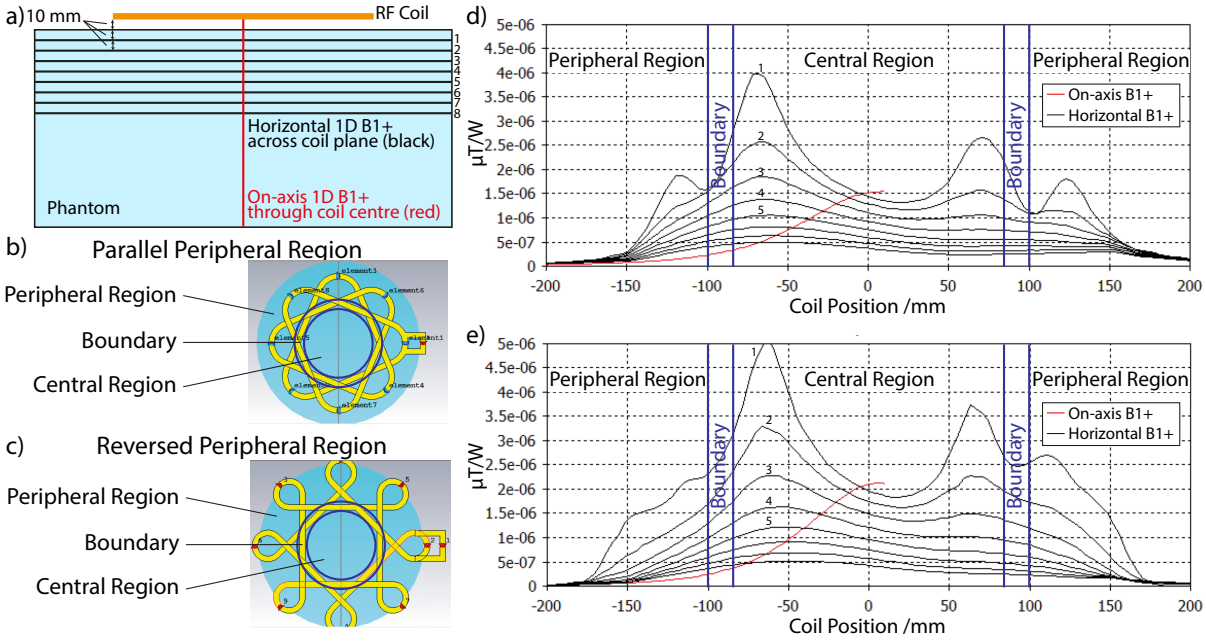

Figure 5.3: 1D plots of B_1^+ comparing field from a parallel peripheral region and a reversed peripheral region. (a) Diagram showing coil loading setup and 1D B_1^+ vertical on axis (red) and horizontal across coil plane (black). (b) Boundary region of parallel peripheral region coil setup (equivalent to pre-clinical star shaped multi-layer design). (c) Boundary region of reversed peripheral region coil setup example. (d) B_1^+ for $1\,\mathrm{W}$ power input through coil centre and horizontally across the coil plane y-z plane at $1\,\mathrm{cm}$ depths for parallel peripheral region. (e) B_1^+ for $1\,\mathrm{W}$ power input through coil centre and horizontally across the coil plane y-z plane at $1\,\mathrm{cm}$ depths for reversed peripheral region.

5.2.2.2 Distributed Lumped Elements

The conductor end of one layer must be electrically connected to the beginning of another layer, forming a continuous loop. Lumped elements, such as capacitors and current suppression circuits (LC traps), are used to electrically bridge across the dielectric layers as they are the most common method of ensuring the operational characteristics of an RF coil (i.e. correct resonance frequency or 'tuning' and minimised reflected power or 'matching'). However, lumped elements can cause unwanted local distortions to the EM field profile of the coil, termed 'hotspots', which lead to sharp increases in local energy deposition from the electric field as well as forming resonances that disrupt the magnetic field profile. In addition, both capacitors and traps must be placed at regular intervals on the conductor track as a safety mechanism to minimise undesired EM interactions inside the conductor. Therefore, another major advantage of the revised multi-layer coil design is that the tessellated structure allows for all lumped elements to be positioned on the periphery of the coil, thus removing EM field distortions from

the central region of increased sensitivity.

5.2.2.3 Decoupling of Neighbouring Elements

The peripheral regions of two adjacent multi-layer elements within an array can be overlapped for decoupling. This will minimise the inhomogeneities of the B_1^+ field on the central region. The peripheral regions of the multi-layer coil are overlapped, such that the field from the central region is undisturbed. The use of coil outer edges for geometric decoupling has been previously patented [3]. Further experimental validation of the ability for the multi-layer design to efficiently geometrically decouple with improved B_1^+ uniformity is presented in section 6.4.1.1.

5.2.3 Estimating Multi-layer Q-Value

A rough approximation of the potential Q-values of these clinical designs can be made through the theoretical scaling of resistance and inductance for a multi-layer design compared to a single loop. Assuming the magnitude of the time varying current, I, is the same between a single loop and multi-layer coil, $I_{\text{Multi-layer}} = I_{\text{Loop}}$, we can estimate the theoretical increase in loaded Q-value using equation 2.35, by taking into account the total coil inductance, L_{Coil}, and total resistance, R_{Total} (assuming the coil is well matched to $50\,\Omega$). Using the resonance frequency, ω, and the total coil capacitance, C_{Coil}, we can determine L_{Coil} using equation 3.10. For the four-layer multi-layer coil, it was found that $L_{\text{Multi-layer}} \approx L_{\text{Loop}} \times 10$. The total resistance of a loaded coil, R_{Total}, has two main contributions: resistance of the coil components R_{Coil}, and sample resistance from coil capacitive coupling to the sample R_{Sample}, as discussed in section 2.1.4.4. We expect similar R_{Sample} for a given multi-layer design compared with a corresponding loop coil of similar FOV. Therefore, the majority of the increased resistance of the multi-layer design arises from increased R_{Coil}. The ratio of R_{Coil} to R_{Sample} can be calculated for both coils using benchtop measurements (section 3.3.1.4). We determine for the coil resistances of both coils: $R_{\text{Coil(Multi-layer)}} \approx 8 \times R_{\text{Coil(Loop)}}$. The exact ratio of the contributions from the sample and coil resistance depends on two factors: a lower resonance frequency and a larger coil size both shift the balance towards a more sample-dominated regime. For a ^{13}C human cardiac multi-layer coil (at approximately $30\,\text{MHz}$), we measure $R_{\text{Sample}} \approx 5 \times R_{\text{Coil}}$. As such, in the case of human coils, the fast scaling of the multi-layer coil resistance with respect to layers is suppressed by the large contribution of sample resistance, where $R_{\text{Total(Multi-layer)}} \approx 3 \times R_{\text{Total(Loop)}}$. Therefore,

larger Q-values (and SNR) improvements are achieved at lower frequencies and larger coil sizes; this was the primary motivation towards the construction of human multi-layer coils at $30\,\mathrm{MHz}$ on ^{13}C. The overall Q_{Loaded} can be approximated from the L and R for the multi-layer and loop coils: this translates to approximately $Q_{\text{Loaded(Multi-layer)}} \approx 3 \times Q_{\text{Loaded(Loop)}}$, and following equation 2.38, $\text{SNR}_{\text{Multi-layer}} \approx 1.7 \times \text{SNR}_{\text{Loop}}$, is equivalent to a $70\,\%$ increase in SNR with the multi-layer coil.

5.3 Multi-layer Optimisation

So far in this work, discussion on the parameters of specific multi-layer designs have been limited. Given the complex structure of the conductors as a result of the tessellation, at this stage we have very limited understanding of an 'optimum' multi-layer design. This section aims to address this lack of understanding, by determining specific optimal multi-layer parameters through EM simulations. The EM simulations setup and example results for human multi-layer coils at $30\,\mathrm{MHz}$ are presented in section 5.3.1. Following this, a parameter sweep is performed through the parameterised model of the multi-layer design, and an optimum design is defined through simulated B_1 field uniformity versus B_1 efficiency curves in subsection 5.3.2. Secondly, possible conductor designs are investigated aiming to reduce the proximity effect and coil resistance through looking at tapered and cylindrical conductor designs in section 5.3.3.

5.3.1 EM Simulation Setup

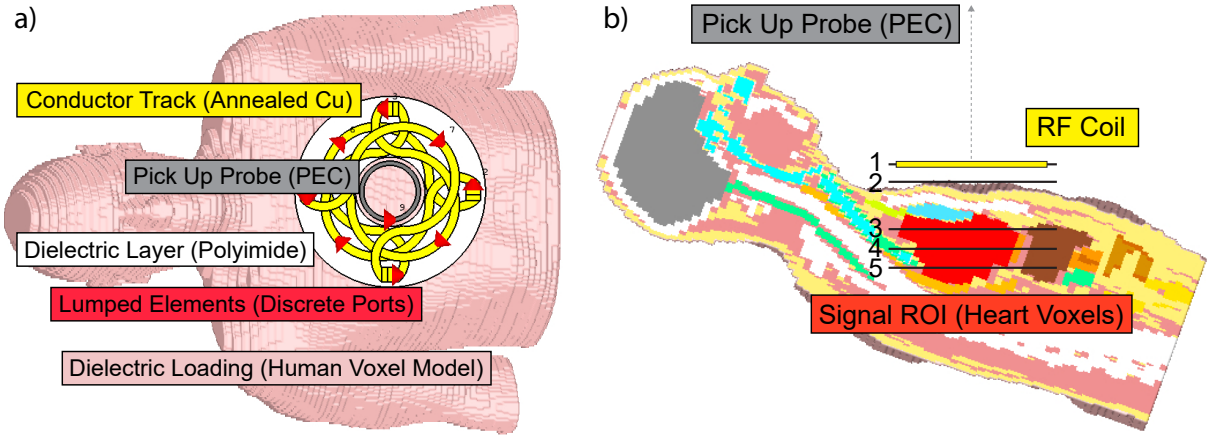

Figure 5.4: EM simulation setup for surface coil on human voxel model. (a) Top view of coil position over the heart of a human voxel model, showing simulation components. (b) Side view of coil position showing signal ROI (heart), height of the coil above the body, and depth of $0\,\mathrm{mm}$ (approximately representing the body surface), $60\,\mathrm{mm}$ (approximately representing the top of heart), $90\,\mathrm{mm}$ (approximately representing the middle of heart), and $120\,\mathrm{mm}$ (approximately representing the bottom of heart).

Utilising the protocol described in Appendix E, and the curved conductor design from section 5.2.1, the multi-layer coil can be constructed from the five parameters as presented in section 5.2.1: (1) radius of central region, $R1$, (2) radius of peripheral region, $R2$, (3) offset, O, (4) width, W, and (5) number of layers, N. The value of these parameters determine the EM field profile generated from the coil, and so further field improvements could be gained through optimisation of the multi-layer design with respect to these parameters. EM simulations were used to determine both the transmit and receive performance for parameterised coil designs. Each specific parameter value represents one multi-layer element design. For consistent comparison across all element designs, an identical simulation setup was used across all multi-layer variations as shown in Figure 5.4. The coil element was positioned $10\,\mathrm{mm}$ above the surface of the torso of the human voxel model, Hugo [4], with the coil central axis through the centre of the heart. A pick-up probe was placed $400\,\mathrm{mm}$ above the centre of the coil, to minimise coupling even to the largest multi-layer coil design. All conductor layers used material properties of annealed copper, the pick up probe was created as a perfect electrical conductor (PEC). EM simulations using time domain (FDTD) were performed according to the protocol described in section 3.2.2, for hexahedral meshing at $30.98\,\mathrm{MHz}$. The exact number of mesh cells varied

depending on the complexity and depth of the multi-layer coil, local meshing of the multi-layer design was implemented with minimum meshing density criteria to capture coils with tighter curvatures. Typically, 3 to $8\,\mathrm{million}$ mesh cells were required for the simulation. The tuning and matching was performed manually post-simulation using the 'co-simulation' feature; whilst automated matching to $50\,\Omega$ is possible, the coupled nature of tuning and matching, and multiple resonances of the multi-layer structure, meant it was not feasible to automatically tune and match the coil to the correct resonance. Automated parameter sweeping was not possible, as manual input needed to be made after each simulation for coil tuning. This limited the extensiveness of the parameter sweep, and full sweeps of every parameter were unfeasible.

5.3.1.1 Field Uniformity versus Efficiency

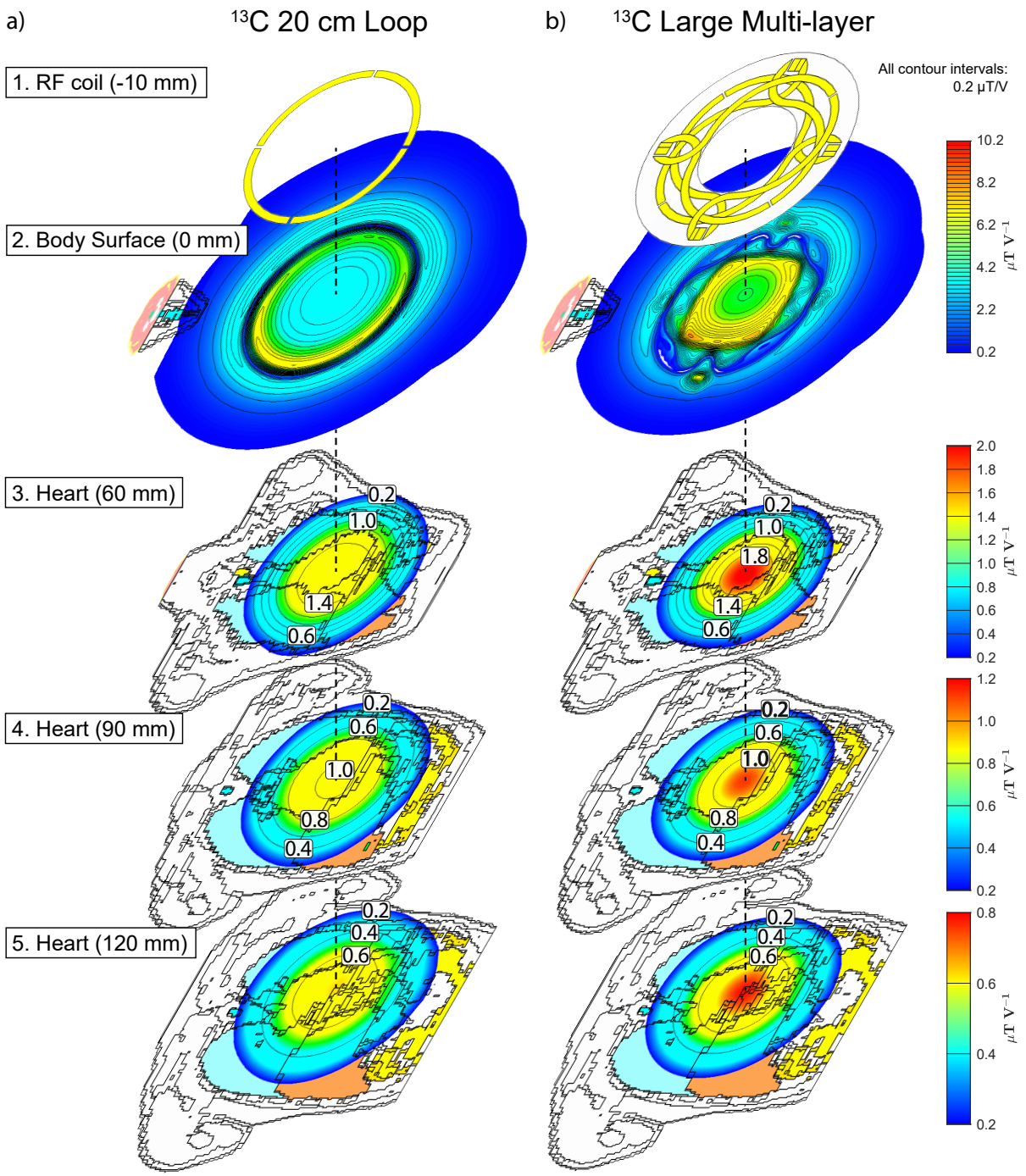

Figure 5.5: 2D simulated B_1^+ of 20 cm loop (a) and large multi-layer coils (b) at four depths corresponding to the reprsentation in Figure 5.4: $0\,\mathrm{mm}$ (body surface), $60\,\mathrm{mm}$ (top of heart), $90\,\mathrm{mm}$ (middle of heart), and $120\,\mathrm{mm}$ (bottom of heart), with $0.2\,\mu\mathrm{T\,V^{-1}}$ contours.

The B_1 field strength from a single RF element sharply falls off away from the coil centre. Typically the 2D field profile is captured to compare against different coils, as an example, the

20 cm diameter loop with parameters [$R = 100\,\mathrm{mm}$, $W = 10\,\mathrm{mm}$] was compared against a multi-layer coil of comparable size with parameters [$R1 = 90\,\mathrm{mm}$, $R2 = 40\,\mathrm{mm}$, $O = -18\,\mathrm{mm}$, $W = 10\,\mathrm{mm}$, $N = 4$], in Figure 5.5. This figure shows the 2D field at approximately the anterior wall of the heart ($60\,\mathrm{mm}$ from the surface of the body), the middle of the heart ($90\,\mathrm{mm}$ from the surface of the body), and the posterior wall of the heart ($120\,\mathrm{mm}$ from the surface of the body). Whilst it is clear that the multi-layer coil achieves higher B_1^+ values throughout the three slices, it is not clear whether a slightly smaller or larger multi-layer coil would have offered a fairer comparison with regards to the coil FOV. For optimisation of a coil design, numerous different coils are compared, as such, it is necessary to condense the 2D field profile information into single values that could be easily compared. An efficient method of comparing the field profile of coils is displaying the two competing factors: B_1^+ uniformity and B_1^+ efficiency. A plot of these two competing factors provides a direct visualisation of their trade-off, summarises the coil EM field profile, and allows clear identification of the optimal coil design within a given coil geometry.

To construct this plot from simulated results, in this setup the ROI is taken as the heart voxels, and field values are exported across the heart volume at $2\,\mathrm{mm}$ resolution. Subsequently calculations for B_1^+ uniformity and B_1^+ efficiency are performed, as described previously, and condensed as a single point on a plot of B_1^+ uniformity against B_1^+ efficiency. Additionally, B_1^+ uniformity versus B_1^+ efficiency curves can be generated by sweeping a parameter, such as coil radius, as shown below in Figure 5.6. This is a compact method of visualising and comparing the trade-off between coil designs.

5.3.2 Parameter Sweep Results

Within the constraint of the Ω conductor shape, each conductor is made of two peripheral arcs of radius $R2$, connected to a central loop of radius $R1$. $R1$ and $R2$ were swept through at $5\,\mathrm{mm}$ intervals, with EM simulations performed at representative combinations of $R1$ and $R2$, to generate a B_1 field uniformity versus efficiency curve. The uniformity versus efficiency curve was then compared to the curve achieved from a sweep of conventional loop coil radii. The ratio of $R1$ and $R2$ determines the ratio of the central region and peripheral region areas, whilst the sum of $R1$ and $R2$ determines the dimensions of the outer extent of the coil. Initial testing suggested that the offset, O, is highly dependent on $R2$, and it was determined that the optimal

overlap for maximum field uniformity-efficiency (which increases the peripheral region area and reduces the conductor overlap), is the maximum overlap allowed by $R2$. Finally, an N of four and six conductor layers were investigated separately. The effect of the width, W, is explored later in section 5.3.3.1 with alternative conductor designs.

5.3.2.1 Transmit Optimisation

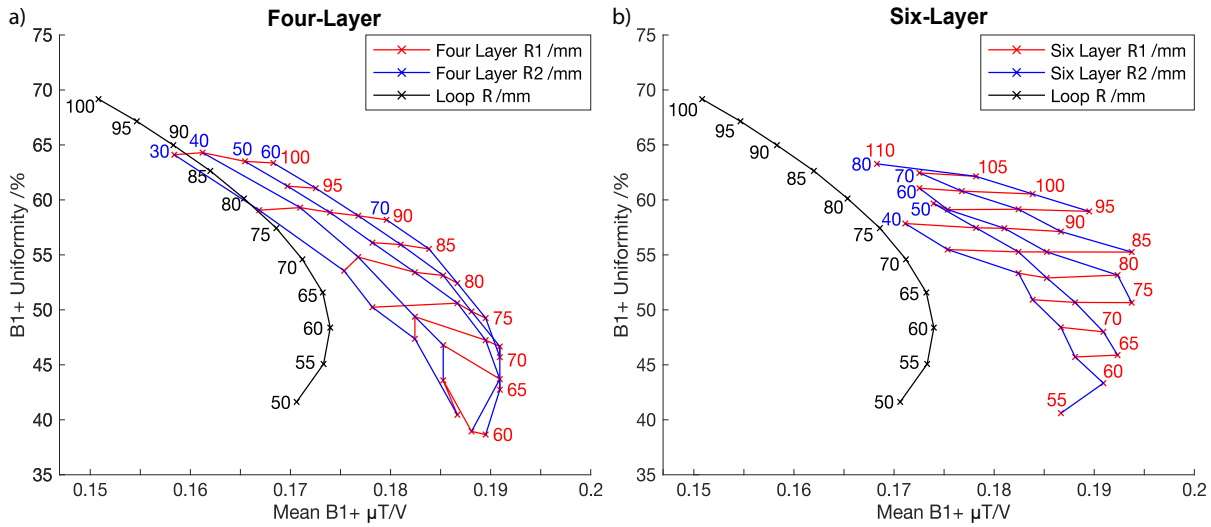

Figure 5.6: Simulated mean B_1^+ versus B_1^+ uniformity plot of four-layer (a) and six-layer (b) multi-layer coil $R1$ and $R2$ parameter sweeps compared to conventional loops. Constant $R1$ isolines are shown in red, constant $R2$ isolines are shown in blue, and loop radius is shown in black.

A single field efficiency-uniformity curve was generated from conventional single loops of radius 50 to $100\,\mathrm{mm}$ every $5\,\mathrm{mm}$, spanning the common human coil dimensions. The field efficiency-uniformity curves for transmit performance are shown in Figure 5.6. The red lines represent constant $R1$ isolines, such that the points along a given red line have a fixed $R1$ with varying $R2$ value determined by the intersection with the blue lines. Conversely, the blue lines represent constant $R2$ isolines, such that the points along a given blue line have fixed $R2$ with varying $R1$. As conventional single loops are represented by only the radius, R, the black lines represent sweeping R values. A maximum peak B_1 efficiency of $0.174\,\mu\mathrm{T\,V^{-1}}$ with corresponding B_1 uniformity of $48.4\,\%$ was achieved by the loop coil of radius $60\,\mathrm{mm}$. The four-layer multi-layer design showed increases in field efficiency for a given uniformity compared to conventional loops. With the four-layer multi-layer design, a peak field efficiency of $0.191\,\mu\mathrm{T\,V^{-1}}$ and corresponding B_1 field uniformity of $48.8\,\%$ was achieved with

an $R1 = 75\,\mathrm{mm}$, an $R2 = 70\,\mathrm{mm}$, and an $O = 40\,\mathrm{mm}$; this represents a $9.8\,\%$ increase in mean B_1^+ compared to the maximum B_1^+ conventional coil design. The six-layer multi-layer designs showed greater field efficiency and uniformity improvements over the four-layer multi-layer design and conventional loops. In this case, $R1$ values higher than what is presented in figure 5.6 were unable to be achieved due to spatial constraints. A peak field efficiency of $0.194\,\mu\mathrm{T\,V^{-1}}$ and corresponding B_1 field uniformity of $55.3\,\%$ was achieved with an $R1 = 85\,\mathrm{mm}$, an $R2 = 70\,\mathrm{mm}$, and an $O = 30\,\mathrm{mm}$; this represents an $11.4\,\%$ increase in mean B_1^+ as well as a $7\,\%$ increase in comparison to the optimum conventional coil design.

An increase in $R1$ increases B_1 field uniformity but decreases B_1 field efficiency as well as receive sensitivity for a corresponding $R2$, whilst an increase in $R2$ increases the B_1 field efficiency without a corresponding decrease in B_1 uniformity for a given $R1$. $R1$ determines the size of the central region; a larger $R1$ leads to a larger overall coil, representing the expected field uniformity-efficiency curve as that of a conventional loop. However, this curve is shifted towards a higher B_1 efficiency due to higher magnetic field density in the overlapping central region. The B-field formed in peripheral regions from the Ω design constructively adds to the field from the central region, improving the field uniformity. Overall, these combined effects allow increasing $R2$ to increase the B_1^+ efficiency and receive sensitivity of the coil. In the limit where $R2$ approaches $0\,\mathrm{mm}$, the coil design becomes a stacked solenoid which has been shown to be no more effective than a conventional loop, in section 4.2.1.3.

5.3.2.2 Receive Optimisation

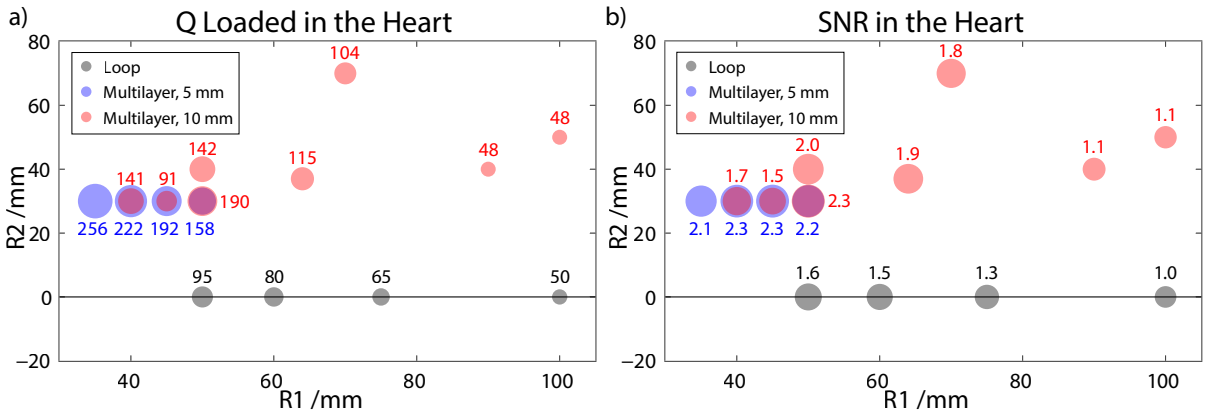

Figure 5.7: Bubble plots showing (a) Q_{Loaded} and (b) SNR values (represented by area) for four layer multi-layer designs of varying $R1$ (x-axis), $R2$ (y-axis) and width of 5 and $10\,\text{mm}$ (shown in blue and red colours respectively), and R of conventional circular loops plotted along the x-axis (shown in black).

Receive RF coil performance was characterised by the relative SNR (normalised such that the smallest SNR is 1), according to equation 2.38, where B_1^- is the anticlockwise rotating component of the B_1 field, and Q_{Loaded} is the Quality (Q) factor. As above, the three parameters: $R1$, $R2$ and O were investigated, with the additional conductor width, W, at $5\,\text{mm}$ and $10\,\text{mm}$. The conventional loop coil optimised for SNR has a radius of $50\,\text{mm}$, and achieved a mean B_1^- of $0.171\,\mu\text{T}\,\text{V}^{-1}$, Q_{Loaded} value of 95.28 and a relative SNR of 1.67. For four-layer multi-layer coils, the highest SNR was achieved with a coil of $R1 = 40\,\text{mm}$, $R2 = 30\,\text{mm}$, $O = 10\,\text{mm}$, $W = 5\,\text{mm}$, and yielded a mean B_1^- of $0.164\,\mu\text{T}\,\text{V}^{-1}$, a Q_{Loaded} value of 191.8 and a relative SNR of 2.47, which represents a $101\,\%$ increase in resonance efficiency and a $47.9\,\%$ increase in SNR over the optimum loop coil. Whilst further SNR gain may be achieved with six-layers, this was not investigated at the time due to time constraints. As smaller coils exhibit higher loaded Q-values, the optimum receive coil is smaller than the optimum transmit coil. An increase in $R1$, leading to a larger overall coil, decreases the SNR as expected. $R2$ determines the size of the peripheral region, and a larger $R2$ leads to less conductor overlap, thus less EM shielding and losses from proximity effects. A high Q design is achieved with the increased inductance from numerous layers.

Overall, the multi-layer coil design shows improvements in both transmit and receive performance when compared against loop coils of comparable sizes. As such, across all coil foot-

prints, for a given field uniformity, at least one multi-layer coil can directly replace conventional loops for improved B_1^+ and SNR.

5.3.3 Alternative Conductor Designs

To further reduce the losses from proximity effects and EM shielding of lower conductor layers, two alternative conductor designs were investigated beyond a 2D conductor of constant width. Section 5.3.3.1 details EM simulations of a multi-layer coil with tapered conductors. Additionally, motivated by on-going debate as to whether cylindrical or tape conductors offer better coil performance, section 5.3.3.2 compares cylindrical and tape conductors of comparable width through simulation of multi-layer coils.

5.3.3.1 Tapered Conductor

The transmit and receive performance on-axis for multi-layer coils of uniform conductor widths were compared against a tapered multi-layer design, where the conductor width was reduced from $10\,\mathrm{mm}$ to $5\,\mathrm{mm}$ in regions of direct conductor overlap. A tapered design reduces the area of conductor overlap, reducing areas of high resistance. However, there is a trade-off as the reduction in conductor track width reduces surface area, thus increasing resistance from the skin effect. Frequency domain EM simulations were performed; finite element methods were used with (approximately $200\,000$) tetrahedral mesh cells used to better capture the curvature of the coil. The conductor was modelled as a standard $0.07\,\mathrm{mm}$ ($2\,\mathrm{oz}$) depth annealed copper. Four different multi-layer coil conductor designs, shown in Figure 5.8, were simulated in both the loaded state (with the coil element positioned $10\,\mathrm{mm}$ from a phantom with dielectric properties that represent human loading) and the unloaded state (with only the coil element itself).

1. Tapered $5\,\mathrm{mm}$ and $10\,\mathrm{mm}$ conductor widths ($10\,\mathrm{mm}$ in non-overlap regions, $5\,\mathrm{mm}$ in overlap regions)
2. Uniform $5\,\mathrm{mm}$ conductor width
3. Uniform $7.5\,\mathrm{mm}$ conductor width
4. Uniform $10\,\mathrm{mm}$ conductor width

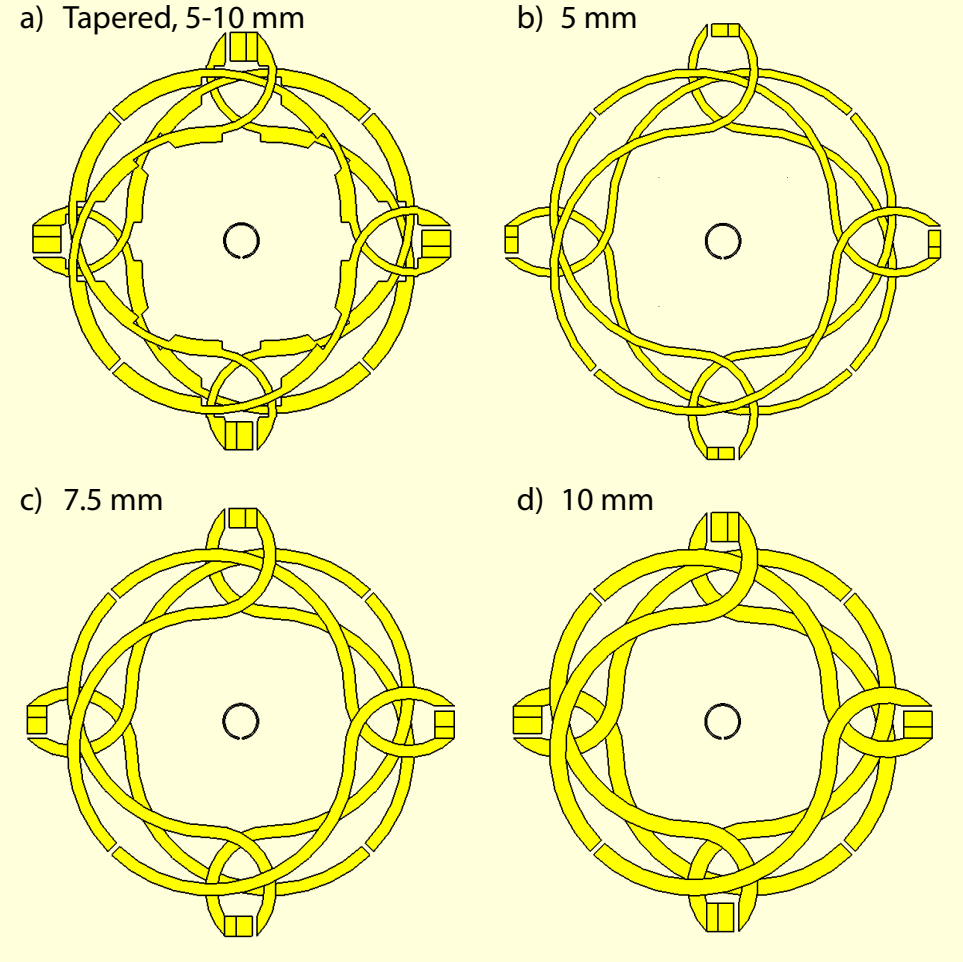

Figure 5.8: EM Model showing the conductor design of four multi-layer coils. (a) Tapered design with $10\,\mathrm{mm}$ width copper tape in non-overlapping copper regions, and $5\,\mathrm{mm}$ width in overlapping copper regions. (b) Uniform design with $5\,\mathrm{mm}$ width copper tape. (c) Uniform design with $7.5\,\mathrm{mm}$ width copper tape. (d) Uniform design with $10\,\mathrm{mm}$ width copper tape.

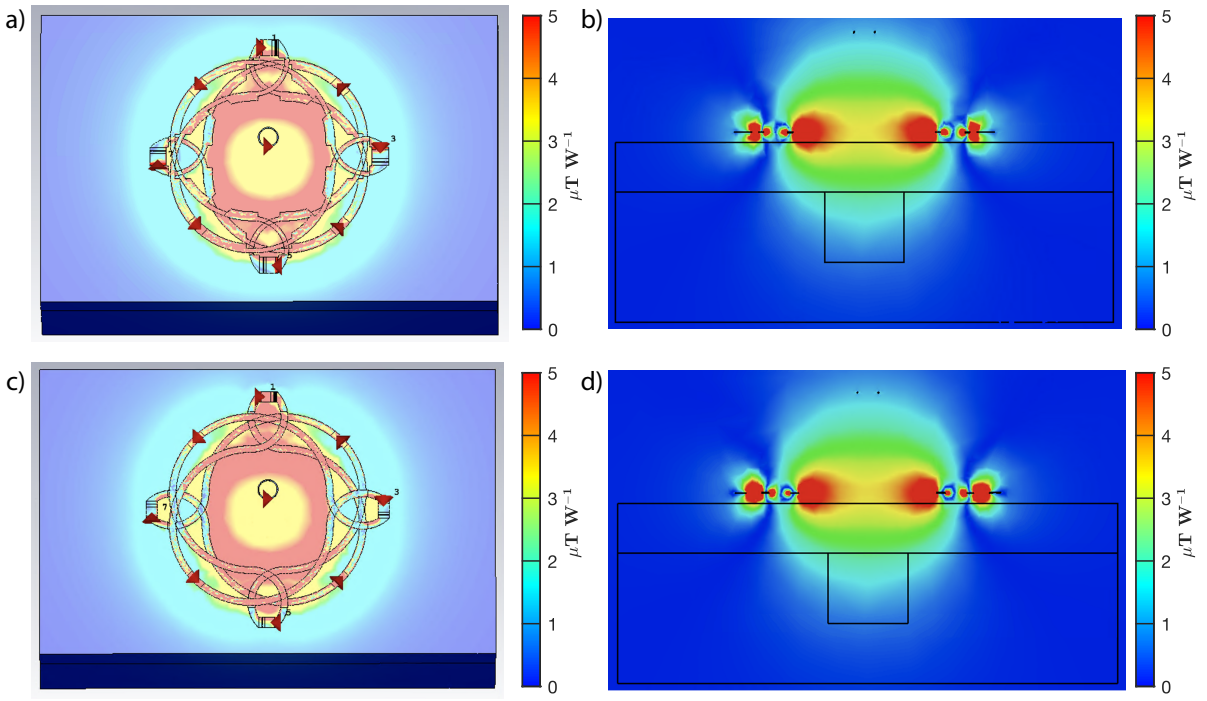

Figure 5.9: Surface and cross-section B_1^+ fields of multi-layer coils with tapered and uniform conductor track widths. (a) Surface B_1^+ for tapered conductor of width $5\,\mathrm{mm}$ and $10\,\mathrm{mm}$. (b) Cross-section B_1^+ tapered conductor of width $5\,\mathrm{mm}$ and $10\,\mathrm{mm}$. (c) Surface B_1^+ for uniform conductor of width $7.5\,\mathrm{mm}$. (d) Cross-section B_1^+ for uniform conductor of width $7.5\,\mathrm{mm}$.

Visually, the surface and cross-section B_1^+ field profiles between the tapered and $7.5\,\mathrm{mm}$ uniform conductors are similar showing no adverse effects to the homogeneity, with the tapering design as shown in Figure 5.9. From Figure 5.10 showing the on-axis B_1^+ of the four coils, the transmit performance from the tapered multi-layer coil design at the coil centre is $7.2\,\%$ lower than a uniform conductor of width $10\,\mathrm{mm}$, and very similar ($1.9\,\%$ lower) to a uniform conductor width of $7.5\,\mathrm{mm}$. The highest B_1^+ was achieved with a uniform conductor width of $10\,\mathrm{mm}$, with the B_1^+ decreasing as conductor width decreases; this result is likely due to the thinner conductors leading to current crowding.

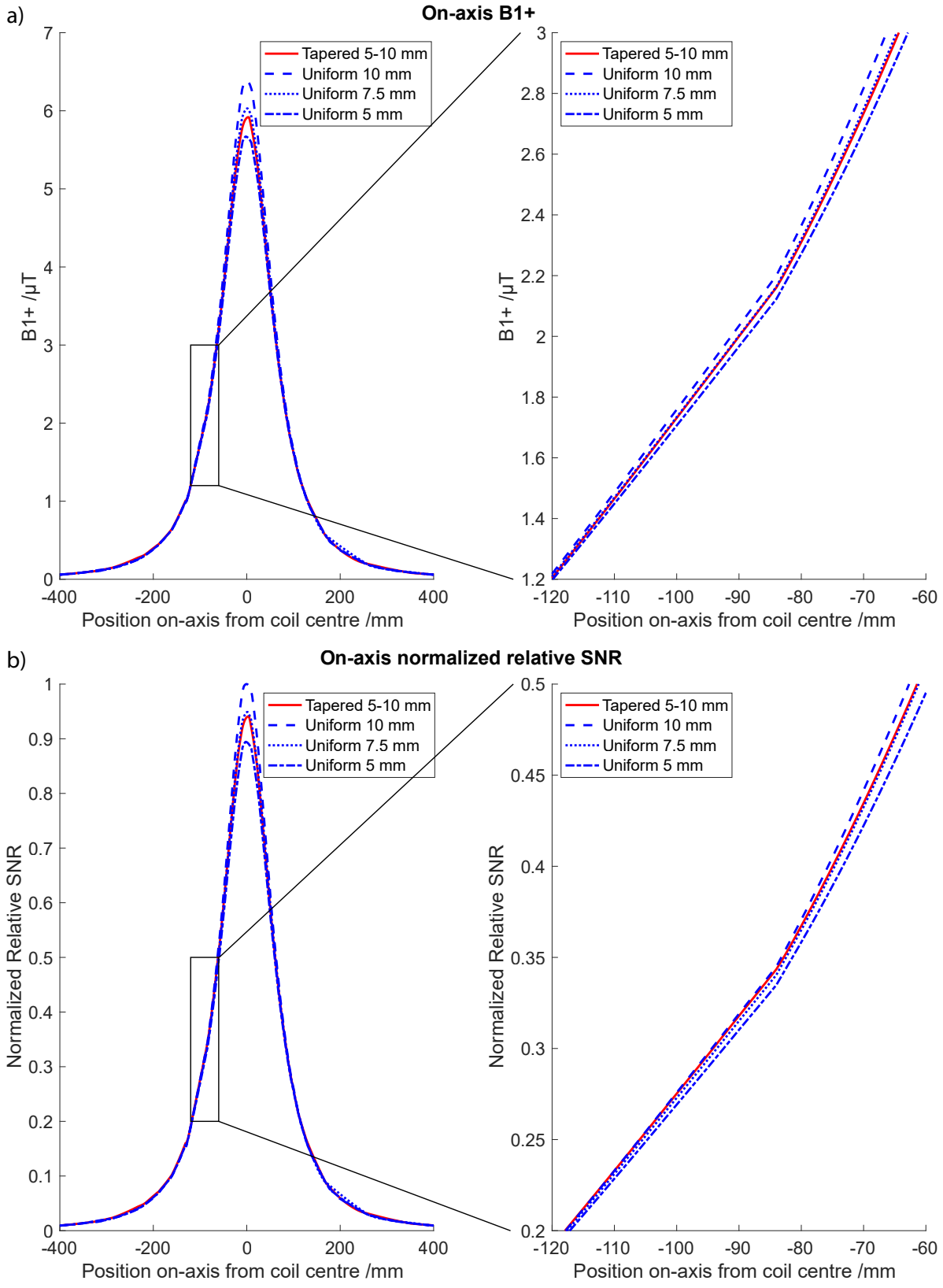

Figure 5.10: On-axis B_1^+ and SNR plots for loop and multi-layer coils with tapered and uniform conductor widths, through the coil centre. (a) B_1^+ plots for 1 W stimulation into coil (left), with zoomed in section of plot (right). (b) Normalised relative SNR plot (left), with zoomed in section of plot (right).

Table 5.1: Summary of $Q_{\text{Unloaded}}/Q_{\text{Loaded}}$ and R_{Coil} normalised by R_{Sample} for uniform and tapered multi-layer conductor designs. In addition, $R_{\text{Total}}/R_{\text{Sample}}$ can be calculated as $R_{\text{Coil}}/R_{\text{Sample}}$ $+1$.

Copper Tape	$Q_{\text{Unloaded}}/Q_{\text{Loaded}}$	$R_{\text{Coil}}/R_{\text{Sample}}$
Uniform $10\,\text{mm}$	6.082	0.197
Uniform $7.5\,\text{mm}$	6.318	0.188
Uniform $5\,\text{mm}$	6.479	0.183
Tapered 5 – $10\,\text{mm}$	7.088	0.164

The relative SNR was calculated from EM simulations, by assuming the sample resistance was the same for all coils. This is a valid assumption as all four multi-layer coils exhibit an approximately similar FOV. This assumption allowed the relative total resistance to be calculated from the simulated loaded and unloaded Q-values. SNR was calculated from Q-factors, converted to resistances, as listed in Table 5.1. The corresponding on-axis SNR plot shows minor improvements compared to B_1^+ in the tapered conductor design, as this design offers the lowest coil resistance, which translates to the lowest total resistance, and therefore a higher Q-loaded value. This increase in Q-loaded however still does not sufficiently offset the poor B_1^-. Hence, the SNR (proportional to the B_1^- and the square root of Q-loaded) is still degraded. SNR performance of the tapered multi-layer design at the coil centre is $5.9\,\%$ lower than the $10\,\text{mm}$ conductor, and $0.9\,\%$ lower than the $7.5\,\text{mm}$ conductor. However, the tapered multi-layer coil does achieve marginally higher SNR at depths beyond $80\,\text{mm}$, which is our region of interest. The results indicate that the additional complexity associated with tapering may not be worthwhile to pursue for this set of parameters. Whilst the receive performance of the tapered design is marginally improved, due to a decrease in coil resistance, the difference is minimal, as the desired decrease in proximity effect from the overlapped area was most likely offset by a similar undesired decrease in surface area restricting current flow.

5.3.3.2 Cylindrical Conductor

The transmit and receive performance on-axis for both single loop coil designs and multi-layer coil designs with hollow cylindrical conductors were compared against conventional uniform-width tape conductors. Ideally, cylindrical rod conductors will increase the conductor surface area by a factor of π compared to tape conductors (with width of equal diameter to the rod), for the same amount of EM shielding in a projection of the coil plane. From previous litera-

ture, benchtop measurements of cylindrical and tape conductor designs suggest that cylindrical conductors improve Q at lower frequencies (work done in the region of $0.5\,\mathrm{T}$ $^1\mathrm{H} \approx 20\,\mathrm{MHz}$) [5, 6] without substantially altering the coil inductance, however with diminishing returns at higher frequencies (over $3\,\mathrm{T}$ $^1\mathrm{H}$, equivalent to over $120\,\mathrm{MHz}$ [7]). In our multi-layer design, we believe that cylindrical conductors boasting a greater surface area and smaller overlapping regions will lead to a reduction in current crowding, and correspondingly lower losses from proximity effects. However, the clear primary drawback to using cylindrical conductors is the increased vertical size of the coil, from a total four-layer multi-layer thickness of approximately $4\,\mathrm{mm}$ to $44\,\mathrm{mm}$ (with $1\,\mathrm{cm}$ diameter cables), requiring significantly more space, and bringing the effective centre of the coil further from the sample. This could be alleviated by using flexible cylindrical conductors, or exploring other 'vertical' conductor geometries. However, due to the increased complexity of the model required for flexibility, this was not taken into account in the EM simulations.

Frequency domain EM simulations were performed using finite element methods, with approximately $200\,000$ tetrahedral mesh cells for tape conductors and $500\,000$ tetrahedral mesh cells for cylindrical conductors. Four single loop coil simulations were performed, with 15 cm diameter conventional single loop coil designs compared to two larger multi-layer coils. The 15 cm diameter loop coil was chosen to give the optimum on-axis B_1^+ performance for loop coils. The larger multi-layer coil achieves both improved field uniformity and efficiency compared to the 15 cm loop. The models include two loop coils constructed from $5\,\mathrm{mm}$ and $10\,\mathrm{mm}$ width tape conductors, two loop coils constructed from $5\,\mathrm{mm}$ and $10\,\mathrm{mm}$ diameter cylindrical conductors, and two multi-layer coils constructed from $10\,\mathrm{mm}$ width tape and $10\,\mathrm{mm}$ diameter cylinders, as shown in Figure 5.11. For all six cases, coil designs were simulated in both the loaded state (with a coil element positioned on a phantom with dielectric properties of muscle tissue) and the unloaded state (with only the coil element itself). The cylindrical conductor was simulated with a wall thickness of $1\,\mathrm{mm}$, whilst the tape conductor was simulated with a standard depth of $0.07\,\mathrm{mm}$ ($2\,\mathrm{oz}$ copper), both modelled as annealed copper.

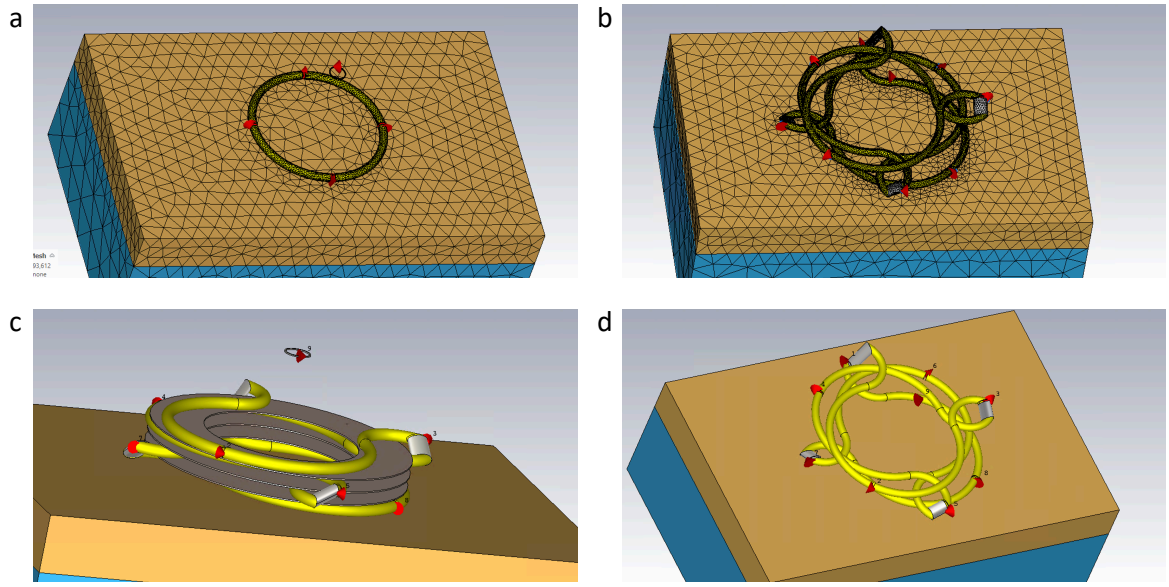

Figure 5.11: EM model for cylindrical conductor RF coils. (a) $10\,\mathrm{mm}$ cylindrical conductor loop coil with tetrahedral meshing. (b) $10\,\mathrm{mm}$ cylindrical conductor four-layer multi-layer coil with tetrahedral meshing. (c) Multi-layer coil image with 'pick-up probe' and polyimide dielectric insulators between layers. (d) Multi-layer coil image with segments of PEC connection between layers.

As the physical extent of all four single loop coils are approximately identical, sample resistance was assumed to be the same across all simulations. Similarly, for the two multi-layer coils, sample resistance was assumed to be the same. The thickness of the coil varied, with the cylindrical conductor loop coils of thickness $10\,\mathrm{mm}$, and the cylindrical conductor multi-layer coil of thickness $44\,\mathrm{mm}$, with each layer stacked vertically and separated by a $1\,\mathrm{mm}$ thick dielectric insulator (polyimide).

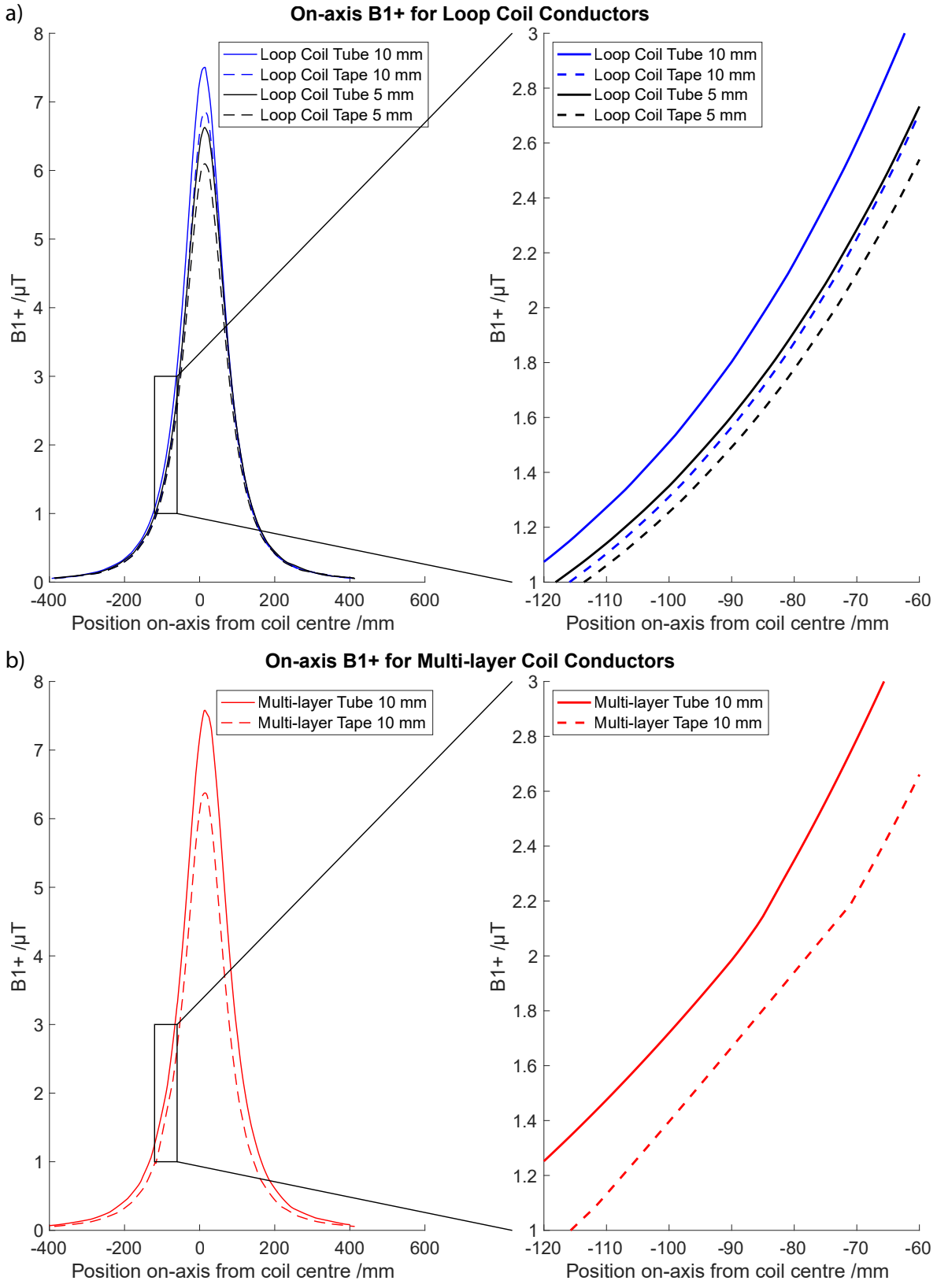

Figure 5.12: On-axis B_1^+ plots for loop and multi-layer coils with cylindrical and tape conductors, through coil centre. (a) B_1^+ plots for 1 W stimulation into loop coils, and zoomed in section of B_1^+ plot for loop coils. (b) B_1^+ plots for 1 W stimulation into multi-layer coils, and zoomed in section of B_1^+ plot for loop coils.

For loop coils, the on-axis B_1^+ at the coil centre is shown to increase by $9.4\,\%$ when going from a $10\,\mathrm{mm}$ width tape to a $10\,\mathrm{mm}$ diameter cylinder, and increase by $8.7\,\%$ from a $5\,\mathrm{mm}$ width tape to a $5\,\mathrm{mm}$ diameter cylinder. Similar improvements at depth, for both $10\,\mathrm{mm}$ and $5\,\mathrm{mm}$ cases, are shown in 5.12. The $10\,\mathrm{mm}$ diameter cylindrical conductors performed better than the $5\,\mathrm{mm}$ diameter cylindrical conductors due to a larger surface area for current flow. For the multi-layer designs, greater improvements in transmit are seen with a $19.8\,\%$ increase from a $10\,\mathrm{mm}$ width tape to a $10\,\mathrm{mm}$ diameter cylinder. The 15 cm diameter loop coil was chosen for comparison because the on-axis B_1^+ of the multi-layer with $10\,\mathrm{mm}$ tape conductor is comparable to the on-axis B_1^+ of the loop coil with $10\,\mathrm{mm}$ tape. Thus we can assume a $19.8\,\%$ increase from the loop coil $10\,\mathrm{mm}$ tape to the multi-layer $10\,\mathrm{mm}$ cylinder. Visually the surface and cross section B_1^+ field profile (Figure 5.13) for the multi-layer design with a cylindrical conductor is vastly improved compared to the tape conductor, despite the increased coil thickness and further effective coil centre to our region of interest

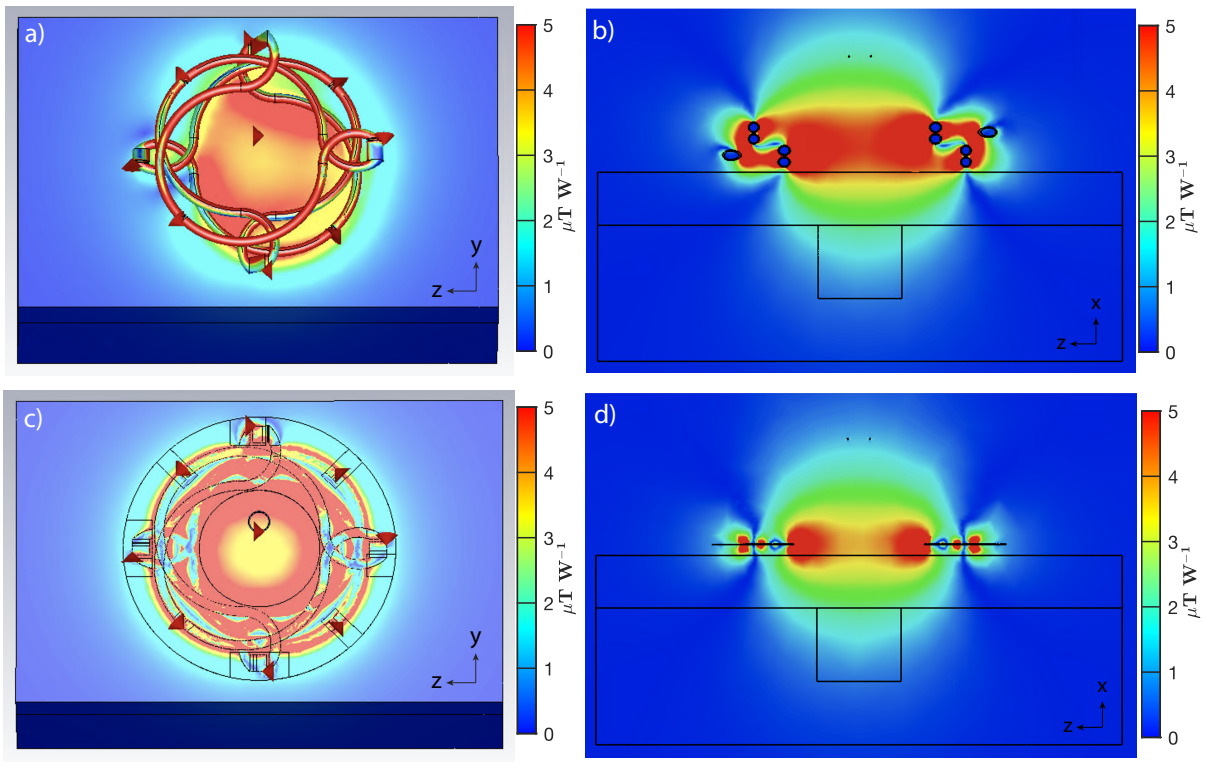

Figure 5.13: Surface and cross-section B_1^+ fields of multi-layer coil with tape and cylindrical conductors. (a) Surface B_1^+ for $10\,\mathrm{mm}$ cylindrical conductor. (b) Cross-section B_1^+ for $10\,\mathrm{mm}$ cylindrical conductor. (c) Surface B_1^+ for $10\,\mathrm{mm}$ tape conductor. (d) Cross-section B_1^+ for $10\,\mathrm{mm}$ tape conductor.

SNR was calculated from the B_1^- and Q-factors measured in Table 5.2. The corresponding

1D SNR plots through the coil central axis is shown in Figure 5.14. For loop coils, the corresponding on-axis SNR show the receive performance at the coil centre is increased by $11.1\,\%$ from a $10\,\mathrm{mm}$ width tape to a $10\,\mathrm{mm}$ diameter cylinder, and increased by $15.0\,\%$ from a $5\,\mathrm{mm}$ width tape to a $5\,\mathrm{mm}$ diameter cylinder. Greater improvements in receive performance were seen with the multi-layer coil, at the coil centre with a $26.6\,\%$ increase in SNR from the $10\,\mathrm{mm}$ width tape to a $10\,\mathrm{mm}$ diameter cylindrical conductor. For both coil designs, we believe the increase in SNR over B_1^+ with a cylindrical conductor was due to reduced coil noise from the increased surface area, as shown in Table 5.2.

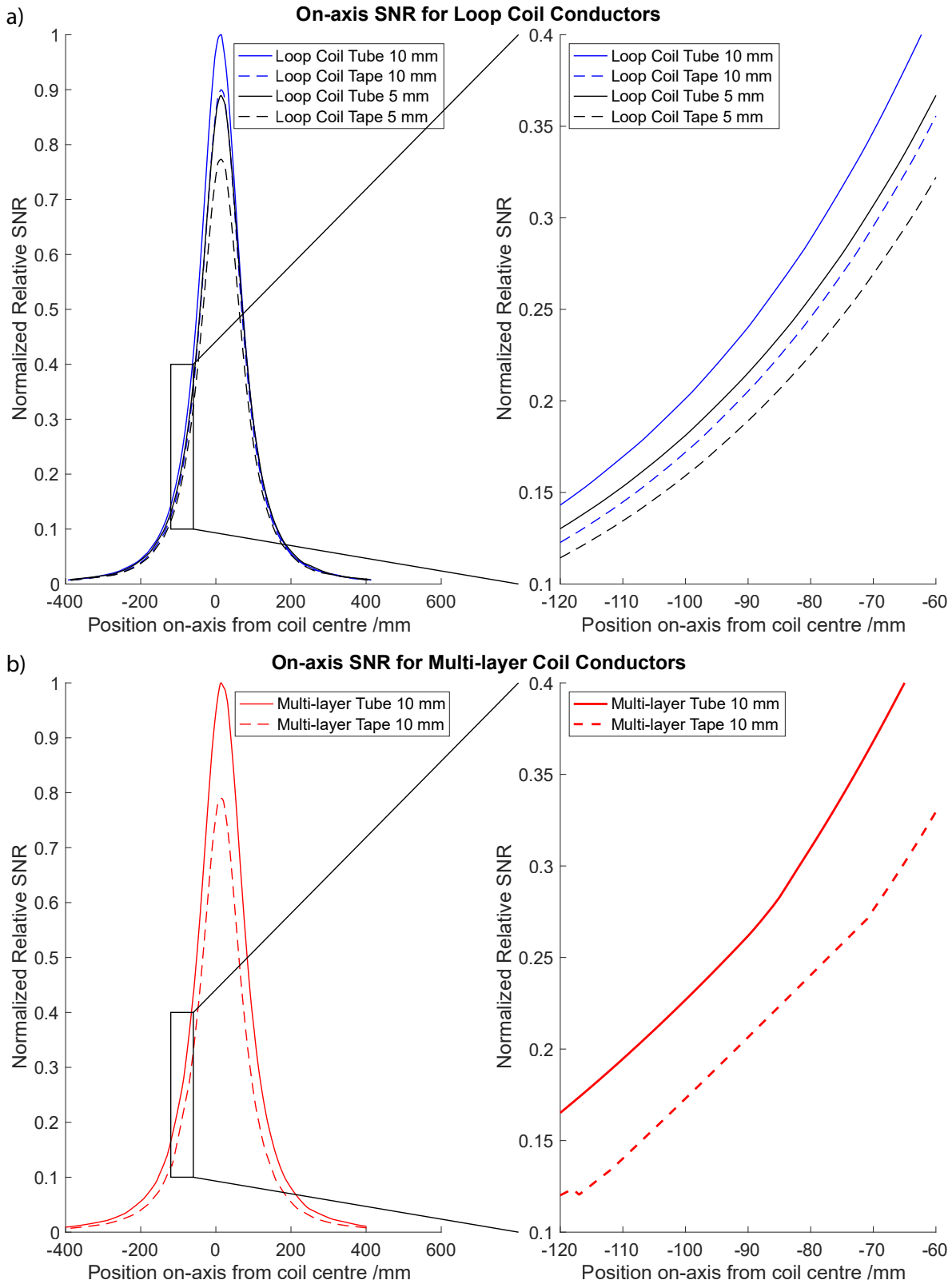

Figure 5.14: On-axis SNR plots for loop and multi-layer coils with tapered and uniform conductor widths, through coil centre. (a) Normalised relative SNR plot of loop coils (left), with zoomed in section of plot (right). (b) Normalised relative SNR plot of multi-layer coils (left), with zoomed in section of plot (right).

Table 5.2: Summary of $Q_{\text{Unloaded}}/Q_{\text{Loaded}}$ and $R_{\text{Coil}}/R_{\text{Sample}}$ values for cylindrical and tape conductors for both multi-layer and loop coil designs. Similarly, $R_{\text{Total}}/R_{\text{Sample}}$ can be calculated as $R_{\text{Coil}}/R_{\text{Sample}}$ $+1$.

Conductor Type	$Q_{\text{Unloaded}}/Q_{\text{Loaded}}$	$R_{\text{Coil}}/R_{\text{Sample}}$
Multi-layer Cylinder $10\,\text{mm}$	21.363	0.049
Multi-layer Tape $10\,\text{mm}$	6.267	0.190
Loop Coil Cylinder $10\,\text{mm}$	3.832	0.353
Loop Coil Tape $10\,\text{mm}$	3.524	0.396
Loop Coil Cylinder $5\,\text{mm}$	3.992	0.334
Loop Coil Tape $5\,\text{mm}$	3.022	0.494

In summary, the cylindrical conductor improves both transmit and receive performance for surface coils. Greater improvements were seen in general for receive due to the reduced coil resistance over tape conductors. In particular, for the multi-layer design, a significantly larger reduction in coil resistance was seen due to the reduction in proximity effects, which corresponded to a greater increase in receive performance. The coil thickness could be alleviated with flexible cylindrical conductors, whilst bringing the effective coil centre closer to the ROI. With regards to construction of a cylindrical conductor RF coil, there are currently single loop coil designs which use high impedance co-axial cables; however, there has been no work on multiple layers. Alternative 3D conductor geometries may be used to provide advantages to the coil design, such as the use of a flattened cylinder, which would reduce the vertical dimension of the coil, although a cylinder was simulated due to ease of modelling. Despite the theoretical improvements, due to the limited time of this project, cylindrical multi-layer prototypes were not constructed, although it is a promising avenue for future work.

5.4 Human Multi-layer Prototype Coils

Based on the promising results from the EM simulations above, the next step was the construction of a series of prototype multi-layer coils for X-nuclei MRI on a $3\,\text{T}$ Siemens Tim Trio MRI whole body human system. The multi-layer coils were characterised through field maps obtained on the scanner, which allowed verification of the simulated data and quantification of improvements obtained from this novel coil design over conventional loop elements. Such field maps may be obtained on phantoms or a human subjects; in the case of coil characterisation, there are several benefits of initial testing on phantoms over human participants. Phantom scans

allow higher resolution B_1 and SNR maps to be obtained from numerous averages over long scan duration that would be unfeasible with human participants. Additionally, phantom scans are more reproducible and not subject to biological variation as expected from human scans, and a higher RF power can be played out with more relaxed safety limitations. This section presents the construction and phantom testing of multi-layer coils for two nuclei; ^{13}C (section 5.4.1), and ^{31}P (section 5.4.2).

5.4.1 Carbon Multi-layer

Two Tx-Rx multi-layer designs were constructed for ^{13}C cardiac MRI on a clinical $3\,\mathrm{T}$ scanner at 30.98 MHz: a smaller multi-layer coil with an $R1 = 65\,\mathrm{mm}$, an $R2 = 37\,\mathrm{mm}$, and an $O = 15\,\mathrm{mm}$ more optimised for Rx performance, and comparable to a $10\,\mathrm{cm}$ standard loop, and a larger multi-layer coil with an $R1 = 90\,\mathrm{mm}$, an $R2 = 40\,\mathrm{mm}$, and an $O = 18\,\mathrm{mm}$ which was simulated above in Figure 5.5, more optimised for Tx performance, and comparable to a $20\,\mathrm{cm}$ standard loop. To give an idea of where both coils designs lie within the B_1^+ field uniformity-efficiency plot, the simulated B_1^+ trade-off plot for all coils compared in this section are shown in Figure 5.15. From this figure, we can see the small multi-layer design was selected to achieve higher field efficiency whilst still having the uniformity of the highest efficiency loop coil. Additionally, the larger multi-layer design was selected for higher field uniformity whilst still having the field efficiency of the highest efficiency loop coil.

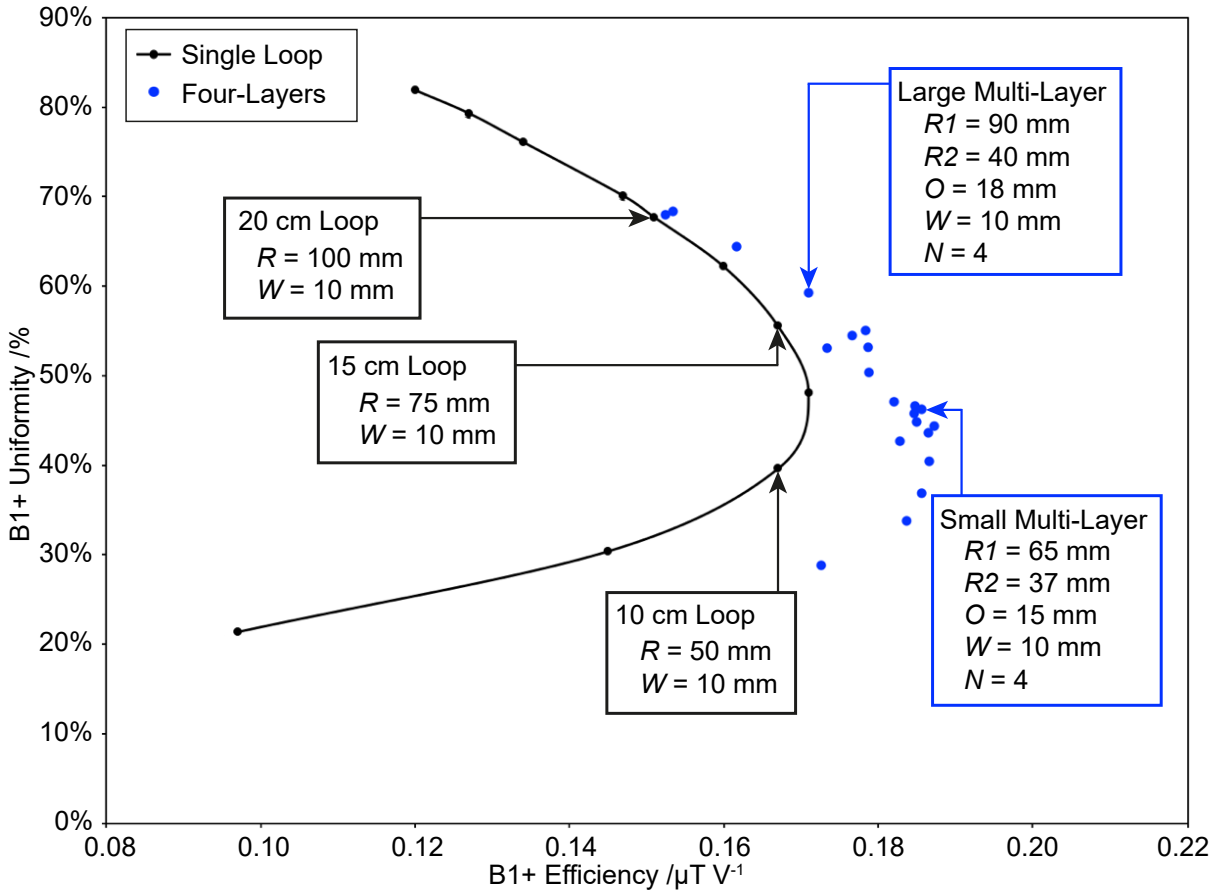

Figure 5.15: B_1^+ efficiency versus uniformity plot for all five constructed ^{13}C coils. The small multi-layer and large multi-layer coils are shown in blue against other comparable multi-layer design parameters. The three conventional single loops of radius 10, 15, and 20 cm are shown in black along a range of diameters.

5.4.1.1 Coil Construction

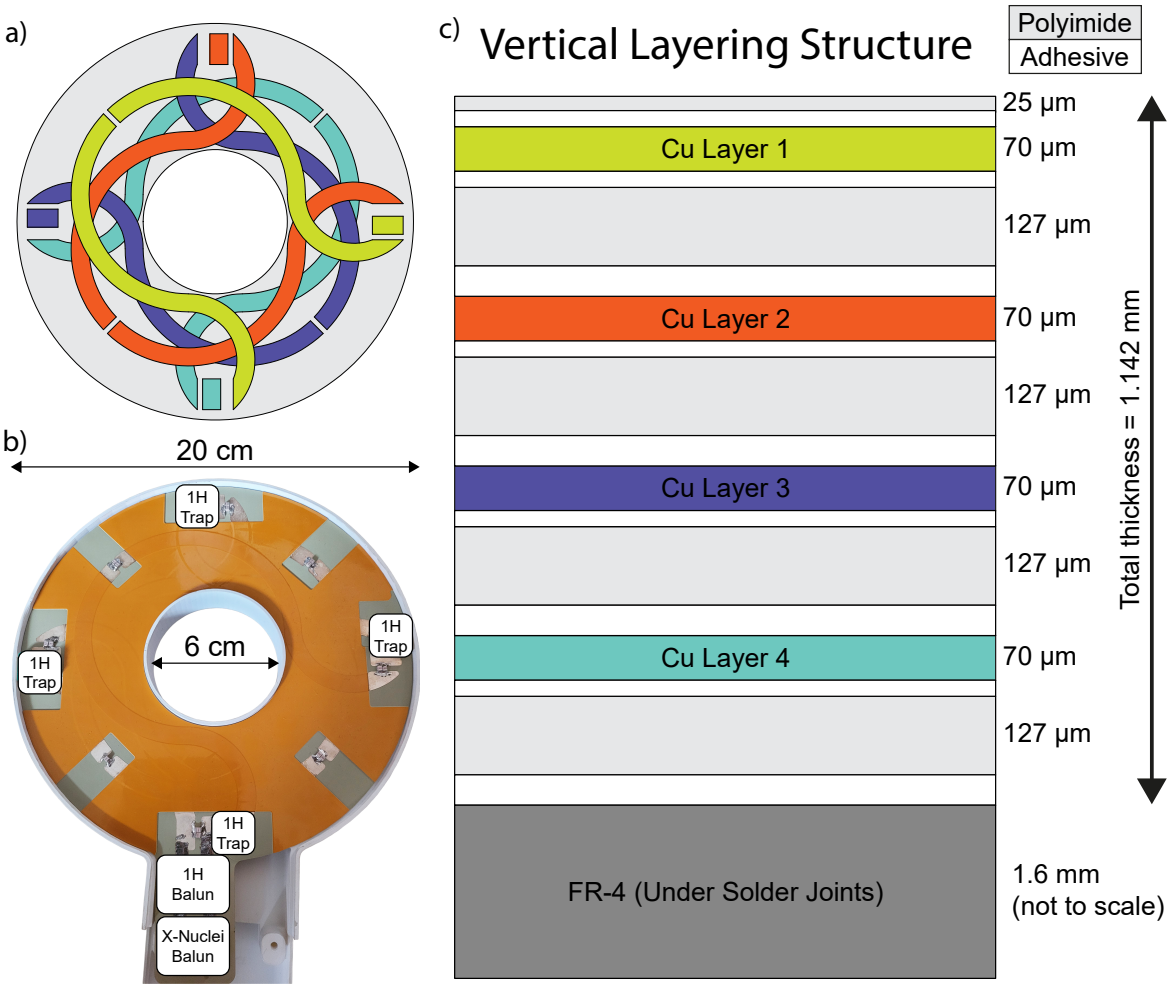

Figure 5.16: Vertical layering structure of both smaller and larger multi-layer PCB. (a) Diagram of conductor overlapping design. (b) Photo of PCB showing position of lumped elements and scale, with conductor covered by polyimide. (c) Layering structure of four individual $0.07\,\mathrm{mm}$ thick copper layers, with a total PCB thickness of $1.142\,\mathrm{mm}$.

The multi-layer PCB consisted of four conductor layers, separated by dielectric insulator layers and adhesive. The dielectric layer was constructed from polyimide tape, specifically $0.127\,\mathrm{mm}$ FR0110 Kapton^{TM} (manufactured by DuPont, Delaware, US). The coil PCBs were designed according to the multi-layer protocol in Appendix E, and fabricated by Flexible Technology Limited (Rothesay, UK). The overall layering structure and coil PCB photo are shown in Figure 5.16. Tin was used to coat solder pads for better adhesion to affix lumped elements such as capacitors. Each dielectric insulation layer comprised of slots cut out from the edge to access solder pads, such that the top layer insulator had all solder pad lots cut out, and each subsequent

layer below had slots cut out for the solder pads that need to be accessed from above. The flexibility of the PCB necessitated structural support underneath the solder pads, to prevent the solder joints from cracking. FR4 pads (which are composed of woven fibreglass cloth with an epoxy resin binder that is flame resistant) of $1.6\,\mathrm{mm}$ thickness were placed beneath the solder joints. The size of the FR4 pads was a balance between supplying sufficient structural support whilst not compromising the flexibility of the overall PCB. Four ^{1}H traps were arranged to bridge between the conductor layers, and one ^{1}H balun and one ^{13}C balun were constructed using PulseTeq's design onto the coil element, to be consistent with the PulseTeq Ltd loop coil design to which the multi-layer coils were compared. Additional ^{1}H bazooka baluns were placed at even separations along the cable to the scanner interface.

The two multi-layer coils were compared to three commercially available loop coils with a range of coverage for cardiac MRI, of $10\,\mathrm{cm}$, $15\,\mathrm{cm}$, and $20\,\mathrm{cm}$. From a dimension perspective, the larger multi-layer coil had a comparable diameter and FOV to the 20 cm loop (consistent with measured B_1 field uniformity), whilst the smaller multi-layer coil had a comparable diameter with the 10 cm loop (similarly consistent with measured B_1 field uniformity). The expected B_1^+ efficiency and uniformity of these simple loop coils is highlighted in Figure 5.18.

5.4.1.2 Scanner and Simulation Setup

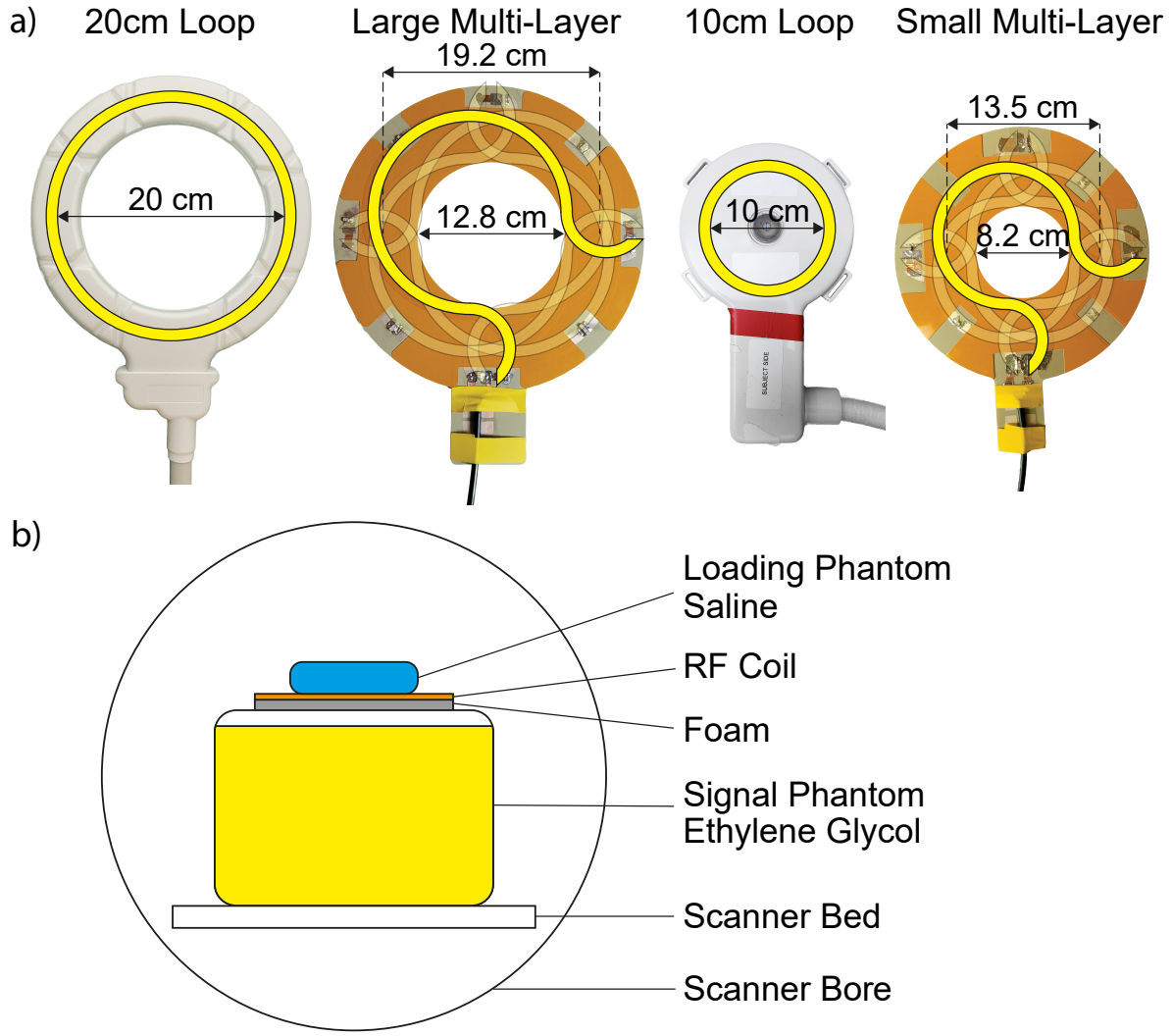

Figure 5.17: ^{13}C phantom experiment setup. (a) photos showing four coil of two comparable sizes with inner conductor track illustrated as the yellow overlay: the 20 cm loop, the large multi-layer, the 10 cm loop and the small multilayer coil. (b) diagram of RF coil setup in scanner with ^{13}C signal phantom of ethylene glycol and loading phantom of saline.

Accurate mapping of the human coil B_1 field profiles on ^{13}C was challenging due to low signal reception of the ^{13}C nuclei and the larger FOV compared to pre-clinical coils. Accurate B_1^+ and SNR maps were obtained using the fully sampled coil characterisation methods described in section 3.4. A series of gradient echo scans with $20\,\mathrm{mm}$ isotropic voxels and sampling voltages at a variable density were performed. To represent a human cardiac scan setup, all coils were positioned $10\,\mathrm{mm}$ above a torso phantom of ethylene glycol (approx. $30\,\mathrm{cm} \times 40\,\mathrm{cm} \times 50\,\mathrm{cm}$) with natural ^{13}C abundance ($0.4\,\mathrm{M}$ ^{13}C), as shown in Figure 5.17. A saline bag was used for

representative dielectric loading, and all coils were checked to be matched to $-20\,\mathrm{dB}$ or better using a network analyzer connected to the coil within the scanner before a scan. A circular ROI was defined, of radius $40\,\mathrm{mm}$, positioned $100\,\mathrm{mm}$ from the surface of the coil along the central axis. The dimension and position of the ROI was motivated from observation of cardiac scans of human subjects, with the distance from the chest wall to the heart typically ranging from $60\,\mathrm{mm}$ (anterior wall) to $140\,\mathrm{mm}$ (posterior wall). Differing from the previous set of EM simulations which were performed on a human voxel model with the ROI taken as the heart voxels, EM simulations in this section are performed on a loading and signal phantom model with a representative dielectric constant, resistivity and conductivity compared with the phantom used. The ROI from the EM simulations was ensured to be consistent with the ROI defined from scanner measurements, of radius $40\,\mathrm{mm}$, centred $100\,\mathrm{mm}$ from the coil central axis. This tailored simulation setup allowed the simulated and measured 2D field maps for the human multi-layer coils to achieve closer agreement compared to the previous pre-clinical multi-layer field maps in section 4.3.2.

5.4.1.3 B1 and SNR Results

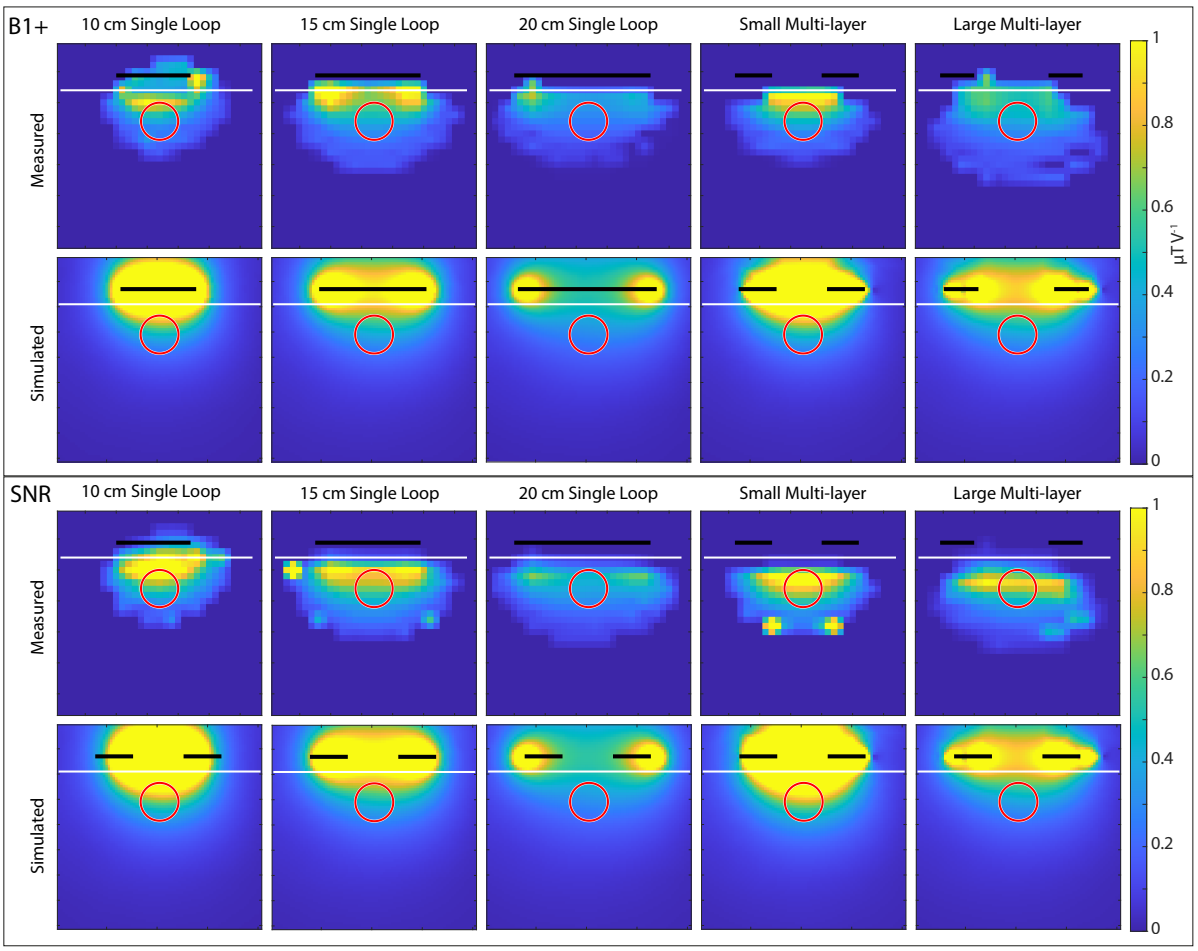

Figure 5.18: 2D field maps of B_1^+ showing transmit performance and SNR showing receive performance, obtained from scanner measurements and EM simulations, for all five coils: 10 cm loop, 15 cm loop, 20 cm loop, small multi-layer, and large multi-layer.

The 2D B_1^+ and SNR maps for all five coils are shown in Figure 5.18, with the summary of the B_1^+ and SNR fields shown in Table 5.3. Here, B_1^+ efficiency is calculated as the mean B_1^+ in $\mu\mathrm{T\,V^{-1}}$, B_1^+ uniformity as a percentage from one minus the coefficient of variation, and mean SNR normalised by peak SNR in ROI across all coils. The full 1D on-axis plots for all coils, both simulated and measured, can be found in Appendix G. Comparing the three conventional loop coils, the smallest 10 cm loop coil achieved a B_1^+ efficiency of $0.433\,\mu\mathrm{T\,V^{-1}}$ (measured) and $0.509\,\mu\mathrm{T\,V^{-1}}$ (simulated), the lowest B_1^+ uniformity of $57.0\,\%$ (measured) and $59.7\,\%$ (simulated), and the highest relative SNR of 0.756 (measured) and 0.867 (simulated). The 15 cm loop achieved a B_1^+ efficiency of $0.435\,\mu\mathrm{T\,V^{-1}}$ (measured) and $0.421\,\mu\mathrm{T\,V^{-1}}$ (simulated), B_1^+ uniformity of $73.8\,\%$ (measured) and $72.5\,\%$ (simulated), and relative SNR of 0.770

(measured) and 0.591 (simulated). The 20 cm loop coil achieved the lowest B_1^+ efficiency of $0.262\,\mu\mathrm{T\,V^{-1}}$ (measured) and $0.310\,\mu\mathrm{T\,V^{-1}}$ (simulated), highest B_1^+ uniformity of $80.4\,\%$ (measured) and $80.7\,\%$ (simulated), and lowest relative SNR of 0.457 (measured) and 0.382 (simulated). Comparing the two multi-layer coils, the larger multi-layer coil achieved a B_1^+ efficiency of $0.393\,\mu\mathrm{T\,V^{-1}}$ (measured) and $0.400\,\mu\mathrm{T\,V^{-1}}$ (simulated), B_1^+ uniformity of $79.9\,\%$ (measured) and $74.1\,\%$ (simulated), and relative SNR of 0.783 (measured) and 0.483 (simulated). The transmit performance: B_1^+ efficiency and uniformity of the larger multi-layer coil is comparable to the 15 cm loop; however, the receive SNR is higher than that of the 15 cm loop and comparable to that of the 10 cm loop. The smaller multi-layer coil achieved a B_1^+ efficiency of $0.497\,\mu\mathrm{T\,V^{-1}}$ (measured) and $0.535\,\mu\mathrm{T\,V^{-1}}$ (simulated), B_1^+ uniformity of $62.8\,\%$ (measured) and $62.7\,\%$ (simulated), and relative SNR of 1.0 (measured) and 1.0 (simulated). It should be noted that the unexpected bright spots in Figure 5.18 are due to poor curve fitting at specific voxels which have been up-sampled.

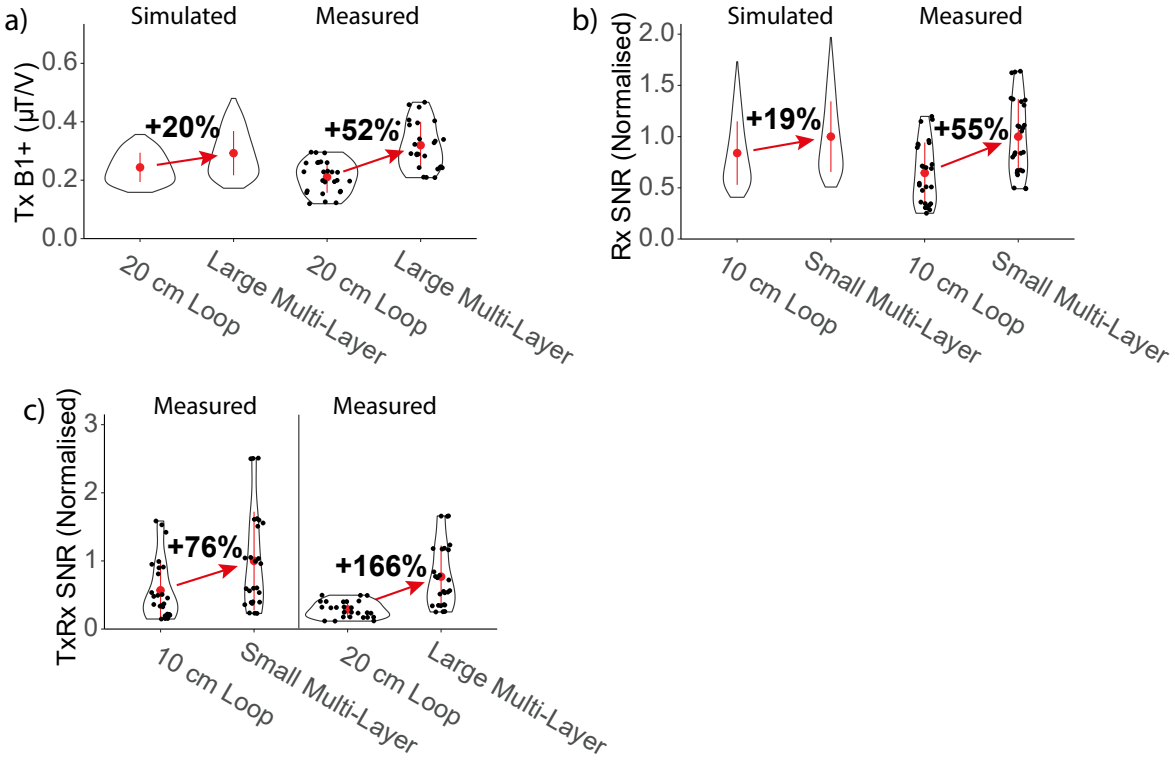

Figure 5.19: Violin plots showing distribution of B_1^+ and SNR voxels within the defined circular ROI. (a) B_1^+ plot between the 20 cm loop and large multi-layer coils showing $20\,\%$ increase B_1^+ from simulated results and $52\,\%$ increase B_1^+ from measured results. (b) SNR plot between the 10 cm loop and small multi-layer coils showing $19\,\%$ increase B_1^+ from simulated results and $55\,\%$ increase B_1^+ from measured results. (c) TxRx metric of B_1^+ multiplied by SNR showing $76\,\%$ increase from 10 cm loop to small multi-layer, and $166\,\%$ increase from 20 cm loop to large multi-layer.

Table 5.3: Summary of B_1^+ efficiency, B_1^+ uniformity and mean SNR in ROI for five coils. Two multi-layer coils: 'smaller' and 'larger', and three single loop coils of diameters: 10, 15, and 20 cm.

	Single Layer			Multi-Layer	
Measured ROI	10 cm Loop	15 cm Loop	20 cm Loop	Small Coil	Large Coil
Mean B_1^+ /μT V^{-1}	0.433	0.435	0.262	0.497	0.393
B_1^+ Uniformity	57.0 %	73.8 %	80.4 %	62.8 %	79.9 %
Relative SNR	0.756	0.770	0.457	1.000	0.783

Simulated ROI	10 cm Loop	15 cm Loop	20 cm Loop	Small Coil	Large Coil
Mean B_1^+ /μT V^{-1}	0.509	0.421	0.310	0.535	0.400
B_1^+ Uniformity	59.7 %	72.5 %	80.7 %	62.7 %	74.1 %
Relative SNR	0.867	0.591	0.382	1.000	0.483

Using the field uniformity data as a baseline, the small multi-layer coil best compares with the 10 cm loop, whilst the large multi-layer coil best compares with the 20 cm loop. To quantify the improvements of the coil, the distribution of voxel magnitude for B_1^+ and SNR in both simulated and measured cases are shown as violin plots. The violin plot shows the mean, standard deviation and the outline as a rotated kernel density plot to represent the distribution of data points as a probability density function, where a wider segment corresponds to higher probability density. B_1^+ and SNR violin plots are used to visualise the distribution of voxel magnitude, where each voxel within the ROI corresponds to a data point within the plot. For simulated data, due to the high number of voxels, the individual data points are not shown, but only the outer profile. In Figure 5.19, the most significant multi-layer results are summarised: the transmit performance for the large multi-layer coil, the receive performance for the small multi-layer coil, and the combined transmit receive performance for both coils. Compared to the 20 cm loop, the large multi-layer coil shows a $20\,\%$ increase in simulated B_1^+ efficiency, and a $52\,\%$ increase in measured B_1^+ efficiency. The vertically stretched and thinner violin profile of the large multi-layer coil suggests a greater distribution of B_1^+ values, and higher peak B_1^+ values. Compared to the 10 cm loop, the small multi-layer coil shows a $19\,\%$ increase in simulated SNR, and a $55\,\%$ increase in measured SNR. The violin profile of both coils are comparable, suggesting a comparable spread of B_1^+ values. Overall in transmit receive operation, the small multi-layer coil shows $76\,\%$ increased overall SNR compared to the 10 cm loop, and the large multi-layer coil shows $166\,\%$ increased overall SNR compared to the 20 cm loop. Here, a substantially narrower violin profile is seen with the large multi-layer coil, with three-fold higher peak B_1^+ values.

5.4.2 Phosphorous Multi-layer Coil

Based on the theoretical and measured improvements of the ^{13}C multi-layer coils described above, we decided to construct a ^{31}P multi-layer coil for use in clinical research. The sections below describe the EM simulation and scanner measurements performed as the first step of coil characterisation.

5.4.2.1 Coil Construction

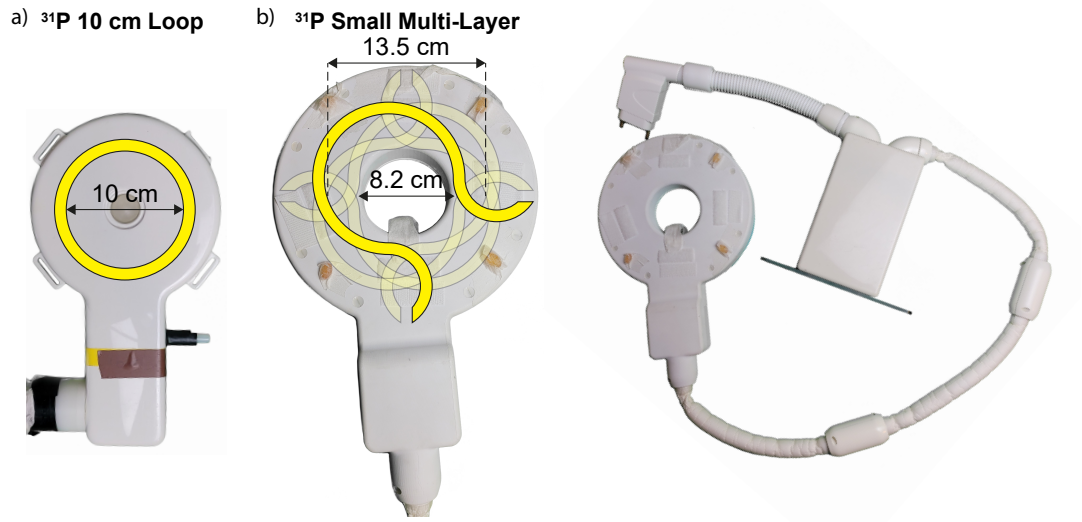

Figure 5.20: Photos of ^{31}P coils showing conductor track overlaid for comparison. (a) 10 cm loop coil, (b) small multi-layer coil element (left) with T/R box, baluns and coil plug (right)

A Tx-Rx multi-layer coil (depicted in Figure 5.20) was constructed for ^{31}P cardiac MRI on a clinical $3\,\mathrm{T}$ scanner at $49.98\,\mathrm{MHz}$, as a joint project between PulseTeq Ltd and the University of Oxford. The construction consists of a single printed circuit board (PCB manufactured by Flexible Technology Ltd) acting as a transmit-receive RF coil element, connected to a T/R box. The multi-layer PCB consisted of four conductor layers of $2\,\mathrm{oz}$ copper ($0.07\,\mathrm{mm}$), separated by dielectric insulator layers of $0.127\,\mathrm{mm}$ Kapton. The coil PCB base reused the 'smaller' ^{13}C multi-layer design described above, with an $R1 = 65\,\mathrm{mm}$, an $R2 = 37\,\mathrm{mm}$, and an $O = -15\,\mathrm{mm}$. Two ^{1}H traps were tested and placed on the left- and right-hand side of the coil for decoupling from the ^{1}H body coil. One ^{1}H balun and one ^{31}P balun were positioned at the base of the coil element to reduce common mode currents at their corresponding frequencies on the coil. Two ^{1}H bazooka baluns were placed along the coaxial cable between the T/R box and RF coil element, to minimise common mode currents at ^{1}H frequencies on the cable. The PCB was placed inside a custom 3D printed fire-retardant coil housing that enclosed the PCB. Both the PCB and coil housing had a central cut out to allow phantom and fiducial placements (forming a donut shape). The smaller multi-layer coil of diameter $82\,\mathrm{mm}$ to $125\,\mathrm{mm}$ was chosen for higher field efficiency and minimised field penetration 'past the heart'; the most comparable commercially available RF coil was a $10\,\mathrm{cm}$ diameter Tx-Rx loop coil manufactured by PulseTeq Ltd, shown in Figure 5.20.

5.4.2.2 B1 and SNR Values

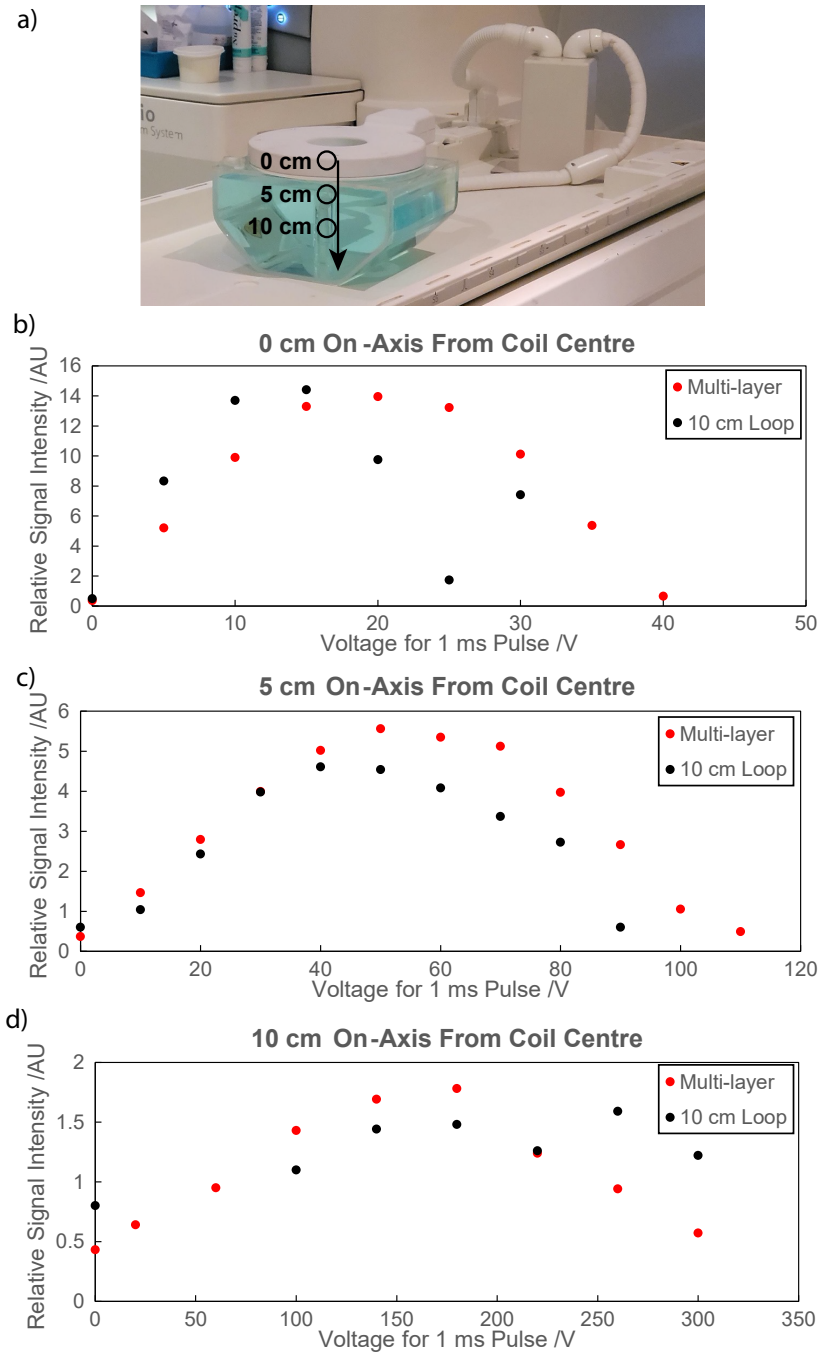

Figure 5.21: Power Calibration to compare on-axis coil transmit performance for 10 cm loop and small multi-layer ^{31}P coils. (a) Photo showing positioning of coil on loading phantom and locations of ^{31}P fiducial. (b) Voltage versus relative signal plot showing more efficient transmit of 10 cm loop at coil centre. (c) Plot showing similar transmit efficiency between two coils at $5\,\mathrm{cm}$ from coil centre. (d) Plot showing more efficient transmit of small-multilayer at $10\,\mathrm{cm}$ from coil centre.

The ^{31}P coils were initially characterised on the scanner to ensure correct operation. The multi-layer coil was compared to the existing 10 cm loop ^{31}P coil. Both coils were placed on a 'PulseTeq loading phantom', in the shape of a cylinder, with a hollow central cylinder for placement of fiducials at various depths. Within this gap, a small ($1\,\mathrm{cm}$ diameter) spherical concentrated phenylphosphonic acid (PPA) fiducial was placed, for supplying the ^{31}P signal. This experimental setup is shown in Figure 5.21a. The fiducial was displaced vertically along the cylindrical gap, and positioned at $0\,\mathrm{cm}$, $5\,\mathrm{cm}$, and $10\,\mathrm{cm}$ from the coil surface for measurements. A typical non-localised spectroscopy sequence (of a simple pulse-acquire type, described in section of D.2.1 Appendix D) was run at a series of voltages for each coil at each depth, fully relaxed with TR $= 5\,\mathrm{s}$. A rect pulse with $1\,\mathrm{ms}$ pulse duration and the voltage required to achieve a $90°$ excitation was used to calculate the B_1^+ at each depth, from equation 3.13.

Table 5.4: Voltage required to achieve a $90°$ excitation for the multi-layer and 10 cm loop coils at $0\,\mathrm{cm}$, $5\,\mathrm{cm}$, and $10\,\mathrm{cm}$ depth on-axis from the coil centre.

Fiducial Depth on Axis /cm	Multi-layer $90°$ /V	10 cm Loop $90°$ /V
0	20	15
5	50	40
10	180	Undefined

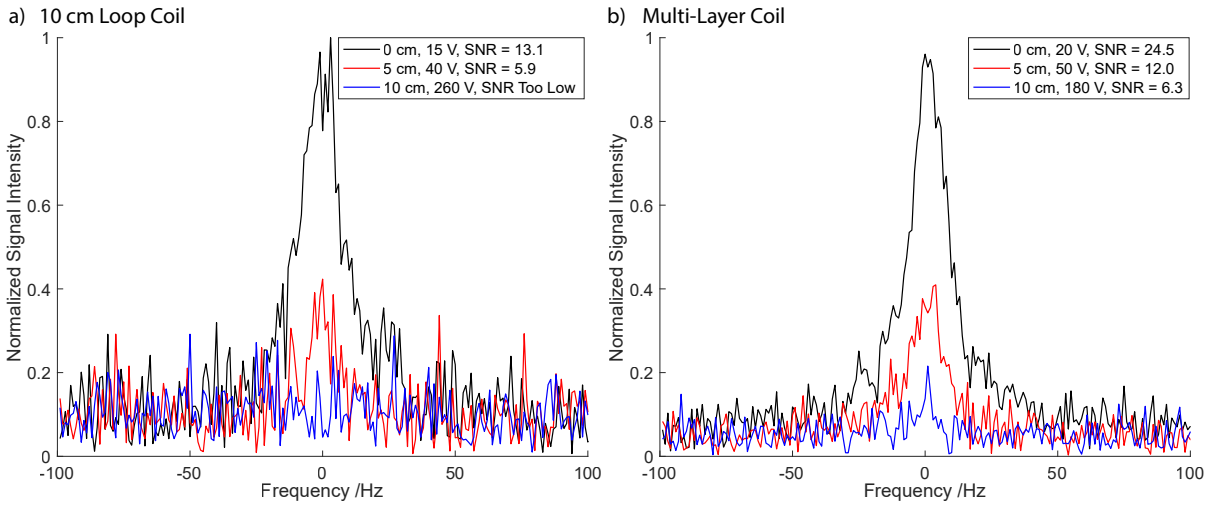

Figure 5.22: Spectra of peak signal to compare on-axis coil receive performance for 10 cm loop and multi-layer ^{31}P coils. (a) SNR of 10 cm loop coil, showing SNR of 13.1 at coil centre (black), 5.9 at $5\,\mathrm{cm}$ depth (red), and SNR below noise level at $10\,\mathrm{cm}$ depth (blue). (b) SNR of small multi-layer coil showing SNR of 24.5 at coil centre (black), 12.0 at $5\,\mathrm{cm}$ depth (red), and 6.3 at $10\,\mathrm{cm}$ depth (blue).

From Table 5.4, showing the voltage required to achieve a 90° excitation, the 10 cm loop achieves higher B_1^+ on-axis close to the coil ($< 5\,\mathrm{cm}$), whilst the multi-layer coil achieves higher B_1^+ at depth ($> 5\,\mathrm{cm}$), as shown in Figure 5.21. This result is expected as the multi-layer coil is marginally larger (approximate inner conductor diameter of $8\,\mathrm{cm}$ and outer conductor diameter of $18\,\mathrm{cm}$) than the 10 cm loop ($10\,\mathrm{cm}$ conductor diameter). For a larger coil diameter, we would expect increased depth penetration but lower B_1^+ efficiency. With the multi-layer design, the depth penetration is improved (with approximately $30\,\%$ higher field uniformity), whilst the B_1^+ efficiency is comparable. Subsequently, the SNR was calculated using non-localised spectroscopy, at each depth, using the peak signal magnitude at the first $90°$ excitation divided by the standard deviation of noise. A crude baseline correction was performed on the signal peak, by subtracting the noise mean. More significantly, in Tx-Rx, the final SNR measured by the non-localised spectroscopy shows an approximately two-fold SNR improvement with the multi-layer coil at both $0\,\mathrm{cm}$ and $5\,\mathrm{cm}$ depths compared to the 10 cm loop coil, as shown in Figure 5.22. At the $10\,\mathrm{cm}$ depth, the signal from the 10 cm loop was too low to determine SNR prior to post-processing, whilst the signal received by the multi-layer coil was still detectable.

5.5 Multi-layer Heating Tests to Ensure Patient Safety

RF heating causes safety concerns as addressed in section 3.5; this section aims to address the safety of the novel multi-layer coil design. Beyond the safety considerations of a conventional loop coil, one additional challenge of the multi-layer design is the potentially increased coupling to the ^{1}H body coil from two design features. Firstly, the intricate conductor structure formed from the overlapping conductor layers results in the formation of several resonant loops; the size and field profile of these loops are highly dependent on the construction parameters of the multi-layer design. Secondly, a significantly longer continuous conductor track is created. As a result, the unexpected loops may resonate at the ^{1}H frequency, and the multi-layer design may still couple to the ^{1}H body coil despite the presence of ^{1}H traps. This coupling may lead to EM hotspots, causing distortions to ^{1}H localisation scans, and potentially causing excessive SAR from X-nuclei scans. Blocking each resonant loop formed using a ^{1}H trap is unfeasible due to the increase in ESR of each additional ^{1}H trap as well as spatial constraints of the small coil footprint. As such, this section investigates the ^{1}H coupling, to ensure the coupling for

the multi-layer design within tolerance for a typical surface coil. The coil heating is investigated from both an SAR perspective, obtained from EM simulations (section 5.5.1), and also temperature changes, obtained from scanner experiments (section 5.5.2). Finally, section 5.5.3 proposes RF power and voltage safety limits for human scanning.

5.5.1 SAR from EM Simulations

EM simulations were used to determine SAR values for the ^{13}C and ^{31}P multi-layer coils on a human voxel model, the methods of which are presented in section 3.5.2.1. H-field, E-field, Power Loss and Surface Current monitors were recorded at $30.98\,\mathrm{MHz}$ and $49.98\,\mathrm{MHz}$, for ^{13}C and ^{31}P resonance frequencies at $3\,\mathrm{T}$ correspondingly. The coils were positioned $10\,\mathrm{mm}$ from the torso with the coil centre aligned with the centre of a human voxel model, to represent dielectric loading conditions and coil positioning in a clinical scan. Time domain simulations using the FDTD algorithm were performed with approximately $3\,000\,000$ hexahedral mesh cells. The SAR was calculated using CST, according to the IEEE/IEC (International Electrotechnical Commission) 62704-1 standard, averaged over $10\,\mathrm{g}$ mass, and normalised by input power, as such the SAR values shown below are obtained for $1\,\mathrm{W}$ of input power.

To provide context for SAR performance, a comparison of peak $10\,\mathrm{g}$ averaged SAR over the torso surface was made between the small multi-layer coil and the 10 cm loop and 15 cm loop coils; these loop coils were chosen as they represented the closest coil dimensions to the small multi-layer coil. The results for the combinations are shown in Figure 5.23. The simulated ^{13}C 10 cm loop achieved a peak SAR $0.351\,\mathrm{W\,kg^{-1}}$. which was higher than the ^{13}C small multi-layer peak SAR of $0.318\,\mathrm{W\,kg^{-1}}$. The simulated ^{31}P 15 cm loop achieved a peak SAR of $0.437\,\mathrm{W\,kg^{-1}}$, which was lower than the ^{31}P small multi-layer peak SAR of $0.459\,\mathrm{W\,kg^{-1}}$.

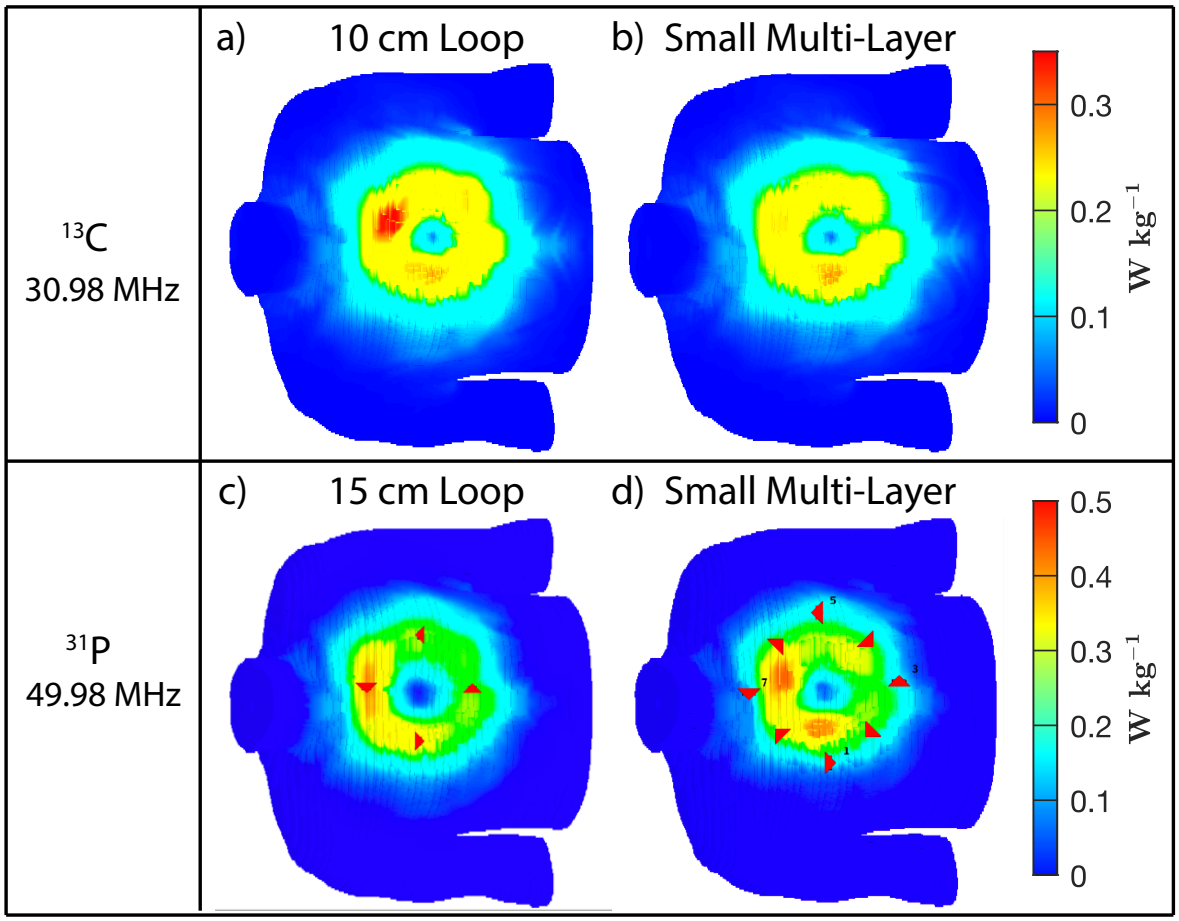

Figure 5.23: SAR maps on the surface of the torso for (a) 10 cm and (b) small multi-layer loops at the ^{13}C frequency, and for (c) 15 cm and (d) small multi-layer loops at the ^{31}P frequency. ^{13}C SAR maps are shown on a 0 to 0.35 W kg^{-1} scale, whilst ^{31}P SAR maps are shown on a 0 to 0.5 W kg^{-1} scale to capture peak SAR values.

Observations from Figure 5.23 show that the small multi-layer coil has lower SAR than the 10 cm loop at the ^{13}C frequency, and higher SAR than the 15 cm loop at the ^{31}P frequency. We note that the outer dimension of the small multi-layer PCB sits between the diameter of the 10 and 15 cm loops. Additionally, the SAR of the multi-layer coil at the ^{31}P frequency is higher than that at the ^{13}C frequency. This is consistent with observations of increased peak SAR from smaller coil diameters and higher frequencies. As such, there is little reason to expect the overall heating from the multi-layer design to be different compared to conventional loops. However, the specific surface SAR hot-spots from the multi-layer coil may differ on the PCB itself due to the complex overlapping conductor structure. As such the EM heating was investigated in greater detail in the following sections.

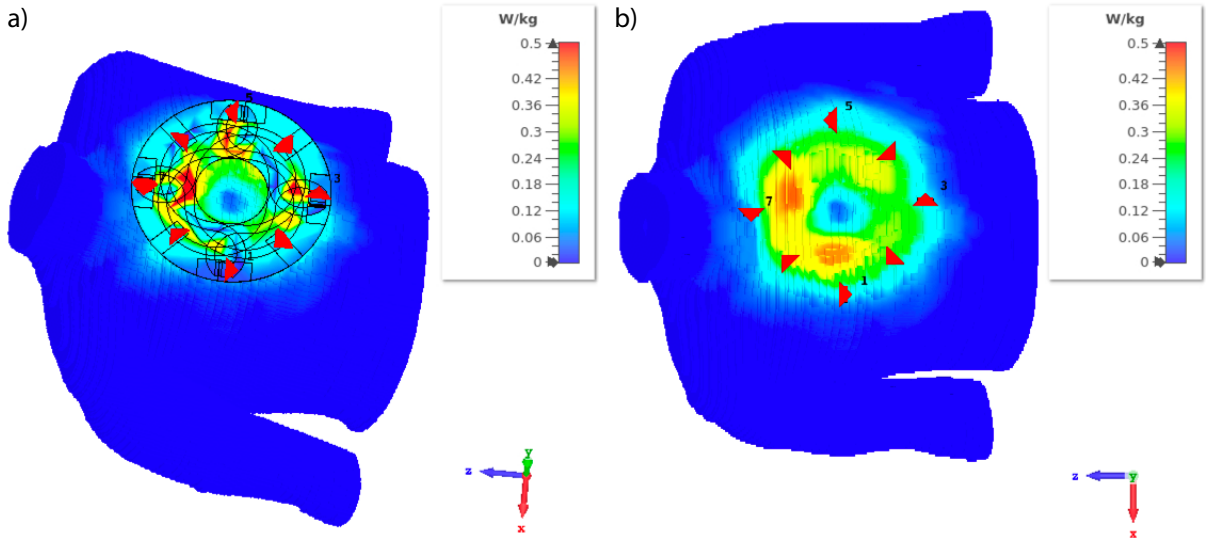

Figure 5.24: Simulated $10\,\mathrm{g}$ averaged SAR of the ^{31}P multi-layer coil positioned on a standard male human voxel model. (a) Coil included showing maximum SAR $> 0.5\,\mathrm{W\,kg^{-1}}$ (for $1\,\mathrm{W}$) in conductor cross overs regions. (b) Without coil, showing maximum SAR $< 0.5\,\mathrm{W\,kg^{-1}}$ (for $1\,\mathrm{W}$) on the body.

Local regions of higher SAR were determined to be consistent with regions where copper tracks overlap with neighbouring layers. Two particular hotspots were seen from EM simulations, such as the forward and left sections of the PCB 'ring'. Figure 5.24a shows SAR on the human voxel model and RF coil PCB; the highest SAR was recorded on the dielectric layer of the PCB, whilst Figure 5.24b shows SAR on the human voxel model only, where a maximum SAR of $0.459\,\mathrm{kg^{-1}}$ was seen.

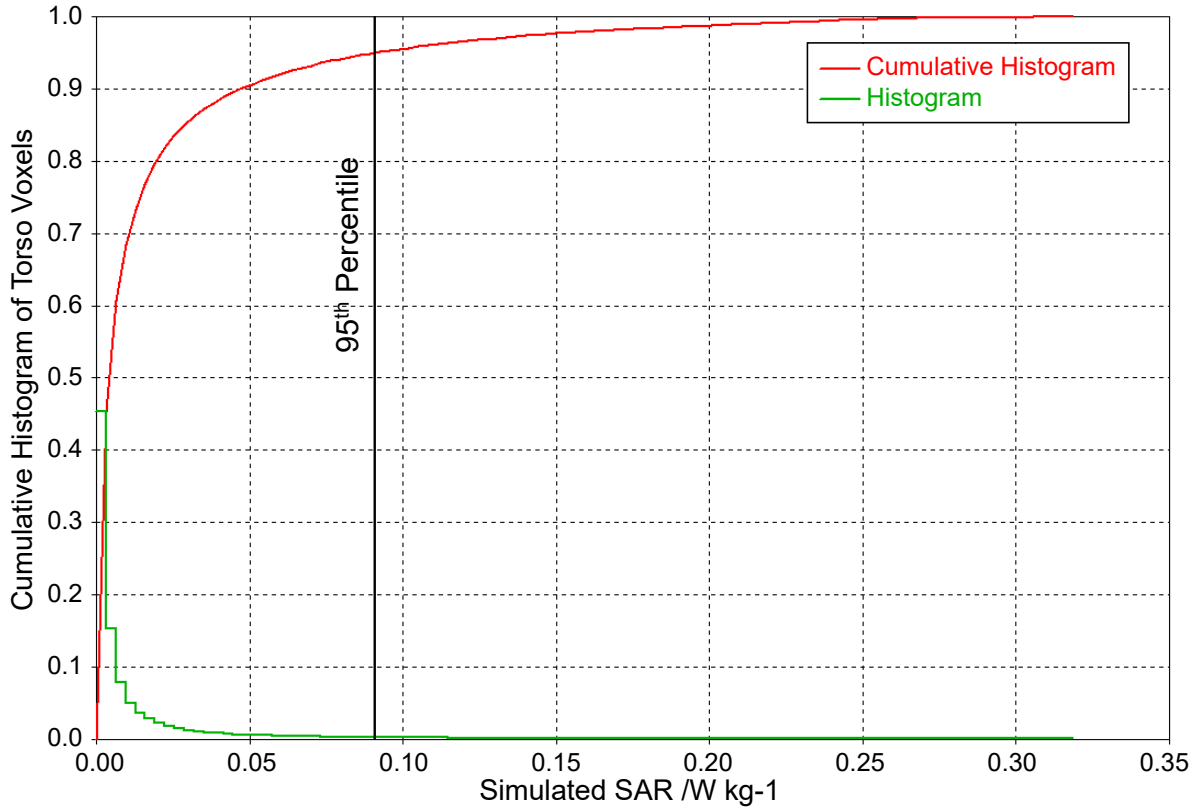

Figure 5.25: Simulated cumulative histogram of SAR, showing 95th percentile SAR at $0.092\,\mathrm{W\,kg^{-1}}$ for the surface coil positioned on a human voxel model torso.

Lastly, it is instructive to look at the distribution of SAR within the torso, through a cumulative histogram, as shown in Figure 5.25. The following general SAR metrics were obtained for $1\,\mathrm{W}$ power for the ^{31}P small multi-layer coil. These metrics were subsequently compared to heating measurements made on the scanner.

- Maximum SAR inside torso $= 0.459\,\mathrm{W\,kg^{-1}}$
- 95th Percentile SAR inside torso $= 0.092\,\mathrm{W\,kg^{-1}}$
- Mean SAR averaged inside torso $= 0.018\,\mathrm{W\,kg^{-1}}$

The 95th percentile SAR over the torso is significantly lower than the maximum SAR, indicating the peak SAR is very localised, as is the case for surface elements.

5.5.2 Scanner Temperature Measurements

Assessment of any changes in temperature from high power ^{1}H and ^{31}P scans were performed to demonstrate energy deposition. The multi-layer coil was positioned on $2\,\mathrm{kg}$ of pork mince,

as described in section 3.5.2.2. Six high-SAR scans with different experimental setups were run on ^{31}P and ^{1}H on the Siemens $3\,\mathrm{T}$ Trio, with two temperature probes (channel 1 and channel 2) positioned in several hotspots identified by the simulations to measure the temperature change, coil spacing and SAR levels. A SAR conversion (k)-value is used which scales the allowed SAR limits on Siemens scanners, the value was determined from the simulated SAR for $1\,\mathrm{W}$ input power, with units of kg^{-1}. The ^{31}P scans were run with $k = 1\,\mathrm{kg}^{-1}$, which is double the proposed value for this coil of $k = 2\,\mathrm{kg}^{-1}$ as a safety margin. The ^{1}H heating tests were run at the 1st level mode, which is $200\,\%$ of the maximum SAR compared to the normal level mode used in clinical scans (as discussed in section 3.5.2.3). Temperature probes were positioned according to predetermined hotspots from EM simulations and thermal images taken by an infrared (IR) camera (IR lens, f$= 6.8\,\mathrm{mm}$, FLIR, Oregon US). The coil maximum voltage was limited to $300\,\mathrm{V}$ to ensure safety of the coil components.

5.5.2.1 Experimental Setup

The setup of the six temperature measurement scans performed in the scanner are shown in Figure 5.26, and listed below. The corresponding temperature measurements taken with an IR camera are shown in Figure 5.27 for experiments 1–3 and Figure 5.28 for experiments 4–6.

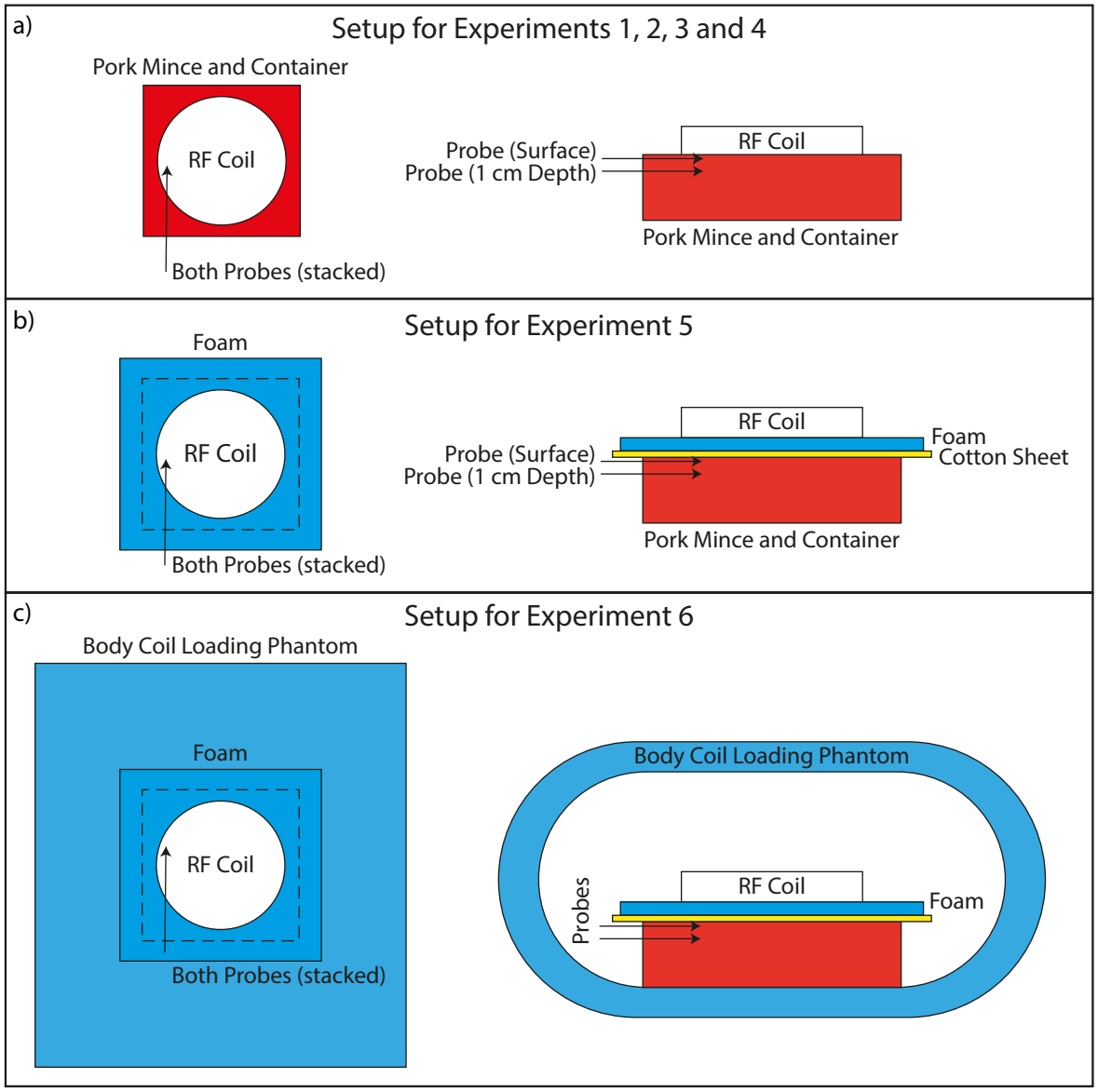

Figure 5.26: Cross-sectional and top-down diagrams showing position of temperature probes for RF coil heating tests. (a) RF coil placed on the pork container which mimics patient heating during X-nuclei scans. (b) A $1\,\mathrm{cm}$ thick layer of foam is placed between the coil and pork container to determine the difference in temperature change with additional separation with the coil in X-nuclei scans. (c) Additionally a body coil loading phantom was positioned such that the volume coil was well matched. This allows the high power ^{1}H scans to be performed on the coil, and temperature changes from proton scan and coupling to X-nuclei coil to be measured.

Experiment 1

Sequence:	Non-localised ^{31}P spectroscopy (TR 610, $300\,\mathrm{V}$, rectangular pulse duration $4\,\mathrm{ms}$), on-scanner SAR $= 99\,\%$, scan duration $25\,\mathrm{min}$.
Position:	Temperature probes placed at top hotspot, channel 1 on surface, channel 2 at $1\,\mathrm{cm}$ below surface.

Experiment 2

Sequence:	Non-localised ^{31}P spectroscopy (TR 610, 300 V, pulse duration 4 ms), on-scanner SAR = 99 %, scan duration 25 min.
Position:	Temperature probes placed at left hotspot (patient left), channel 1 on surface, channel 2 at 1 cm below surface.

Experiment 3

Sequence:	^{31}P Dante Sequence (300 V positive adiabatic pulse, 300 V negative adiabatic pulse, 63 V DANTE train), on-scanner SAR 100 %, scan duration 10 min 15 s.
Position:	Temperature probes placed at left hotspot (patient left), channel 1 on surface, channel 2 at 1 cm below surface.

Experiment 4

Sequence:	^{1}H Turbo Spin Echo (body coil, TR 615, 800 V), 1st level SAR limit - on-scanner SAR 100 % (equivalent to normal level 200 %).
Position:	Temperature probes placed at right hotspot (patient right), channel 1 on surface, channel 2 at 1 cm below surface.

Experiment 5

Sequence:	^{1}H Turbo Spin Echo (body coil, TR 615, 800 V), 1st level SAR limit - on-scanner SAR 100 % (equivalent to normal level 200 %).
Position:	Temperature probes placed at right hotspot (patient right), channel 1 on surface, channel 2 at 1 cm below surface.
Notes:	A thin (5 mm) piece of 'ZOTEK F' foam was positioned between the coil and pork. A layer of cotton gown was then placed between the foam and pork to replicate usual patient conditions.

Experiment 6

Sequence:	^{1}H Turbo Spin Echo (body coil, TR 615, 800 V), normal level SAR limit - on-scanner SAR 100 %.
Position:	Temperature probes placed at right hotspot (patient right), channel 1 on surface, channel 2 at 1 cm below surface.
Notes:	In addition to the foam and cotton gown in Experiment 5, a large hollow cylindrical Siemens body loading phantom was positioned inside the body coil, with the experimental setup positioned inside the cylindrical phantom. Experiment 6 was set up to mimic the expected loading in a conventional clinical MRI scan, and conventional SAR limits on ^{1}H.

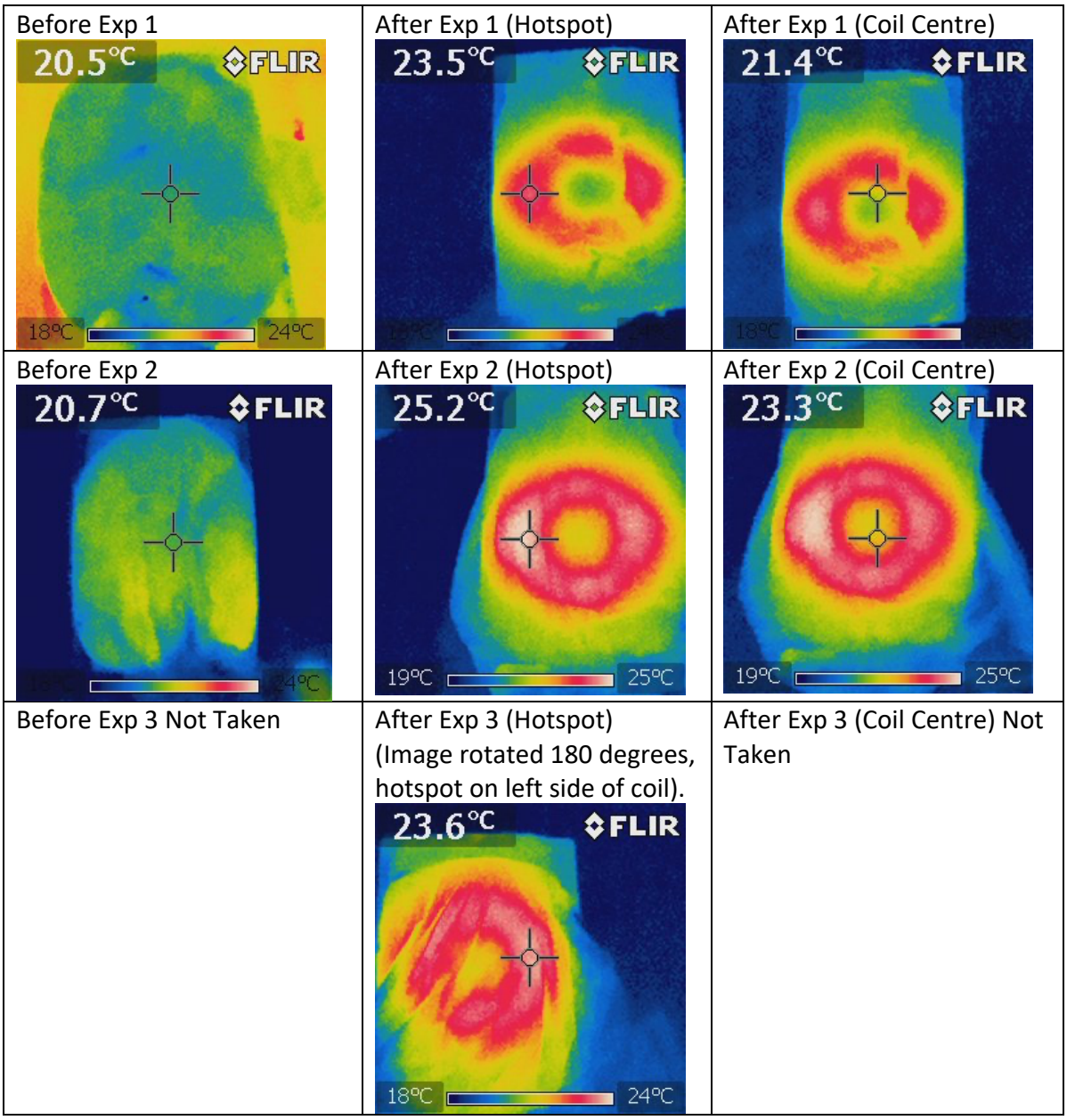

Figure 5.27: Thermal camera images of pork mince showing the heat map from using the ^{31}P multi-layer coil for RF transmit. Column 1 images were taken before the experiment. Column 2 images were taken at the hotspots, corresponding to the position of the temperature probes, immediately after the experiment. Column 3 images were taken approximately at the coil centre immediately after the experiment.

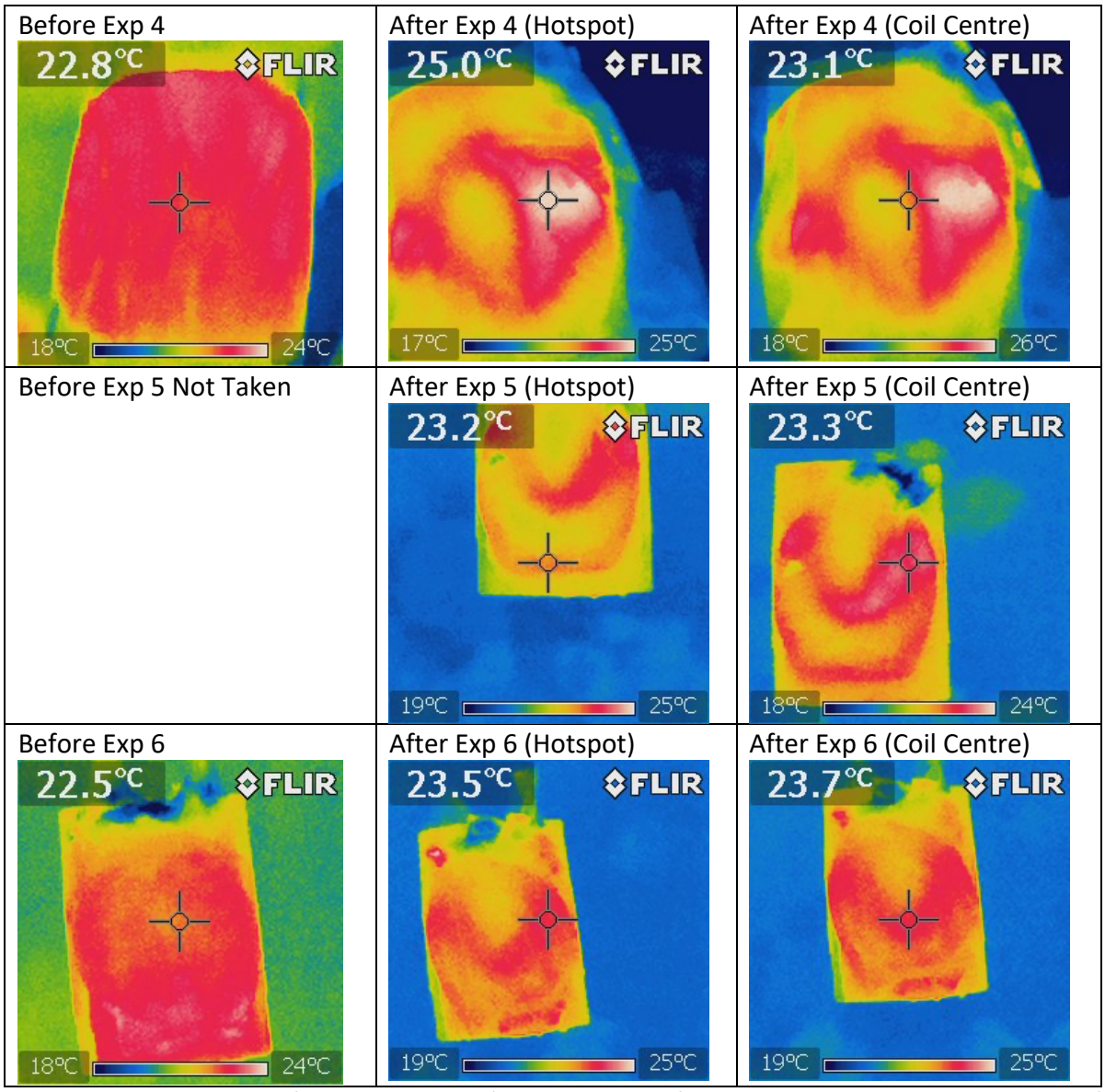

Figure 5.28: Thermal camera images of pork mince showing heat map from using ^{1}H body coil for RF transmit. Experiments 5 and 6 show smearing of hotspot due to insulation from foam. Column 1 images were taken before the experiment. Column 2 images were taken at the hotspots, corresponding to the position of the temperature probes, immediately after the experiment. Column 3 images were taken approximately at the coil centre immediately after the experiment.

5.5.2.2 Power Absorbed Calculation

Temperature recordings were carried out; rapid temperature fluctuations resulting from the $0.1\,^{\circ}\mathrm{C}$ measurement accuracy of the measurement probe were observed. The fluctuations were smoothed using a $60\,\mathrm{s}$ rolling mean and plotted in Figure 5.29 for experiments 1–3 and Figure 5.30 for experiments 4–6. Due to heat dissipation in the pork mince, the measured temperature

increases non-linearly over time. As such, a 'worst case' k-value was calculated using the temperature gradients over 5 minutes, sampled at every $1\,\mathrm{s}$, over the full scan duration. All analysis was performed in MATLAB (MathWorks, Massachusetts, US). The full list of measured temperature changes for each experiment over the full scan, as well as 5-minute duration maxima are shown in Table 5.5. The SAR and measured k-values were calculated as $k_{\mathrm{Measured}} = \frac{P_{\mathrm{Absorbed}}}{P_{\mathrm{Average}}}$, from the duty cycle and temperature gradient as described in Methods, section 3.5.2.2. The results are listed in Table 5.5 below. The highest k-value (corresponding to the worst case heating) was determined to be $1.06\,\mathrm{kg}^{-1}$, and as such, the heating effects from the multi-layer coil are well within the safety limits.

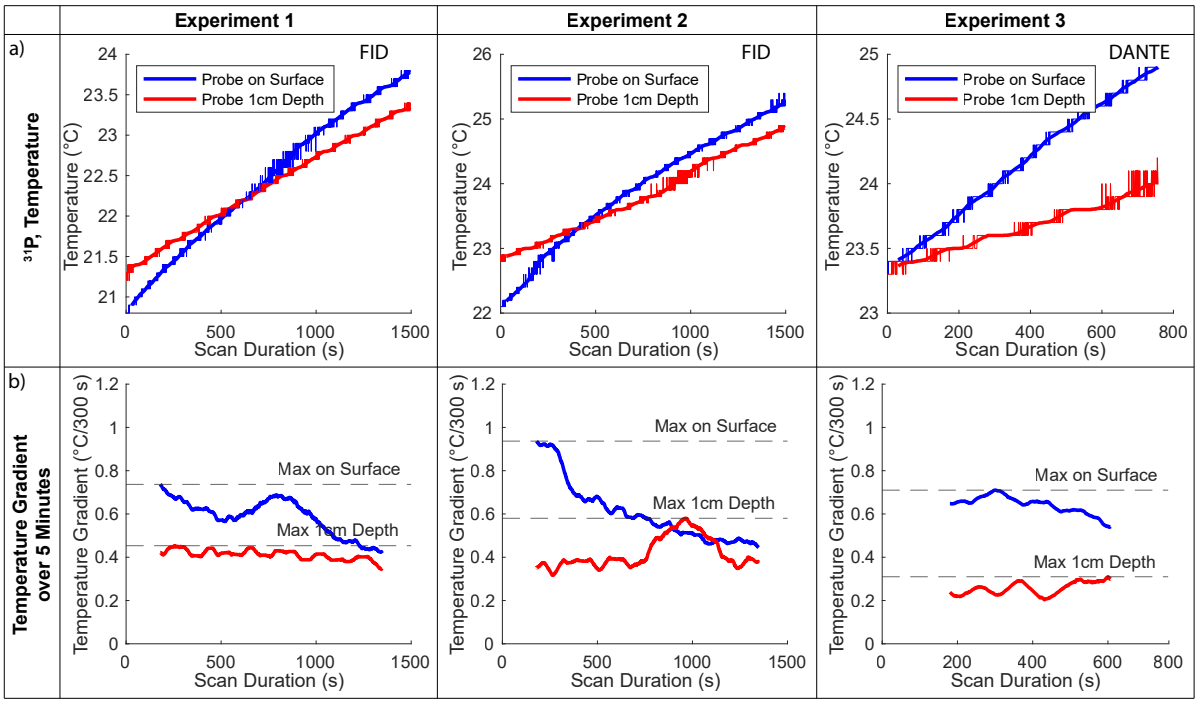

Figure 5.29: ^{31}P multi-layer transmit heating measurements from temperature probes. Top Row: Plots of temperature over full scan duration. Bottom row: Plots of temperature change over a 5-minute window across the full scan duration.

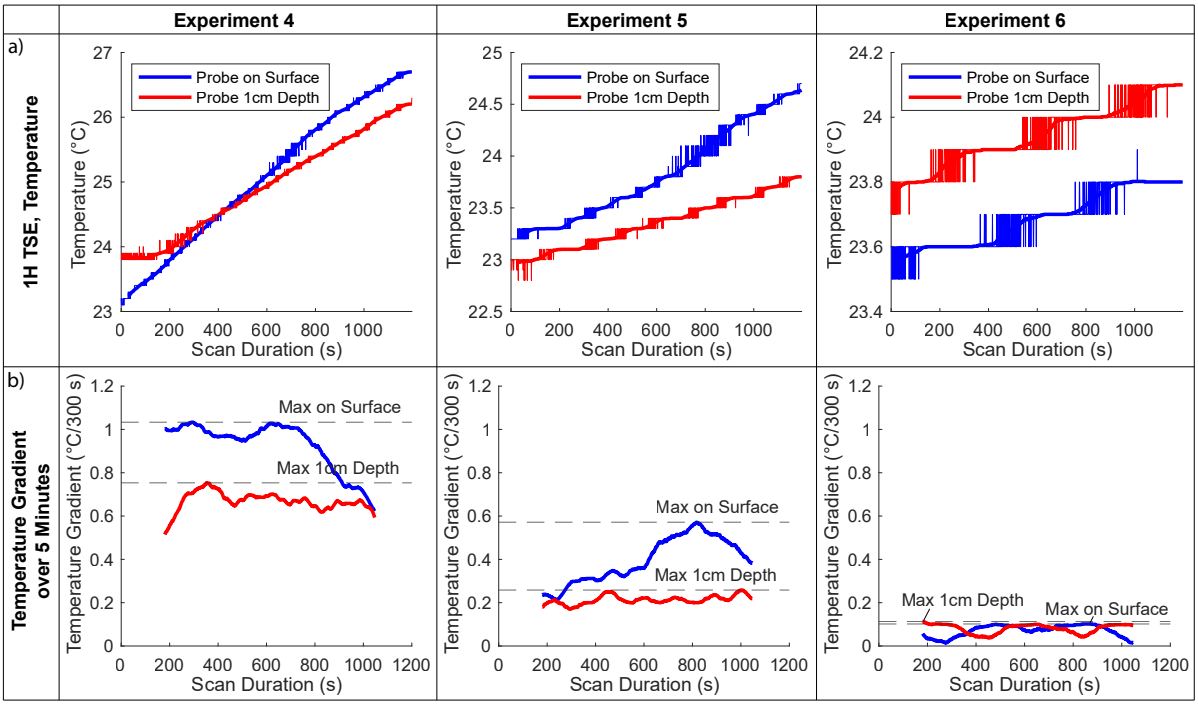

Figure 5.30: ^{1}H body coil transmit heating measurements from temperature probes. Top Row: Plots of temperature over full scan duration. Bottom row: Plots of temperature change within a 5-minute window over the full scan duration.

Table 5.5: Calculations for power absorbed values and k-values. Averaged metrics are calculated as the temperature change over the full scan duration, and the maximum metrics are calculated as the maximum 5-minute temperature change. The top table shows results for ^{31}P experiments 1–3, and the bottom table shows results for ^{1}H experiments 4–6.

	Tx Coil Used	^{31}P Multi-layer Coil					
	Experiment Number	**Experiment 1**		**Experiment 2**		**Experiment 3**	
	Total Scan Duration /s	1500		1500		760	
	Probe Position	**Surface**	**Depth** 1 cm	**Surface**	**Depth** 1 cm	**Surface**	**Depth** 1 cm
Simulated	Input Voltage /V	300	300	300	300	–	–
	Peak Input Power /W	1800	1800	1800	1800	–	–
	Average Input Power /W	11.8	11.8	11.8	11.8	–	–
Over Full Scan Duration	ΔT /°C	3.0	2.1	3.1	2.0	1.5	0.9
	Average Power Absorbed /W kg^{-1}	5.00	3.50	5.17	3.33	4.93	2.96
	Average k /kg^{-1}	0.42	0.30	0.44	0.282	–	–
Over 5 Minute Duration	**Max** ΔT /°C	0.74	0.45	0.94	0.58	0.71	0.31
	Max Power Absorbed /W kg^{-1}	6.14	3.78	7.81	4.83	5.92	2.62
	Max k /kg^{-1}	0.52	0.32	0.66	0.41	–	–

	Tx Coil Used	^{1}H Body Coil					
	Experiment Number	**Experiment 4**		**Experiment 5**		**Experiment 6**	
	Experiment Setup	**No Foam**		**Foam**		**Foam + Body Loading**	
	Total Scan Duration /s	1200		1200		1200	
	Probe Position	**Surface**	**Depth** 1 cm	**Surface**	**Depth** 1 cm	**Surface**	**Depth** 1 cm
Over Full Scan Duration	ΔT /°C	3.6	2.3	1.5	1.0	0.3	0.4
	Average Power Absorbed /W kg^{-1}	7.50	4.79	3.13	2.08	0.63	0.83
Over 5 Minute Duration	**Maximum 5 Minute** Δ**T /°C**	1.03	0.75	0.57	0.26	0.10	0.13
	Maximum Power Absorbed /W kg^{-1}	8.61	6.28	4.76	2.15	0.85	1.06

5.5.3 Proposed Safety Limits in Coil Files

The multi-layer coil, EM simulations produced a peak SAR of $0.459\,\mathrm{W\,kg^{-1}}$, and temperature measurements running at 1st level operation ($200\,\%$ energy of typical scan) produced a measured k-value of $1.03\,\mathrm{kg^{-1}}$, both of which are well within the safety limits in the Table 3.1 in section 3.5.2.3. These values were compared to existing ^{31}P surface coils at OCMR, and shown to be similar to both an existing two-loop concentric ^{31}P surface coil, and the 10 cm loop ^{31}P coil, shown in Table 5.6. As such, the multi-layer design, whilst exhibiting slightly increased energy deposition (on the order of 20 – $30\,\%$), does not pose any concern for safety.

Table 5.6: Comparison of measured and simulated SAR values, SAR conversion (k-value) and voltage limit settings for the ^{31}P multi-layer coil at: 5-minute max, full scan average, and against existing ^{31}P surface coil data.

^{31}P Surface Coil	Measured k /kg^{-1}	Simulated SAR /$\mathrm{W\,kg}^{-1}$	Proposed k-Value /kg^{-1}	Voltage Limit /V
Multi-layer 5-min Maximum	0.662	–	2	250
Multi-layer Average	0.438	0.459	2	250
Concentric	0.219	0.479	2	300
Concentric (amended)	0.184	–	1	300
10 cm Loop	–	–	2	250

Discussion of the heating and SAR results are presented below, where justification of the ^{31}P SAR, ^{1}H heating, and maximum amplitude are given in the following three subsections:

5.5.3.1 Limiting SAR conversion (k-value)

Close agreement was seen between simulated SAR ($0.459\,\mathrm{W\,kg}^{-1}$) and average measured SAR ($0.438\,\mathrm{W\,kg}^{-1}$) for $1\,\mathrm{W}$ in Table 5.6, indicating correct operation of the coil and power deposition as predicted (power is being deposited into the sample). Still, the maximum SAR over a 5-minute duration ($0.662\,\mathrm{W\,kg}^{-1}$) was not significantly higher than the average SAR, and still lower than the proposed SAR conversion value of $2\,\mathrm{W\,kg}^{-1}$. A maximum worst case absorbed power of $7.8\,\mathrm{W\,kg}^{-1}$ (surface), and $3.8\,\mathrm{W\,kg}^{-1}$ (at $1\,\mathrm{cm}$ depth) were measured at the 1st level operating mode, which is still well within the IEC limits (less than $10\,\mathrm{W\,kg}^{-1}$). A temperature rise on the surface was seen; a maximum of $3.1\,^{\circ}\mathrm{C}$ was achieved over $1500\,\mathrm{s}$ of continuous heating at $5.2\,\mathrm{W\,kg}^{-1}$, corresponding to the position of ^{1}H traps. However, in human participants blood circulation will reduce the extent of this local heating. For a sufficient safety buffer, a SAR limit of $k = 2\,\mathrm{kg}^{-1}$ was implemented, which gives an approximate maximum absorbed power of $2.6\,\mathrm{W\,kg}^{-1}$ (surface), and a substantially lower temperature rise.

5.5.3.2 Minimising Proton Heating

The hotspots seen were consistent with the locations of the ^{1}H traps, which are expected to create local B_1^+ distortions at the ^{1}H frequency which result in a higher E-field, corresponding to a higher temperature rise locally. To alleviate the heating around the ^{1}H trap from being conducted onto the skin of the patient, and to minimise radiated heating from ^{1}H traps, a $5\,\mathrm{mm}$

thick Zotek foam was permanently placed on the coil, to increase the separation between the ^{1}H traps and the body. Experiment 5 (with the foam affixed) shows a temperature increase of $1.5\,^{\circ}\mathrm{C}$ on the surface over $20\,\mathrm{min}$, suggesting that the foam reduces the temperature increase by half compared to the temperature increase observed in Experiment 4. The average power absorbed locally at the hotspot decreases from $7.50\,\mathrm{W\,kg^{-1}}$ (Exp 4) to $3.14\,\mathrm{W\,kg^{-1}}$ (Exp 5). Experiment 6 uses the cylindrical body loader phantom to approximate clinical scan conditions, with normal level SAR (at $100\,\%$); a significantly reduced temperature increase of $0.4\,^{\circ}\mathrm{C}$ was seen over $20\,\mathrm{min}$, with a corresponding average power absorbed of $0.83\,\mathrm{W\,kg^{-1}}$.

5.5.3.3 Limiting Maximum Voltage

Experiments 1–3 were performed at a maximum voltage of $300\,\mathrm{V}$, with a combined duration of over $1\,\mathrm{h}$. No indications of dielectric breakdown between the layers or degradation of capacitors were seen. Discrete capacitors used for construction are all rated at $1.5\,\mathrm{kV}$ or above, and positioned as parallel groups of three, to bridge conductor gaps and layers. Due to the nature of the multi-layer design, dielectric breakdown between layers is a concern, and was seen in previous pre-clinical prototypes (section 4.3.2). The dielectric insulator used was FR0110 Kapton, which has a dielectric strength of $137\,\mathrm{kV\,mm^{-1}}$. At the design thickness of $127\,\mu\mathrm{m}$, this corresponds to a breakdown voltage of $17.4\,\mathrm{kV}$. This greatly exceeds the expected potential difference between two neighbouring layers of the ^{31}P coil. The maximum transmit voltage was down-rated to $250\,\mathrm{V}$, in an effort to minimise degradation of the coil components, namely capacitors, and the pre-amplifier.

5.6 Multi-layer Acquired Human Data

An ongoing study at OCMR uses ^{31}P MRS to measure altered cardiac energy metabolism [8] in dilated cardiomyopathy and coronary artery disease. Unlike hyperpolarized ^{13}C, ^{31}P MRS does not require preparation of the signal externally, which introduces variability in the signal level and additional costs. Thus, the ^{31}P MRS study was an ideal application to test the clinical multi-layer design. The ^{31}P multi-layer coil developed previously in section 5.4.2 was used to acquire human scan data. This was compared to the existing 10 cm loop coil (PulseTeq Ltd), photos of both coils are shown in Figure 5.31. The scans were acquired in collaboration with Will Watson and Jack Miller at OCMR, as part of an ongoing ^{31}P variability study. As part of

the protocol, a 1D CSI scan was performed; the results from this sequence were used, as CSI is better suited to quantify the potential improvements of the multi-layer coil.

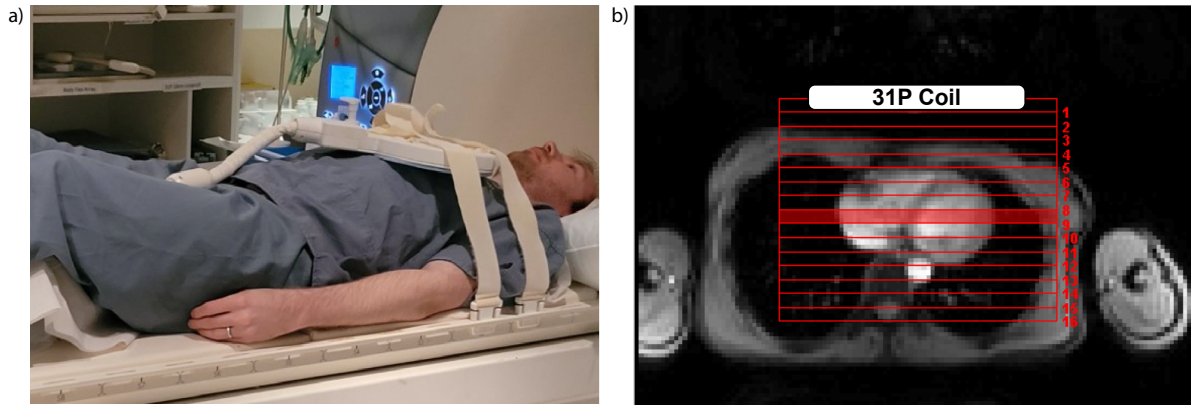

Figure 5.31: Human cardiac ^{31}P multi-layer coil setup. (a) Photograph of the coil positioned on a volunteer for cardiac MRI. (b) Voxel position for 1D CSI on a ^{1}H axial slice of the heart, showing the selected voxel and relative position of the ^{31}P coil.

5.6.1 1D CSI Scan Setup

A 1D UTE-CSI (Ultrashort TE Chemical Shift Imaging, Appendix D) was run with 16 phase encode steps for depth, TR $330\,\mathrm{ms}$, and 125 averages. The 1D CSI was oriented such that the voxels were parallel to the chest wall, to fully cover the heart, and centred on the coil central axis. A $25\,\mathrm{mm}$ 'B_1-insensitive train to obliterate signal' (BISTRO) saturation band [9] was placed across the skeletal muscle, to remove skeletal muscle ^{31}P signal contamination. The voxel of interest was chosen as the most apical cardiac voxel, that was not contaminated by skeletal muscle; an example of the 1D CSI positioning and voxel selections are shown in Figure 5.31, where voxel 8 was selected as the voxel of interest.

The PCr/ATP ratio, used to determine cardiac energetics, was measured between the two coils over five participants, on a Siemens $3\,\mathrm{T}$ Trio system. The subject was positioned supine in the scanner, with the coil central axis positioned at the centre of the heart. To ensure consistent positioning of the coils relative to the subject, proton localisers were used to image the locations of a PPA fiducial and cod liver oil phantoms positioned around the coil. Baseline correction of the measured ^{31}P spectra, and spectral peaks were fitted using the AMARES (advanced method of accurate, robust and efficient spectroscopic fitting) method [10, 11] in the Oxford Spectroscopy Analysis (OXSA) toolbox [12]. Peaks for PCr and α-, β- and γ-ATP phosphoryl groups were

fit in the time domain, using prior knowledge of expected peak frequencies, J-coupling constants between ATP peaks, relative peak amplitudes (PA), and relative phases. Quantification certainty was determined using Cramer-Rao Lower Bounds (CRLB), which measure the coefficient of variation in signal amplitude of the four metabolites. The central frequency of the scan was set at the halfway point between PCr and γ-ATP (approximately $70\,\mathrm{Hz}$ lower than the PCr peak).

5.6.2 Multi-Layer Coil Results

5.6.2.1 Spectral SNR

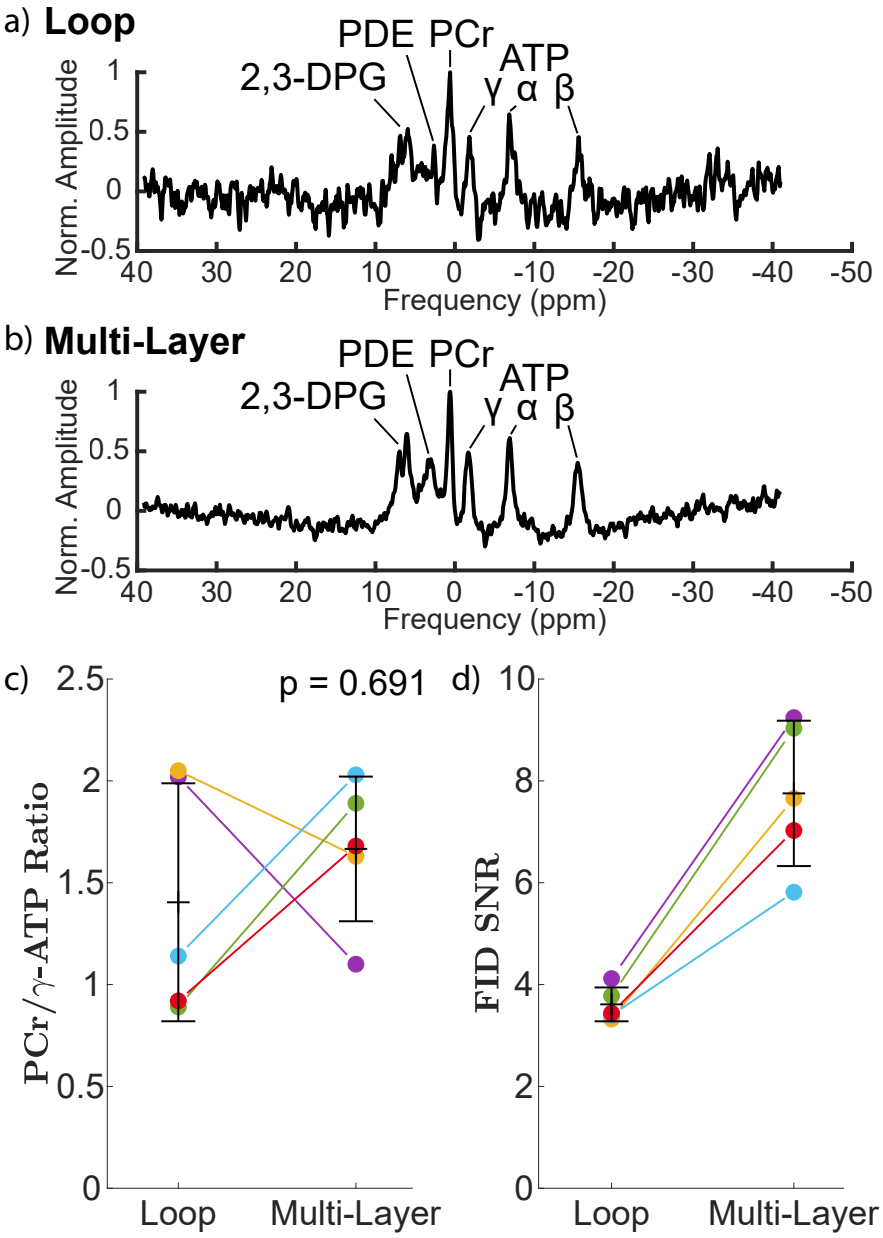

Figure 5.32: Human cardiac ^{31}P multi-layer coil comparison on five volunteers. (a) Example ^{31}P spectra obtained from the loop coil. (b) Example ^{31}P spectra obtained from the multi-layer coil. (c) PCr/γ-ATP ratio for both coils across five volunteers, showing no significant difference with $p = 0.691$. (b) FID SNR for both coils, showing an approximately two-fold increase in SNR measured by the multi-layer coil.

Table 5.7: Spectral SNR from the 10 cm loop and multi-layer coil over five participants, showing an improvement factor of 1.7 to 2.7, with an average SNR improvement of 2.3 times.

Participant	1	2	3	4	5	Average
10 cm Loop Spectral SNR	4.12	3.32	3.79	3.40	3.44	3.61
Multi-layer Spectral SNR	9.24	7.66	9.03	5.82	9.24	8.20
Improvement Factor	2.2	2.3	2.4	1.7	2.7	2.3

Subsequently, the overall spectral SNR was calculated in the time domain by taking the signal as the magnitude of the first data point divided by the standard deviation of the noise from the last 100 data points. Table 5.7 shows the spectral SNR for both multi-layer and 10 cm loop coils running in Tx-Rx for five participants within the voxel of interest. The SNR of the multi-layer coil was observed to be 2.3 times higher than the 10 cm loop on average. This large increase in SNR is a consequence of both transmit efficiency improvements (of more than $20\,\%$) multiplied by receive sensitivity improvements (of more than $50\,\%$), and additionally the improved depth penetration of the multi-layer coil. This substantial two-fold improvement in SNR can be visually seen in the two example spectra of Figure 5.32, and is the key result of the work in this thesis.

5.6.2.2 PCr/ATP Ratio and Variability

Table 5.8: PCr/γ-ATP ratio from the 10 cm loop and multi-layer coil over five participants, showing an average ratio of 1.40 ± 0.59 for the 10 cm loop and 1.66 ± 0.35 for the multi-layer coil.

Participant	1	2	3	4	5	Average	SD
10 cm Loop PCr/γ-ATP	2.02	2.05	0.89	1.14	0.92	1.40	0.59
Multi-layer PCr/γ-ATP	1.10	1.63	1.89	2.03	1.68	1.66	0.35

We can determine two metrics: the predominant metric used in human cardiac ^{31}P MRS, the PCr/ATP ratio, and a normalised coefficient of variation, the CRLB/peak-amplitude (PA) ratio. Firstly, the PCr/ATP ratios before any corrections (typically from T_1 or blood related effects) are presented in Table 5.8. There was no correlation in the PCr/γ-ATP ratio across the five participants, the mean PCr/ATP ratio and standard deviation was consistent across the two coils: of 1.40 ± 0.59 from the 10 cm loop and 1.66 ± 0.35 from the multi-layer coil, with a p-value of 0.691. The increase in SNR from the multi-layer coil is reflected in the more consistent PCr/γ-

ATP ratios, with lower variation across the five healthy participants. Secondly, a normalised metric of CRLB divided by peak-amplitude was used to compare the curve fit quality for the multi-layer and 10 cm loop. CRLB/PA was calculated for all five participants, and the overall $25\,\%$ interquartile range (IQR), median, $75\,\%$ IQR and mean of the CRLB/PA was recorded. For each of the four peaks identified, and an additional PCr/γ-ATP metric, the CRLB/peak amplitude is shown in Table 5.9 and Figure 5.33. A lower CRLB/PA indicates a better fit to the spectral data, as a result of less variation from the noise. As such, a coil that achieves a lower CRLB/PA gives greater confidence of the data fit. The CRLB/PA from the multi-layer coil was found to be consistently approximately $50\,\%$ of that from the 10 cm loop for all five volunteers. The propagation of individual uncertainty from PCr and γ-ATP to the PCr/γ-ATP ratio is $50\,\%$ lower with the multi-layer coil compared to the 10 cm loop. A $50\,\%$ lower improvement CRLB/peak amplitude is consistent with the two-fold spectral SNR increase of the multi-layer coil.

Table 5.9: Cramer-Rao lower bound divided by peak amplitude ratio for 10 cm loop and multi-layer coils, showing interquartile ranges and mean of PCr, three ATP metabolites, and the PCr/γ-ATP ratio.

		Metabolite CRLB/PA				
		PCr	γ-ATP	β-ATP	α-ATP	PCr/γ-ATP
10 cm Loop	IQR Q1	0.146	0.289	0.244	0.205	0.324
	Median	0.170	0.291	0.283	0.296	0.336
	IQR Q3	0.198	0.295	0.359	0.363	0.355
	Mean	0.178	0.292	0.383	0.314	0.342
Multi-layer	IQR Q1	0.063	0.123	0.137	0.107	0.138
	Median	0.084	0.152	0.165	0.123	0.173
	IQR Q3	0.088	0.154	0.209	0.126	0.178
	Mean	0.074	0.143	0.172	0.119	0.160

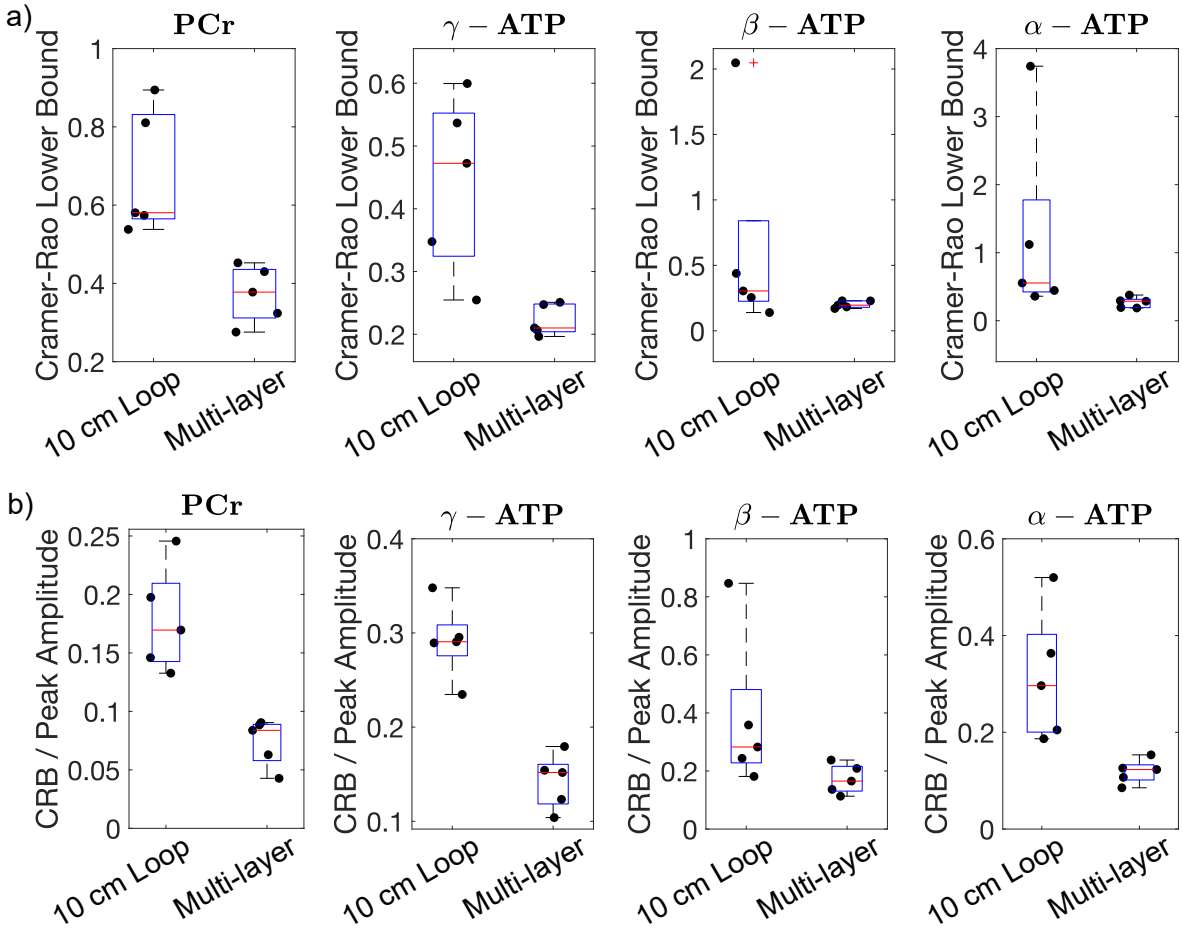

Figure 5.33: CRLB (a) and CRLB/PA (b) for 10 cm loop and multi-layer coils, showing data of individual data points for five participants over PCr, and three ATP metabolites.

5.7 Discussion

This chapter follows the development and extensive characterisation of the novel multi-layer design for human TxRx surface coils. Specifically, the improved conductor design was manufactured as a PCB and constructed for ^{13}C and ^{31}P, where significant improvements in transmit and receive performances were seen for both nuclei leading to an increase of around $30\,\%$ in B_1^+ efficiency, and $50\,\%$ in SNR, over existing loop designs.

5.7.1 Overview

This chapter improves on the pre-clinical multi-layer design by using curved conductors. The curved conductor structure forms a peripheral coil region beneficial for field uniformity from three aspects: removing the region of lower B-field by changing the direction of current flow

on the periphery; allowing distributed lumped elements to be placed at the coil periphery; and allowing decoupling of neighbouring elements when using more than one element. EM simulations were used to sweep parameters in order to identify the optimal multi-layer coil design, and allowed two optimised coil designs to be constructed: a 'smaller' multi-layer design with higher B_1^+ efficiency and SNR, and a 'larger' multi-layer design for improved field uniformity and coverage. Phantom experiments on both ^{13}C and ^{31}P indicated an improvement of B_1^+ efficiency upwards of $30\,\%$, and a $50\,\%$ increase in SNR over the commercially available conventional loop designs. Extensive safety and heating measurements were performed to ensure that the increased coupling to the ^{1}H body coil was sufficiently suppressed, and safety limits were imposed onto the coil in line with typical loop coils. Lastly, a two-times increase in SNR was achieved with the ^{31}P multi-layer coil compared to a conventional loop coil of comparable diameter, on five healthy participants.

5.7.2 Further Work

Whilst this chapter has collected substantial evidence that a single multi-layer element offers significant improvements in transmit and receive performance when compared to conventional loops of all dimensions, one major requirement for the widespread adoption of the design is for multiple multi-layer elements to be successfully arranged in an array. The intricate conductor design and four-fold rotational symmetry of the multi-layer coil results in extra steps in geometric decoupling compared to conventional loops. Successful implementation of the design, however, will allow the high sensitivity of individual multi-layer elements to be retained in an array configuration. This work forms a substantial part of the following chapter, Chapter 6.

Further work on the single element design may involve development of a six-layer multi-layer design, which was shown to achieve further B_1^+ efficiency improvements over four-layers, which may further translate to SNR improvements. Additionally, construction of a ^{1}H human multi-layer coil, at a higher frequency of $60\,\mathrm{MHz}$ for $1.5\,\mathrm{T}$ or $120\,\mathrm{MHz}$ for $3\,\mathrm{T}$ would be useful commercially. Whilst this was beyond the scope of this work focusing on multi-nuclear coils for cardiac MRI, the increased sensitivity of the multi-layer design could significantly benefit ^{1}H MRI in the clinic. As an example, a $50\,\%$ increase in receive sensitivity would reduce the scan duration by more than two-fold, at the same SNR. This would allow a greater throughput of patients, or allow for higher resolution scans of the same duration. However,

the inherent 'parasitic' capacitance (which is not necessarily undesired) and high inductance present challenges in tuning the multi-layer coil to high frequencies. Hypothetically, for a larger multi-layer coil design even with no lumped capacitors, the capacitance from the overlapping sandwich of conductor layers may result in the resonant frequency being too low and untunable to the 120 MHz required. A lower inductance multi-layer design, which is smaller with fewer layers, or possesses a smaller central overlapping region, may be optimised for ^{1}H MRI. As a next step, a grant has been awarded through Oxford University Innovations (Oxford, UK) in collaboration with PulseTeq Ltd to continue the development of a multi-layer ^{1}H receive array in 2022.

References

[1] Riad, S. M. "Circuit structure including RF/wideband resonant vias". US5886597A. Virginia Tech Intellectual Properties Inc, V. P. I. and University, S. 1997.

[2] Lamy, Y. P. et al. "RF characterization and analytical modelling of through silicon vias and coplanar waveguides for 3D integration". In: *IEEE Transactions on Advanced Packaging* 33 (4 2010). ISSN: 15213323. DOI: 10.1109/TADVP.2010.2046166.

[3] Kim, K. and Lee, J. "Radio frequency coil for magnetic resonance imaging and magnetic resonance imaging system". US20170160354A1. Ltd, S. E. C. 2014.

[4] Gjonaj, E. et al. "High-resolution human anatomy models for advanced electromagnetic field computations". In: *IEEE Transactions on Magnetics* 38.2 (2002), pp. 357–360. DOI: 10.1109/20.996096.

[5] Giovannetti, G. et al. "Conductor geometry and capacitor quality for performance optimization of low-frequency birdcage coils". In: *Concepts in Magnetic Resonance* 20B (1 Feb. 2004), pp. 9–16. ISSN: 1043-7347. DOI: 10.1002/cmr.b.20005.

[6] Giovannetti, G. et al. "Low-Field MR Coils: Comparison between Strip and Wire Conductors". In: *Applied Magnetic Resonance* 39 (4 Dec. 2010), pp. 391–399. ISSN: 0937-9347. DOI: 10.1007/s00723-010-0173-5.

[7] Ahmad, S. F. et al. "Recent Progress in Birdcage RF Coil Technology for MRI System". In: *Diagnostics* 10 (12 Nov. 2020), p. 1017. ISSN: 2075-4418. DOI: 10.3390/diagnostics10121017.

[8] Neubauer, S. et al. “31P magnetic resonance spectroscopy in dilated cardiomyopathy and coronary artery disease. Altered cardiac high-energy phosphate metabolism in heart failure.” In: *Circulation* 86 (6 Dec. 1992), pp. 1810–1818. ISSN: 0009-7322. DOI: 10.1161/01.CIR.86.6.1810.

[9] Luo, Y. et al. “BISTRO: An outer-volume suppression method that tolerates RF field inhomogeneity”. In: *Magnetic Resonance in Medicine* 45 (6 June 2001), pp. 1095–1102. ISSN: 07403194. DOI: 10.1002/mrm.1144.

[10] Rodgers, C. T. et al. “Human cardiac 31P magnetic resonance spectroscopy at 7 tesla”. In: *Magnetic Resonance in Medicine* 72 (2 Aug. 2014), pp. 304–315. ISSN: 0740-3194. DOI: 10.1002/mrm.24922.

[11] Vanhamme, L., Boogaart, A. van den, and Huffel, S. V. “Improved method for accurate and efficient quantification of MRS data with use of prior knowledge”. In: *J Magn Reson* 129 (1 1997), pp. 35–43.

[12] Purvis, L. et al. “OXSA: An open-source magnetic resonance spectroscopy analysis toolbox in MATLAB”. In: *Plos One* 12 (9 2017).

6 | Multi-Element Arrays

6.1 Introduction

6.1.1 Motivation For Multiple Elements

Single elements face an inherent trade-off between B_1^+ uniformity and efficiency, as shown in section 5.3.2. For human X-nuclei imaging, typically a high field uniformity or good coil FOV over a larger ROI are required; examples include high B_1^+ uniformity over the heart, or B_1^+ coverage over the lungs. Here, a large single element would provide sufficient B_1^+ uniformity but with insufficient transmit or receive efficiency, and the sharp EM field drop-off is unavoidable. By utilising multiple smaller elements positioned around the body, the total transmit power is split across each element, and the uniformity of the combined transmit fields from each element can be improved beyond the limit of a single element. On receive, multiple smaller elements are typically fed into individual receive circuitry (namely individual preamplifiers) to allow for higher receive sensitivity and coil coverage when combined, provided that sufficient depth penetration into the ROI is achieved.

So far, the work presented in this thesis has focused on the development and characterisation of single element TxRx RF coils. At clinical research sites, typically one of two possible RF coil configurations are used for ^{13}C cardiac MRI. The first configuration consists of separate transmit and receive elements, with multiple overlapping elements in an array to cover the heart. A common coil construction utilising this configuration consists of two transmit elements above and below the torso in Tx combined with smaller receive array elements in Rx. One example of this design is the large 'clamshell' coil constructed by Rapid Biomedical, used at sites such as: University of California, San Francisco, (UCSF, US) [1], Aarhus University (Denmark) [2], and Sunnybrook Research Institute, Toronto (Canada) [3]. For previous hyperpolarized ^{13}C studies, the University of Oxford has used a similar variant comprising of a 'large Helmholtz pair' for transmit with eight rectangular receive elements [4], also constructed by Rapid Biomedical. A second configuration for ^{13}C cardiac MRI comprises of multiple individual TxRx elements, typically consisting of two to four loops of 10 cm to 20 cm diameter. An example is the two TxRx element 20 cm diameter circular loop manufactured by PulseTeq Ltd, used at sites such as: The

University of Texas Southwestern Medical Center (UTSW, US) [5] and Aarhus University [6, 7]. Overall, these two array coil configurations offer a compromise in the trade-off between field uniformity and efficiency, between the two extremes of single elements with a high B_1^+ efficiency and low uniformity, and volume coils with a low B_1^+ efficiency and high uniformity. This chapter aims to characterise the field uniformity and efficiency of both existing coil configurations and to construct an improved transmit and receive array through optimisation using EM simulation and scanner measurements.

6.1.2 Proton and X-nuclei Array Developments

^{1}H MRI is substantially more common than X-nuclei, and as such, the majority of RF coil array development has been on ^{1}H arrays. Over the last 30 years, significant advances in ^{1}H RF arrays have been achieved [8]. There are three major evolutionary jumps of the array design: the first was switchable arrays, which allow individual elements to be electronically switched (turned 'on/off') [9] when the total number of channels is limited. Subsequently, phased arrays utilised elements which partially overlap with neighbouring elements, such that each element is decoupled from the nearest neighbour. With N receive elements, where each element is connected to an individual receive channel, the combined signal would experience a factor of $\sqrt{N}$ improved SNR [10, 11]. Lastly, parallel arrays have been utilised over the last 10 years, which allow parallel imaging (PI). The receive sensitivity map of each individual coil element is known (or measured), allowing for different weightings to be applied from the signal in different elements. This provides some spatial encoding information to reduce the need for as many gradient-encoding steps, and accelerates the overall scan duration. Typically, a large number of coil elements are required for sufficient scan acceleration through PI [12]. More recently, development by the primary MRI vendors (Siemens, GE, and Phillips) has been focused towards increased array conformity to the patient, and a higher density of elements with more numerous, smaller elements. Whilst some advances can be translated to X-nuclei arrays, the vast majority of these ^{1}H array developments are intended for receive-only (Ro) arrays, to be used in conjunction with a transmit only (To) birdcage volume coil. With the differences in wavelengths and available RF power between ^{13}C and ^{1}H MRI, there is scope for optimisation of both B_1^+ for transmit array design, and sensitivity for a receive array design.

6.1.3 Tx and Rx Array Design Requirements

The requirements for element size and element number differ slightly between optimal transmit arrays and optimal receive arrays. As such, discussions of transmit and receive array optimisation are separated in this chapter. There are two benefits from using more than one transmit element: firstly, the additional elements were positioned around the ROI to allow for theoretically improved B_1^+ uniformity, by reducing the distance between the ROI and the closest coil element. Secondly, when specific relative phase shifts are applied to each coil element, the region enclosed by the elements will exhibit an improved B_1^+ efficiency from a stronger circular polarization of the H-field. However, input power, P_{Input}, is divided (typically evenly) across the number of elements; with N coil elements, the individual power supplied to each element, P_{Coil}, is equal to P_{Input}/N. Therefore, the individual voltage supplied to each coil element is represented by $V_{\text{Coil}} = V_{\text{Input}}/\sqrt{N}$. As generated B_1^+ magnitude is the B_1^+ efficiency multiplied by the V_{Input}, the expected B_1^+ strength from a given element of an N-element array is a factor of $\sqrt{N}$ smaller than the B_1^+ magnitude from a single element coil. Typically, the B_1^+ magnitude for an array element is even lower when accounting for losses from the additional circuitry needed for power splitting and phase shifting.

Whilst the B_1^+ field from transmit arrays are scaled by $1/\sqrt{N}$, the corresponding B_1^- field from receive arrays is independent of the number of elements. Consequently, each element of a receive array retains its individual high sensitivity, provided that sufficient decoupling is achieved amongst the elements. In this case, the receive FOV can be expanded over a larger volume with no deterioration in sensitivity (although the depth penetration is still limited by the dimensions of the individual elements). Practically, however, multiple elements in close proximity inductively couple, which leads to two detrimental effects on the receive performance: firstly, the B_1^- field from the element is skewed by the coupling, reducing receive sensitivity and depth penetration into the sample. Secondly, the additional resistance from the coupled coil contributes towards the overall resistance of the first coil, reducing coil sensitivity. Therefore for maximum SNR to be received, coupling must be minimised between all elements. Two techniques are typically used to minimise coupling: firstly geometric decoupling, where nearest-neighbouring elements are overlapped by a set amount to produce zero mutual inductance. Secondly, between more distant coil neighbours, low input impedance preamplifiers are

used to decouple the elements from one another [11]. The main challenge of a receive coil design is to satisfy as far as possible the condition for all elements to be decoupled from each other, within the spatial constraints of the coil. Therefore, when compared to transmit arrays, an optimum receive array should comprise of a greater number of smaller elements.

6.1.4 Chapter Overview

Currently, coils for clinical hyperpolarized ^{13}C MRI comprise of either To and Ro elements (as is the case with Oxford and Toronto) or multiple individual Tx/RX elements (such as UTSW). This chapter aims to characterise both coil configurations and determine an optimum design in the case of ^{13}C cardiac MRI. This work is presented in three sections. Firstly, section 6.2 investigates the optimal number, position and phase shift of TxRx elements. This work is based on the 20 cm diameter loop coils previously used at UTSW, and characterises the B_1^+ transmit performance compared to existing common coil designs. Secondly, section 6.3 describes the designs and construction of an optimal four element Tx array, which is compared against the commercially available large Helmholtz pair through EM simulations, and benchtop and scanner measurements. Lastly, section 6.4 investigates the potential for multi-layer coils (as described in Chapters 4 and 5) to be geometrically decoupled in an overlapped configuration, allowing the translation of the high SNR of a single multi-layer coil into receive arrays.

6.2 Characterising Multiple TxRx Elements

The main benefit of individual TxRx elements is the ability to position the elements around the torso. As an example, the well-known quadrature configuration comprises of two elements. For cardiac imaging, this would comprise of one element placed above the chest and the second element placed to the left of the chest rotated by $90°$ with a phase shift of $90°$. This will theoretically improve the B_1^+ field efficiency by a factor of $\sqrt{2}$ within the centre of the heart [13, 14]. For B_1^- field efficiency increase, the phase shift must be reversed to $-90°$, typically achieved using a quadrature hybrid combiner [15]. This concept is further utilised in the recent development of parallel transmit (pTx typically) for high field ^{1}H MRI scans [16]. pTx divides the coil into separate independently powered transmit elements, allowing for more individual control of the RF excitation and consequently B_1^+ from each coil element for improved field

uniformity [17, 18]. Nevertheless, for ^{13}C MRI, multiple individual elements positioned around the body can still achieve both an increased B_1^+ uniformity and an increased B_1^+ efficiency, provided that the coil elements are set up optimally. This optimal element setup would require the correct number and size of elements, positioning around the torso, and an optimal phase shift to be applied.

6.2.1 Optimising 20 cm Loop Elements

At this early stage, individual TxRx elements of $20\,\mathrm{cm}$ diameter were investigated; these coil elements were readily available from our industrial partner, PulseTeq Ltd. EM simulations were performed to determine the transmit B_1^+ field achieved from the combination of between one and four 20 cm loop coils. Additionally, the flexibility of $20\,\mathrm{cm}$ elements allowed the elements to conform over any area of the torso with a constant $10\,\mathrm{mm}$ separation between the skin and the coil surface. These elements provide good depth penetration, with sufficient B_1^+ up to approximately $15\,\mathrm{cm}$ into the torso. The only configuration offered commercially is the 'Helmholtz configuration', where the current flow in the two elements is parallel (or equivalently a $180°$ phase difference is applied) and the elements are separated vertically by more than one coil diameter. For this investigation, EM simulations were used to determine the B_1^+ field through iterating over the position, phase, and number of 20 cm elements.

6.2.1.1 EM Simulation Setup

For transmit performance characterisation, two primary metrics were recorded: B_1^+ efficiency, and B_1^+ uniformity. B_1^+ efficiency was calculated as the mean B_1^+ over the ROI divided by the voltage, in units of $\mu\mathrm{T\,V^{-1}}$. Field uniformity was calculated as one minus the coefficient of variation (CV). CV is a dimensionless measure of variation, which is determined as the standard deviation of B_1^+ normalised by the mean B_1^+. The orientation and phase difference was varied for two, three, and four 20 cm diameter elements for cardiac ^{13}C MRI. The B_1^+ field from a single 20 cm element over the heart was well characterised previously in section 5.4.1.3, but is included again here for completeness. Each orientation, phase, and position requires an individual simulation; the method for one such EM simulation is described in the Methods chapter, section 3.2.2. E- and H-field monitors were placed at $30.98\,\mathrm{MHz}$, and all coils were tuned and matched with an S_{11} of $-20\,\mathrm{dB}$ or lower, representing less than $1\,\%$ reflected power.

In all cases with more than one coil, coupling between coil elements was reduced as far as possible. In orientations where two loops are overlapped, or in a quadrature configuration with one coil rotated $90°$ from the other, the S_{21} was ensured to be $-15\,\mathrm{dB}$ or lower. In orientations where two loops are in a Helmholtz configuration, due to the large depth penetration of the coil, the S_{21} was typically in the range of -10 to $-13\,\mathrm{dB}$. Decoupling through EM simulation is extremely time consuming as each iterative overlap and position requires a new simulation; discussions of achieving decoupling through EM simulation and benchtop measurements are presented later in the chapter, in section 6.4.1. All simulations were performed with a human voxel model (Hugo), with coil elements consistently positioned $10\,\mathrm{mm}$ above the surface of the torso, and centred on the heart. To capture the B_1^+ field representative of real-world coil positioning, all element models were cylindrically deformed around the torso. The conformity of the coil element would bring the effective coil centre closer to the ROI, improving B_1^+ efficiency. In the case of cardiac imaging, the ROI was taken as the voxels in the human model corresponding to heart tissue. The following orientations and phase configurations were investigated, and are identically labelled in Figure 6.1:

1. Single loop:
   (a) Placed above the chest (anterior).
2. Dual loops:
   (a) 'Helmholtz configuration', element 1 on the torso anterior, element 2 on the posterior, with a $180°$ phase shift.
   (b) 'Array configuration', elements 1 and 2 on the torso anterior overlapped for decoupling.
      i. With $0°$ phase shift.
      ii. With phase shift calculated from the angle between the coil centres and ROI centre, in this case a $75°$ phase shift.
   (c) 'Quadrature configuration', element 1 on torso the anterior, element 2 on the left lateral side, with a $90°$ phase shift.
3. Three loops:
   (a) Element 1 on the torso anterior, element 2 on the left lateral side, element 3 on the posterior, with a $90°$ phase shift between elements 1 and 2, and a $90°$ phase shift between elements 2 and 3.

4. Four loops:
   (a) 'Array configuration', elements 1 and 2 on the torso anterior overlapped for decoupling, elements 3 and 4 on the posterior, with overlap for decoupling.
      i. With $0°$ phase between overlapping elements, and a $180°$ phase between the anterior and posterior elements.
      ii. With a $90°$ phase shift between subsequent elements.
      iii. With the phase shift calculated from the angle between the coil centres and ROI centre, in this case phases of 0, 75, 205, $245°$.

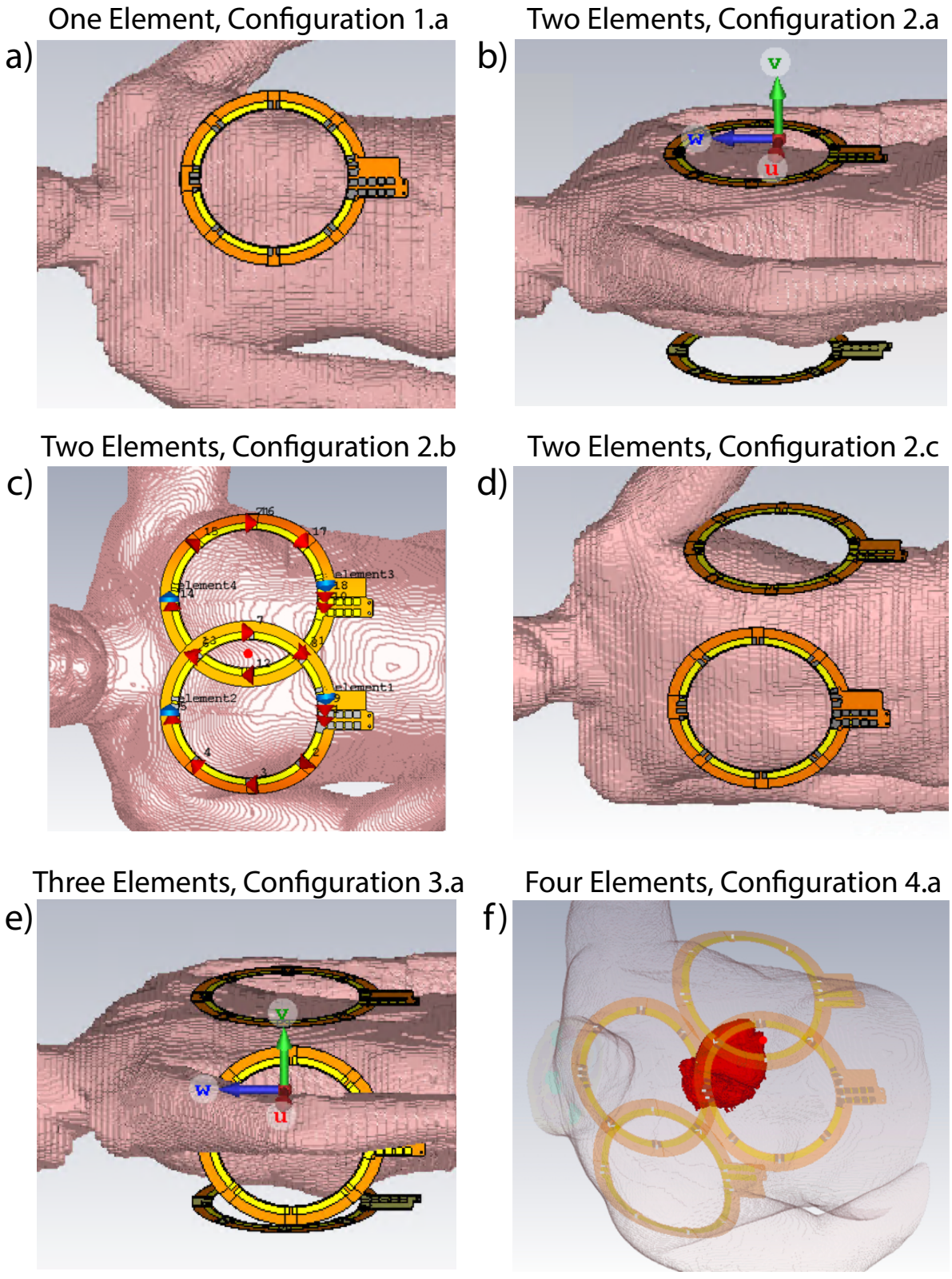

Figure 6.1: TxRx coil orientations investigated for optimised cardiac imaging. Common single coil configuration above the chest (a; '1.a'); common two coil configurations in 'Helmholtz configuration' (b; '2.a'), 'Array configuration' (c; '2.b'), and 'Quadrature configuration' (d; '2.c'); Triple coil configuration (e; '3.a'); and four coil 'Array configuration' (f; '4.a').

6.2.1.2 Results: Elements, Position and Phase

All ^{13}C cardiac transmit results are summarised below in Table 6.1. As a baseline, a single element positioned on the torso achieved a B_1^+ efficiency of $0.133\,\mu\mathrm{T\,V^{-1}}$ with uniformity of $67\,\%$. For two elements, the highest B_1^+ efficiency was achieved by the configuration where both elements were positioned on the top of the torso, overlapped such that there was maximum decoupling. Substantially improved efficiency was achieved with a $75°$ relative phase (corresponding to the relative angle formed between two coil centres and the centre of ROI). On the other hand, the highest B_1^+ uniformity was achieved by two elements in the Helmholtz configuration with one element above the torso and the other element below, correspondingly with a $180°$ relative phase. This high uniformity was due to the fields from both coils combining to penetrate through the entire heart, without the typical steep field drop-off from a single element.

For three elements, the field profile is balanced between B_1^+ mean and uniformity, showing an improvement in both B_1^+ uniformity and B_1^+ efficiency compared to two elements in the quadrature configuration. For four elements, due to the large size of each element and limited space with four elements positioned around the body, only one orientation was feasible for decoupling. This configuration comprises of two elements above and two elements below the torso, where the neighbouring elements are decoupled through overlap. With the four element setup, the first phase configuration achieves the highest B_1^+ uniformity at the expense of limited B_1^+ efficiency, whilst the second and third phase setups achieve comparable uniformity and efficiency values.

Table 6.1: Summary of B_1^+ efficiency, uniformity and additional B_1^+ metrics for one to four 20 cm diameter loops, positioned in the configurations displayed previously in Figure 6.1 with corresponding phase shifts.

Label	Element	Position on Torso	Relative Phase /°	B_1^+ Mean /μT	B_1^+ Uniformity	CV	StDev /μT	Max /μT	Min /μT
1.a	Single	Top	0°	0.133	67 %	0.332	0.044	0.268	0.059
2.a	Dual	Helmholtz	0, 180°	0.098	79 %	0.210	0.021	0.170	0.068
2.b.i	Dual	Top Overlapped	0, 0°	0.120	68 %	0.324	0.039	0.423	0.054
2.b.ii	Dual	Top Overlapped	0, 75°	0.183	63 %	0.366	0.067	0.423	0.074
2.c	Dual	Top & Left Quadrature	0, 90°	0.096	60 %	0.401	0.039	0.213	0.024
3.a	Three	Top & Left & Bottom	0, 90, 180°	0.121	70 %	0.297	0.036	0.224	0.054
4.a.i	Four	Top Bottom Overlapped	0, 0, 180, 180°	0.087	81 %	0.191	0.017	0.246	0.058
4.a.ii	Four	Top & Bottom Overlapped	0, 90, 180, 270°	0.132	73 %	0.267	0.035	0.274	0.058
4.a.iii	Four	Top & Bottom Overlapped	0, 75, 205, 245°	0.131	74 %	0.257	0.034	0.274	0.058

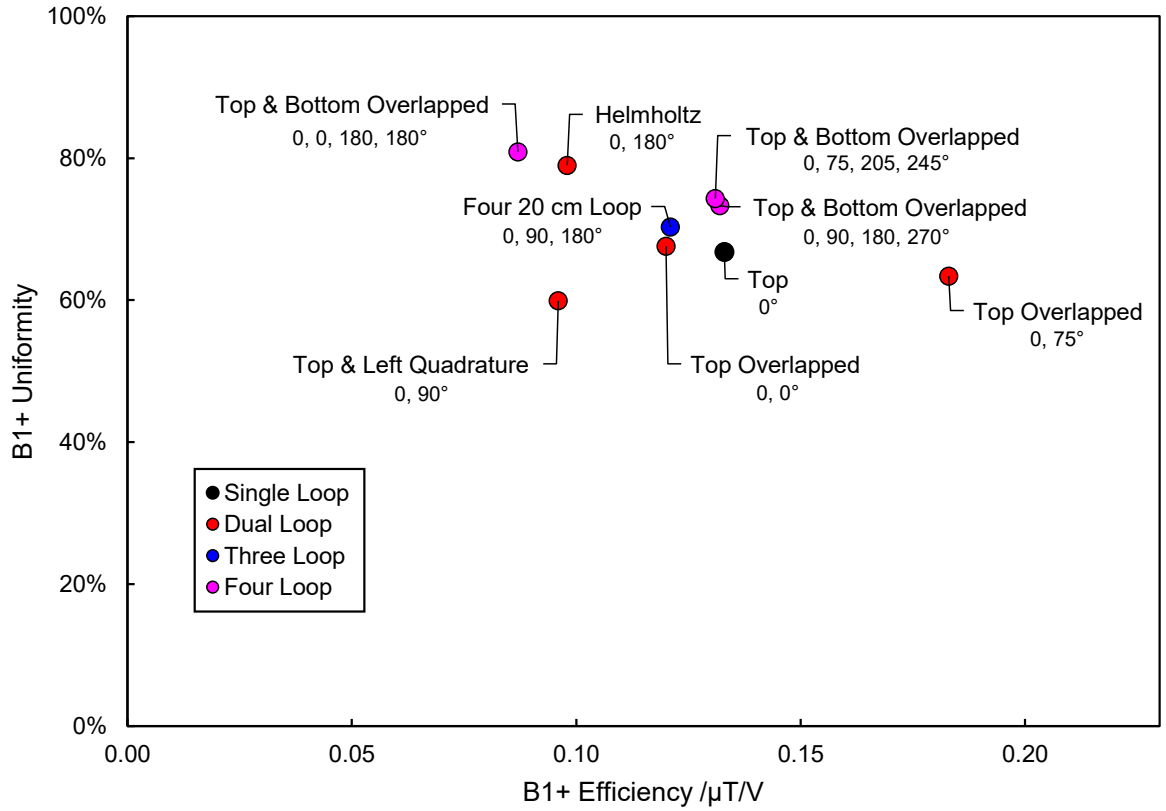

Figure 6.2: B_1^+ efficiency versus uniformity plot for single, dual, three, and four 20 cm elements, positioned around the body with specific phase shifts.

Overall, two viable designs using multiple 20 cm elements were identified for cardiac ^{13}C MRI, out-competing the transmit performance of a single element. The optimum setup for high B_1^+ efficiency is to use two elements positioned on top of the torso with $0, 75°$ phases, with B_1^+ of $0.183\,\mu\mathrm{T\,V^{-1}}$ representing a $37.6\,\%$ increase compared to a single element with comparable uniformity. The optimum configuration for high B_1^+ uniformity is using four elements with relative phases of $0, 0, 180, 180°$ achieving a uniformity of $81\,\%$. If both a high uniformity and higher B_1^+ efficiency are desired, the relative phases of $0, 75, 205, 245°$ achieves $0.131\,\mu\mathrm{T\,V^{-1}}$ mean B_1^+ efficiency with a uniformity of $74\,\%$. This B_1^+ efficiency is comparable to that of a single loop of $0.133\,\mu\mathrm{T\,V^{-1}}$, and achieves a substantial increase in uniformity from $67\,\%$ of a single element. These results show that strong improvements in coil transmit performance (of over $30\,\%$ increased field strength and $14\,\%$ increased field uniformity) can be achieved through optimising the number of elements, the relative phase, and the relative orientation of the coil.

6.2.1.3 Four Element Example Field Profile

The most promising design from this study, that of the four 20 cm elements with individual relative phases of 0, 75, 205, $245°$, is presented in more detail for subsequent comparison against other existing coil designs. The EM simulation model of the four elements, and the positioning of the coil around the body and heart, is shown in Figures 6.3 and 6.4. The S-parameter plots indicate good coil tuning and matching, with the S_{ii} of all four coils measured to be lower than $-20\,\mathrm{dB}$, and adequately minimised cross-coupling the S_{ij} ranging from $-11.5\,\mathrm{dB}$ to $-21.9\,\mathrm{dB}$. The large depth penetration of elements and close proximity between the opposing elements through the torso (top and bottom pairs) limited the extent of element decoupling that could be achieved. The 2D B_1^+ field map and vertical 1D plot through the centre of the heart for the phase configuration of 0, 75, 205, $245°$ are shown in Figure 6.3 c and Figure 6.4 c respectively. Good uniformity was achieved across approximately $20\,\mathrm{cm}$ depth, with a field strength of approximately $0.6\,\mu\mathrm{T\,V^{-1}}$. Within the ROI, a mean B_1^+ of $0.131\,\mu\mathrm{T\,V^{-1}}$ was achieved, with a B_1^+ uniformity of $74\,\%$. Finally, a ($10\,\mathrm{g}$ averaged) peak SAR of $0.171\,\mathrm{W\,kg^{-1}}$ was seen on the torso, with a hotspot around the sections of coil overlap (for decoupling) of approximately 0.10 to $0.12\,\mathrm{W\,kg^{-1}}$.

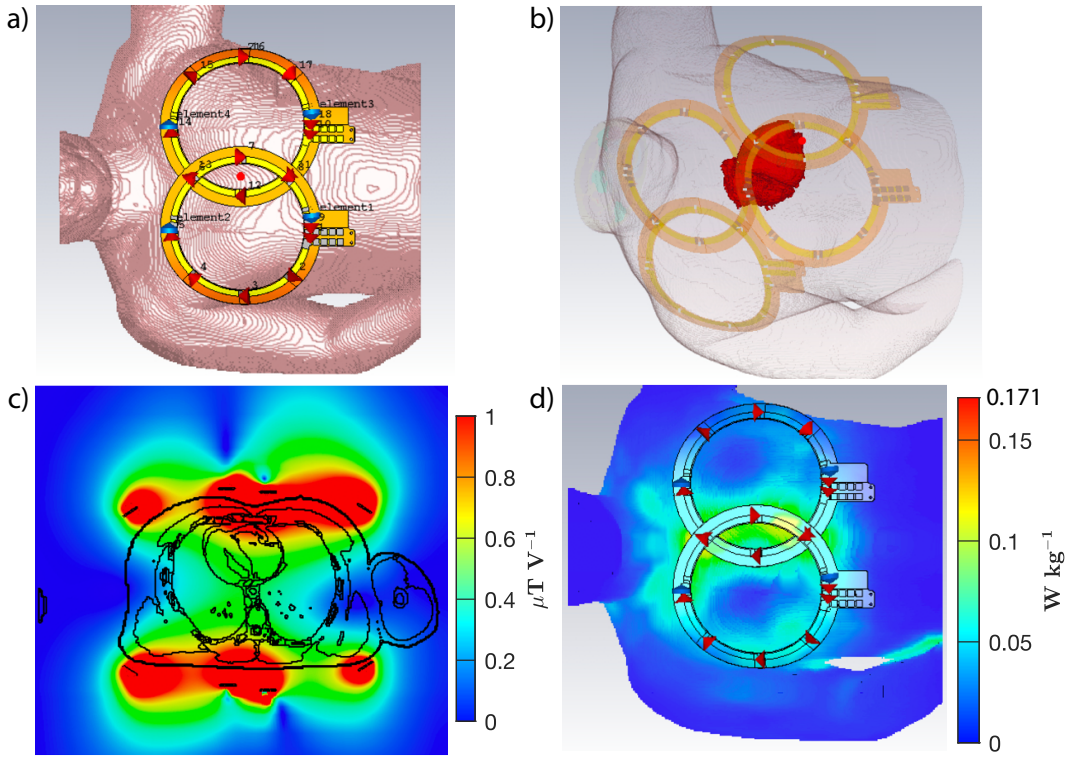

Figure 6.3: EM simulation of four 20 cm loop element, with 0, 90, 180, $270°$ phase. (a) and (b) EM model of 20 cm loop coil positioning. (c) 2D B_1^+ field map cross section through the torso. (d) SAR averaged over $10\,\mathrm{g}$ on torso surface.

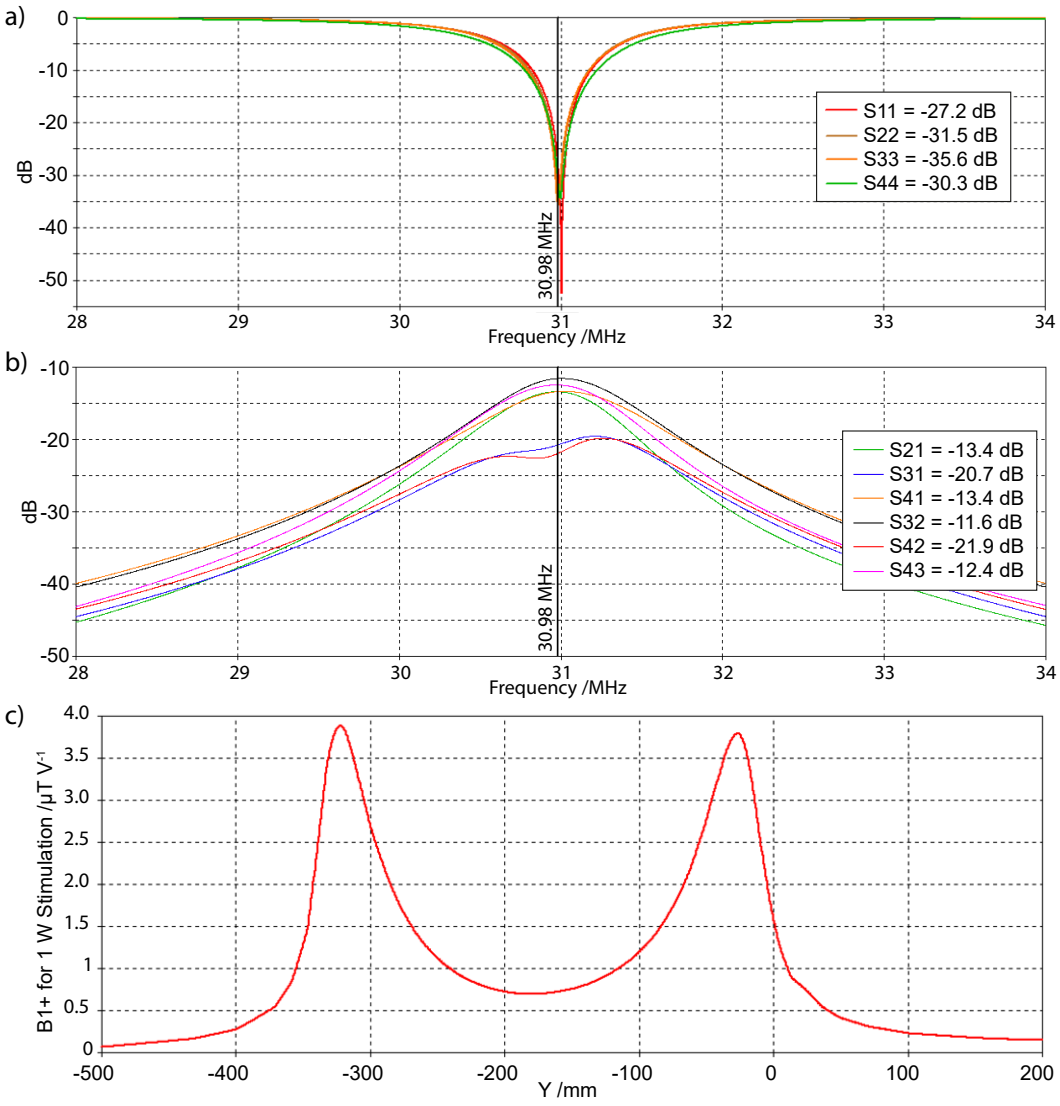

Figure 6.4: EM simulation of four 20 cm loop element, with 0, 90, 180, $270°$ phase. (a) Reflection S_{ii} coefficient of less than $-20\,\mathrm{dB}$. (b) Transmission S_{ij} coefficient showing coil decoupling. (c) On-axis 1D B_1^+ plot through ROI centre, where zero on the x-axis corresponds to the centre of the top coil element.

6.2.2 Comparison against Existing Coil Designs

Direct comparison of the coils modelled in this work against two existing commonly used ^{13}C coil designs allows for quantification of improvements made through optimisation and coil design. In addition to the four-element 20 cm loops simulated above, the transmit field profile of two alternative transmit coil designs were characterised through EM simulation. A large Helmholtz pair was simulated that represents a typical transmit coil configuration for cardiac ^{13}C MRI, with large elements that cover the entire torso. Additionally, a birdcage volume

coil for imaging the body was simulated; this simulated coil was retuned from an approximate model constructed of the existing Siemens ^{1}H body coil on the Trio scanner. Whilst ^{13}C birdcage volume coils are being developed for ^{13}C MRI (specifically for GE MRI systems with larger X-nuclei power amplifiers), currently there are no existing publications regarding their design or field profile. The B_1^+ field profiles of all three designs were obtained through EM simulation, following the method described in section 3.2.2, with the coil placed on a human voxel model and the ROI taken as the heart voxels.

6.2.2.1 Large Helmholtz Pair

The large Helmholtz pair was modelled after the existing two element Tx coil used at OCMR (constructed by Rapid Biomedical), Oxford, for hyperpolarized ^{13}C studies. Additionally, the field from the clamshell Tx coil used by various sites (similarly constructed by Rapid Biomedical, described above in section 6.1.1) is comparable to the two element Tx coil at Oxford, and is well represented by this EM modelling. The EM model for the Tx coil consists of two large square loops, dimensions $28.4\,\mathrm{cm} \times 28.4\,\mathrm{cm}$, placed in a Helmholtz configuration above and below the torso. At this stage, only EM simulations were used for coil comparison for consistency and minimal external factors; measured scanner field maps of this coil are presented later in section 6.3.1.1. The coil elements were positioned over the heart, vertically separated $10\,\mathrm{mm}$ above and below the torso as shown in Figures 6.5 and 6.6 below. It should be noted that in this simulation setup, the transmit coils were brought closer to the torso for fair compassion, however in practice, due to the transmit only design, the transmit elements are further away from the torso to accommodate the receive elements. Adequate coil tuning and matching was achieved with S_{11} and S_{22} of lower than $-20\,\mathrm{dB}$; however, extremely strong coupling was present with an S_{21} and S_{12} of around $-4.3\,\mathrm{dB}$. The strong coupling between elements is primarily due to the large size and depth penetration of the coils. The 2D B_1^+ field map and vertical 1D plot through the centre of the heart are depicted in Figure 6.5 d and Figure 6.6 b, showing high B_1^+ uniformity with a corresponding field strength of $0.4\,\mu\mathrm{T}$ for $1\,\mathrm{W}$ of power input. Within the ROI, a mean B_1^+ of $0.073\,\mu\mathrm{T\,V^{-1}}$ was achieved, with a B_1^+ uniformity of $91\,\%$. A ($10\,\mathrm{g}$ averaged) peak SAR of $0.164\,\mathrm{W\,kg^{-1}}$ was seen on the torso, with a hotspot around the conductor regions on the edge of the torso (sides and neck) of approximately 0.10 to $0.14\,\mathrm{W\,kg^{-1}}$.

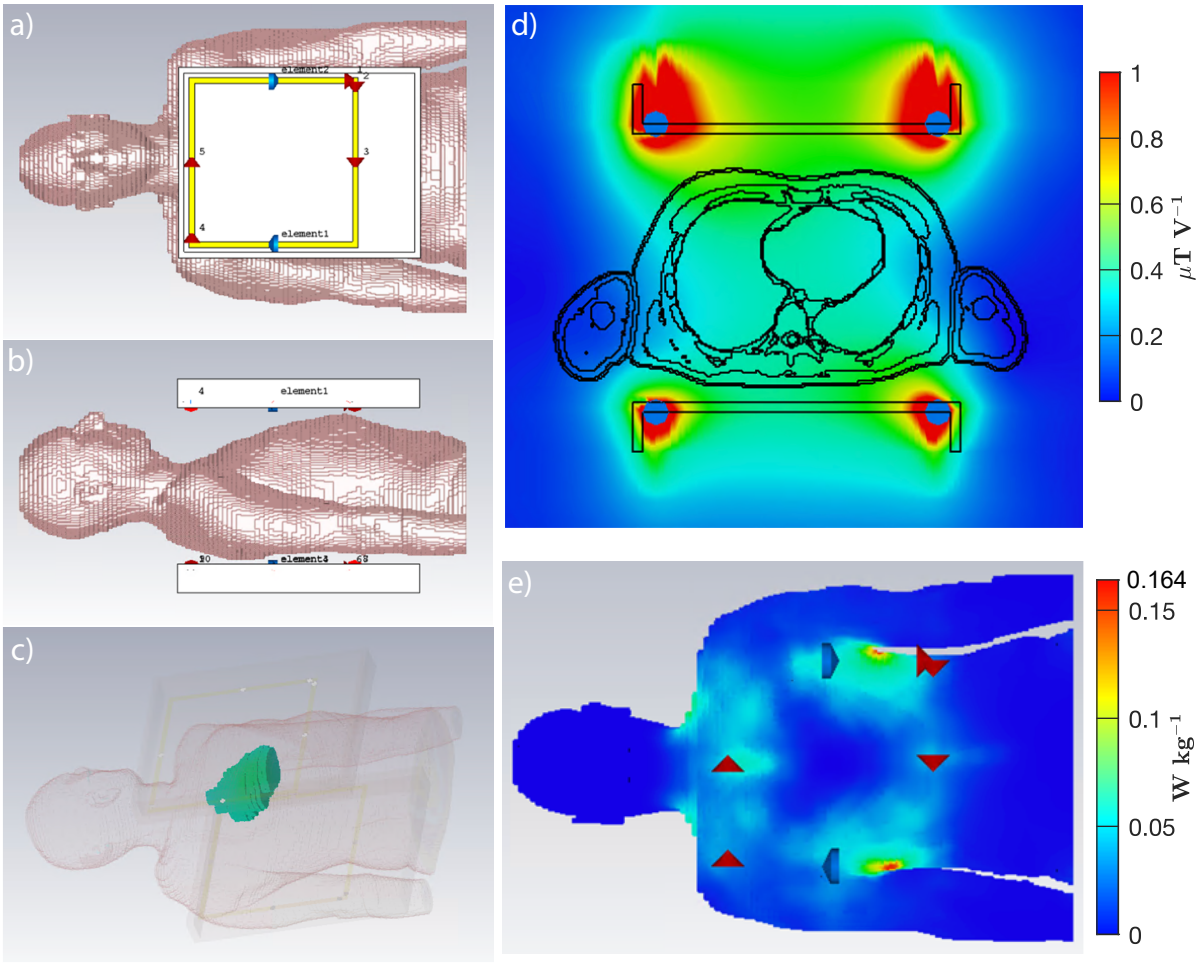

Figure 6.5: EM simulation of large $28\,\mathrm{cm} \times 28\,\mathrm{cm}$ Helmholtz pair with 0, $180°$ phase. (a) and (b) EM model coil position on the torso. (c) B_1^+ field on surface of heart voxels. (d) 2D B_1^+ field map cross section through the torso. (e) SAR averaged over $10\,\mathrm{g}$ on torso surface.

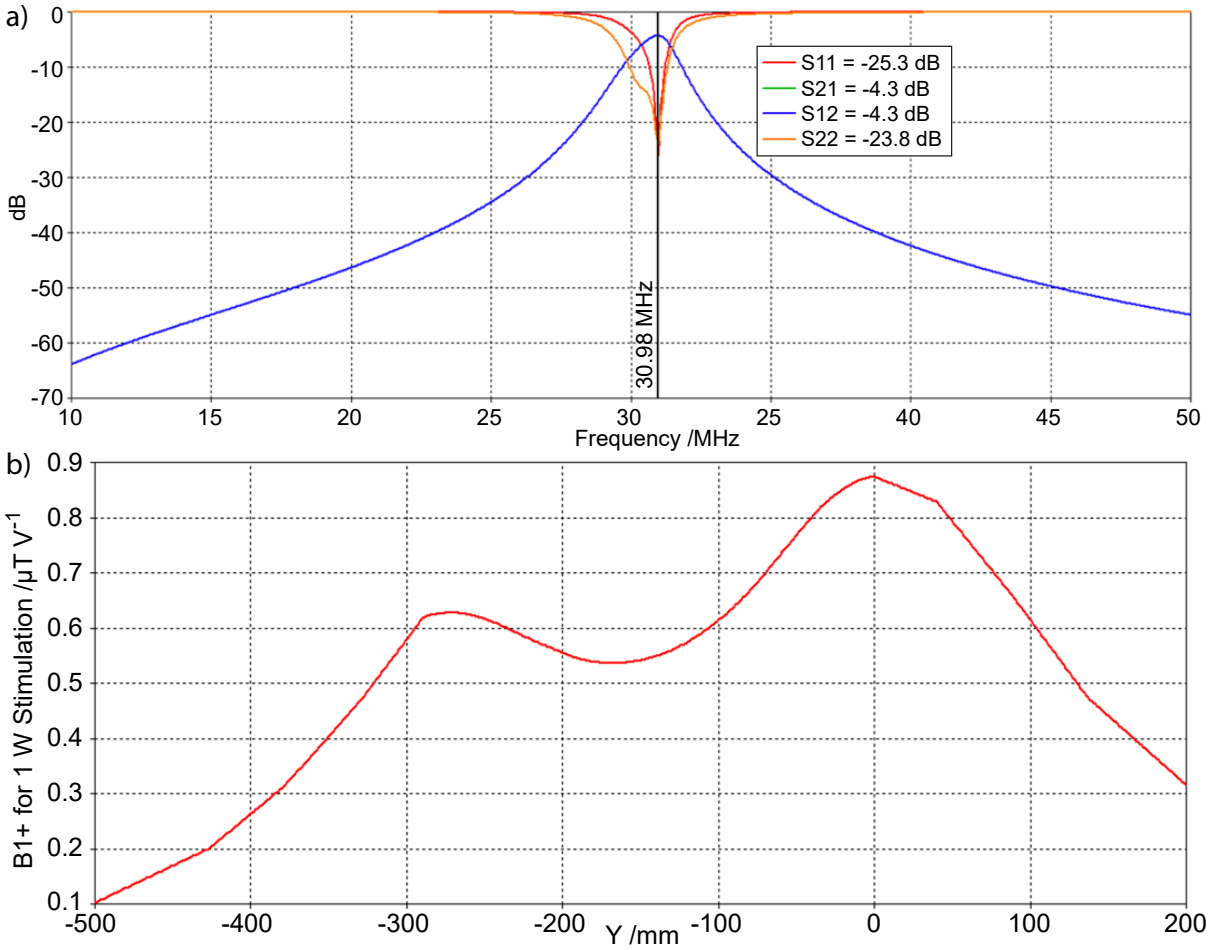

Figure 6.6: EM simulation of large $28\,\mathrm{cm} \times 28\,\mathrm{cm}$ Helmholtz pair with $0, 180°$ phase. (a) Reflection S_{ii} coefficient of less than $-20\,\mathrm{dB}$ and transmission S_{21} showing high amount of coupling at $-4.3\,\mathrm{dB}$. (b) On-axis 1D B_1^+ plot through ROI centre, where zero on the x-axis corresponds to the centre of the top coil element..

6.2.2.2 Quadrature Birdcage

Despite several ^{31}P body coils, there are no published designs of a human ^{13}C body coil. In this work an EM model of an approximate Siemens ^{1}H body coil for the $3\,\mathrm{T}$ Trio scanner was modelled and retuned for ^{13}C MRI at $30\,\mathrm{MHz}$. Birdcage volume coil designs typically comprise of two end-rings, with a series of parallel rungs connecting the two rings. With applied RF power, concentric H-fields are formed along each conductor, with the overall B_1^+ field formed within the enclosed volume of the coil comprising of the circular B_1^+ fields combined from the individual rungs. Typically, more rungs lead to improved field uniformity; however, this creates more resonance modes. Much like a filter, birdcage designs can either be high pass, low pass or band-pass; this design element is determined by the position of lumped element capacitors on

the rungs, rings, or both, respectively. The birdcage volume coil modelled here comprised of 16 rungs set up in a band-pass configuration such that capacitors were placed on both the end rings and rungs, leading to 48 discrete ports. The birdcage design was modelled with a diameter of $620\,\mathrm{mm}$ and length $600\,\mathrm{mm}$, enshrouded by a thick EM shield typical for volume coils to minimise coupling to external objects, as shown in Figure 6.7. The human voxel model was imported with $2\,\mathrm{mm}$ isotropic resolution, and positioned such that the centre of the heart was in isocentre of the volume coil. The coil was excited in a quadrature configuration to achieve a stronger B_1^+ circular polarization. To achieve this, two excitation input ports were selected on the rungs separated by $90°$ (in this case, rung 1 and rung 5), with a $90°$ phase shift applied at the input. The human voxel model was rotated about the centre such that the two excitation ports were placed symmetrically across the mid-line of the body voxel model, allowing coil loading to be symmetrical across both input ports for optimal S_{11} and S_{22}. Post-simulation, a series of resonance modes are observed (dependent on the number of rungs) in the volume coil through the S-parameters [19]. The correct resonance mode, representing the zeroth order homogeneous mode, was determined visually by simulating the B_1^+ at each resonance mode and selecting the mode with the highest B_1^+ uniformity across the coil FOV. Subsequently, the coil was tuned with the desired resonance at $30\,\mathrm{MHz}$, with S_{11} and S_{22} lower than $-20\,\mathrm{dB}$. A high magnitude of coupling was seen between the two quadrature excitation ports, with S_{21} and S_{12} of around $1.7\,\mathrm{dB}$, which is typical of the quadrature birdcage design. The 2D B_1^+ field map is shown in Figure 6.7 c, showing excellent field uniformity of $98.5\,\%$ with a poor field efficiency of $0.3\,\mu\mathrm{T\,V^{-1}}$ compared to all other coil designs, summarised in Table 6.2.

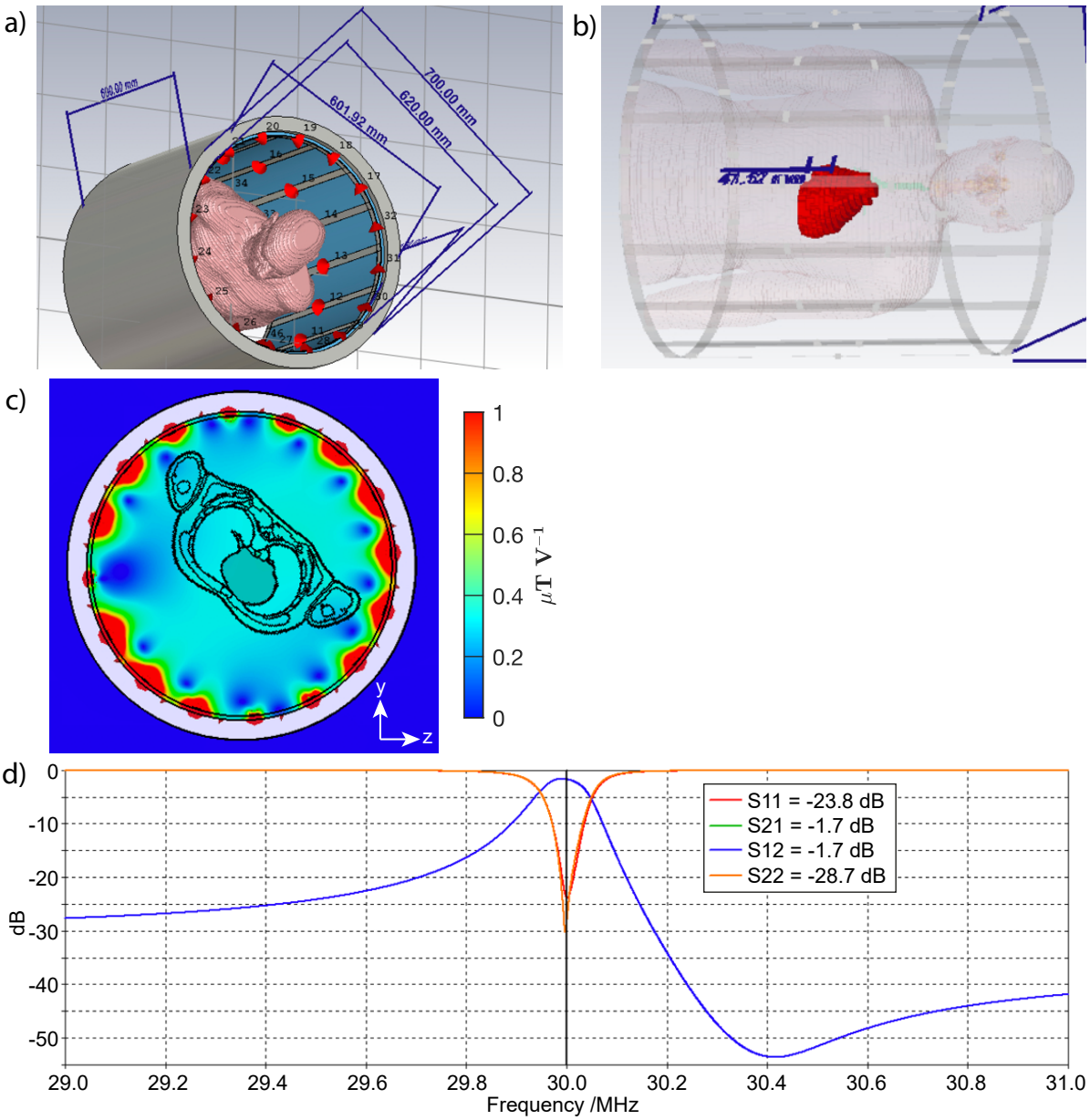

Figure 6.7: EM simulation of quadrature birdcage volume coil with 16 rungs. (a) and (b) EM model of volume coil positioned isocentre with the heart. (c) 2D B_1^+ field map cross section through the torso. (d) Reflection S_{ii} coefficient of less than $-20\,\mathrm{dB}$ and transmission S_{21} showing high amount of coupling at $-1.7\,\mathrm{dB}$.

6.2.3 Overall Field Comparison

The B_1^+ efficiency versus uniformity values for the four channel 20 cm loop (at previously described configurations) was compared against the large Helmholtz pair and the quadrature birdcage coil designs; the results are summarised below in Table 6.2. The four 20 cm loops achieved up to twice the B_1^+ efficiency and had approximately 10 – $20\,\%$ lower uniformity

compared to the other designs. The larger $28\,\mathrm{cm}$ Helmholtz pair, however, was non-optimal due to strong coupling between the two loops and the EM field inefficiently radiated across a volume significantly larger than the heart. Additionally, the B_1^+ field strength of the birdcage coil would be insufficient without a larger dedicated ^{13}C power amplifier, as the maximum voltage achievable with the Siemens Trio system of approximately $300\,\mathrm{V}$ would result in a B_1^+ field of $17.1\,\mu\mathrm{T}$, which may be insufficient for typical pulse sequences. Overall, whilst the 20 cm diameter loops lacked the field uniformity, both the two element Helmholtz pair and birdcage coil achieved poor transmit performance due to their unnecessarily large FOV for cardiac MRI. Figure 6.8 empirically shows the trade-off across the three coil designs, with additional single element coil B_1^+ values included for comparison. Previously, section 5.3.2.1 shows that for a conventional single loop, the B_1^+ uniformity versus efficiency curve generated by sweeping coil diameter is highly non-linear. However, it is interesting to note, that whilst the trade of between B_1^+ efficiency and uniformity is expected, there is no reason to expect this trade off to be linear. When plotting the different classes of simulated coil designs (ranging from signal elements, to multiple element arrays and volume coils) in Figure 6.8, good linearity is seen between B_1^+ efficiency and uniformity, with R^2 of 0.8963.

Table 6.2: Summary of B_1^+ metrics within a ROI for three coil designs: four-element 20 cm loops at two optimum phase configurations, a two-element large Helmholtz pair, and quadrature birdcage design.

TX Element Design	Phase Difference /°	B_1^+ Mean /μT	B_1^+ Uniformity	CV	StDev /μT	Max /μT	Min /μT
Four 20 cm Loops	0, 75, 205, 245	0.131	74%	0.257	0.034	0.274	0.058
Four 20 cm Loops	0, 0, 180, 180	0.087	81%	0.191	0.017	0.246	0.058
Two Large 28 cm Loop Pair	0, 180	0.073	91%	0.087	0.006	0.091	0.073
Quadrature Birdcage	0, 90	0.057	99%	0.015	0.001	0.060	0.055

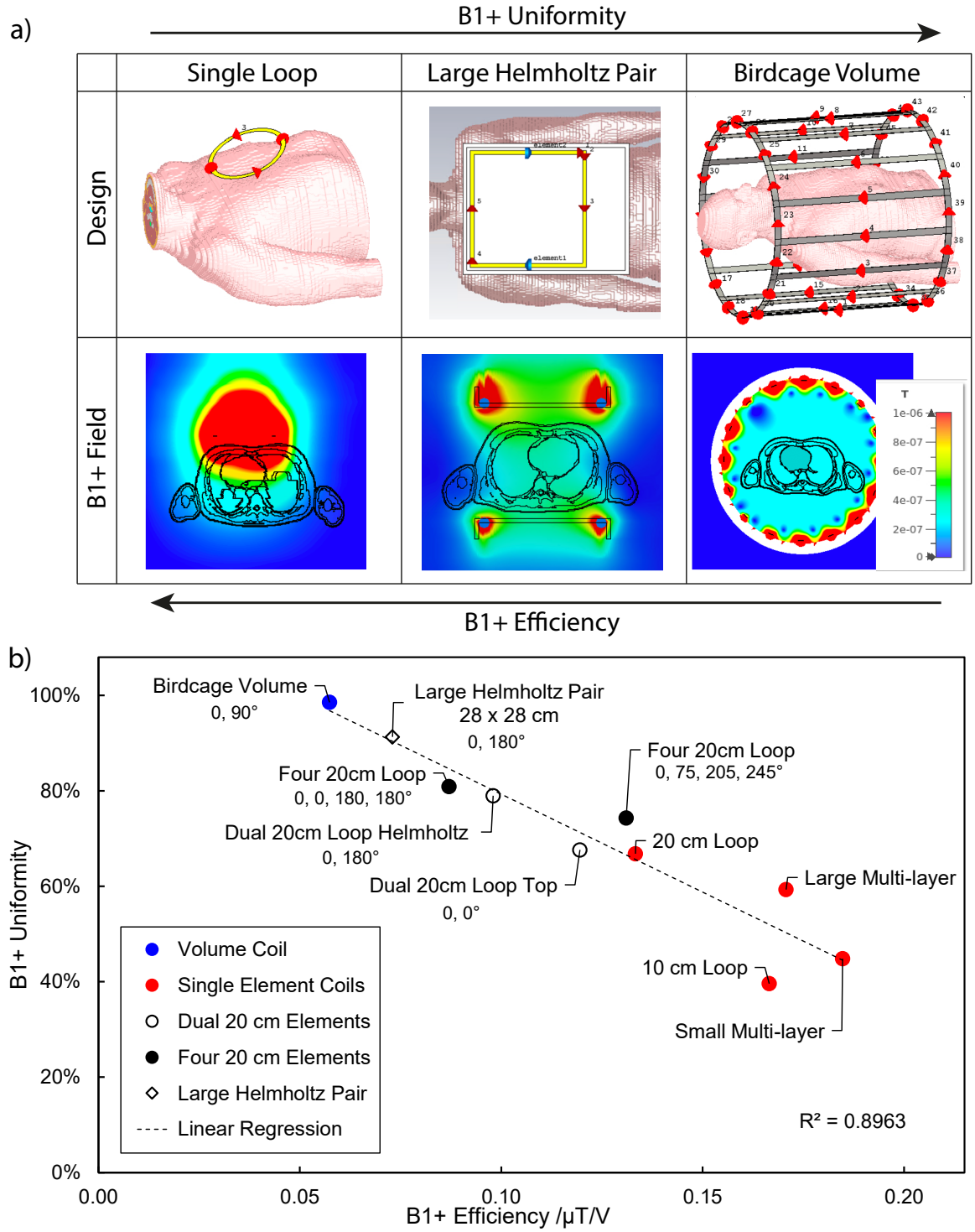

Figure 6.8: Overall simulated B_1^+ values from different existing coil designs showing the trade-off between B_1^+ uniformity and B_1^+ efficiency. (a) EM model and 2D B_1^+ field for a single loop, large Helmholtz pair, and birdcage coil, ordered in increasing B_1^+ uniformity and decreasing B_1^+ efficiency from left to right. (b) Plot of B_1^+ efficiency and B_1^+ uniformity for the birdcage coil (filled blue marker), dual Tx Rx element 20 cm loops (outlined circle markers), four element 20 cm loops (filled black markers), large Helmholtz pair (outlined diamond marker) and single element coils (filled red markers). A linear regression line is plotted, which shows the trade-off between B_1^+ efficiency and uniformity across these coil designs, with an R^2 of 0.8963.

The field efficiency and uniformity from this section serves as a benchmark for comparison in subsequent sections. The key to achieving high B_1^+ uniformity without the corresponding poor B_1^+ efficiency on transmit is to design elements with EM fields localised in the heart area without excess EM fields around the torso. In the following section, we further explore the possibility of using phase shifts and element overlap to improve field efficiency.

6.3 Developing a Four Element Tx Array

Following on from the work optimising the position of four 20 cm loops, it was found that the optimum position for ^{13}C cardiac imaging consists of two elements above the torso and two elements below. Additionally, B_1^+ efficiency improvements were obtained by optimising the phase shift between the four elements. However, the 20 cm loops were insufficiently large, as the B_1^+ uniformity was around $10\,\%$ lower compared to the existing large Helmholtz pair, and even lower compared to a volume coil. As such, there is room for improved B_1^+ performance by exploring element dimension, overlap distance, and phase shifts.

As a brief overview of the work in developing a Tx array, section 6.3.1 uses EM simulations to identify two array designs selected for their improved B_1^+ uniformity and efficiency trade-off. Both arrays were constructed, and benchtop measurements and EM simulations of 2D B_1^+ field profiles were compared to determine improvements in B_1^+ through varying overlap in section 6.3.2. Scanner measurements were performed on the constructed four element Tx arrays to verify phase improvements from previous EM simulations for comparison to the existing large Helmholtz pair detailed in section 6.3.3. Finally, section 6.3.4 compares the performance of the designed transmit coil within the general scope of cardiac imaging.

6.3.1 Simulating Tx Element Designs

EM simulations were performed using FDTD with hexahedral meshing, which efficiently captured the rectangular coil elements and allowed a human voxel model to be implemented. The E- and H-field monitors were recorded at $30.98\,\mathrm{MHz}$. For investigation of the optimal design, surface elements were positioned above and below the torso. For comparison against previously simulated coil designs, B_1^+ efficiency and uniformity were calculated inside only the heart voxels of a human voxel model. Each individual channel was tuned to achieve a reflec-

tion of $-20\,\mathrm{dB}$ (S_{11}) or better. A $0.03\,\Omega$ effective series resistance (ESR) was added to each discrete port to represent resistive losses in capacitors.

The transmit performance of arrays is particularly susceptible to patient size; as patient size changes, the optimum coil dimensions change. It is unfeasible to optimise a coil for all possible patient sizes: as an example, a smaller vertical separation will require less depth penetration and experience stronger vertical element coupling, and is suited better by a smaller element dimension. For consistency across all simulated results in this chapter, the elements were positioned with a predefined vertical separation of $250\,\mathrm{mm}$, with the ROI taken as the voxels of the human heart model.

6.3.1.1 Optimising Dimension Parameters

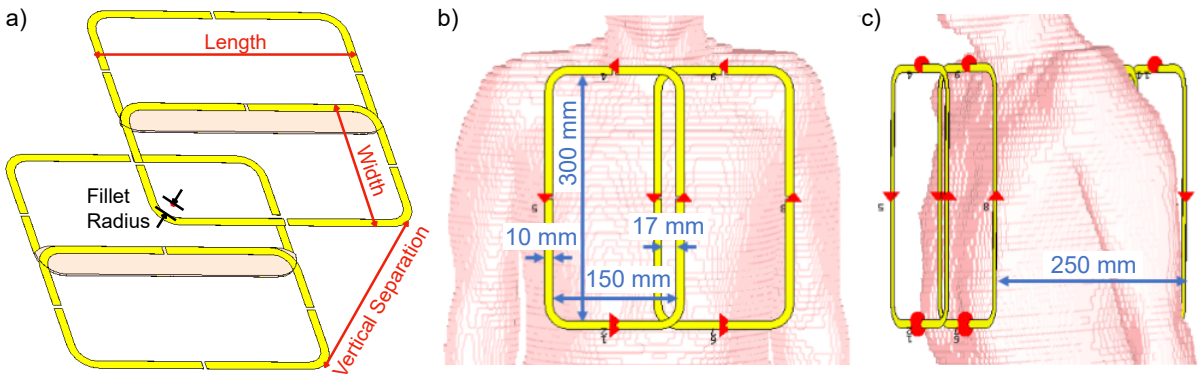

Figure 6.9: EM model showing a four element Tx array constructed from four design parameters: fillet radius, length, width, and element overlap.

Previous work has shown that square elements achieve improved B_1^+ uniformity and coverage compared to circular elements [20]. However, square elements comprised of sharp corners lead to unwanted EM hotpots (similarly to the star-shaped multi-layer designs described in Chapter 4). The sharp edges of the square conductor can be reduced using a 'fillet' tool (Solidworks), where the fillet radius is defined as the outer radius of curvature of the conductor. Given the conductor width of $10\,\mathrm{mm}$, a $10\,\mathrm{mm}$ fillet represents a square conductor with a curved outer edge, with a sharp inner edge. A $0\,\mathrm{mm}$ fillet represents a square conductor with sharp outer edge and inner edge. Values above $10\,\mathrm{mm}$ represent curving of both the inner and outer conductor edges. In total, three parameters representing element dimension were investigated (shown in Figure 6.9), fillet radius, element width and length, and element overlap. Presently, the

element overlap implemented corresponds to the optimal overlap for geometric decoupling (of minimum S_{21} between two elements). The parameters length, width, and fillet radius are investigated with the overlap kept at the optimum, and subsequently in section 6.3.1.2 the element overlap and phase are varied.

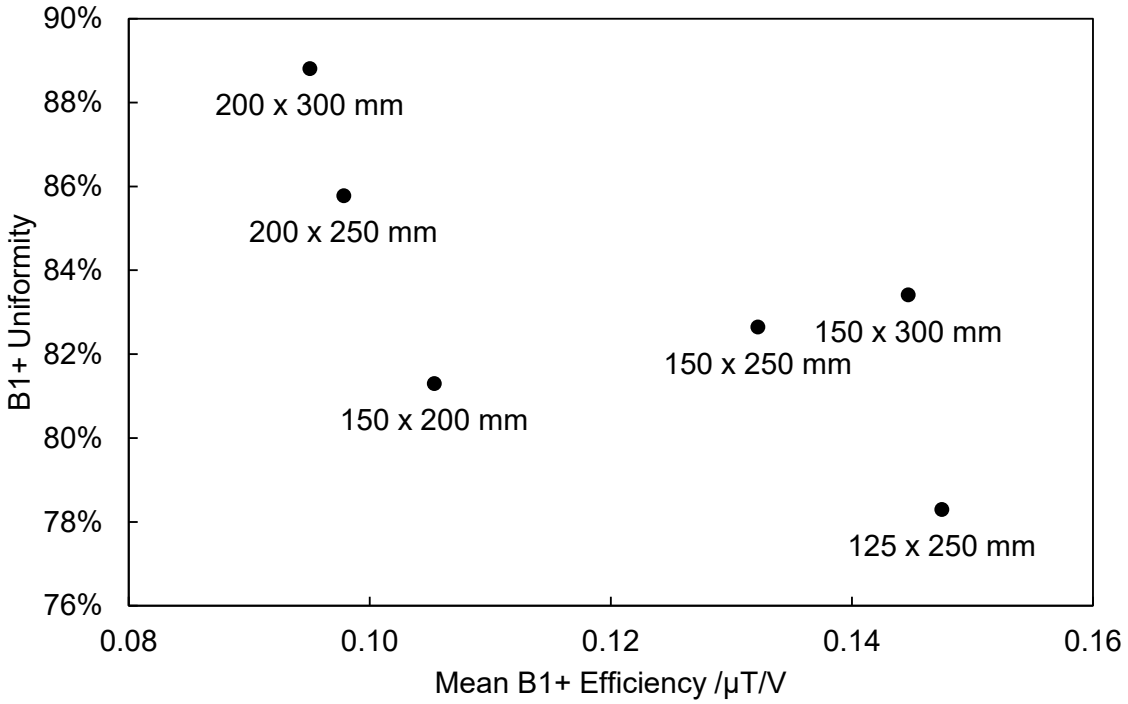

Figure 6.10: Mean B_1^+ field efficiency versus B_1^+ field non-uniformity plot at $250\,\mathrm{mm}$ vertical separation. Several element dimensions for a four-loop array are plotted, each with a fillet radius of $10\,\mathrm{mm}$ and elements overlapped individually for optimum decoupling. Two designs that stand out are $200\,\mathrm{mm} \times 300\,\mathrm{mm}$ with high B_1^+ uniformity and $150\,\mathrm{mm} \times 300\,\mathrm{mm}$ with high B_1^+ efficiency.

Numerous coil designs and parameters were simulated; the full dataset optimising the four element array is shown in Appendix H. To efficiently visualise the data from the coil elements, the B_1^+ metrics were summarised using plots of B_1^+ field efficiency versus uniformity. The element dimensions (width and length) are varied with a constant fillet radius of $10\,\mathrm{mm}$ in Figure 6.10. Amongst the six element dimensions compared, two designs showed good B_1^+ efficiency and uniformity: with the $150\,\mathrm{mm} \times 300\,\mathrm{mm}$ element showing a skew towards efficiency, and the $200\,\mathrm{mm} \times 300\,\mathrm{mm}$ element showing a skew towards higher uniformity. The fillet radius was varied from 0 to $30\,\mathrm{mm}$ for two element dimensions in Figure 6.11: four $150\,\mathrm{mm} \times 300\,\mathrm{mm}$ elements (shown in red) were compared against two $200\,\mathrm{mm} \times 200\,\mathrm{mm}$ elements (of compara-

ble area, shown in blue) in a Helmholtz configuration. It was found that typically a $30\,\mathrm{mm}$ fillet improved the B_1^+ efficiency in both two and four element configurations (which is expected as the element becomes more circular). However, it was found that in the four loop case, the magnitude of improvements were much larger, and further improvements in B_1^+ uniformity were achieved from $20\,\mathrm{mm}$ to $30\,\mathrm{mm}$ fillet radius.

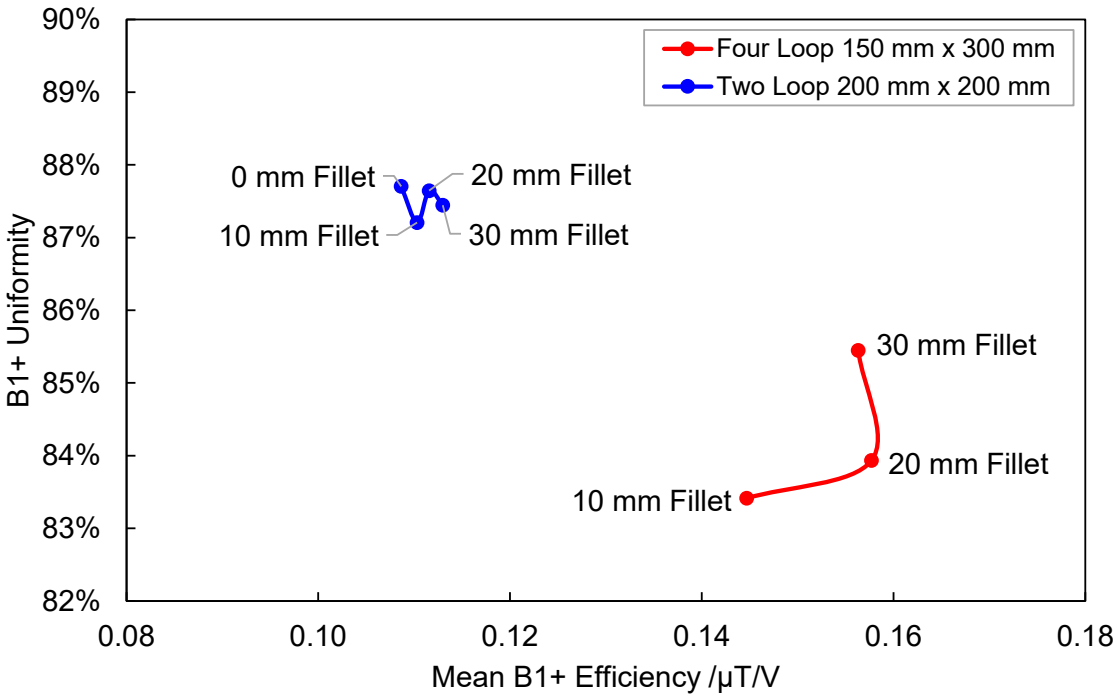

Figure 6.11: Mean B_1^+ field efficiency versus B_1^+ field non-uniformity plot at $250\,\mathrm{mm}$ vertical separation. Fillet radius is varied from 0 to $30\,\mathrm{mm}$ on a $150\,\mathrm{mm} \times 300\,\mathrm{mm}$ four loop array (red), and on a $200\,\mathrm{mm} \times 200\,\mathrm{mm}$ two loop coil (blue).

Overall, two elements were identified and investigated further:

1. Element dimensions of $150\,\mathrm{mm} \times 300\,\mathrm{mm}$, fillet radius of $30\,\mathrm{mm}$, referred to as 'small element design', with greater B_1^+ efficiency.
2. Element dimensions of $200\,\mathrm{mm} \times 300\,\mathrm{mm}$, fillet radius of $30\,\mathrm{mm}$, referred to as 'large element design', for greater B_1^+ uniformity

6.3.1.2 Optimising Overlap and Phase Shift

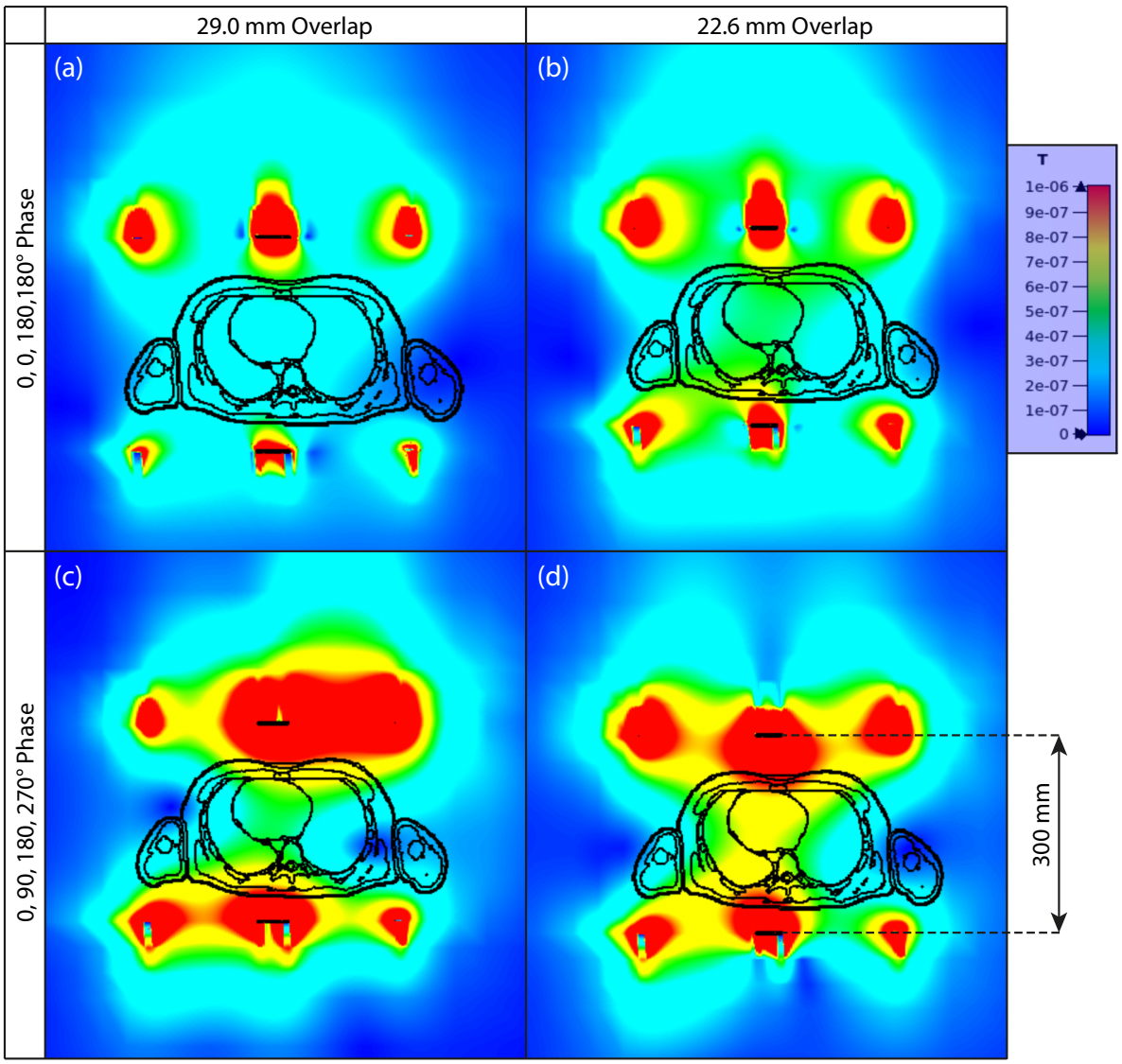

Figure 6.12: 2D Cross sectional B_1^+ field from four element array of $200\,\mathrm{mm} \times 300\,\mathrm{mm}$ as shown in figure 6.9, with $300\,\mathrm{mm}$ vertical separation at: (a) $29\,\mathrm{mm}$ overlap with 0, 0, 180, $180°$ phase, (b) $22.6\,\mathrm{mm}$ overlap with 0, 0, 180, $180°$ phase, (c) $29\,\mathrm{mm}$ overlap with 0, 90, 180, $270°$ phase, and (d) $22.6\,\mathrm{mm}$ overlap with 0, 90, 180, $270°$ phase.

Following the investigation into element dimensions, two additional parameters were investigated: the element overlap distance and the relative phase shift. For two identical overlapping elements, the overlap distance (width of the overlap region) is determined as the coil width minus the distance between the centre of the two elements. The optimum overlap represents the position with zero mutual inductance between two elements. Whilst it is well-known that elements positioned at this overlap are geometrically decoupled [10], which is necessary for

high receive sensitivity, the associated lower Q-values from non-optimal overlaps may not necessarily offset the potential increase in B_1^+ by shaping the field to be more centrally positioned over the ROI. In a case of non-optimised overlap (for example when the overlap is smaller than optimum), the EM field is concentrated within the overlapping region of the two elements. For cardiac MRI, this overlapping region is closer to the heart ROI, as opposed to the decoupled case, where B_1^+ 'lobes' are at the centre of the coil elements. As such, a specific overlap distance that is smaller than the optimal overlap may theoretically increase the B_1^+ efficiency. This is highly dependent on the organ being imaged; for example, in the case of lung MRI, the coils should be optimally decoupled to minimise EM field at the overlap region to minimise the field skewing towards the overlap region. However, as a result of the concentrated B_1^+ field in the coil overlap region, the optimum phase may not be determined by the angle between the coil centres and ROI centres. As the effects of phase shift and element overlap were highly coupled, the simulations presented in this section attempt to characterise the effects on B_1^+ field from both overlap and phase simultaneously. Such effects on the B_1^+ field are illustrated visually in Figure 6.12, showing improvements in the B_1^+ field when changing the optimum overlap ($29\,\mathrm{mm}$) to a less than optimum overlap ($22.6\,\mathrm{mm}$), and improvements from the changing the standard Helmholtz phase (0, 0, 180, $180°$) to a circularly polarized phase (0, 90, 180, $270°$).

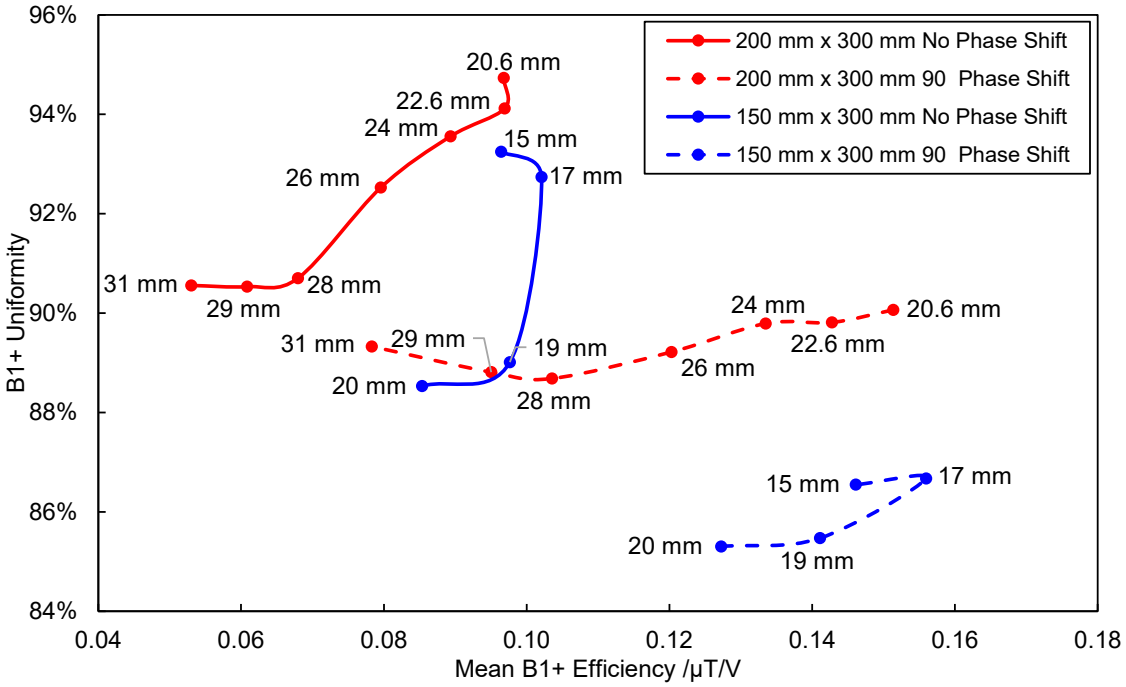

Figure 6.13: Mean B_1^+ field efficiency versus B_1^+ field non-uniformity plot at $300\,\mathrm{mm}$ vertical separation. Overlap distance of $200\,\mathrm{mm} \times 300\,\mathrm{mm}$ element array (red) and $150\,\mathrm{mm} \times 300\,\mathrm{mm}$ four loop arrays (blue) were compared with phase configurations of 0, 0, 180, $180°$ (solid lines), and 0, 90, 180, $270°$ (dashed lines).

EM simulations were performed to iterate over element overlaps at two phase shifts using the large element design ($200\,\mathrm{mm} \times 300\,\mathrm{mm}$), positioned at $300\,\mathrm{mm}$ vertical separation (which better represents large array positioning over typical patients compared to $250\,\mathrm{mm}$). Additionally, as a point of comparison, the element overlap and phase shift effects on the B_1^+ field were compared from the small element design ($150\,\mathrm{mm} \times 300\,\mathrm{mm}$), at $300\,\mathrm{mm}$ vertical separation. Using B_1^+ efficiency versus uniformity plots, a series of overlap distances were investigated: for the larger element design, between $31\,\mathrm{mm}$ and $20.6\,\mathrm{mm}$, and for the smaller element design, between $20\,\mathrm{mm}$ and $15\,\mathrm{mm}$. The range of overlap values for both coils include the position for optimum decoupling and the minimum overlap for both elements to be reasonably tuned at $30\,\mathrm{MHz}$. For both elements, two phase configurations were investigated: firstly 'no phase shift' of 0, 0, 180, $180°$ phases, and secondly a '$90°$ phase shift' of 0, 90, 180, $270°$ phases. Figure 6.13 shows B_1^+ efficiency versus uniformity curves from iterating element overlap for the four possible combinations. comparing the field values, the larger element (red) achieves a higher field uniformity and field efficiency compared to the smaller element (blue) across all overlaps.

The optimum overlap width for the larger element was achieved at $29\,\mathrm{mm}$ for maximum decoupling, whilst the optimum overlap width for the smaller element was achieved at $20\,\mathrm{mm}$ for maximum decoupling. In both cases an improvement in B_1^+ efficiency was achieved using an overlap distance that was less than the optimum. For the larger loop, the overlap width for the highest B_1^+ efficiency was $20.6\,\mathrm{mm}$; this was the lower bound achievable with a tuned element (less overlap led to excessively strong coupling making coil tuning challenging), with an S_{21} and S_{43} of $-6.1\,\mathrm{dB}$ and $-7.4\,\mathrm{dB}$ respectively, as shown in Table 6.3. For the smaller loop, the overlap width for the highest B_1^+ efficiency was $17\,\mathrm{mm}$, beyond which the B_1^+ efficiency decreased, corresponding to an S_{21} and S_{43} of $-7.3\,\mathrm{dB}$ and $-5.7\,\mathrm{dB}$ respectively. At the optimum overlap, the larger element design achieved the same B_1^+ efficiency as the smaller element design, whilst simultaneously achieving around $5\,\%$ improved uniformity.

Introducing a $90°$ phase shift from the 0, 0, 180, $180°$ phase to the 0, 90, 180, $270°$ phase (in Figure 6.13 shown as a shift from the solid lines to the dashed lines) between horizontally overlapped elements significantly improved B_1^+ efficiency. The B_1^+ increased from $0.10\,\mu\mathrm{T\,V^{-1}}$ to $0.15\,\mu\mathrm{T\,V^{-1}}$, representing a $50\,\%$ increase, although this was at the expense of some B_1^+ uniformity with a $5\,\%$ decrease. This increase in B_1^+ efficiency and decrease in B_1^+ uniformity is consistent with the results from section 6.2.1.1 comparing four element 20 cm diameter loops. In both cases, the larger element design achieved better uniformity when compared to the smaller element design. Overall, compared to the large Helmholtz pair, both small and large element designs with no phase shift (0, 0, 180, $180°$ case) achieved an approximately $20\,\%$ improved B_1^+ efficiency and simultaneously $5\,\%$ improved B_1^+ uniformity. With a phase shift applied (0, 90, 180, $270°$ case), compared to the large Helmholtz pair, the larger element achieved a $100\,\%$ increase in B_1^+ efficiency, with almost comparable uniformity ($2\,\%$ lower). The smaller element also achieved a $100\,\%$ increase in B_1^+ efficiency but with $5\,\%$ less uniformity over the large Helmholtz pair.

6.3.2 Benchtop Measurements to Investigate Overlap

Results from the previous section show that both array designs offer substantial transmit B_1^+ improvements over simulated existing coil designs, when specific phases and overlaps are applied. Importantly, the optimum overlap value for decoupling does not coincide with the overlap value for maximum B_1^+ efficiency. For the larger $200\,\mathrm{mm} \times 300\,\mathrm{mm}$ array, the best

Table 6.3: Overall summary of large element designs ($200\,\mathrm{mm} \times 300\,\mathrm{mm}$), small element design ($150\,\mathrm{mm} \times 300\,\mathrm{mm}$), and large Helmholtz pair ($284\,\mathrm{mm} \times 284\,\mathrm{mm}$) results. S-parameters showing horizontal element decoupling S_{21} and vertical element decoupling S_{43} are compared over a range of horizontal overlap widths. Additionally, the B_1^+ uniformity and efficiency over two phase shift configurations: 0, 0, 180, $180°$ and 0, 90, 180, $270°$ are compared over across horizontal overlap width.

			Decoupling		0, 0, 180, 180° Phase Shift		0, 90, 180, 270° Phase Shift	
Coil Design	Dimensions /mm	Overlap Width /mm	S_{21} /dB	S_{43} /dB	B_1^+ efficiency /μT V^{-1}	B_1^+ uniformity	B_1^+ efficiency /μT V^{-1}	B_1^+ uniformity
Large Element Design	200×300	20.6	-6.134	-7.417	0.0968	94.73 %	0.1513	90.06 %
	200×300	22	-7.340	-7.543	0.0969	94.12 %	0.1428	89.81 %
	200×300	24	-7.696	-7.329	0.0893	93.56 %	0.1335	89.79 %
	200×300	26	-8.236	-7.508	0.0796	92.53 %	0.1203	89.22 %
	200×300	28	-9.646	-9.180	0.0680	90.70 %	0.1036	88.68 %
	200×300	29	-10.225	-11.813	0.0608	90.53 %	0.0950	88.81 %
	200×300	31	-8.890	-19.405	0.0530	90.56 %	0.0783	89.33 %
Small Element Design	150×300	15	-3.831	-4.300	0.0964	93.25 %	0.1461	86.55 %
	150×300	17	-5.219	-5.259	0.1021	92.74 %	0.1559	86.67 %
	150×300	19	-7.061	-5.624	0.0977	89.01 %	0.1411	85.47 %
	150×300	20	-7.323	-5.716	0.0854	88.53 %	0.1273	85.30 %
Large Helmholtz Rapid Pair	284×284	–	-4.218	–	0.0759	91.33 %		

decoupling was achieved with approximately $29\,\mathrm{mm}$ overlap, and the best B_1^+ efficiency was achieved with approximately $22\,\mathrm{mm}$ overlap (and phase of 0, 90, 180, $270°$). With the smaller $150\,\mathrm{mm} \times 300\,\mathrm{mm}$ array the situation was similar, with the best decoupling achieved with approximately $20\,\mathrm{mm}$ overlap, and the best B_1^+ efficiency achieved with approximately $17\,\mathrm{mm}$ overlap. In this section, both array designs were constructed with the aim of optimum transmit performance, and therefore the overlap was chosen to coincide with the highest B_1^+ efficiency: $22\,\mathrm{mm}$ and $17\,\mathrm{mm}$ respectively.

6.3.2.1 Tx Array Construction

The two arrays were constructed in collaboration with PulseTeq RF engineers: firstly, the smaller $150\,\mathrm{mm} \times 300\,\mathrm{mm}$ array with $30\,\mathrm{mm}$ fillet and $17\,\mathrm{mm}$ overlap, and secondly, the larger $200\,\mathrm{mm} \times 300\,\mathrm{mm}$ array with $30\,\mathrm{mm}$ fillet and $22\,\mathrm{mm}$ overlap. Each element was constructed with $2\,\mathrm{oz}$ thick copper tape of $1\,\mathrm{cm}$ width, adhered onto a $1\,\mathrm{mm}$ FR4 sheet which offered some limited flexibility, sufficient for the coils to be wrapped around the torso. Neighbouring elements were vertically separated by $1\,\mathrm{mm}$ using the FR4 sheets; the elements were not fixed in place, to allow for convenient adjustment of the overlap width in the scanner. Each pair of elements make up a 'paddle', with two paddles (positioned above and below the torso) constructed for each coil. Photos of the element designs on one paddle are shown in Figure 6.14. No ^{1}H traps or baluns were implemented to limit the complexity and minimise additional variables in coil comparison, as at this stage no proton localisation scans were performed.

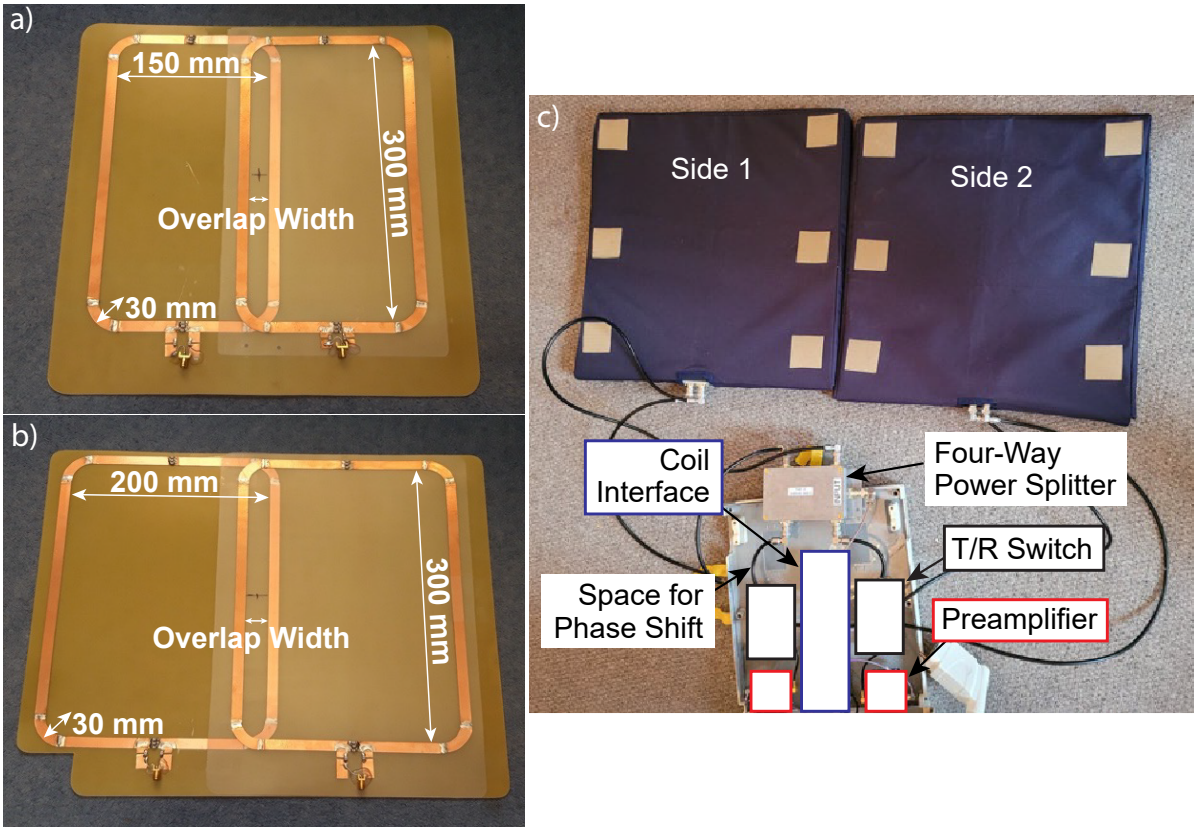

Figure 6.14: (a) Photograph of $150\,\mathrm{mm} \times 300\,\mathrm{mm}$ coil with indicated overlap width. (b) Photograph of $200\,\mathrm{mm} \times 300\,\mathrm{mm}$ coil with indicated overlap width. (c) Photograph of coil connection to T/R box, showing four-way power splitter on transmit and two channel receive.

One significant challenge faced when placing the coil into the scanner was the strong coupling between the coil elements and the scanner bore. Due to the large element sizes and lack of EM shielding, once the element was placed inside the scanner bore at $300\,\mathrm{mm}$ separation, the resonance frequency of the elements shifted to a lower frequency as the inductance increased from coupling to the scanner bore. As the scanner bore was not accounted for during the simulations, this led to differences in S-parameters between benchtop measurements, scanner measurements and EM simulations. Therefore, to account for the coupling, the capacitance in the coil elements was adjusted within the scanner such that the coil was poorly matched outside the scanner, but well matched inside the scanner. Additionally, the optimum overlap for geometric decoupling was also affected by the coupling between the array elements and the volume coil. For the large $200\,\mathrm{mm} \times 300\,\mathrm{mm}$ element, the overlap for minimum S_{21} with optimal decoupling was found to be $22\,\mathrm{mm}$, and the less-than-optimal overlap value was chosen to be $17\,\mathrm{mm}$. For the $150\,\mathrm{mm} \times 300\,\mathrm{mm}$ element, the overlap for minimum S_{21} with optimal

decoupling was found to be $19\,\mathrm{mm}$, and the less-than-optimal overlap value was chosen to be $15\,\mathrm{mm}$.

Overall, when the coils were well decoupled at the optimum overlap for decoupling, all elements were tuned and matched at $30.98\,\mathrm{MHz}$, with reflection scattering (S_{11}) at $-20\,\mathrm{dB}$ or lower, and transmission scattering (S_{21}) at $-15\,\mathrm{dB}$ or lower between the two elements pairs within the same paddle, with stronger coupling of approximately -8 to $-10\,\mathrm{dB}$ (S_{41}) seen across paddles. However, at less-than-optimal overlap distances, significant coupling was seen between two element pairs within the same paddle, of approximately $-6\,\mathrm{dB}$ (S_{21}). This would have affected the tune and match of the coil, resulting in $-10\,\mathrm{dB}$ or higher (S_{11}). In previous EM simulations, coils were re-tuned to be made resonant at each overlap; however this was impractical for benchtop measurements, and therefore, the less-than-optimal overlap coils were constructed less 'efficiently'.

6.3.2.2 Benchtop Setup and Method

The potential $50\,\%$ B_1^+ improvement from reducing overlap width and element phase was investigated using benchtop measurements. Scanner measurements are noisy, which degrades the B_1^+ uniformity from signal variation instead of intrinsic element design, whereas benchtop measurements are not prone to such issues. B_1^+ proportional values were obtained on a purpose-built rig using a benchtop setup by placing pick up probes at various positions of the array, using equation 6.1 [21], where B is the B_1^+ field/unit current in the coil, M_0 is the magnetisation per unit volume (which is proportional to field strength), V_s is the sample volume, r is the circuit resistance, Δf is the bandwidth, and $\hat{B}$ is the B_1^+ field per unit current.

$$\text{SNR} = \frac{\omega \hat{B} M_0 V_s}{\sqrt{4 k_B r \Delta f}} \tag{6.1}$$

Here, we can define $\beta = \frac{\omega B1}{\sqrt{50r}} = \frac{\omega B1}{\sqrt{100P}}$ for two elements, where P is the dissipated power. Subsequently, β can be calculated from the S_{21} on the network analyzer and search probe area, A: $\beta = \frac{S_{21}}{A}$. The received SNR field profile was proportional to the B_1^+ field profile. For the benchtop measurements, coils were positioned above a representative loading phantom. S_{21} was sampled of each channel using a network analyser with a search probe of area of $126.6\,\mathrm{mm}^2$. The signal was split into two channels using a Wilkinson power splitter (Con-

structed by PulseTeq) [22], which ensured correct coil matching at all overlaps. Measurements were taken on a 2D grid of $12\,\mathrm{cm} \times 12\,\mathrm{cm}$ at every $3\,\mathrm{cm}$, with y-depths of 4, 8, and $12\,\mathrm{cm}$. Here, the $4\,\mathrm{cm}$ depth is close to the coil, the $8\,\mathrm{cm}$ depth represents near to the top of the heart, and the $12\,\mathrm{cm}$ depth represents the midpoint of the heart. From the approximate symmetry, at a separation of $30\,\mathrm{cm}$ we assumed the B_1^+ field at $4\,\mathrm{cm}$ depth was equivalent to the field at $26\,\mathrm{cm}$, with $8\,\mathrm{cm}$ equivalent to $22\,\mathrm{cm}$, and $12\,\mathrm{cm}$ equivalent to $18\,\mathrm{cm}$. Corresponding EM simulations of the coils were performed, with the B_1^+ fields exported on 2D planes at 4, 8, and $12\,\mathrm{cm}$ depths at a $1\,\mathrm{mm}$ isotropic resolution onto MATLAB.

6.3.2.3 Field Maps Varying Overlap

The normalised B_1^+ efficiency and B_1^+ coefficient of variation were measured using benchtop and EM simulations on 2D planes parallel to the surface of the coils. Two comparisons were made from the three field map measurements:

1. Comparison 1 was made between the arrays of two element sizes, both at optimal overlap width for decoupling:
    - $150\,\mathrm{mm} \times 300\,\mathrm{mm}$ elements with $19\,\mathrm{mm}$ overlap width, Figure 6.15 a.
    - $200\,\mathrm{mm} \times 300\,\mathrm{mm}$ elements with $22\,\mathrm{mm}$ overlap width, Figure 6.15 b.
2. Comparison 2 was made between the $200\,\mathrm{mm} \times 300\,\mathrm{mm}$ array at two overlap widths:
    - Overlap distance of $22\,\mathrm{mm}$ at the optimum separation, Figure 6.15 b.
    - Overlap distance of $17\,\mathrm{mm}$ at less than optimal separation, Figure 6.15 c.

a) Array Dimensions $150\,\mathrm{mm} \times 300\,\mathrm{mm}$, Optimum Overlap $(19\,\mathrm{mm})$

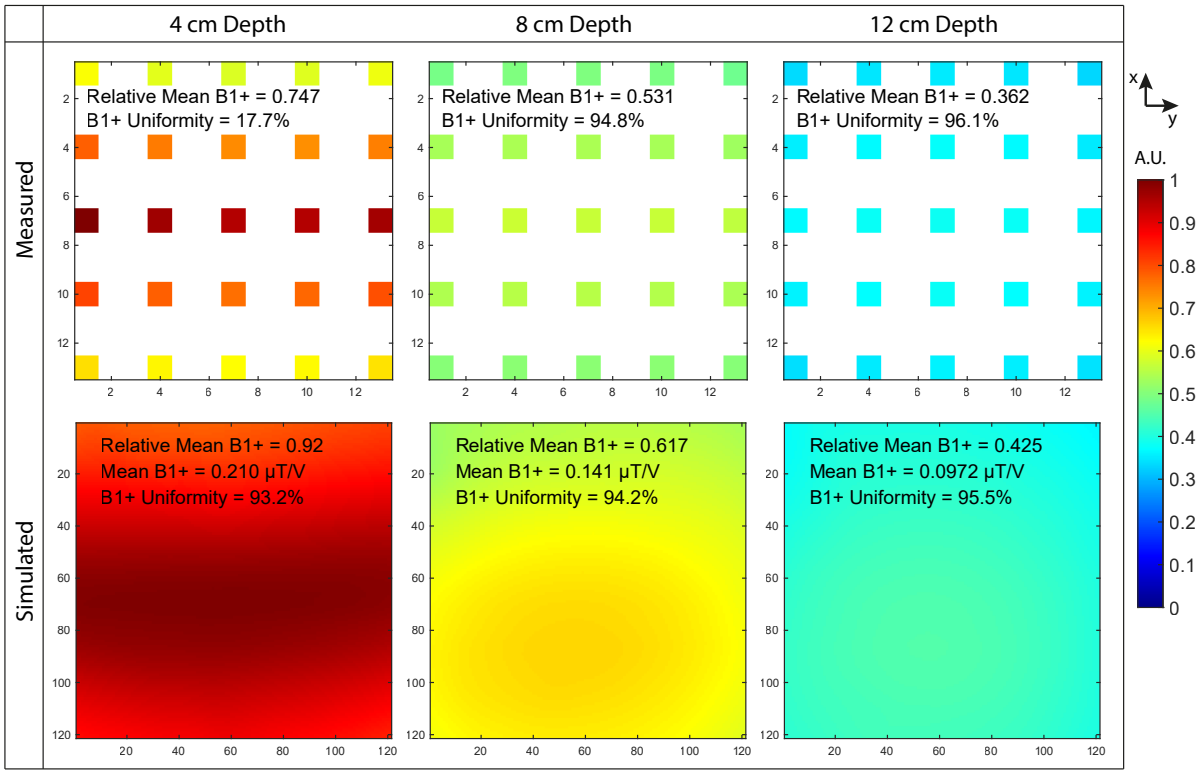

b) Array Dimensions $200\,\mathrm{mm} \times 300\,\mathrm{mm}$, Optimum Overlap $(22\,\mathrm{mm})$

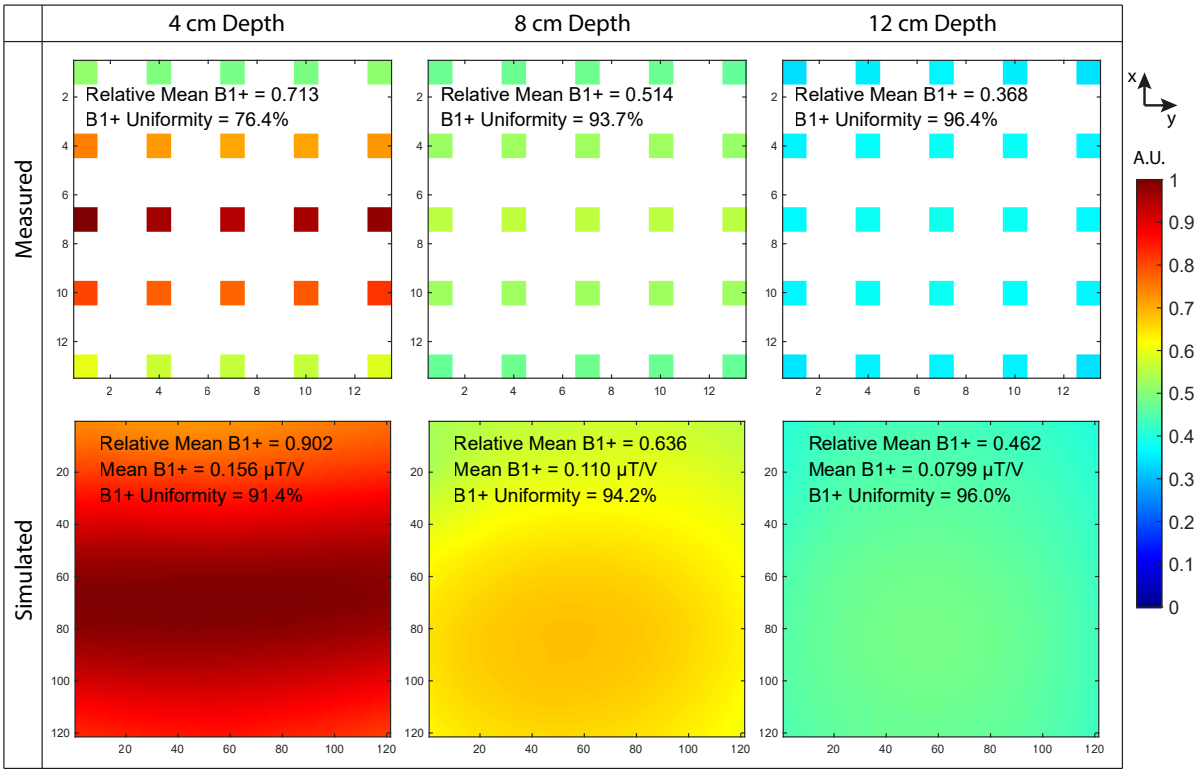

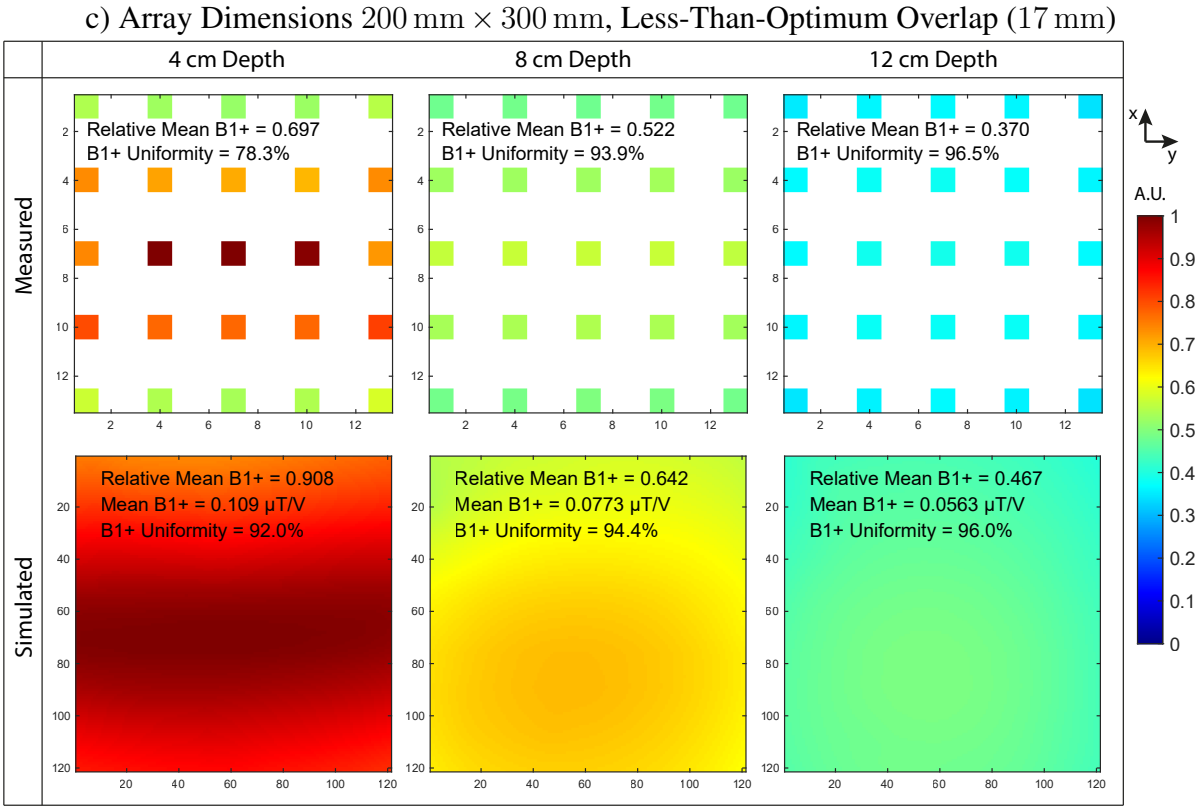

Figure 6.15: Simulated and benchtop 2D B_1^+ fields, show uniformity at depths of 4, 8, and 12 cm from the coil plane. (a) Benchtop (top row) and simulated (bottom row) B_1^+ for 150 mm × 300 mm array with optimum decoupled 19 mm element overlap. (b) Benchtop (top row) and simulated (bottom row) B_1^+ for 200 mm × 300 mm array with optimum decoupled 22 mm element overlap. (c) Benchtop (top row) and simulated (bottom row) B_1^+ for 200 mm × 300 mm array with less-than-optimum 17 mm element overlap.

In these 2D field values, the uniformity is measured over the entire 120 mm × 120 mm 2D slice, and the relative mean B_1^+ is normalised such that the peak B_1^+ value gives 1. Comparing the 150 mm × 300 mm and 200 mm × 300 mm element design both at optimum separations, a discrepancy was seen in B_1^+ uniformity between the simulated and benchtop values at the 4 cm depth closer to the coil elements, but was minimal at the greater depths of 8 cm and 12 cm. At 8 cm depth, the larger array showed a B_1^+ uniformity of 93.7 % measured and 94.2 % simulated, which is approximately comparable to the smaller array showing a uniformity of 94.8 % measured and 94.2 % simulated. At 12 cm depth, the larger array achieved a B_1^+ uniformity of 96.4 % measured and 96.4 % simulated, which is marginally higher than the smaller array with a uniformity of 96.1 % measured and 95.5 % simulated. The changes in B_1^+ uniformity indicated between these coil designs are very small, this is due to the method of calculating uniformity, using one minus the coefficient of variation. In both cases, as the coils are very

uniform, and therefore the coefficient of variation is substantially smaller than one, this suppresses differences in field variability. However, this small difference in uniformity, translates to approximately $20\,\%$ lower B_1^+ field variation from the larger coil, which better represents the substantial improvement. The benchtop measurements are only able to provide a normalised B_1^+ indication; the larger array achieves approximately a $9\,\%$ higher measured relative mean B_1^+ compared to the smaller array.

Comparing the $200\,\mathrm{mm} \times 300\,\mathrm{mm}$ element at the optimum separation of $22\,\mathrm{mm}$ against the less than optimum separation of $17\,\mathrm{mm}$, the discrepancy of B_1^+ uniformity between simulated and benchtop values was greatest at the $4\,\mathrm{cm}$ depth, whilst better agreement was seen at the $8\,\mathrm{cm}$ and $12\,\mathrm{cm}$ depths. At $8\,\mathrm{cm}$ depth, the $17\,\mathrm{mm}$ (less-than-optimal) overlap configuration showed a uniformity of $93.9\,\%$ measured and $94.4\,\%$ simulated, which is comparable to the $22\,\mathrm{mm}$ optimum overlap configuration of $93.7\,\%$ measured and $94.2\,\%$ simulated. At $12\,\mathrm{cm}$ depth, both uniformities are comparable again across measured and simulated data. The measured relative mean B_1^+ at $17\,\mathrm{mm}$ overlap is lower than at $22\,\mathrm{mm}$ overlap for both depths, whilst the simulated relative mean B_1^+ at $17\,\mathrm{mm}$ overlap is higher than at $22\,\mathrm{mm}$ overlap for both depths. This indicated that the poorer B_1^+ efficiency at $17\,\mathrm{mm}$ overlap is due to the poor tuning and matching of the coil at these less-than-optimum overlaps. Therefore, to utilise the improved B_1^+ efficiency at less-than-optimum overlaps, the elements must be re-tuned to account for the additional coupling. Whilst the B_1^+ efficiency improvements may be substantial, the coils would need to be completely rebuilt, and as such this would require further investigation beyond the scope of this work.

6.3.3 Scanner Measurements to Investigate Phase

The effects on the B_1^+ from different phase configurations cannot be determined through benchtop measurements. In this section, scanner field maps were used to compare with simulated values. With both arrays placed on volunteers in the scanner, it was found that a $300\,\mathrm{mm}$ vertical separation better represents the expected coil position. So far, both EM simulations in section 6.3.1 and benchtop measurements in section 6.3.2 show that the larger $200\,\mathrm{mm} \times 300\,\mathrm{mm}$ array achieved improved B_1^+ uniformity at $300\,\mathrm{mm}$ vertical separation when compared to the smaller $150\,\mathrm{mm} \times 300\,\mathrm{mm}$ array, without significant loss of B_1^+ efficiency. Therefore, the larger array was selected for scanner measurements, and only this array design was subsequently investi-

gated in this work. Understanding the magnitude of change in B_1^+ efficiency and uniformity by introducing a phase difference is important, and a key motivating factor towards running scanner B_1^+ maps. In this section, B_1^+ and SNR maps were obtained on the $3\,\mathrm{T}$ Siemens Trio scanner using the larger element ($200\,\mathrm{mm}$ width $\times$ $300\,\mathrm{mm}$ length, $30\,\mathrm{mm}$ fillet) coil.

Whilst the coil design was intended to be used in transmit, it was necessary to modify the coil elements to also be capable of receive; this was to allow the signal from the scanner to be measured, without adding separate receive only elements which would have introduced additional complexities at this stage. For scanner transmit measurements, a four-way splitter was implemented to allow for four channel transmit, as shown above in Figure 6.14. However, the current interface box only had two working receive chains, and upgrading two additional receive channels would require additional preamplifier components, and would have taken substantially longer to build and test. The aim was to determine the transmit B_1^+ field with no interest in the receive performance, so to make progress, only two receive channels were used. From all previous simulations, B_1^+ was approximately symmetric between the upper and lower channels, therefore we assumed the measured field from the bottom pair of channels could be mirrored to represent the top.

To achieve the 0, 0, 180, $180°$ phase shifts across the four elements, the direction of current flow of the bottom paddle was reversed by flipping the coil $180°$. To achieve the 0, 90, 180, $270°$ phase shifts, the bottom paddle was reversed, and a $90°$ phase shift was applied to elements 2 and 4. As a proof of concept, this was initially achieved using a long cable of approximately $2.42\,\mathrm{m}$ (calculated as $9.68\,\mathrm{m}/4$), equivalent to a quarter wavelength. Whilst this is a simple approach, there are additional potential losses compared to the 0, 0, 180, $180°$ case. With no cable baluns, there is potentially stronger coupling between the cable and transmit coil, leading to common mode currents on the cable shield. This will alter the tune and match of the coil, as well as reduce the power delivery into the coil.

6.3.3.1 Scanner Experimental Setup

The two paddles of the array were positioned above and below a hollow cylindrical loading phantom with an approximate height of $300\,\mathrm{mm}$, providing approximately $300\,\mathrm{mm}$ of separation between the two pairs. The strength of dielectric loading applied to the coil by the loading phantom was adjusted to best represent the loading of a human body by increasing or decreasing

the conformity of the paddles onto the cylindrical loading phantom. An ethylene glycol phantom was positioned inside the loading phantom for ^{13}C signal, with an approximate dimension of $300\,\mathrm{mm}$ width, $200\,\mathrm{mm}$ height, and $500\,\mathrm{mm}$ length, as shown in Figure 6.16. Here, the signal phantom was approximately $40\,\mathrm{mm}$ from the bottom paddle and approximately $60\,\mathrm{mm}$ from the top paddle.

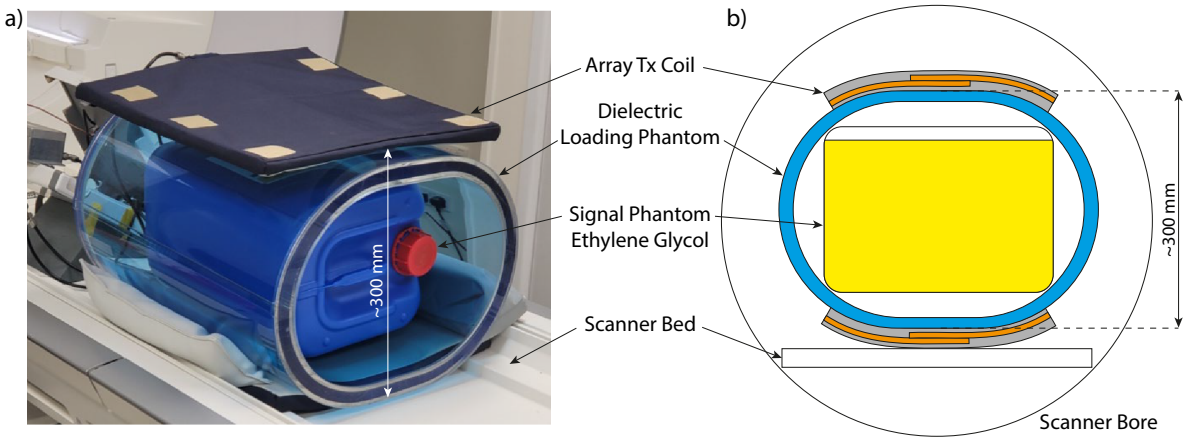

Figure 6.16: Four element array coil setup for scanner field maps, with a hollow cylindrical body loading phantom and ethylene glycol for signal. (a) Photograph and (b) diagram of the coil and phantoms used.

The standard fully sampled B_1^+ mapping protocol was implemented; the protocol is described in the Methods chapter, section 3.4. The specific scan parameters are described here: a series of 2D gradient echo were run (Siemens: FLASH sequence, TE $= 3750\,\mathrm{ms}$, TR $= 7.1\,\mathrm{ms}$, Resolution $= 32 \times 32$, FOV $= 480\,\mathrm{mm}$, Slice Thickness $= 30\,\mathrm{mm}$, Averages $= 32$, Pulse Duration $= 2\,\mathrm{ms}$). The images were acquired at incremental voltages: $60\,\mathrm{V}$, $120\,\mathrm{V}$, $180\,\mathrm{V}$, $240\,\mathrm{V}$, $300\,\mathrm{V}$, $360\,\mathrm{V}$, and $388\,\mathrm{V}$ The voltage was increased linearly (which differs from the variable density sampling method used for single element coils) as greater uniformity of flip angles across the coil FOV were expected. The scanner files were modified to allow a voltage of $388\,\mathrm{V}$ to be supplied to the coils, delivering $194\,\mathrm{V}$ to each channel (dividing $388\,\mathrm{V}$ by $\sqrt{4}$). This higher voltage was required as firstly, the total RF power was split between four channels, and secondly B_1^+ inefficient coil elements of larger dimensions were used.

6.3.3.2 Phase Shift Results

B_1^+ fields were calculated within a ROI from the 2D B_1^+ maps, defined as $90\,\mathrm{mm}$ vertically from the upper paddle bottom surface and $30\,\mathrm{mm}$ horizontally off-centre to represent an approximate

position of a human heart inside the scanner, taking into account the greater left ventricular size. The ROI radius was defined as $60\,\mathrm{mm}$, with an effective thickness of $30\,\mathrm{mm}$ due to the thickness of one slice.

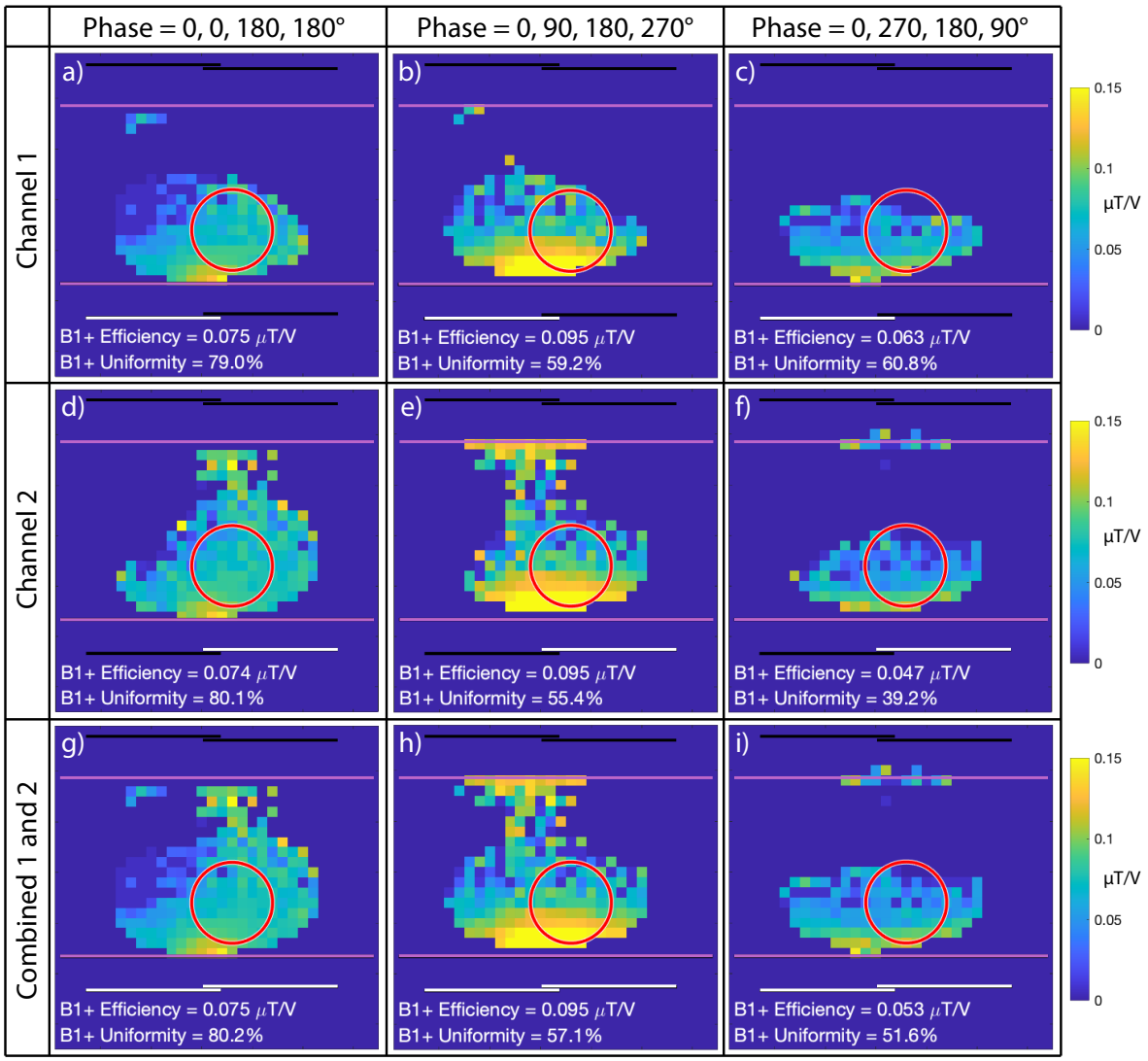

Figure 6.17: 2D B_1^+ maps obtained from scanner measurements with four channel Tx, and varied Rx channels. Three phases are investigated: Helmholtz configuration $(0, 0, 180, 180°)$, right-handed configuration $(0, 90, 180, 270°)$, and an inefficient left-handed configuration $(0, 270, 180, 90°)$. Active receive channels are shown in white, and inactive receive channels are shown in black. The purple horizontal line represents the upper and lower edge of the signal phantom, and the red circle represents the ROI. Row 1 (a to c) shows receive on channel 1, row 2 (d to f) shows receive on channel 2, and row 3 (g to i) shows receive on channels 1 and 2 digitally combined.

The array transmit performance at two main phases were investigated through scanner measurements and EM simulations: the 'conventional phase' of $0, 0, 180, 180°$, and the 'right-handed

phase' of $0, 90, 180, 270°$. An additional phase of $0, 270, 180, 90°$ was also included as an example; this represents the incorrect 'left-handed phase'. Figure 6.17 shows the B_1^+ maps from four Tx channels combined with the two Rx channels (from the bottom paddle). Three receive configurations were investigated: channel 1 Rx, channel 2 Rx, and combined channel 1 and channel 2 Rx in post-processing. A summary of the B_1^+ efficiency and phase is shown in Table 6.4. A B_1^+ of $0.075\,\mu\mathrm{T\,V^{-1}}$ was achieved with the array at conventional phase values of $0, 0, 180, 180°$ into the four channel transmit. With a $90°$ phase shift applied to elements 2 and 4, resulting in a $0, 90, 180, 270°$ phase, a B_1^+ of $0.095\,\mu\mathrm{T\,V^{-1}}$ was achieved. This equates to a $27\,\%$ increase in field strength within the ROI compared to the conventional phase setup; the region of increased B_1^+ efficiency can be clearly seen as the overlap region between the two elements. When the opposite phase shift is applied, resulting in a $0, 270, 180, 90°$ phase, a B_1^+ of $0.053\,\mu\mathrm{T\,V^{-1}}$ was achieved, indicating the incorrect direction of circular polarization. It should be noted that in all three phase configurations, strong coupling is seen between the bottom and top elements; whilst the signal was primarily received within the FOV of the bottom paddle, some signal was received at the top paddle, particularly in the case with $90°$ additional cable phase shifts. This suggests that the cable reduced the coil element isolation and introduced additional coupling. Additionally, it should be noted that the $0, 90, 180, 270°$ phase configuration achieved a B_1^+ uniformity of approximately $57\,\%$, which is substantially lower than the B_1^+ uniformity of $80\,\%$ from the $0, 0, 180, 180°$ configuration. Whilst we can assume that the majority of this decrease in uniformity is accounted for by the phase change, another factor could be the skewed field profile, which introduces greater noise into the ROI (evident at the upper region of the ROI). In all cases, substantially lower B_1^+ uniformity values were seen due to the noisy scans within the ROI.

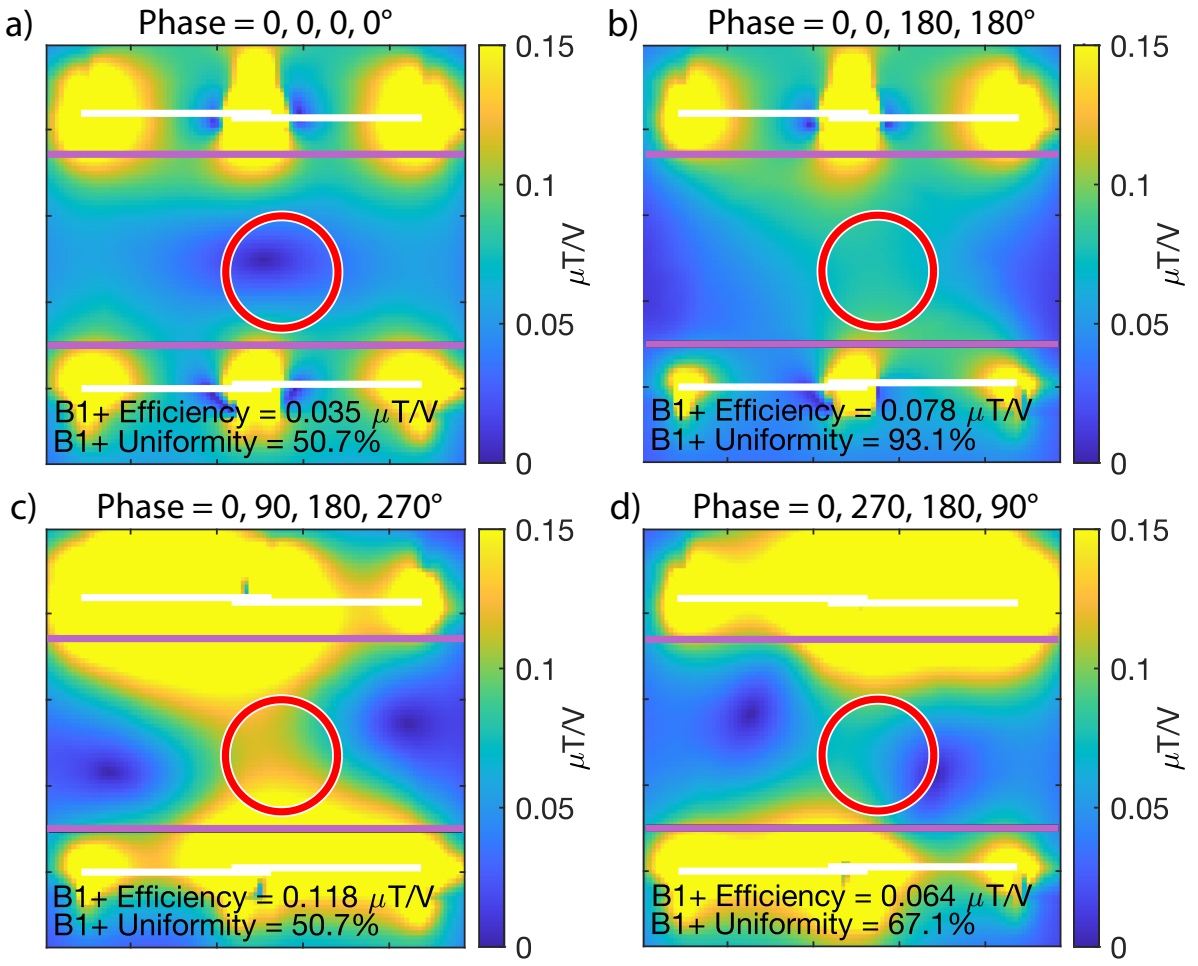

Figure 6.18: EM simulation showing B_1^+ of four element Tx array at four phase configurations. (a) Inefficient zero phase: $0, 0, 0, 0°$, (b) Helmholtz phase: $0, 0, 180, 180°$. (c) right handed phase: $0, 90, 180, 270°$, and (d) an inefficient left-handed configuration: $0, 270, 180, 90°$.

Figure 6.18 compares the simulated B_1^+ field from four phases: the standard Helmholtz phase ($0, 0, 180, 180°$), both the $90°$ shifted phases, the efficient right handed phase ($0, 90, 180, 270°$) and the inefficient left handed phase ($0, 270, 180, 90°$), and the inefficient zero phase ($0, 0, 0, 0°$). The latter two phases were added as a point of comparison, and would not be selected for coil construction. It should be noted that in the two $90°$ shifted field maps (both RH and LH), there is asymmetry in the B_1^+ field between the coil elements as the circular polarization matches that of the B_1^+ interaction with the dielectric material. A simulated B_1^+ of $0.078\,\mu\mathrm{T\,V^{-1}}$ was achieved with the conventional $0, 0, 180, 180°$ phase; this is extremely consistent with the measured B_1^+ of $0.076\,\mu\mathrm{T\,V^{-1}}$. For the $0, 90, 180, 270°$ phase, a simulated B_1^+ of $0.118\,\mu\mathrm{T\,V^{-1}}$ was achieved, equating to a $51\,\%$ increase over the conventional phase. At this phase shift, poorer agreement was seen between simulated and measured B_1^+, with a $24\,\%$ increase from

the measured results to the simulated results. For the opposite left-handed phase, a simulated B_1^+ of $0.064\,\mu T\,V^{-1}$ was achieved. Overall, in both right-hand and left-hand phase shift cases, the simulated fields were approximately $20\,\%$ higher than the measured fields. The lower measured B_1^+ values may be accounted for by the reduction of power transmission into the coil, due to potentially increased coupling between the long cables used for phase shifting as described above. The difference in B_1^+ uniformity can be attributed to the use of different voxel sizes and increased noise from the scanner-measured field maps, leading to an increase in voxel signal magnitude variation. However, despite the 0, 90, 180, $270°$ phase achieving around 30 – $50\,\%$ increased B_1^+ efficiency compared to the Helmholtz configuration, this increase comes with a corresponding $30\,\%$ decrease in B_1^+ uniformity.

Table 6.4: Summary of B_1^+ in ROI obtained from simulated and measured 2D field maps obtained using the large four element array.

			(0, 0, 180, 180°) Phase Shift		(0, 90, 180, 270°) Phase Shift	
	Tx Channels	Rx Channels	B_1^+ efficiency /$\mu T\,V^{-1}$	B_1^+ Uniformity	B_1^+ efficiency /$\mu T\,V^{-1}$	B_1^+ Uniformity
Simulated	1, 2, 3, 4	1, 2, 3, 4	0.0779	93.1 %	0.118	50.7 %
Scanner	1, 2, 3, 4	1	0.0751	79.0%	0.0949	59.2 %
	1, 2, 3, 4	2	0.0736	80.1 %	0.0949	55.4 %
	1, 2, 3, 4	1, 2	0.0747	80.2 %	0.0948	57.1 %

6.3.3.3 Comparison with Helmholtz Coil

The four element TxRx array was compared to the existing large Helmholtz pair constructed by Rapid Biomedical with two square loops (dimensions $284\,mm \times 284\,mm$), through both EM simulations and scanner measurements. The B_1^+ efficiency and B_1^+ uniformity were recorded within the ROI used throughout this section. The B_1^+ results for the large Helmholtz pair are shown in Figure 6.19a and Table 6.5. The large Helmholtz pair achieved a B_1^+ efficiency within the ROI of $0.076\,\mu T\,V^{-1}$, with a uniformity of $91.2\,\%$. For the four element array, in the standard 0, 0, 180, $180°$ phase configuration, the simulated B_1^+ efficiency in the ROI is $0.078\,\mu T\,V^{-1}$ with a uniformity of $93.1\,\%$, which represents a minor increase in both B_1^+ uniformity and B_1^+ efficiency compared to the large Helmholtz pair. For the four element array with a phase configuration of 0, 90, 180, $270°$, the measured B_1^+ efficiency is $0.118\,\mu T\,V^{-1}$ with uniformity of $67.1\,\%$. This represents a substantial increase in field efficiency, albeit with a loss of field uniformity.

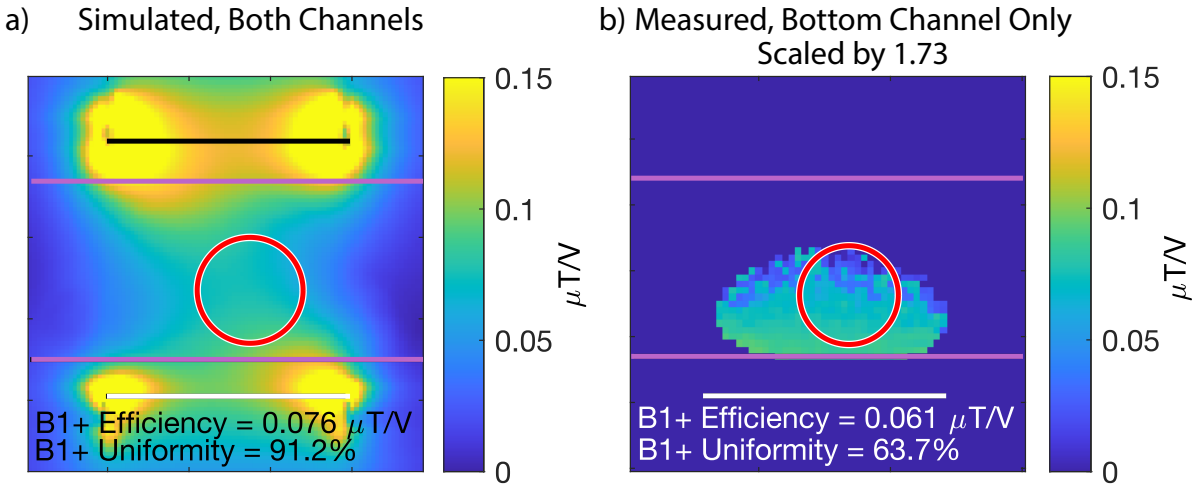

Figure 6.19: 2D B_1^+ for large Helmholtz loop: (a) simulated B_1^+ with transmit on both elements, and (b) measured B_1^+ with transmit only on the bottom element.

For the large Helmholtz pair, scanner B_1^+ field maps were previously acquired by Justin Lau at OCMR, with a similar phantom setup. However, there are three main differences in scanner measurements for the large Helmholtz pair compared to the scanner measurements above:

- **Sequence:** A different B_1^+ mapping sequence was used with a spiral trajectory read-out [23]. Differences in scan parameters were present, namely a resolution of 64×64 was used for this coil compared to the resolution of 32×32 used for the four element Tx coil.
- **Transmit Channels:** Due to the rigid design of the large Helmholtz pair by Rapid Biomedical, we were unable to fit both top and bottom elements with the cylindrical loading phantom inside the scanner bore. As such, only the bottom element was placed inside the scanner. The top element was placed outside the scanner (but was still connected to the coil). A scaling factor for the measured B_1^+ was determined through EM simulations (as described later in this section).
- **Receive Channels:** Within each paddle, there is one transmit only element with four receive only elements, compared to the four element array where each element is operating in transmit-receive. Therefore, with multiple individual receive elements, the large Helmholtz array will measure higher SNR, leading to less noise variation across the B_1^+ map.

Post processing of the acquired data to B_1^+ maps was performed using the same B_1^+ mapping protocol. The simulated B_1^+ for the large Helmholtz pair (bottom element only) in the ROI

was $0.0439\,\mu T\,V^{-1}$ with a uniformity of $68.6\,\%$, and the measured B_1^+ was $0.0350\,\mu T\,V^{-1}$ with a uniformity of $63.8\,\%$. It should be noted that measured values were $25\,\%$ lower than the simulated values, possibly indicating some discrepancy in the coil construction. To take into account the potential increase in transmit performance when hypothetically both elements were placed in the scanner bore, the ratio between B_1^+ efficiency from the bottom paddle to B_1^+ efficiency from both paddles was determined through EM simulations, and calculated to be 1.73. This scaling value was multiplied by the measured B_1^+ map of the large Helmholtz pair to determine the equivalent B_1^+ value for the complete Rapid Coil, resulting in a scaled measured B_1^+ in the ROI of $0.0606\,\mu T\,V^{-1}$, as shown in Table 6.5, and Figure 6.19. With this scaling applied, we can compare with the four channel array. The B_1^+ efficiency within the ROI from the four element array was previously measured to be $0.0747\,\mu T\,V^{-1}$ (with 0, 0, 180, $180°$ phase), and 0.0948 (with 0, 90, 180, $270°$ phase) representing a $23\,\%$ and $56\,\%$ increase in B_1^+ efficiency respectively. The B_1^+ field uniformity cannot be determined through the measured scanner results due to the aforementioned differences in sequence and experimental setup.

Table 6.5: Summary of B_1^+ in ROI obtained from simulated and measured 2D field maps obtained using the large Helmholtz pair.

			0, 180° Phase Shift	
	Tx Channels	Rx Channels	B_1^+ Efficiency /$\mu T\,V^{-1}$	B_1^+ Uniformity
Simulated	2	2	0.0439	68.6 %
	1, 2	1, 2	0.0760	91.2 %
Scanner	2	2	0.0350	63.8 %
Scanner (scaled)	1, 2	1, 2	0.0606	–

Lastly, the SAR between the two arrays was compared through EM simulations, with results shown in Table 6.6. The four element array with 0, 0, 180, $180°$ phase indicated a peak SAR of $0.222\,W\,kg^{-1}$, $23\,\%$ higher than that of the large Helmholtz pair, $0.180\,W\,kg^{-1}$. The four element array with 0, 90, 180, $270°$ phase configuration indicated a higher peak SAR of $0.283\,W\,kg^{-1}$, $56\,\%$ higher than that of the large Helmholtz pair, consistent with the greater B_1^+ improvements due to the higher magnitude of EM field. However, it should be noted that in both of these coils, the peak SAR is relatively low for surface coils (such as the SAR from single elements discussed in section 5.5.1). As such, in a scenario where unlimited RF power

was available, the mean SAR would be the first limiting factor towards safe energy deposition. The mean SAR over the torso is comparable between the two coil designs: $0.0146\,\mathrm{W\,kg^{-1}}$ for the four element array at both phase configurations, and $0.0140\,\mathrm{W\,kg^{-1}}$ for the large Helmholtz pair, and so both designs offer similar max allowed RF power.

Table 6.6: Max and mean SAR (averaged over $10\,\mathrm{g}$) within torso, compared between large four element array and large Helmholtz pair.

			$10\,\mathrm{g}$ SAR in Body Voxels	
Number of Elements	Element Dimension (L × W)	Phase Shift /°	Max SAR /W kg^{-1}	Mean SAR /W kg^{-1}
4	300 × 200	0, 0, 180, 180°	0.222	0.0146
4	300 × 200	0, 90, 180, 270°	0.282	0.0146
2	284 × 284	0, 180°	0.180	0.0140

6.3.4 Simulated Coil Comparison

Thus far, the constructed four element design has been compared to the existing large Helmholtz pair for ^{13}C MRI at $30\,\mathrm{MHz}$. The four element array has shown substantially improved B_1^+ efficiency measured through EM simulations and scanner measurements, as well as comparable B_1^+ uniformity through EM simulations. To determine the improvements and applications of these array designs, the coil was characterised against a greater range of existing coil designs.

In this section, the B_1^+ field was calculated within the heart voxels of a human voxel model (not a cylindrical ROI as in the previous section). All coils were positioned appropriately over the torso for cardiac imaging. Coil elements were positioned with a minimum separation of $10\,\mathrm{mm}$ from the surface of the torso. With a range of transmit channels, the RF power was divided equally between the number of elements. For array elements in a Helmholtz configuration, a vertical separation of $300\,\mathrm{mm}$ was applied between the top and bottom array pair (approximately the distance required for the human voxel model), with a 180° phase shift. Conversely, for multiple individual elements using the 20 cm circular loop, as described in section 6.2, a $250\,\mathrm{mm}$ vertical separation was applied to better represent the close conformity of the coil.

6.3.4.1 Overview B1 Efficiency Uniformity Within ROI

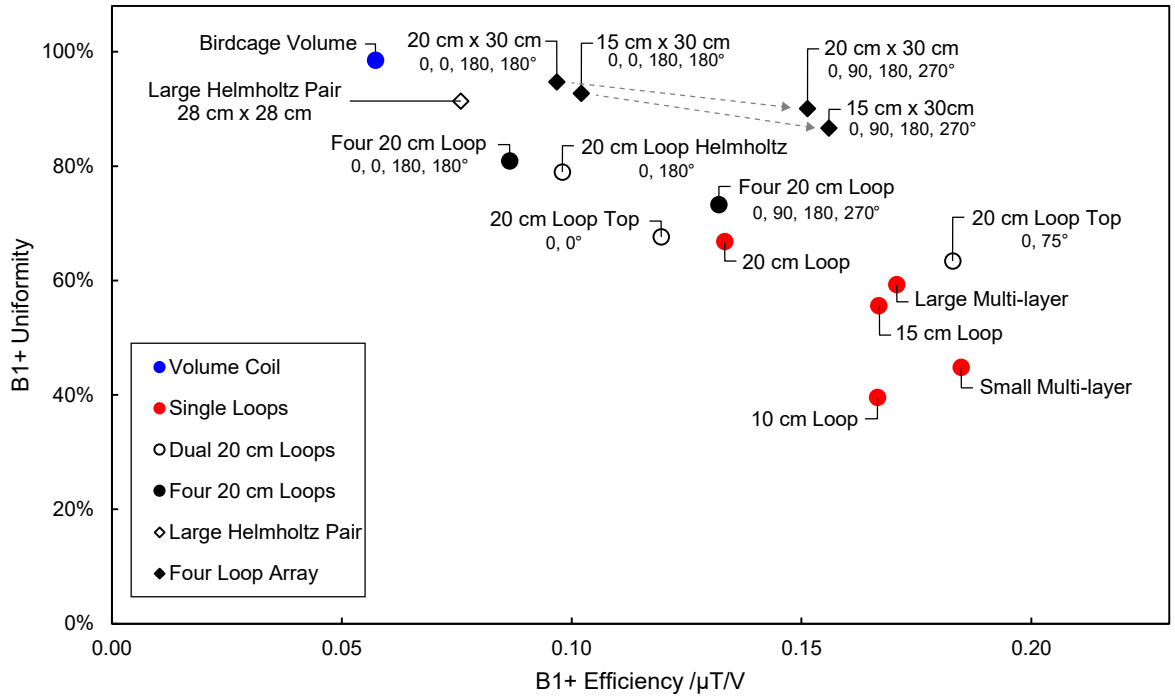

Figure 6.20: Mean B_1^+ field efficiency versus B_1^+ field non-uniformity plot. The final four loop $200\,\mathrm{mm} \times 300\,\mathrm{mm}$ array design was compared against existing simulated Tx coil performances, with arrows representing change in B_1^+ efficiency (x-dir) and B_1^+ uniformity (y-dir) from introducing a $90°$ relative phase difference.

A previously developed B_1^+ trade-off plot was used to show efficiency versus uniformity for a range of simulated coils in Figure 6.20. A summary of the full comparison data showing the dimensions, element horizontal overlap, element vertical overlap, and applied phase shifts are shown in Table 6.7. The B_1^+ values for both the smaller $150\,\mathrm{mm} \times 300\,\mathrm{mm}$ and larger $200\,\mathrm{mm} \times 300\,\mathrm{mm}$ four element arrays (black filled diamond markers) showed good uniformity compared to all other coil designs except the birdcage volume coil. Introducing a $90°$ relative phase shift between neighbouring elements (0, 90, 180, $270°$), as shown by the dashed arrows, improved the B_1^+ efficiency by approximately $60\,\%$, pushing the B_1^+ efficiency of arrays into field strengths more commonly expected of single loops (red filled circle markers). However, this additional B_1^+ efficiency came at the cost of decreased field uniformity. An important comparison is that with the current large Helmholtz pair (black outlined diamond marker), which achieved similar uniformity to the four element arrays when 0, 90, 180, $270°$ phase was applied, but approximately $50\,\%$ poorer efficiency. Comparing the results from sec-

tion 6.2 with individual 20 cm elements, these offered a compromise between the high B_1^+ efficiency of single elements and the high B_1^+ uniformity of arrays. The two performing coil designs at this stage were determined to be the dual Helmholtz pair (black outlined circle markers), and the four channel configuration (black filled circle markers). However, compared to the more optimised four element array of this chapter, the four individual 20 cm loops offered no improvement, particularly when taking into account optimising overlap and phase. Nevertheless, the dual 20 cm loops offer improved B_1^+ uniformity over smaller single elements if a particularly high efficiency is needed. This figure summarises again that multi-layer designs described in the previous section offer increased B_1^+ efficiency over comparable single element loops, and therefore investigation into multi-layer arrays would allow potentially significant B_1^+ efficiency and SNR improvements.

Overall, we can summarise these results so far into three regimes:

- For high B_1^+ efficiency: Two and four 20 cm diameter loops in a Helmholtz configuration and circularly polarised configurations respectively. However, taking into account that the large multi-layer element was $50\,\%$ more B_1^+ efficient than the 20 cm loop, there is a strong motivation to investigate the possibility of using several multi-layer elements individually or in arrays.
- Theoretically, for high B_1^+ uniformity but still limited RF power: Four $200\,\mathrm{mm} \times 300\,\mathrm{mm}$ elements with $30\,\mathrm{mm}$ fillet radius should be used in two paddles, with each paddle containing two elements at a $17\,\mathrm{mm}$ overlap (less than the optimum for decoupling at $22\,\mathrm{mm}$). A phase shift of 0, 90, 180, $270°$ should be applied between the four elements. This achieved $90\,\%$ B_1^+ uniformity, and double the B_1^+ of a conventional array of the same dimensions.
- With unlimited RF power: As expected, the 16 rung birdcage coil (similar to the existing ^{1}H body coil on a Siemens scanner) could be used for better uniformity compared to all other designs.

Table 6.7: Summary of simulated element designs showing B_1^+ efficiency and uniformity averaged over the heart voxels, across different overlap widths, vertical separations and phase configurations.

Number of Channels / Elements	Element Design	Dimensions	Element Horizontal Overlap /mm	Element Vertical Separation /mm	Phase Shift /°	B_1^+ Efficiency /μT/V	B_1^+ Uniformity	Frequency /MHz
1	Circular	100 mm (diameter)				0.167	39.6 %	30.00
1	Circular	150 mm (diameter)				0.167	55.6 %	30.00
1	Circular	200 mm (diameter)				0.133	66.8 %	30.98
1	Small Multi-layer					0.185	44.8 %	30.00
1	Large Multi-layer					0.171	59.3 %	30.00
2	Circular	200 mm (diameter)		250	0, 180°	0.098	79.0 %	30.98
2	Circular	200 mm (diameter)	Optimal		0, 0°	0.120	67.6 %	30.98
2	Circular	200 mm (diameter)	Optimal		0, 75°	0.183	63.4 %	30.98
4	Circular	200 mm (diameter)	Optimal	250	0, 0, 180, 180°	0.087	80.9 %	30.98
4	Circular	200 mm (diameter)	Optimal	250	0, 0, 180, 180°	0.132	73.3 %	30.98
2	Square	284 mm × 284 mm (L×W)		300	0, 180°	0.076	91.3 %	30.98
4	Square	150 mm × 300 mm (L×W), 30 mm (fillet)	17	300	0, 0, 180, 180°	0.102	92.7 %	30.98
4	Square	150 mm × 300 mm (L×W), 30 mm (fillet)	17	300	0, 90, 180, 270°	0.156	86.7 %	30.98
4	Square	200 mm × 300 mm (L×W), 30 mm (fillet)	20.6	300	0, 0, 180, 180°	0.097	94.7 %	30.98
4	Square	200 mm × 300 mm (L×W), 30 mm (fillet)	20.6	300	0, 90, 180, 270°	0.151	90.1 %	30.98
2	Birdcage	620 mm (diameter), 600 mm (length)			0, 90°	0.057	98.5 %	30.00

6.4 Developing a Multi-layer Rx Array

It is not possible to optimise for both transmit and receive performance of RF coils simultaneously; as described in section 6.1.3, the intrinsic differences between transmit and receive result in the optimum receive coil ideally having more numerous elements, with smaller individual dimensions. Therefore, one such aforementioned ^{13}C cardiac coil design is the use of two large Tx elements with individual smaller Rx elements. On transmit, section 6.3 has shown that it is possible to obtain substantial B_1^+ uniformity improvements by optimising for element design, and simultaneously B_1^+ efficiency improvements through optimising phase and element overlap distance. Additionally, on receive, development of the novel human multi-layer element design in Chapter 5 has allowed a $50\,\%$ increase in SNR over conventional loops of the same dimension.

Whilst it is likely possible to create a large multi-layer transmit array with preserved uniformity, the size required provides design and construction challenges at this point of the project; this discussion is presented in Chapter 7. To utilise the receive sensitivity of the multi-layer design, we needed to determine whether it was possible to construct a multi-layer receive array; primarily, multi-layer elements need to be geometrically decoupled to retain the sensitivity of individual elements. The decoupling efficiency of the multi-layer design is compared against conventional single loop coils in section 6.4.1. Furthermore, due to the asymmetry of the multi-layer design, three possible overlap angles exist between two multi-layer elements; the EM field from these different overlaps is characterised in section 6.4.2. Finally, bringing together the work on this project, a multi-layer receive array is constructed in section 6.4.3, intended to be used with the previously developed optimum transmit array. Whilst further efficiency and uniformity may be gained from the multi-layer design, the simpler rectangular loop was chosen to isolate multi-layer receive improvements. Due to the global coronavirus pandemic, the availability of scanner testing and coil construction was severely disrupted, and as such, this section focuses mainly on EM simulation results.

6.4.1 Geometric Decoupling

In an ideal case of a receive array, the EM fields generated from one coil remain completely unchanged in the presence of neighbouring coil elements. However, in practice, perfect decou-

pling is not achievable; some magnitude of EM coupling between the two coil elements exists, leading to imperfect isolation, increased coil resistance, loss of sensitivity, and a skewed B_1^+ field. Transmission scattering parameters between two elements, S_{ij}, can quantify the extent of coupling between elements i and j. Typically, during coil construction the element overlap between two nearest neighbour elements is varied; subsequent benchtop measurements are made using a network analyzer to determine the overlap of the two elements such that an S_{21} of $-15\,\mathrm{dB}$ or less, is observed. This process is iterated across all other nearest neighbour element pairs. An identical protocol can be implemented through EM simulations, which allow more accurate coil placement. This is, however, more time consuming, as each overlap distance requires a new simulation. Here, two element decoupling setups were investigated as an initial proof-of-concept, and the S_{21}-parameters and B_1^+ field were characterised. Additional three element decoupling setups were performed which demonstrate the overlap in a 2D overlap configuration; this can be generalised to more numerous arrays. Overall, four decoupling sweeps were performed:

- Two 20 cm loop elements
- Two large multi-layer elements
- Three 20 cm loop elements
- Three large multi-layer elements

6.4.1.1 Simulation and Benchtop Setup

For EM models of two and three element setups, all elements were positioned above a simple cuboid loading phantom with representative dielectric properties to a human body instead of a human voxel model, to simplify the EM simulations. A $1\,\mathrm{mm}$ thick polyimide dielectric sheet was placed between the coil elements, offset vertically for electrical insulation. The horizontal overlap distance was swept incrementally until a minimum transmission S_{21} was achieved for $30\,\mathrm{MHz}$. As the overlap changes, the total inductance (self and mutual) changes, leading to resonance frequency shifts and to a degradation in impedance matching efficiency. At each overlap iteration, it was possible to tune and match capacitance in EM simulations, to ensure that resonance was maintained at $30\,\mathrm{MHz}$ with an S_{11} of $-20\,\mathrm{dB}$ or lower. Frequency domain simulations were performed using the FEM algorithm for all decoupling sweeps with approximately $400\,000$ tetrahedral mesh cells used for two elements, and $600\,000$ tetrahedral

mesh cells for three elements. Tetrahedral meshing was chosen to capture the curvature of the multi-layer structure accurately, which is crucial in determining the mutual inductance for decoupling. Simulations were performed with discrete ports for adjustable capacitance, with a $0.03\,\Omega$ resistance positioned at each port to mimic the expected Effective Series Resistance (ESR). For each iteration, the S_{ii} and S_{ij} plots were exported and analysed in MATLAB. For two elements, the swept distance was recorded as the centre-to-centre distance, and normalised such that zero represented optimal decoupling. The centre-to-centre distance metric was used since the outer diameter of the multi-layer design was undefined. Hence, the overlap metric in the previous section 6.3 cannot be easily defined. For three coil elements, elements 1 and 2 were placed at the optimum decoupling overlap as determined from the two element setup. The third element was introduced to form an approximately equilateral triangle, as shown in Figure 6.21 d. Here, the swept distance was recorded as the distance between the centre of the third element to the midpoint between elements 1 and 2.

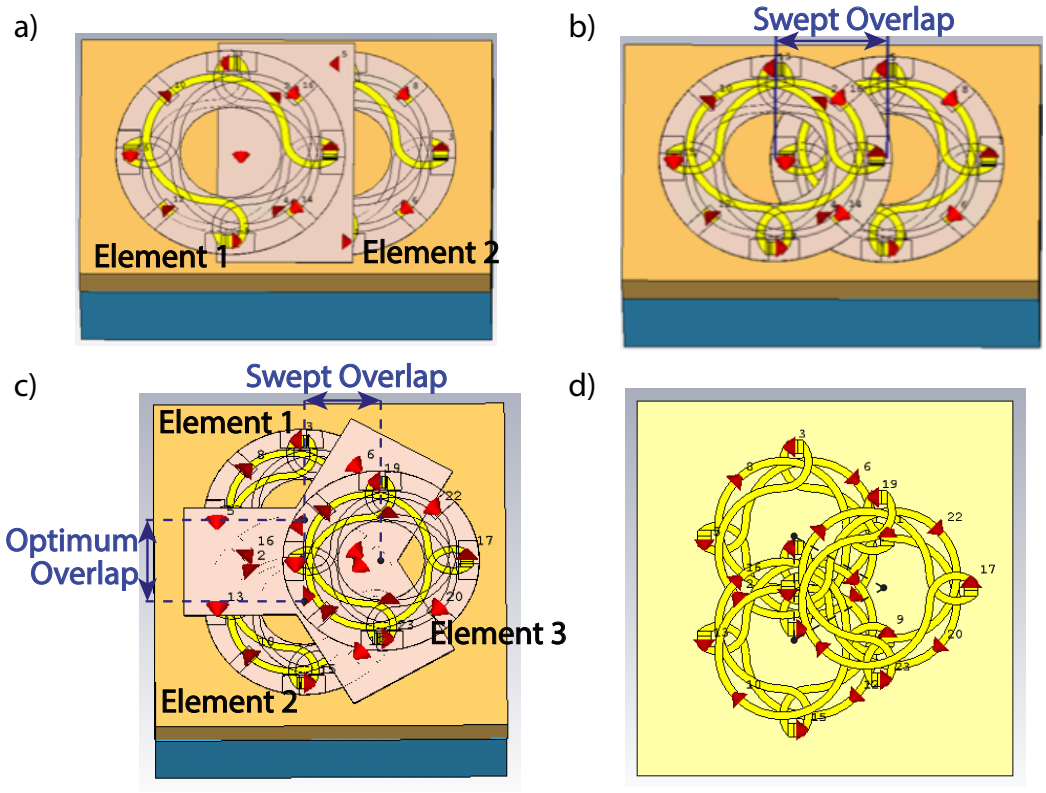

Figure 6.21: EM models showing two- and three-element geometric decoupling for multi-layer coils. Top row: Two-element models. (a) Dielectric insulation using $1\,\mathrm{mm}$ thick polyimide is placed between the two coils. The width of the insulator varied with overlap distance. (b) Coil centre to centre distance was swept to determine optimum overlap for minimum inductive coupling. Bottom row: Three-element models. (c) The far-right coil, coil three, separated with a $1\,\mathrm{mm}$ thick polyimide layer above the second coil. The distance from the centre of third coil to the midpoint between the first two elements was swept for decoupling with third coil. (d) Conductor track and ports shown without dielectric insulation layers, to illustrate the overlap of conductor to cancel mutual inductance.

For benchtop measurements, the coils were similarly positioned on a loading phantom consisting of a large box with aqueous sodium chloride. The two elements were connected to the network analyzer. A sufficiently large phantom of size $70\,\mathrm{cm} \times 50\,\mathrm{cm} \times 40\,\mathrm{cm}$ was built to representatively load the multi-layer elements with enough surface area for several elements to be placed. For benchtop decoupling, an identical protocol was implemented compared to the simulated decoupling, where the overlap distance was swept incrementally until a minimum transmission S_{21} was achieved. However, two aspects of the benchtop decoupling method differed from EM simulations; firstly, coil positioning for benchtop measurements cannot be as accurate, as the elements are required to be fixed down. The S-parameters were taken at $10\,\mathrm{mm}$ iteration steps, instead of the precision of up to $1\,\mathrm{mm}$ in EM simulations. Secondly, the ele-

ments were only well tuned and matched for the optimal decoupling case, where zero external coupling is present. Therefore at non-optimal overlaps, the coils are poorly tuned and a higher S_{11} was seen, which reduced the field strength, and therefore reduced the coupling S_{21}. Compared to benchtop measurement methods, EM simulations have the ability to adjust capacitance at every overlap distance more rapidly, allowing the coil to be always matched at each overlap, a process which would have been too time-consuming to perform for benchtop measurements.

6.4.1.2 Two Multi-layer Element Decoupling

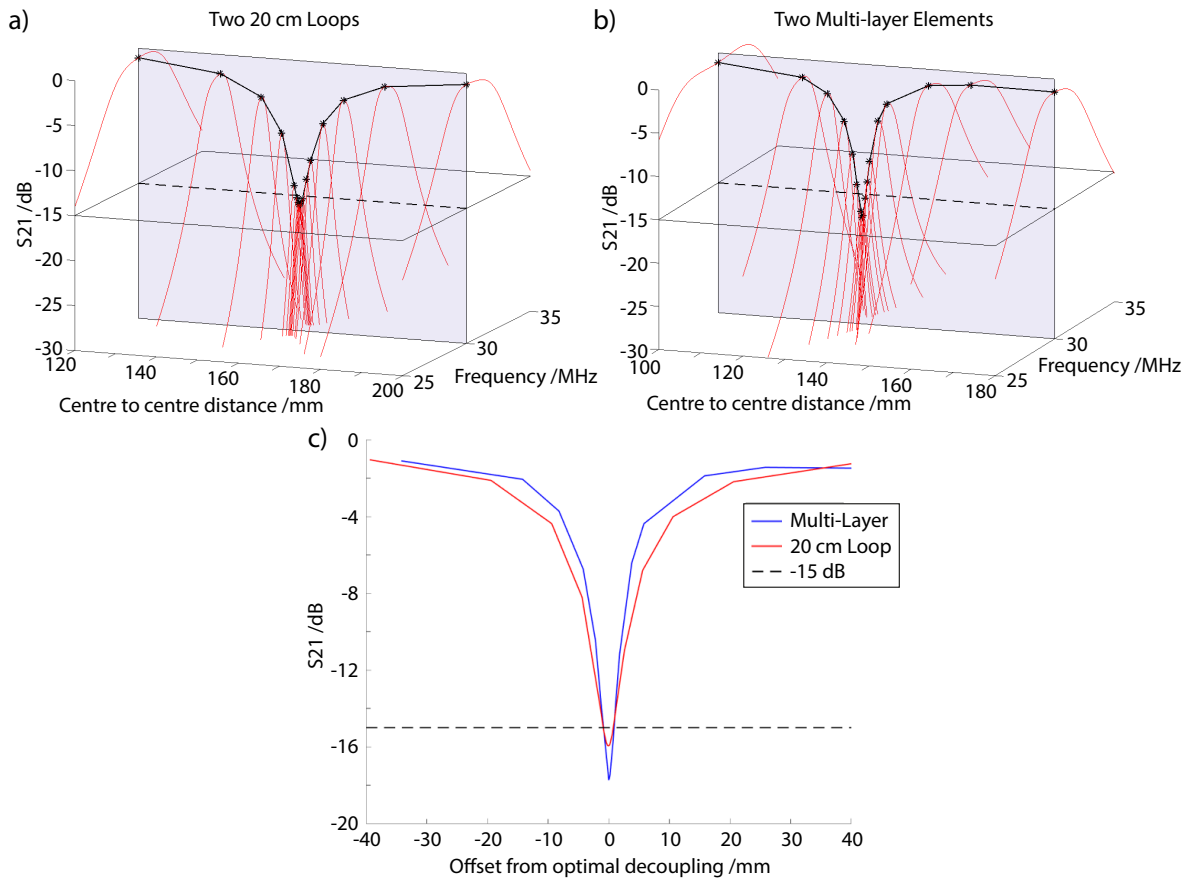

Figure 6.22: Simulated two-element decoupling transmission S-parameter (S_{21}) plots for multi-layer coils and 20 cm diameter loop coils. (a) 3D plot of S_{21} transmission in dB against coil centre to centre distance and frequency for two 20 cm diameter loop coils, tuned to be resonant at $30\,\mathrm{MHz}$. (b) 3D plot of S_{21} transmission in dB against coil centre-to-centre distance and frequency for two multi-layer coils, tuned to be resonant at $30\,\mathrm{MHz}$. (c) Plot of S_{21} against offset from optimal overlap for minimum coupling for two multi-layer elements and 20 cm diameter loop coil elements, with horizontal line positioned at $-15\,\mathrm{dB}$.

Typically, conventional single loop elements are able to decouple with an overlap approximately $30\,\%$ of the element diameter [10]. This exact overlap value depends on factors such as

the element shape, dimensions, and resonance frequency. The extent of decoupling was compared between two multi-layer loop elements and two 20 cm diameter loop elements which served as a benchmark case. Whilst the larger multi-layer elements would be a poor choice for a receive array, the larger elements were used in these decoupling tests as they allowed for higher precision in the overlap positioning of two elements relative to the overall coil dimension. The 20 cm diameter loop elements offered the most comparable coil FOV to the large multi-layer elements. For two 20 cm elements, EM simulations show that the optimum decoupling, corresponding to the minimum S_{21}, was achieved at $30\,\mathrm{MHz}$ with a centre-to-centre overlap of $159.4\,\mathrm{mm}$, with an $S_{21} = -15.96\,\mathrm{dB}$. In comparison, for the two multi-layer elements, optimum decoupling was achieved at $30\,\mathrm{MHz}$ with a centre-to-centre overlap of $134.2\,\mathrm{mm}$, with an $S_{21} = -17.63\,\mathrm{dB}$. For both cases, sufficient decoupling was achieved below the threshold of $-15\,\mathrm{dB}$ across an approximately $2\,\mathrm{mm}$ overlap region, as shown in Figure 6.22c. Whilst the single loop coils possessed a wider decoupling region, allowing for a greater range of element positioning within a coil construction, the multi-layer coil achieved greater optimal decoupling. An example of minimised coupling can be seen in Figure 6.23 a and b, where the two elements were positioned at the optimum overlap distance. When $1\,\mathrm{W}$ stimulation was applied into only multi-layer element 1 (positioned on the right of the figure), there was very little subsequent B_1^+ field on the left element. However, as shown in Figure 6.23 c and d, $5\,\mathrm{mm}$ more overlap than the optimal separation, at $139\,\mathrm{mm}$, $1\,\mathrm{W}$ stimulation showed significantly increased coupling; in this case, both elements became one resonant structure, reducing B_1^+ depth penetration and peak value.

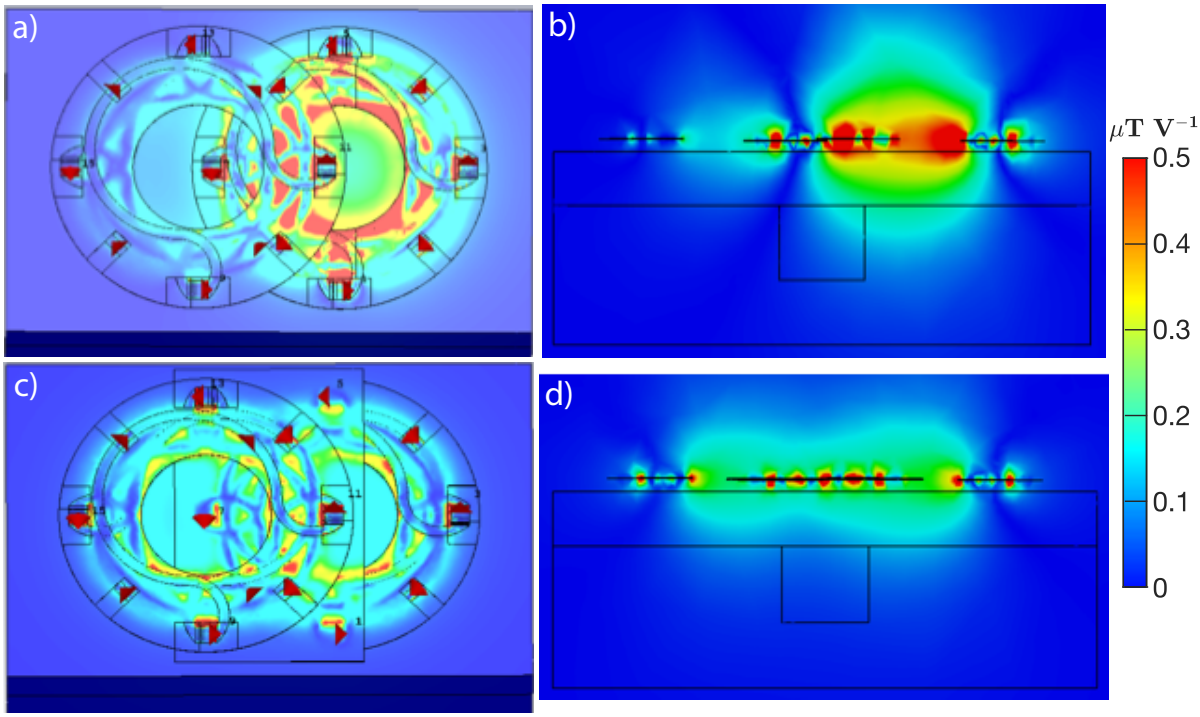

Figure 6.23: Surface and cross-section B_1^+ fields of optimum overlap and larger than optimum overlap between two multi-layer coil elements. (a) Surface B_1^+ at optimum conductor overlap with 1 W excitation into port 1 (right coil). (b) Cross-section B_1^+ at optimum conductor overlap with 1 W excitation into port 1. (c) Surface B_1^+ at larger than optimum overlap with 1 W excitation into port 1 showing strong coupling. (d) Cross-section B_1^+ at larger than optimum overlap with 1 W excitation into port 1 showing strong coupling.

Following this, corresponding benchtop measurements were made to verify the two multi-layer decoupling setups. Figure 6.24 shows the S_{21} of approximately $-15\,\mathrm{dB}$ at the centre-to-centre distance of $130\,\mathrm{mm}$, which is consistent with the simulated optimum S_{21} of $-17.6\,\mathrm{dB}$ at $134\,\mathrm{mm}$ centre-to-centre distance. The worse decoupling performance from benchtop measurements may have been due to unexpected inductive coupling with the external environment, as well as the lower precision of the coil overlap positioning (at $10\,\mathrm{mm}$ intervals). Due to the inability to tune and match the coils between measurements, the S_{11} was shown to be between -5 and $-10\,\mathrm{dB}$ at non-optimal overlaps. This led to the S_{21} at non-optimal overlaps being suppressed by the poor coil efficiency, reducing the EM coupling. As the S_{11} degraded beyond the acceptable limit of $-20\,\mathrm{dB}$ or lower between 125 and $135\,\mathrm{mm}$ centre-to centre distance, the S_{21} dip broadened. This explains the discrepancy in the larger width of the S_{21} dip from benchtop measurements when compared to the simulated case that allowed the coils to be re-tuned at every iteration. As such, EM simulations are preferred over benchtop measurements to

characterise coil decoupling performance, although they are more time consuming. Following this, EM simulations are used to characterise the three multi-layer element configuration.

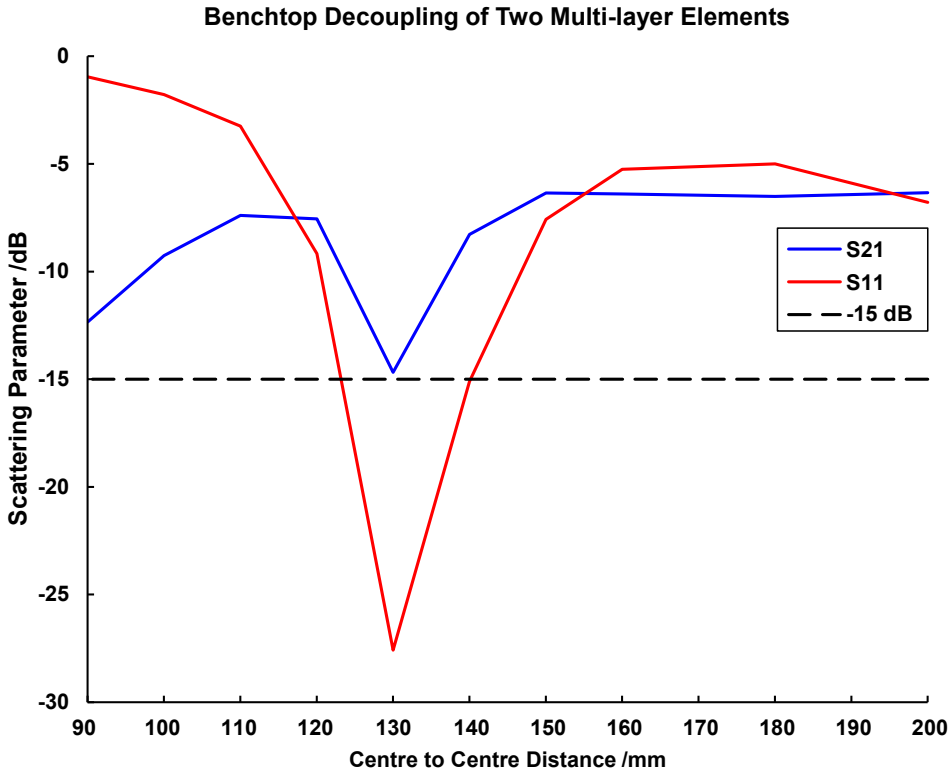

Figure 6.24: Benchtop decoupling of mutli-layer elements show S_{21} and S_{11} against the centre to centre distance measured at steps of $10\,\mathrm{mm}$. A $-15\,\mathrm{dB}$ reference line shows adequate S_{21} decoupling, achieved at the optimum position.

6.4.1.3 Three Multi-layer Element Decoupling

Here, multi-layer decoupling was further generalised with three elements positioned in an approximately equilateral triangle to investigate the possibility of 2D multi-layer array configurations. For comparison, the decoupling of three 20 cm loop elements was also investigated with element 3 positioned in an equilateral triangle pattern separated from element 2 by a second $1\,\mathrm{mm}$ thick dielectric layer. In both cases, the overlap distance between coil elements 1 and 2 was taken as the optimal decoupling distance found in the previous section, with the position of the third element iterated. With the 20 cm diameter loop elements, good decoupling was achieved simultaneously for all three elements, with a vertical overlap distance for all three transmission S-parameters S_{21}, S_{31}, and S_{32} of $-15.34\,\mathrm{dB}$, $-15.08\,\mathrm{dB}$, and $-14.07\,\mathrm{dB}$ respectively, as shown in Figure 6.25. The optimum overlap position was consistent across the three elements (equivalent to the separation of two elements of $159.4\,\mathrm{mm}$), as expected from

the circular element design, and the three-fold rotational symmetry formed from the triangular overlap.

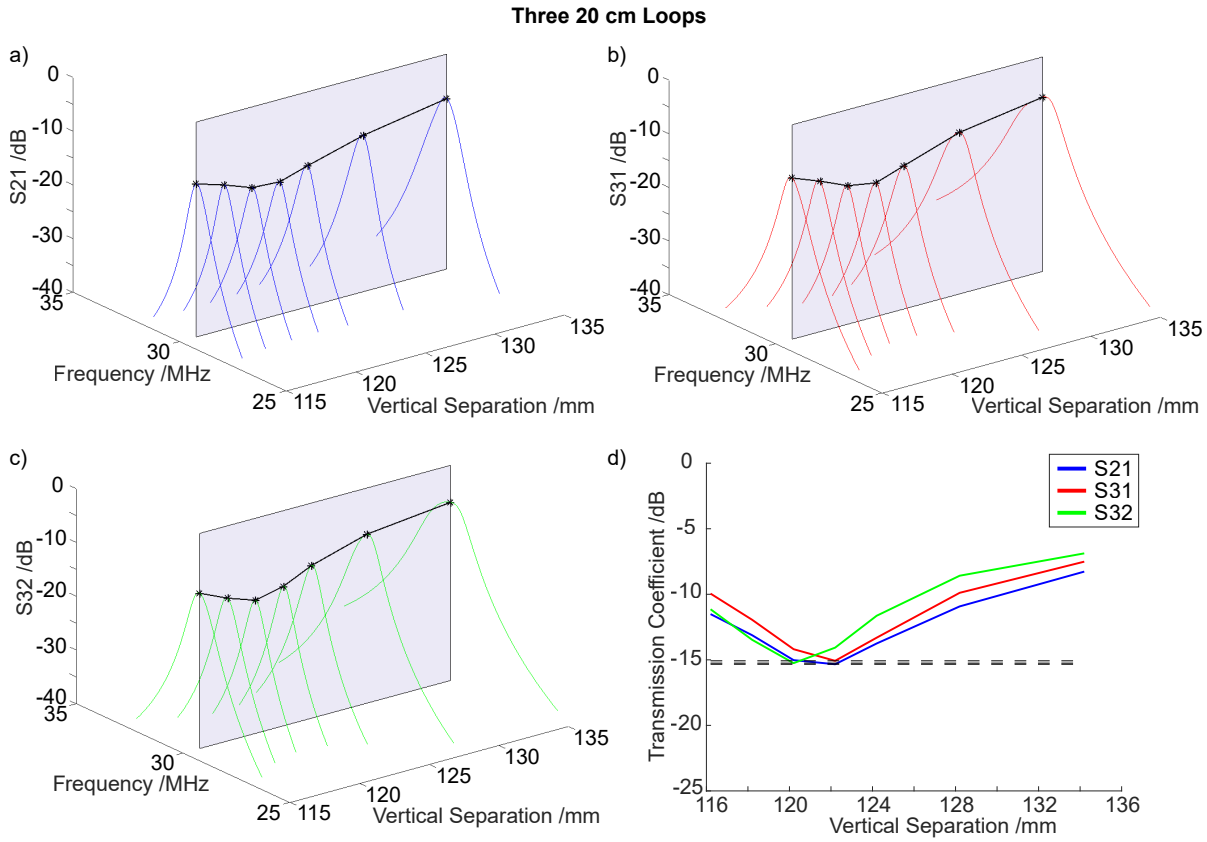

Figure 6.25: Three-element decoupling transmission S-parameter (S_{ij}) plots for conventional 20 cm loop coils. (a) 3D plot of S_{21} transmission (between coil 2 and coil 1) in dB against the distance of coil 3 and frequency, tuned to be resonant at $30\,\mathrm{MHz}$. (b) 3D plot of S_{31} transmission (between coil 3 and coil 1) in dB against the distance of coil 3 and frequency. (c) 3D plot of S_{32} transmission (between coil 3 and coil 2) in dB against the distance of coil 3 and frequency. (d) Plot of transmission S-parameters against the vertical separation between the first two and third coil for geometric decoupling for pairs of combinations from three 20 cm loop elements.

For the decoupling of three multi-layer elements, excellent decoupling was seen between elements 1 and 2 with an $S_{21} = -19.78\,\mathrm{dB}$ at a coil distance of $144\,\mathrm{mm}$, as shown in Figure 6.26. At this separation and frequency, decoupling was achieved for S_{31} and S_{32} with $-11.98\,\mathrm{dB}$ and $-11.74\,\mathrm{dB}$ respectively, which notably does not exceed the arbitrary threshold of $-15\,\mathrm{dB}$. With the multi-layer elements, the optimum overlap position is dependent on the element position. For example, between elements 1 and 3 the optimum was achieved with an $S_{31} = -12.04\,\mathrm{dB}$ with approximately $1\,\mathrm{mm}$ more overlap at $145\,\mathrm{mm}$, and between elements 2 and 3 the optimum was achieved with an $S_{32} = -13.31\,\mathrm{dB}$ with approximately $5\,\mathrm{mm}$ more overlap at $149\,\mathrm{mm}$. As

such, in the case of the multi-layer design, the addition of a third element requires adjustment of the overlap of the first two elements. We believe that the observed difference in optimum overlap across different elements was due to the approximate four-fold rotational symmetry of the multi-layer design, which were incompatible with the current arrangement of elements in a triangular pattern. More optimal decoupling was achieved with the first two elements of the multi-layer design; however, the complex conductor design led to differing optimal overlaps across the three nearest-neighbour couplings of the three elements. Overall, these results indicate that the multi-layer design can successfully decouple in 3D; however, as a proof of concept, the four fold rotational symmetry of this multi-layer design should require the elements to be placed in a square grid array, as shown later in section 6.4.3.1.

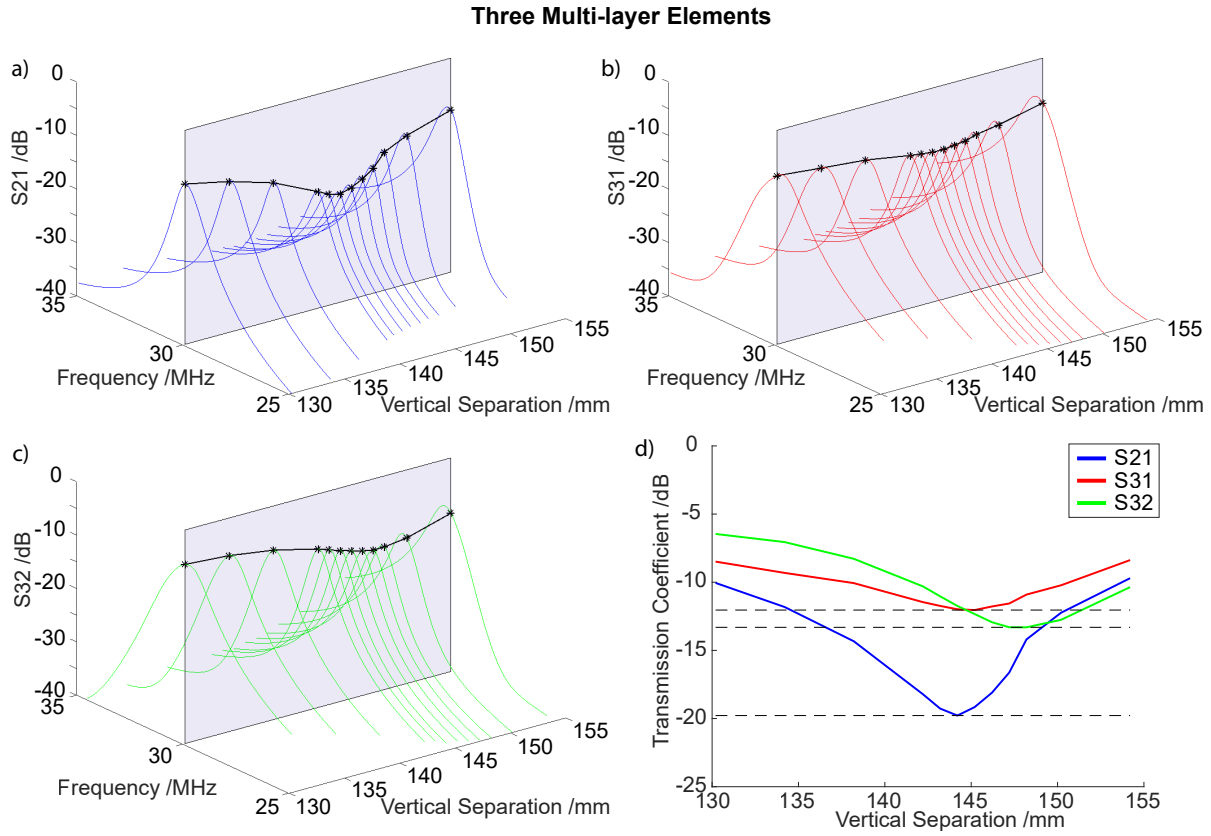

Figure 6.26: Three-element decoupling transmission S-parameter (S_{21}) plots for multi-layer coils. (a) 3D plot of S_{21} transmission (between coil 2 and coil 1) in dB against the distance of coil 3 and frequency, tuned to be resonant at $30\,\mathrm{MHz}$. (b) 3D plot of S_{31} transmission (between coil 3 and coil 1) in dB against the distance of coil 3 and frequency. (c) 3D plot of S_{32} transmission (between coil 3 and coil 2) in dB against the distance of coil 3 and frequency. (d) Plot of transmission S-parameters against the vertical separation between the first two and third coil for geometric decoupling for pairs of combinations from three multi-layer elements.

Examples of the B_1^+ field from coupling of three multi-layer elements are shown in Figure 6.27. Minimised EM coupling across three coil elements was seen with coil elements 1 and 2 placed at their optimum overlap distance, and the third coil at a distance of $144\,\mathrm{mm}$. $1\,\mathrm{W}$ excitation into each of the three elements individually showed minimal EM field in the non-excited coils and a high B_1^+ peak efficiency at the centre. In a second setup, elements 1 and 2 were placed at their optimum overlap distance, with element 3 placed non-optimally at $130\,\mathrm{mm}$ distance. Therefore, there was insufficient overlap for cancellation of mutual inductance between the third element and the first two. Significant coupling was seen with $1\,\mathrm{W}$ excitation into each of the coils, and loss of B_1^+ was seen with excitation into elements 1 and 2, with even greater loss of B_1^+ seen with excitation into element 3.

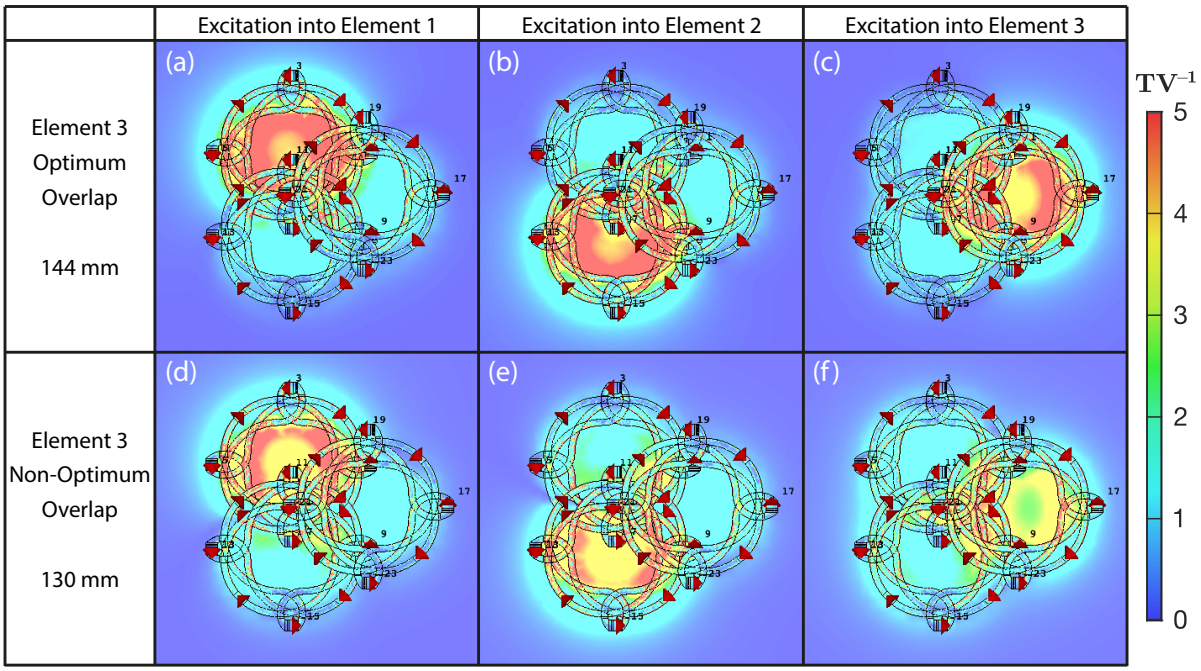

Figure 6.27: Surface B_1^+ fields for two cases, optimised overlap and insufficient overlap, for $1\,\mathrm{W}$ stimulation into each of the three multi-layer coil elements. (a) Optimised overlap ($144\,\mathrm{mm}$) with excitation into coil element 1. (b) Optimised overlap with excitation into coil element 2. (c) Optimised overlap with excitation into coil element 3. (d) Insufficient overlap ($130\,\mathrm{mm}$) with excitation into coil element 1. (e) Insufficient overlap with excitation into coil element 2. (f) Insufficient overlap with excitation into coil element 3.

6.4.2 Multi-layer Phase and Overlap Angle

Previously, section 6.2.1 showed the significant improvements in B_1^+ efficiency and uniformity that can be attained from optimising the relative phase between neighbouring elements.

With conventional loop coils, this improvement can be attributed to the overall H-field being more circularly polarized, such that the component of B_1^+ is larger. In the case of multi-layer elements, we expect less predictable B_1^+ interactions from a phase shift, due to the numerous overlapping layers and less uniform B_1^+ close to the coil, as well as the reversed current direction in the peripheral region. Additionally, section 6.4.1 above shows that the optimal overlap region is dependent on the orientation of the element. Due to the approximate four-fold rotational symmetry of the multi-layer design, the different orientations for overlap could be achieved by rotating the coil about the central axis. As such, both phase shift and overlap orientation between two multi-layer elements were investigated in this section.

6.4.2.1 EM Simulation Setup

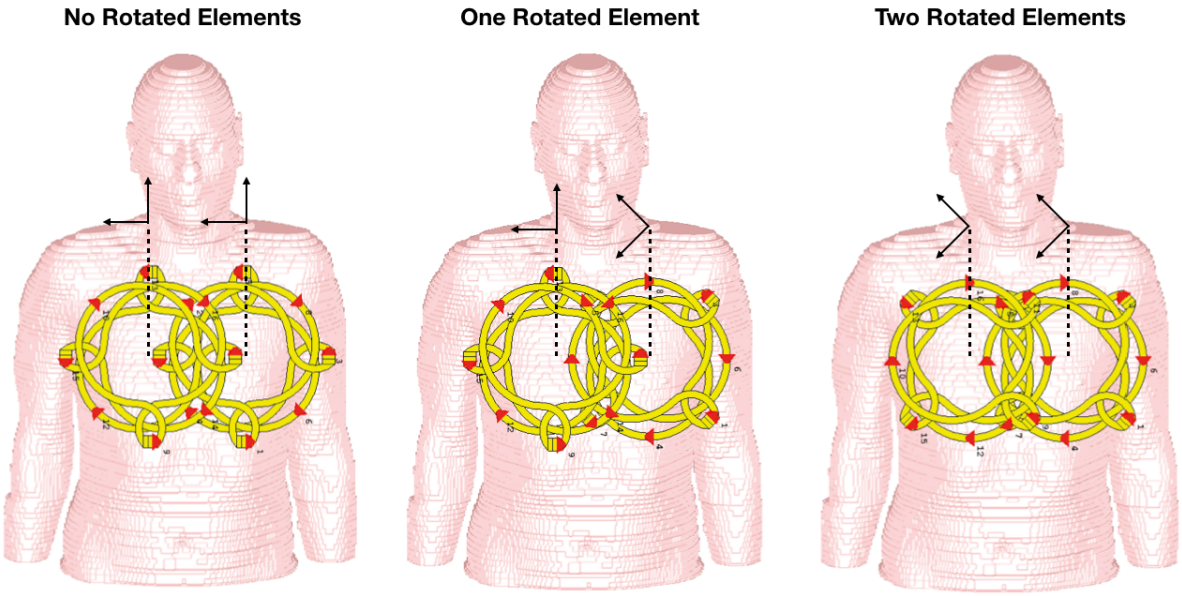

Figure 6.28: Two multi-layer elements are overlapped on the torso of a human voxel model. Due to the approximate fourfold rotational symmetry of the four-layer multi-layer design, three overlap configurations can be formed from two elements, by rotating none, or one or both elements $45°$.

The transmit B_1^+ from a pair of multi-layer elements was compared to a pair of conventional circular loops. The four-layer multi-layer coil exhibits an approximately four-fold rotational symmetry, where three principal orientations exist between a pair of multi-layer coils: no coils rotated (orientation 1), one coil rotated by $45°$ (orientation 2), and both coils rotated $45°$ (orientation 3), as shown in Figure 6.28. The field efficiency and uniformity of the pair of multi-layer

coils across a range of phase shifts in these three orientations were compared against a pair of 15 cm and pair of 20 cm diameter loop coils. The coil element pairs were positioned $10\,\mathrm{mm}$ above a human voxel model with B_1^+ field efficiency and uniformity calculated within the ROI taken as the heart voxel models. The elements were positioned at the optimum overlap as determined by the simulation results in the previous section. As the human voxel model was implemented, hexahedral meshing was required, which led to FDTD time domain simulations with high mesh cell density (approximately $8\,000\,000$) to capture the EM coupling. Sufficient EM isolation between all element pairs was achieved with an S_{21} of $-15\,\mathrm{dB}$ or better. The phase shift between the pair of elements was swept from $-30°$ to $30°$ at $5°$ steps.

6.4.2.2 Two Multi-layer Phase Results

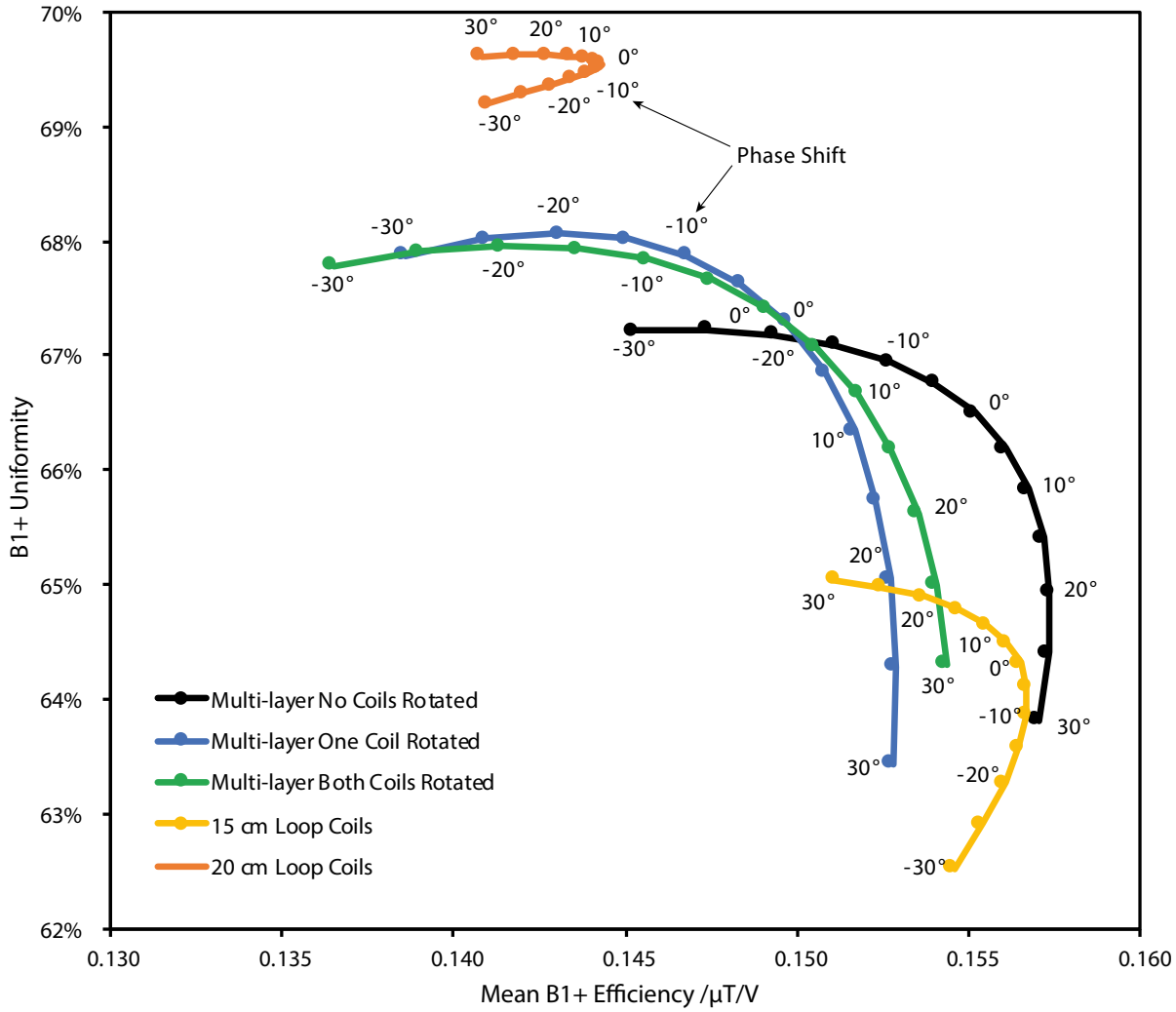

Figure 6.29: B_1^+ uniformity versus efficiency plot for the three configuration formed from the overlap of a pair of multi-layer elements, and pairs of conventional 15 cm elements and 20 cm elements. The uniformity versus efficiency curves compare the phase shift between two elements from $-30°$ to $30°$ in steps of $5°$ (labelled).

Overall, the field uniformity-efficiency trade-off for all five setups (three large multi-layer rotations, 15 cm pair, and 20 cm pair) are plotted in Figure 6.29. The positive phase shifts on multi-layer coils achieved an effect on the B_1^+ curve corresponding to the negative phase shifts on conventional loop coils. This is due to the reversed direction of current flow on the periphery of the multi-layer coil when compared to the centre of the coil, and thus phase shifts have the opposite effect. For loop coils, the optimum efficiency was achieved with an approximately -5 to $-10°$ phase shift (the negative shift represents a right handed polarization), whilst for

multi-layer coils the optimum efficiency was achieved with an approximately $15°$ to $30°$ phase shift. An increase in field uniformity can be traded for field efficiency in both cases, with an optimum field uniformity achieved from a $15°$ phase shift for loop coils, and a $-15°$ phase shift for multi-layer coils. Consistent with previous simulations, the multi-layer coils achieved comparable field efficiency to the 15 cm loop and a greater field uniformity. In addition, the multi-layer coil achieved a greater field efficiency compared to the 20 cm diameter coil, but a poorer field uniformity. Within the multi-layer coil category, the orientation for optimum field uniformity was achieved with one coil rotated, whilst optimum field efficiency was achieved with zero coils rotated. For receive B_1^-, the field profiles still held; however, the phase shift should be reversed for a counter-rotating circularly polarized field. The longer span of the field uniformity field efficiency curve shows the greater sensitivity over phase difference, and the greater control of uniformity and efficiency of the multi-layer design. Additionally, the high variation between uniformity and efficiency across phase and rotation of the multi-layer design may allow improved fine tuning of EM field through control of the phase. Overall, the simulated figures show that the transmit field efficiency and uniformity benefits of the multi-layer coil translate to overlapped multi-layer arrays, although specific overlap orientations and phase shifts are required for maximum B_1^+ efficiency.

6.4.3 Development of Multi-layer Array Prototype

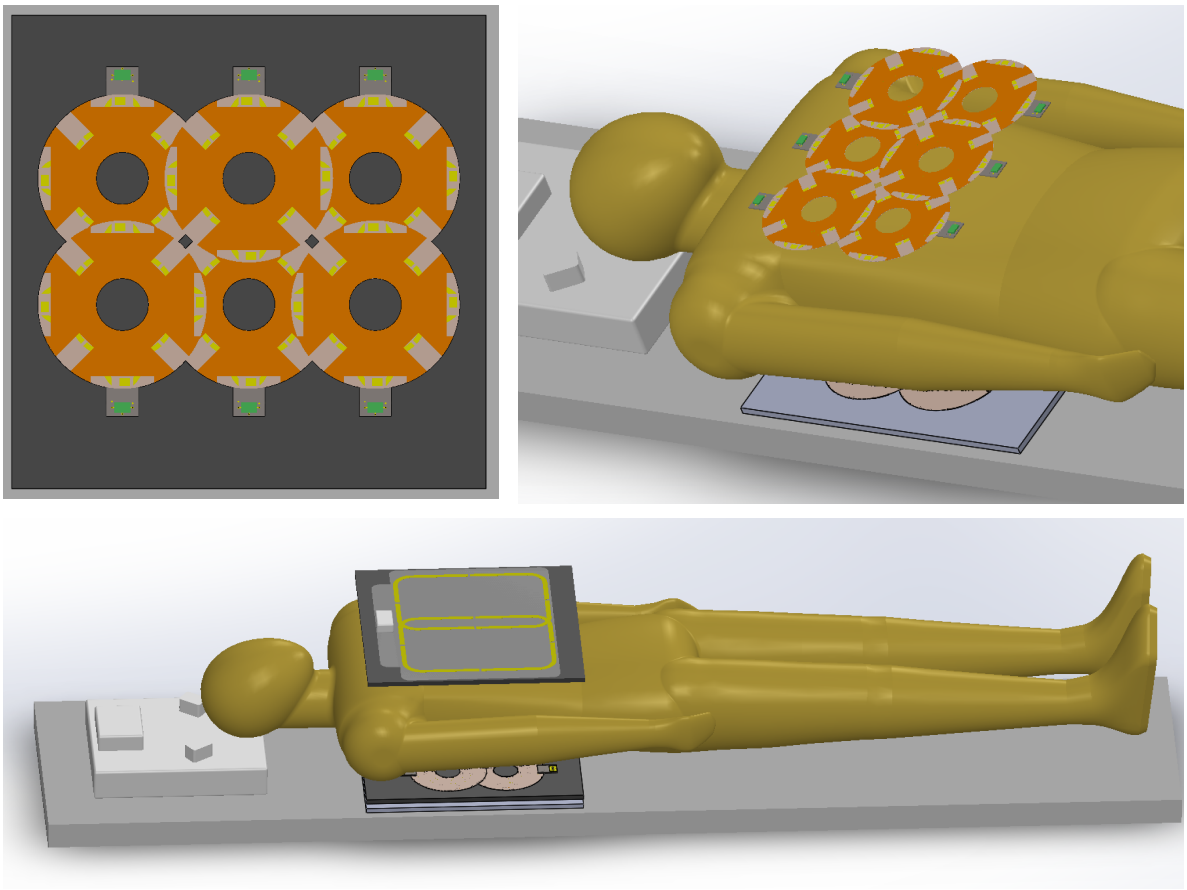

Figure 6.30: CAD model of proposed final ^{13}C array design, with two large transmit elements of $200\,\mathrm{mm} \times 300\,\mathrm{mm}$ with $30\,\mathrm{mm}$ fillet at $17\,\mathrm{mm}$ overlap, with six multi-layer receive elements positioned in a 3 by 2 grid. The transmit and receive elements are separated by a $1\,\mathrm{cm}$ thick foam, and both positioned such that the centre of the receive array coincides with the centre of the transmit array. The coil comprises of two paddles, positioned above and below a model torso obtained as an open source CAD file imported to Solidworks. The interface box is placed beneath the head, approximately $50\,\mathrm{cm}$ from the coil.

This final project sees the development and construction of a multi-layer receive array coil to be used in ^{13}C cardiac MRI studies at Oxford. Unfortunately, the development of this coil was delayed by disruptions to the production and supply of PCBs due to the coronavirus pandemic. At the time of writing, the receive array was only partly complete, and continued construction and development of the array is still to be undertaken. The multi-layer receive array is designed to be used in combination with the Tx only array developed in section 6.3 above, with high B_1^+ uniformity. This Tx array design consists of four $200\,\mathrm{mm} \times 300\,\mathrm{mm}$ elements, with $30\,\mathrm{mm}$ fillet radius, constructed such that the elements are overlapped at $17\,\mathrm{mm}$ ($4\,\mathrm{mm}$

less than the optimum overlap for geometric decoupling when accounting for coupling with the scanner bore). The interface box was designed such that both phase options of $0, 0, 180, 180°$ and $0, 90, 180, 270°$ could be used, for improved B_1^+ uniformity or improved B_1^+ efficiency respectively.

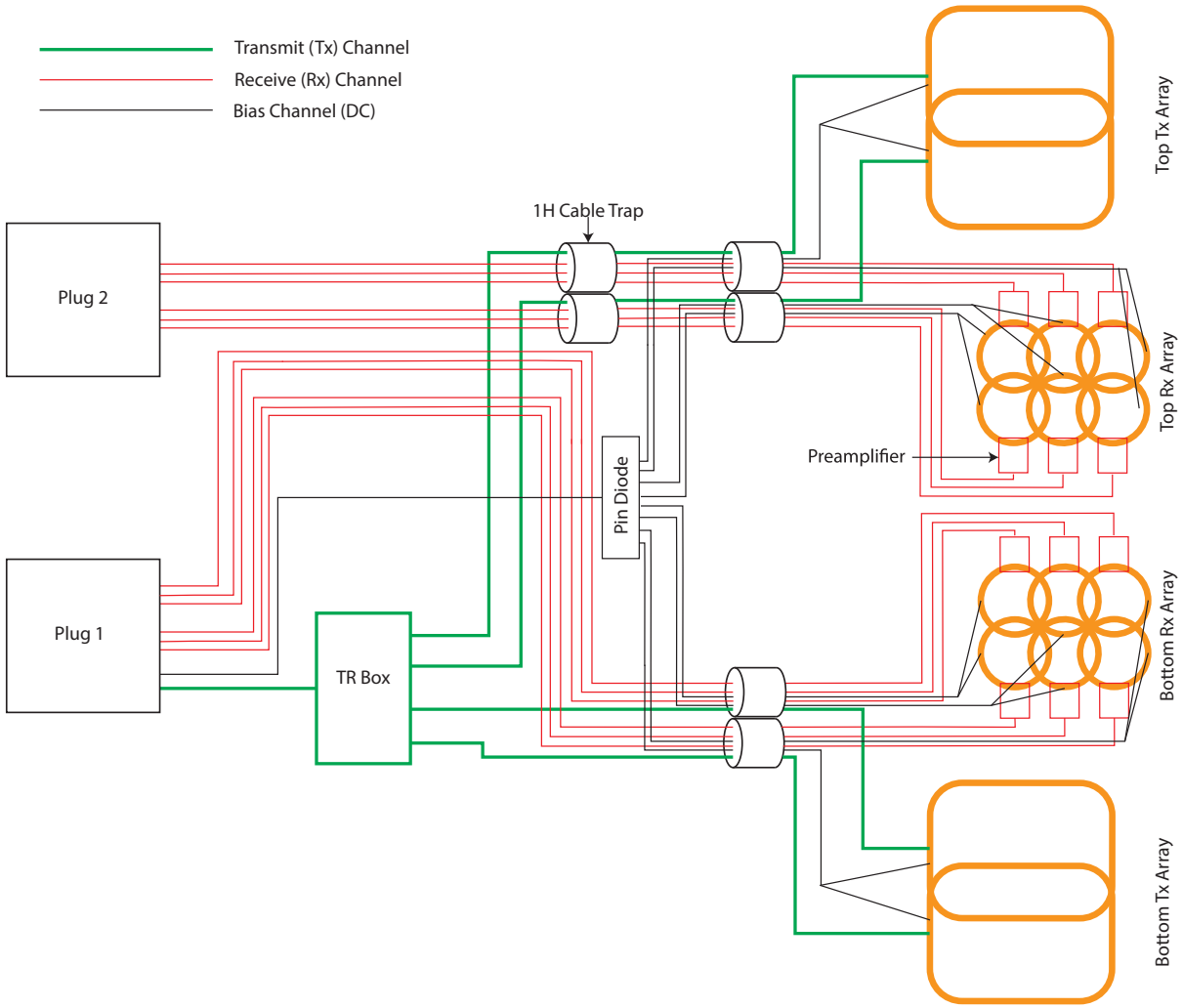

Figure 6.31: Block diagram showing a total of four transmit channels (shown in green) and twelve receive channels (shown in red). Due to the active detuning between transmit and receive determined by the scanner sequence, DC cables need to be connected to the active detuning in transmit and receive elements. Additionally, the proposed position of ^{1}H cable traps are indicated, with two proton traps for the upper paddle, due to the longer distance to the T/R box.

The CAD model for the proposed array coil is shown in Figure 6.30. The outer transmit array is separated by a $1\,\mathrm{cm}$ thick foam layer from the multi-layer receive array. A smaller receive only multi-layer element prototype was constructed (as described below in section) 6.4.3.1, with an initial proposal for 12 total elements, with six in each paddle to fully cover the torso. This array

design requires decoupling between transmit and receive elements, which requires switchable detuning, in the form of active and passive detuning components. This requires additional cabling (supporting DC current and ground) in a 'twisted pair' configuration to supply the DC to the pin diode for switching. The cabling is in addition to the existing four transmit channels and twelve receive channels. Additionally, two sets of cable baluns would need to be implemented, as otherwise the cable bundle would be too thick. The full extent of cabling is shown in Figure 6.31.

6.4.3.1 Receive Only Multi-layer Prototype

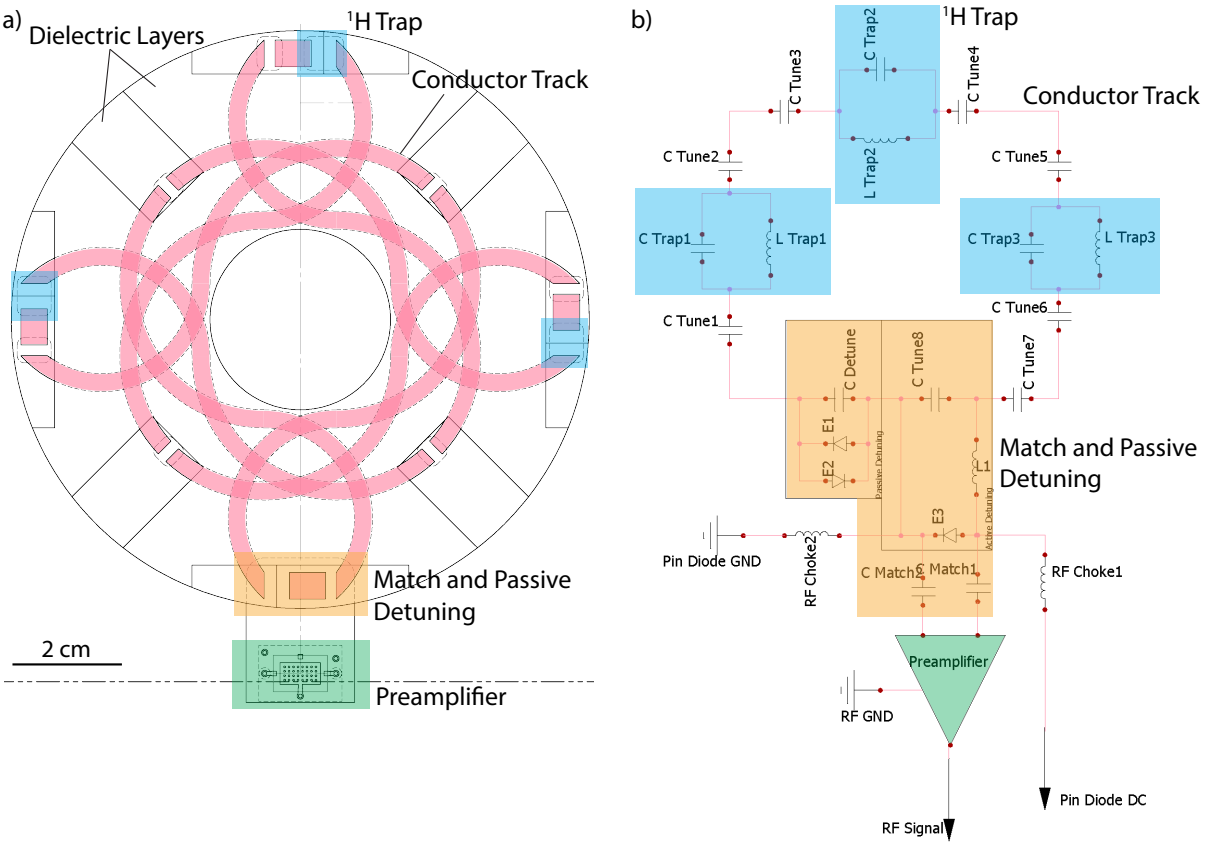

Figure 6.32: ^{13}C multi-layer prototype 3 for receive only. (a) To scale drawing of a single multi-layer coil element showing conductor track layout, dielectric layers, lumped element joints and pre-amplifier position. (b) Schematic diagram showing lumped elements for coil tuning, matching, ^{1}H traps, detuning from the transmit coil, and preamplifier connection.

For receive, high coil sensitivity over the ROI is desired; this is achieved by smaller elements with minimised coil resistance and maximised inductance. The previous 'smaller' multi-layer prototype operating in TxRx mode was shown to achieve a 50 % increased receive SNR com-

pared to conventional loops of the same dimensions in Chapter 5. However, for Rx only, further SNR improvements can be achieved, as shown previously from the parameter sweep for optimising receive in section 5.3.2.2. The four-layer multi-layer design with parameters of $R1 = 40\,\mathrm{mm}$, $R2 = 30\,\mathrm{mm}$, $O = 10\,\mathrm{mm}$, and $W = 5\,\mathrm{mm}$ was shown to achieve $100\,\%$ coil sensitivity and SNR compared to the optimum loop coil in receive. A total of 12 PCBs were manufactured following this design to be eventually constructed into a receive array. The new receive only PCB was constructed with three structural and design changes as described below:

- Smaller coil $R1$ and $R2$ values were used to reduce the coil resistance, and increase coil inductance (overall increasing Q-loaded values), for higher SNR.
- Thinner conductor widths, W, were used to minimise EM shielding and allow for a thinner coil PCB with overall greater flexibility. Additionally, as the coil is in receive only, substantially lower voltages will be used and a single discrete capacitor chip can be placed in the lumped element gap (without the need for three parallel capacitors, as presented in section 3.3.3.1)
- The preamplifier was brought directly onto PCB to reduce travel distance of the induced signal before amplification; this has the effect of minimising noise gained from the cable and external environment. A preamplifier mounting plate was designed into the PCB, for the preamplifier to be flow-soldered directly.

At the time of writing, the multi-layer PCBs prototypes have been successfully manufactured, and two out of 12 multi-layer receive elements have been constructed.

6.5 Discussion

This chapter develops an improved transmit array and an improved receive array for clinical ^{13}C MRI compared to existing commercially available coils. The transmit array was shown to achieve better B_1^+ efficiency and comparable B_1^+ uniformity compared to the commonly used Helmholtz pair and equivalent clamshell coil design through EM simulations, benchtop measurements, and scanner measurements. The receive array utilises the multi-layer design developed in Chapters 4 and 5, where significant increases of SNR of $50\,\%$ were shown. This chapter works on ensuring that the high sensitivity of the multi-layer design is preserved in an array configuration through geometric decoupling.

6.5.1 Overview

Well-designed RF array coils offer improved B_1^+ uniformity compared to single element coils without loss of B_1^+ efficiency. As such, commercially available clinical ^{13}C coil designs for the heart primarily take the form of either multiple individual TxRx elements or large To loops used in conjunction with Ro arrays. In this chapter we characterised both of these designs against existing coil configurations, and developed an improved array design through optimisation of element dimensions, overlap, and phase. With individual Tx elements, the four element configuration provided the highest B_1^+ uniformity and B_1^+ efficiency trade-off. EM simulations were used to determine the optimum element size for a representative separation: these were found to be dimensions of $200\,\mathrm{mm} \times 300\,\mathrm{mm}$ with a $30\,\mathrm{mm}$ fillet. This optimum element was constructed and compared with benchtop measurements.

It was found that two design factors in particular affected transmit performance in the four element configuration. Firstly, we implemented a phase shift to each element that equalled the angle between the centre of the elements and the centre of the ROI. Secondly, we positioned neighbouring elements with an overlap distance less than that required for optimum geometric decoupling; in the case of the $200\,\mathrm{mm} \times 300\,\mathrm{mm}$ array, we used an overlap separation of $17\,\mathrm{mm}$ instead of the optimum $22\,\mathrm{mm}$. With both design aspects combined, $50\,\%$ increased B_1^+ efficiency was measured through EM simulations and scanner measurements. A corresponding decrease in B_1^+ uniformity of approximately $10\,\%$ was observed through EM simulations and benchtop measurements. It was found that the uniformity was better represented by EM simulation and benchtop measurements than scanner measurements, due to the high noise and variability from ^{13}C B_1^+ maps. This array was constructed to form the transmit part of the improved ^{13}C cardiac array coil.

The ability for multi-layer elements to replace existing loop coils in arrays was determined through their ability for geometric decoupling. A further multi-layer prototype was developed, tailored for receive sensitivity. This multi-layer coil design was shown to achieve $100\,\%$ improved receive sensitivity compared to a loop of comparable size. Despite the multi-layer receive array not being complete, we have shown that theoretically the multi-layer design will retain its high sensitivity in an array, allowing a potentially twofold increase in SNR on receive. Discussions of the further works for the four element transmit array and multi-layer receive

array are presented in Chapter 7.

References

[1] Gordon, J. W. et al. “A variable resolution approach for improved acquisition of hyperpolarized 13C metabolic MRI”. In: *Magnetic Resonance in Medicine* 84 (6 2020). ISSN: 15222594. DOI: 10.1002/mrm.28421.

[2] Sánchez-Heredia, J. D. et al. “Multi-site benchmarking of clinical 13C RF coils at 3T”. In: *Journal of Magnetic Resonance* 318 (Sept. 2020), p. 106798. ISSN: 1090-7807. DOI: 10.1016/J.JMR.2020.106798.

[3] Cunningham, C. H. et al. “Hyperpolarized 13C Metabolic MRI of the Human Heart: Initial Experience.” In: *Circulation research* 119 (11 Feb. 2016), pp. 1177–1182. ISSN: 1524-4571. DOI: 10.1161/CIRCRESAHA.116.309769.

[4] Rider, O. J. et al. “Noninvasive In Vivo Assessment of Cardiac Metabolism in the Healthy and Diabetic Human Heart Using Hyperpolarized 13C MRI”. In: *Circulation Research* 126 (6 Mar. 2020), pp. 725–736. ISSN: 0009-7330. DOI: 10.1161/CIRCRESAHA.119.316260.

[5] Reed, G. D. et al. “Characterization and compensation of f0 inhomogeneity artifact in spiral hyperpolarized 13C imaging of the human heart”. In: *Magnetic Resonance in Medicine* 86 (1 2021). ISSN: 15222594. DOI: 10.1002/mrm.28691.

[6] Tougaard, R. S. et al. “Acute hypertensive stress imaged by cardiac hyperpolarized [1-13C]pyruvate magnetic resonance”. In: *Magnetic Resonance in Medicine* 80 (5 2018). ISSN: 15222594. DOI: 10.1002/mrm.27164.

[7] Laustsen, C. et al. “Acute porcine renal metabolic effect of endogastric soft drink administration assessed with hyperpolarized [1-13c]pyruvate”. In: *Magnetic Resonance in Medicine* 74 (2 2015). ISSN: 15222594. DOI: 10.1002/mrm.25692.

[8] Fujita, H. “New Horizons in MR Technology: RF Coil Designs and Trends”. In: *Magnetic Resonance in Medical Sciences* 6 (1 2007), pp. 29–42. ISSN: 1347-3182. DOI: 10.2463/mrms.6.29.

[9] Kaufman, L. et al. “Switchable MRI RF coil array with individual coils having different and overlapping fields of view”. US4881034A. California, U. of. 1989.

[10] Roemer, B. and Edelstein, W. A. “Nuclear magnetic resonance (NMR) imaging with multiple surface coils”. US4825162A. Co, G. E. 1989.

[11] Roemer, P. B. et al. “The NMR phased array”. In: *Magnetic Resonance in Medicine* 16 (2 Nov. 1990), pp. 192–225. ISSN: 07403194. DOI: 10.1002/mrm.1910160203.

[12] Ohliger, M. A. and Sodickson, D. K. “An introduction to coil array design for parallel MRI”. In: *NMR in Biomedicine* 19 (3 May 2006), pp. 300–315. ISSN: 0952-3480. DOI: 10.1002/nbm.1046.

[13] Hoult, D. I., Chen, C.-N., and Sank, V. J. “Quadrature detection in the laboratory frame”. In: *Magnetic Resonance in Medicine* 1 (3 Sept. 1984), pp. 339–353. ISSN: 07403194. DOI: 10.1002/mrm.1910010305.

[14] Glover, G. et al. “Comparison of linear and circular polarization for magnetic resonance imaging”. In: *Journal of Magnetic Resonance (1969)* 64 (2 Sept. 1985), pp. 255–270. ISSN: 00222364. DOI: 10.1016/0022-2364(85)90349-X.

[15] Hyde, J. S. et al. “Quadrature detection surface coil”. In: *Magnetic Resonance in Medicine* 4.2 (1987), pp. 179–184. DOI: https://doi.org/10.1002/mrm.1910040211. URL: https://onlinelibrary.wiley.com/doi/abs/10.1002/mrm.1910040211.

[16] Grissom, W. A., Sacolick, L., and Vogel, M. W. “Improving high-field MRI using parallel excitation”. In: *Imaging in Medicine* 2 (6 Dec. 2010), pp. 675–693. ISSN: 1755-5191. DOI: 10.2217/iim.10.62.

[17] PR, H. and RM, H. *MultiTransmit parallel RF transmission technology*. Philips Healthcare, 2009. URL: https://philipsproductcontent.blob.core.windows.net/assets/20170523/ef14cfe32a7d4d61abdaa77c01681806.pdf.

[18] LL, W. and E, A. *Parallel transmit technology for high field MRI*. Siemens Medical Systems, Magnetom FLASH, 2009. URL: https://www.magnetomworld.siemens-healthineers.com/clinical-corner/case-studies/parallel-transmit-technology-for-high-field-mri.html.

[19] Leifer, M. C. “Resonant Modes of the Birdcage Coil”. In: *Journal of Magnetic Resonance* 124.1 (1997), pp. 51–60. ISSN: 1090-7807. DOI: https://doi.org/10.1006/jmre.1996.7488. URL: https://www.sciencedirect.com/science/article/pii/S1090780796974881.

[20] Rojas, R. and Rodríguez, A. O. “Numerical study of the optimal geometry of MRI surface coils”. In: 2007. DOI: 10.1109/IEMBS.2007.4353183.

[21] Chen, C.-N. et al. “The field dependence of NMR imaging. I. Laboratory assessment of signal-to-noise ratio and power deposition”. In: *Magnetic Resonance in Medicine* 3 (5 1986). ISSN: 15222594. DOI: 10.1002/mrm.1910030508.

[22] Wilkinson, E. J. “An N-Way Hybrid Power Divider”. In: *IRE Transactions on Microwave Theory and Techniques* 8 (1 1960). ISSN: 00972002. DOI: 10.1109/TMTT.1960.1124668.

[23] Tyler, A. et al. “A 3D hybrid-shot spiral sequence for hyperpolarized 13C imaging”. In: *Magnetic Resonance in Medicine* 85 (2 2021). ISSN: 15222594. DOI: 10.1002/mrm.28462.

7 | Conclusion and Further Work

7.1 Thesis Summary

This chapter summarises the collection of results obtained through this project. Previously, the introduction chapter, Chapter 1, identified three aspects of coil development for ^{13}C cardiac MRI: a more efficient RF coil design for increased SNR, an improved method of surface coil comparison and optimisation, and lastly an optimised array for high transmit uniformity and high receive sensitivity over a larger field of view. Through the work conducted in this thesis, we achieved three projects that contribute towards the advancement of ^{13}C MRI.

1. Novel multi-layer coil design with improved B_1^+ and SNR.
2. Adapted B_1^+ and SNR mapping method by fully sampling the power calibration curve at each voxel.
3. Improved array coil for improved coil coverage over the torso.

It should be noted that these developments can be similarly applied to the broader X-nuclei community. A discussion of each of these three pieces of work are presented, with their applications and corresponding limitations.

7.2 Multi-layer Coil design

The novel multi-layer coil design was first presented in results Chapter 4 with ^{13}C and ^{23}Na star-shaped TxRx pre-clinical prototypes. Here, B_1^+ and SNR maps were obtained on the scanner and through EM simulations and compared against single loop elements. Promisingly, around $50\,\%$ increase in B_1^+ efficiency was seen, however no improvements were seen in receive SNR due to inefficiencies in the EM field profile with the straight conductor tracks. This motivated the development of a ^{13}C four layer petal shaped TxRx human prototypes in section 5 constructed using curved conductor tracks. Comparing scanner and simulated results to loop coils of similar dimensions, increases of $30\,\%$ B_1^+ and $50\,\%$ SNR were achieved on transmit and receive respectively. The most significant development from this work is the ^{31}P multi-layer TxRx coil tested for human use. ^{31}P scans were performed on five participants, which showed the multi-layer coil achieved two times the spectral SNR compared to a commercially available

loop coil of the same dimension. Furthermore, optimisation using a parameterised multi-layer design showed that further improvements could still be achieved on transmit-only using additional layers (six layers) of up to $80\,\%$ B_1^+ efficiency and similarly on receive-only with a small optimised receive element. Subsequently, in section 6.4, the potential for multiple multi-layer elements to not couple through partial overlap was verified. This allows multi-layer elements to replace conventional loops in existing array configurations. As such, a multi-layer receive array is being developed with the more optimised receive only multi-layer design.

7.2.1 Applications

Presently, only one working multi-layer prototype has been constructed and approved for human imaging, comprising of a single TxRx element for ^{31}P. The current aim is for this single element multi-layer design to be made commercially available through PulseTeq Ltd for ^{31}P and other common X-nuclei such as ^{13}C and ^{23}Na. Currently, the multi-layer receive array for ^{13}C cardiac MRI is in the process of being developed at OCMR, and will be continued by Prof Tyler's research group. This design could be expanded beyond ^{13}C imaging to other X-nuclei, and also beyond imaging of the heart to other organs in the torso.

7.2.2 Limitations and Further Work

The multi-layer coil design is easier to construct and design for lower frequencies, and larger coil elements in the sample-noise-dominated regime, which led to the translation into human coils. As such, no in-vivo pre-clinical results were obtained with the multilayer design. One such proposal of further work could be the development of improved pre-clincal multi-layer coils for improved animal imaging. Secondly, the multi-layer coil could be developed for ^{1}H $3\,\mathrm{T}$ at $120\,\mathrm{MHz}$. A ^{1}H multi-layer receive array is planned to be jointly developed using funding secured from the OUI (Oxford University Innovations) university challenge seed fund (UCSF) and PulseTeq Ltd. This ^{1}H coil will hopefully be much more widely applicable for MRI beyond the field of X-nuclei.

7.3 Coil Comparison using B1 and SNR mapping

To compare novel and optimal coil designs, a protocol for both fair and accurate characterisation of X-nuclei RF coils is required. Firstly, an accurate B_1^+ and SNR mapping protocol is presented that is robust against low SNR, typical of X-nuclei, and high field profile variation, typical of surface coils. This was achieved by fully sampling the voltage to signal curve using a variable density of voltages, as described in Methods section 3.4, adapted from the double angle method. This protocol allowed for high resolution 2D B_1^+ and SNR maps to be obtained by sacrificing the scan duration with approximately eight hour scans. Following, single values for the metrics: B_1^+ efficiency, B_1^+ uniformity and SNR were obtained by calculating the fields within a representative ROI. Fair comparison was obtained by plotting the inherent trade off between B_1^+ uniformity versus B_1^+ efficiency across coil dimensions, presented in section 5.3.

7.3.1 Applications

The accurate B_1^+ and SNR mapping protocol was used throughout this work for two ^{23}Na pre-clinical multi-layer prototypes in section 4.3, ^{13}C human multi-layer prototype comparison in section 5.4, and optimised ^{13}C transmit array in section 6.3.3. The field mapping protocol successfully characterises a range of pre-clinical and human coil designs for ^{13}C and ^{31}P MRI. This protocol is a simple adaptation of existing methods and can be used to image phantoms on all nuclei with low SNR.

7.4 Optimised Cardiac Array

Currently, two common coil designs are used for ^{13}C cardiac MRI: multiple individual TxRx elements and separate To Ro arrays. Chapter 6 showed that improvements in B_1^+ and SNR can be achieved by separately optimising transmit and receive only arrays at a representative separation of $300\,\mathrm{mm}$. Overall, by optimising element dimensions, reducing the neighbouring element overlap width and using a phase shift determined by the element angles from the ROI for more circular polarization, $50\,\%$ increase in B_1^+ efficiency was shown to be possible through: EM simulations, scanner measurements and benchtop measurements.

7.4.1 Applications

An optimised four element transmit only array, of dimensions $200\,\mathrm{mm} \times 300\,\mathrm{mm}$ and $30\,\mathrm{mm}$ fillet radius, with $17\,\mathrm{mm}$ element overlap (which is $4\,\mathrm{mm}$ less than the optimal for geometric decoupling) was constructed for ^{13}C cardiac MRI. Two phase options were implemented: of $0, 0, 180, 180°$, representing a Helmholtz configuration, and $0, 90, 180, 270°$ representing approximately a circular polarization configuration. This transmit array design can be used for imaging of other organs within the torso, and across other nuclei. The relationship between B_1^+ and frequency is shown in Appendix I. A TxRx version of this array design was constructed by PulseTeq for ^{129}Xe MRI. Furthermore, the optimised transmit only array was modified to be used in combination with the multi-layer receive array in development.

7.4.2 Limitations and Further Work

Changing each of the following three properties: overlap distance, phase configuration and element dimensions will alter the optimum values (that correspond to the maximum B_1^+ efficiency and uniformity) of the other to properties, and therefore it is challenging to determine the optimum B_1^+ from all three properties combined. One limitation of this work is that the improved array design may not be the optimum design, given the time constraints of the project. Smaller incremental improvements in B_1^+ may be attained through further optimisation of the array. Greater B_1^+ improvements may be achieved developing a new larger multi-layer transmit only element that can be implemented as a four channel array for high B_1^+ uniformity. This was beyond the scope of this project, due to the extensive work and high costs associated with such a development.

A | Forms of Maxwell's Equations

Maxwell's equations are presented in three different forms below: differential form in free space, integral form in free space, and differential form in polarizable media.

A.1 Differential form in free space

Here, Maxwell's equations describe the time evolution of electric fields, $\mathbf{E}$, and magnetic fields, $\mathbf{B}$, with permittivity of free space, ϵ_0, permeability of free space, μ_0, charge density, ρ, and current density, $\mathbf{J}$.

$$\nabla \cdot \mathbf{E} = \frac{\rho}{\epsilon_0} \qquad \nabla \cdot \mathbf{B} = 0 \tag{A.1}$$

$$\nabla \times \mathbf{E} = -\frac{\partial \mathbf{B}}{\partial t} \qquad \nabla \times \mathbf{B} = \mu_0 \left(\mathbf{J} + \epsilon_0 \frac{\partial \mathbf{E}}{\partial t} \right) \tag{A.2}$$

A.2 Integral form in free space

Maxwell's equations describing the integral form of the E- and B-fields integrated over closed area, $\mathbf{A}$, closed loop, $\mathbf{s}$, with magnetic flux density $\mathbf{\Phi_B}$, electric current I, and speed of light, c, is shown below:

$$\oint \mathbf{E} \cdot \, d\mathbf{A} = \frac{q}{\epsilon_0} \qquad \oint \mathbf{B} \cdot \, d\mathbf{A} = 0 \tag{A.3}$$

$$\oint \mathbf{E} \cdot \, d\mathbf{s} = -\frac{d\mathbf{\Phi_B}}{dt} \qquad \oint \mathbf{B} \cdot \, \mathbf{s} = \mu_0 I + \frac{1}{c^2} \frac{\partial}{\partial t} \int \mathbf{E} \cdot \, d\mathbf{A} \tag{A.4}$$

A.3 Differential form in polarizable media

Maxwell's equations describing the EM field in a dielectric and magnetic medium is shown below. The electric displacement, $\mathbf{D}$, is described for the case of a polarizing medium as $\mathbf{D} = \epsilon \mathbf{E} + \mathbf{P}$, where $\mathbf{P}$ is the polarization. The magnetic field strength, $\mathbf{H}$, is described for the

case of a polarizing medium as $\mathbf{B} = \mu(\mathbf{H} + \mathbf{M})$, where $\mathbf{M}$ is the magnetisation.

$$\nabla \cdot \mathbf{D} = \rho_{\text{free}} \qquad \nabla \cdot \mathbf{H} = 0 \tag{A.5}$$

$$\nabla \times \mathbf{E} = -\frac{\partial \mathbf{B}}{\partial t} \qquad \nabla \times \mathbf{H} = \mathbf{J}_{\text{free}} + \frac{\partial \mathbf{D}}{\partial t} \tag{A.6}$$

B | Combining Discrete Ports

'AC Combine' post processing allows adjustment of schematic values (namely capacitors for tuning and matching of RF coils) post simulation [AC Combine, CST Studio Suite 2020, 3DS.COM/SIMULIA]. All individual ports can be combined across the simulation frequency into a single combined excitation using AC combine. The method for combining the ports may use one of three options: signal, current or voltage. The combination method should correspond to the type of external port. It was unclear which combination method was most reliable and suited towards RF coil simulation. All three methods were investigated, and the validity of each was determined by the consistency with the expectations that SAR per kg was constant across input power, and B_1^+ was constant across input voltage. Table B.1 indicates that the B_1^+ and SAR are only consistent with power and voltage respectively using signal combination. As such, both signal external ports for excitation and signal discrete ports were used in the EM simulations of RF coils.

Table B.1: Summary of B_1^+ in $\mathrm{T\,V^{-1}}$, and SAR in W/kg across a range of input power for AC combine using current, voltage and signal.

Using AC combine with Current: i.e. $(1\,\mathrm{A})$

Power /W	B_1^+/μT	SAR /$\mathrm{W\,kg^{-1}}$	SAR /$\mathrm{kg^{-1}}$	Voltage /V	B_1^+/Voltage /$\mathrm{\mu T\,V^{-1}}$
1	1.7×10^{-2}	1.1×10^{-3}	1.1×10^{-3}	7.1	2.4×10^{-3}
1.2×10^{3}	5.0×10^{-1}	1.3	1.1×10^{-3}	2.4×10^{2}	2.0×10^{-3}
1.4×10^{4}	2.2	1.6×10^{1}	1.1×10^{-3}	8.5×10^{2}	2.6×10^{-3}
3.1×10^{6}	3.0×10^{1}	3.4×10^{3}	1.1×10^{-3}	1.2×10^{4}	2.4×10^{-3}

Using AC combine with Voltage: i.e. $(1\,\mathrm{V})$

Power /W	B_1^+/μT	SAR /$\mathrm{W\,kg^{-1}}$	SAR /$\mathrm{kg^{-1}}$	Voltage /V	B_1^+/Voltage /$\mathrm{\mu T\,V^{-1}}$
1	3.0×10^{-4}	5.1×10^{-7}	5.1×10^{-7}	7.1	4.2×10^{-5}
1.2×10^{3}	1.2×10^{-2}	6.1×10^{-4}	5.1×10^{-7}	2.4×10^{2}	4.9×10^{-5}
1.4×10^{4}	6.0×10^{-2}	7.3×10^{-3}	5.1×10^{-7}	8.5×10^{2}	7.1×10^{-5}
3.1×10^{6}	5.0×10^{-1}	1.6	5.1×10^{-7}	1.2×10^{4}	4.0×10^{-5}

Using AC combine with Signal:

Power /W	B_1^+/μT	SAR /$\mathrm{W\,kg^{-1}}$	SAR /$\mathrm{kg^{-1}}$	Voltage /V	B_1^+/Voltage /$\mathrm{\mu T\,V^{-1}}$
1	2.5×10^{-1}	2.1×10^{-1}	2.1×10^{-1}	7.1	3.5×10^{-2}
1.2×10^{3}	8.0	2.5×10^{2}	2.1×10^{-1}	2.4×10^{2}	3.3×10^{-2}
1.4×10^{4}	3.0×10^{1}	3.0×10^{3}	2.1×10^{-1}	8.5×10^{2}	3.5×10^{-2}

C | Scattering Parameters

C.1 Quantifying S-parameters

S-parameters are used to monitor coil performance at transmission and reception of RF fields at desired frequencies, and to minimise transmission and reception at undesired frequencies. The S_{11} should be minimised at desired frequencies (to minimise reflected power) and maximised at undesired frequencies (to maximise reflected power). Additionally, the S_{21} should be maximised at desired frequencies (to maximise transmitted power) and minimised at undesired frequencies (to minimise transmitted power). Practically, both S_{11} and S_{21} can be measured on a network analyzer to determine coil performance, however the method of using both differ and there are advantages and disadvantages of both, that will be discussed in the following sections. S-parameters are measured as a complex impedance on a Smith chart, and converted into magnitude. S-parameter values are typically presented in dB, the conversion for both reflection and transmission S-parameters are presented below:

$$S_{ii}(dB) = 20\log_{10}|S_{ii}| \tag{C.1}$$

$$S_{ij}(dB) = 20\log_{10}|S_{ij}| \tag{C.2}$$

The reflection and transmission S-parameters are typically dealt with separately. For reflection, a common benchmark in RF coil construction is to ensure $-20\,\mathrm{dB}$ or lower $S_{11}(dB)$ achieved at the range of frequencies for the RF field to be played at, which corresponds to $1\,\%$ or lower reflected power. An S_{11} of $-20\,\mathrm{dB}$ or lower was achieved for all RF coils constructed throughout this project. For transmission, a common benchmark for adequate decoupling of two neighbouring elements is to ensure $-15\,\mathrm{dB}$ or lower S_{21} achieved within the transmit bandwidth.

C.2 Smith Chart

An alternative method of displaying reflection coefficients, $\Gamma = \frac{V_{reflected}}{V_{incident}}$, is through the use of a Smith chart. The Smith chart allows the simultaneous display of real and imaginary component of impedance, z, normalised by the characteristic impedance Z_0 such that $z = Z_L/Z_0$ in a 2D

plane with polar coordinates. A simple diagram is shown below in Figure C.1. The centre point is impedance matched, for our case (and most commonly) with $Z_0 = 50\,\Omega$. Three common circuit examples that represent the minimum and maximum ranges of transmission line responses are that of: a short circuit, an impedance matched circuit and an open circuit. The short circuit has zero impedance, (as the load is shorted) as on the far left of the Smith chart, with $\Gamma = -1$ (such that all voltage is reflected back, in opposite phase). The impedance matched circuit represents the ideal case of optimum RF coil loading, where $50\,\Omega$ is seen through port 1 with no reactance, leading to $\Gamma = 0$ (such that all voltage is transmitted and no voltage is reflected). This is represented in the Smith chart as crossing the central point where $z = 1$. The final example is an open circuit, where the impedance is infinite, in this case all of the power is reflected back such that $\Gamma = 1$ (equivalent to an open cable). The three points are used in the calibration of S_{11} before a measurement, and performed before coil measurements.

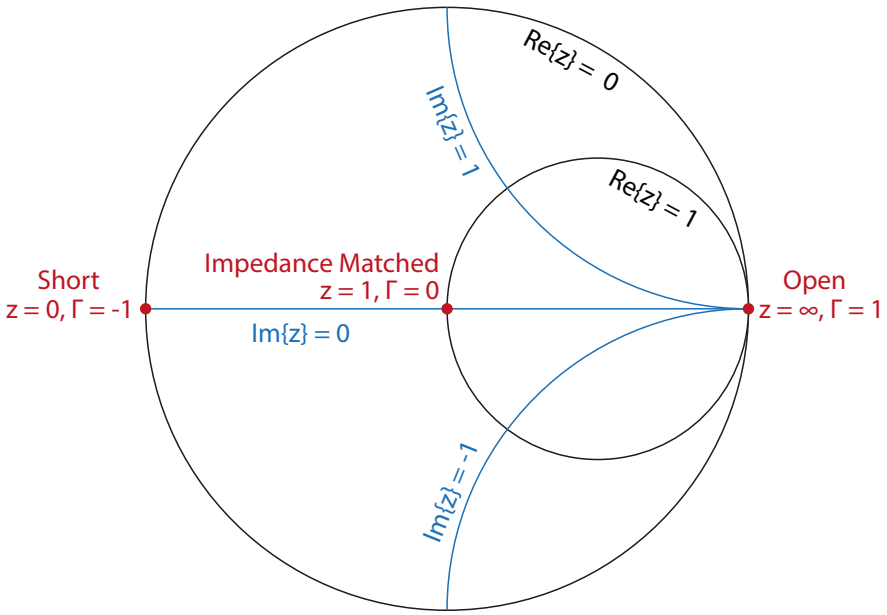

Figure C.1: Simple Smith chart diagram, showing the three states of S_{11} calibration: short ($z = 0$, $\Gamma = -1$), impedance matched ($z = 1$, $\Gamma = 0$), and open ($z = \infty$, $\Gamma = 1$).

D | Existing Scanner Field Mapping Methods

This appendix describes commonly used existing methods for characterising both the B_1^+ and SNR maps on the scanner for X-nuclei coils. This section is split into transmit and receive: section D.1 discusses two common methods of obtaining transmit B_1^+ maps, and section D.2.1 discusses methods of obtaining SNR. The limitation of these methods are highlighted, which paves the way for discussing the modified fully sampled coil characterisation method, in section 3.4.

D.1 Transmit Performance

The aim of transmit mapping techniques is to encapsulate the transmit field, B_1^+, either in the magnitude or phase of a scan image. The majority of B_1^+ mapping methods rely on signal magnitude, however they suffer from T_1 dependence, requiring long acquisition times with long TR to mitigate such dependence, inaccuracies at low flip angles (far from coil), and inaccuracies at multiples of $180°$ flip angles. B_1^+ mapping methods impose a trade off between these limiting factors. Two common methods for mapping transmit performance of X-nuclei coils are the Double Angle Method that encodes B_1^+ in magnitude data, and the Bloch-Siegert method that encodes B_1^+ in phase data.

D.1.1 The Double Angle Method

The Double Angle Method (DAM) is a commonly used simple and efficient B_1^+ mapping technique for surface coils [1, 2]. The DAM involves acquiring two standard gradient echo images, I_1 and I_2, with the second image is acquired at twice the voltage of the first image. The flip angle of the second image, α_2, therefore corresponds to double the flip angle of the first image, α_1, such that $\alpha_2 = 2\alpha_1$. At a voxel, r, the ratio of magnitude image satisfies the relation in equation D.1.

$$\frac{I_2(r)}{I_1(r)} = \frac{\sin\alpha_2(r) f_2(T_1, TR)}{\sin\alpha_1(r) f_1(T_1, TR)} \tag{D.1}$$

Phantom scans do not need to deal with motion compensation, and longer scan times can be used, such that TR $\gg T_1$. A long TR, for example, TR $= 5T_1$ can be used, such that there is practically no T_1 dependence, and $f_2(T_1, TR) = f_1(T_1, TR) = 1$. The flip angle, $\alpha(r)$ is then

calculated at every voxel, r, using equation Equation D.2 below:

$$\alpha(r) = \arccos\left(\left|\frac{I_2(r)}{2I_1(r)}\right|\right) \tag{D.2}$$

Subsequently, $\alpha(r)$ is converted to B_1^+ using equation 2.14, with knowledge of the transmit RF pulse profile and duration.

The advantage of the DAM method is the ease of implementation, requiring only two images, and a relatively short scan duration. However a lack of success was seen with this method, firstly, the acquired B_1^+ maps were noisy on ^{13}C, due to the division of two low SNR magnitude images, and secondly, the method deals poorly with high B_1^+ inhomogeneity (typical of surface coil elements), leading to over tipping of the measured flip angle by multiple revolutions.

D.1.2 The Bloch-Siegert Method

The Bloch-Siegert method, unlike the DAM, encodes B_1^+ information in signal phase. Two equally off resonance RF pulses are applied at $+\omega_{\text{RF}}$ and $-\omega_{\text{RF}}$ of the central frequency, ω_0, for example: $\omega_0 + 4\,\text{kHz}$ and $\omega_0 - 4\,\text{kHz}$, following a conventional spin excitation. By irradiating off resonance, the spin procession can be cancelled, and the primary observed effect is the spin precession frequency shift, which is proportional to $B1^2$ [3]. This method is used extensively in ^{1}H transmit calibration, but has also been implemented for X-nuclei transmit calibration [4].

Using the Bloch-Siegert shift ω_{BS}, in the assumption a large off resonance pulse is applied such that: $\omega_{RF} \gg \gamma B_1$, we can derive an expression of the B_1^+:

$$\omega_{BS} = \frac{(\gamma B_1)^2}{2\omega_{RF}} \tag{D.3}$$

The Bloch-Siegert method encodes the B_1^+ information in the relative phase shift, Φ_{BS}, for a given RF pulse duration T, according to Equation D.4.

$$\Phi_{\text{BS}} = (B^+_{1,\text{peak}})^2 \int_0^T \frac{(\gamma B_{1,\text{normalised}}(t))^2}{2\omega_{\text{RF}}(t)}\mathrm{d}t \tag{D.4}$$

Here, the phase integral is equivalent to the BS shift ω_{BS}, and B_1^+:

$$\Phi_{BS} = \int_0^T \omega_{BS}(t) \tag{D.5}$$

The advantages of this method are the insensitivity to T_1 allowing short TR scans, and the robustness against B_0 inhomogeneities and chemical shift. However, sufficiently high RF power is required to generate the off resonance pulses. With the available hardware for preclinical MRI, we were unable to achieve the desired flip angles on existing X-nuclei coils for successful B_1^+ mapping. The resulting B_1^+ values measured using the Bloch-Siegert method were not consistent with quantification from on-localised power calibrations.

Similarly to the DAM, poor performance with the Bloch-Siegert method was observed, and as such, the use these method for B_1^+ characterisation of surface coils were limited.

D.2 Receive Performance

For coil characterisation, separating the transmit and receive fields is required, however this may be challenging with Tx-Rx surface coils. Typically, methods of obtaining 2D SNR are still influenced by transmit effects. Two methods were investigated towards determining receive sensitivity, firstly a non localised spectroscopy and secondly chemical shift imaging (CSI).

D.2.1 Non-localised Spectroscopy

To obtain spectroscopy from a single volume, the spectroscopy sequence is either localised or non-localised. A non-localised spectroscopy does not use gradients coils, and acquires all signal indiscriminately within the coil FOV. On the other hand, single voxel spectroscopy uses gradient coils with RF coil at $90°$ or $180°$ flip angles to isolate a single cuboid voxel. Due to both simplicity and the non-uniformity of the B_1^+ field, the non-localised spectroscopy was used in this work. Additionally, when the SNR is measured, for the SNR to be fairly compared across different coil designs, the transmit B_1^+ field must be taken into account and neglected across scans.

Initially, a power calibration was performed on a large signal phantom, the SNR was measured from the spectroscopy which achieved a $90°$ flip angle within the phantom. However the large

phantom combined with non-uniform transmit profile led to non-sinusoidal signal responses. As such, a small fiducial was placed at a reproducible position within the coil FOV for the power calibration. For ^{13}C coils, a ^{13}C enriched urea sphere of approximately $1\,\mathrm{cm}$ diameter was placed off centre to the coil.

D.2.2 Chemical Shift Imaging

Chemical Shift Imaging (CSI), represents multi-voxel spectroscopy, using phase encoding to spatially localise voxels [5, 6]. In this work, 2D CSI was used as a rudimentary form of obtaining SNR mapping for preclinical multi-layer coil in section 4.4.2.2, and 1D CSI was used in research scans for the human multi-layer coil in section 5.6.1. In both cases, a non-selective pulse was used to excite the imaging volume, and gradients were used to select the specific voxel. The final image consists of the FOV split into a grid of voxels, with the spectra at each voxel used to quantify SNR. The advantage of CSI over single voxel spectroscopy is that of greater coverage and spatial resolution. CSI is commonly used in ^{1}H spectroscopy, where the disadvantages of CSI include longer acquisition time, low SNR within each individual voxel, and signal contamination from neighbouring voxels. For high resolution comparison of ^{13}C surface coil receive performance in this work, CSI has the primary downside of the measured SNR being affected by the transmit field profile.

References

[1] Insko, E. and Bolinger, L. "Mapping of the Radiofrequency Field". In: *Journal of Magnetic Resonance, Series A* 103 (1 June 1993), pp. 82–85. ISSN: 10641858. DOI: 10.1006/jmra.1993.1133.

[2] Cunningham, C. H., Pauly, J. M., and Nayak, K. S. "Saturated double-angle method for rapid B_1^+ mapping". In: *Magnetic Resonance in Medicine* 55 (6 June 2006), pp. 1326–1333. ISSN: 0740-3194. DOI: 10.1002/mrm.20896.

[3] Sacolick, L. I. et al. "B1 mapping by Bloch-Siegert shift". In: *Magnetic Resonance in Medicine* 63 (5 May 2010), pp. 1315–1322. ISSN: 07403194. DOI: 10.1002/mrm.22357.

[4] Schulte, R. F. et al. “Transmit gain calibration for nonproton MR using the Bloch-Siegert shift”. In: *NMR in Biomedicine* 24 (9 2011). ISSN: 09523480. DOI: 10.1002/nbm.1657.

[5] Pohmann, R., Kienlin, M. V., and Haase, A. “Theoretical Evaluation and Comparison of Fast Chemical Shift Imaging Methods”. In: *Journal of Magnetic Resonance* 129 (2 1997). ISSN: 10907807. DOI: 10.1006/jmre.1997.1245.

[6] Keevil, S. F. *Spatial localization in nuclear magnetic resonance spectroscopy*. 2006. DOI: 10.1088/0031-9155/51/16/R01.

E | Multi-layer Coil Construction Protocol

With the design aspect established, this section describes the protocol for designing a multi-layer coil which minimises conductor overlap, whilst utilising the stacked conductor for increased magnetic flux. This provides the general framework for designing a multi-layer coil, as opposed to a specific single design.

1. Determine single conductor element layer design:
    - Determine number of desired layers, e.g. four layers (more layers higher Q value and flux density but more difficult to construct and tune).
    - From a central point, conductor on layer will have $360/4 = 90°$ of segment not overlapping i.e. layer will span $270°$, but begin at $0°$, and end at $90°$, to connect to other layers.
    - Layer can be created from a simple shape, i.e. preclinical designs can be formed from roughly a Λ shape, and clinical designs can be formed from roughly a Ω shape.
    - Gaps in conductor are created to allow distributed lumped elements (capacitors for tuning/matching and ^{1}H traps) along the conductor length.
2. Tessellated layer to create a rotationally symmetric structure:
    - A point of rotation is defined, which is offset from the coil central axis.
    - The angle of rotation is dependent on number of layers, e.g. for four layers: $360/4 = 90°$. This allows the end of one conductor layer to align with the beginning of the next conductor layer in a top down 'birds-eye' view.
3. Dielectric layers are used to separate conducting layers:
    - Each dielectric layer is unique such that the dielectric layer only allow access to lumped element positions on conductor layers below the given dielectric layer.
    - The lower limit of dielectric layer thickness is determined by the dielectric breakdown voltage required to resist an electrical arc forming between the conductor layers.
    - A top and bottom layer of dielectric material is used to cover and protect the conductor layers.
    - Thick fire retardant pads are placed underneath lumped element gaps for patient safety and stability of solder joint.

F | Preclinical Multi-layer Circuit Simulation

F.0.1 Circuit Simulation

Circuit simulations were performed for the three ^{23}Na preclinical coils at $7\,\mathrm{T}$: small single loop, large single loop and multi-layer as described in section 4.3. Coil and sample losses were calculated using LT-SPICE (Analog Devices, Massachusets, US). All coils were modelled as RLC circuits, matched to the impedance of $50\,\Omega$, with a sinusoidal voltage source at of $400\,\mathrm{V}$ peak, at $79.5\,\mathrm{MHz}$. Tuning and Matching capacitors were determined using S-parameter from EM simulations. The overall coil, sample and total losses, and Q-values are shown in table F.1 for all three coils.

Table F.1: Summary of coil, sample and total loss (in Ω) and Q-loaded, and Q-unloaded values for three coils: multi-layer, small single loop and large single loop.

	Multi-layer	Small Single Loop	Large Single Loop
Coil Loss /Ω	0.199	0.229	0.106
Sample Loss /Ω	0.125	0.0276	1.73
Total Loss /Ω	0.323	0.256	12.3
Q_{Unloaded}	217.6	157.4	185.7
Q_{Loaded}	133.7	140.4	159.5
$Q_{\text{Unloaded}}/Q_{\text{Loaded}}$	1.628	1.121	1.164

Overall, these results were not consistent with the full-wave analysis using EM simulations. As the EM simulations were verified with scanner measurements, investigation into the circuit simulation values were not continued. This demonstrates the need for accurate full-wave simulations to model EM fields.

G | On-Axis B1 and SNR for Carbon Clinical Multi-layer Coils

Measured and simulated 1D on-axis field profile for the small multi-layer coil, large multi-layer coil, and three single loops of diameters 10, 15, and 20 cm at 30 MHz for a clinical 3 T Siemens scanner are shown here. The plotted data corresponds to the 2D B_1^+ and SNR maps as shown in section 5.4.1.3. The 1D B_1^+ is shown below in figure G.1 and the 1D SNR is shown below in figure G.2:

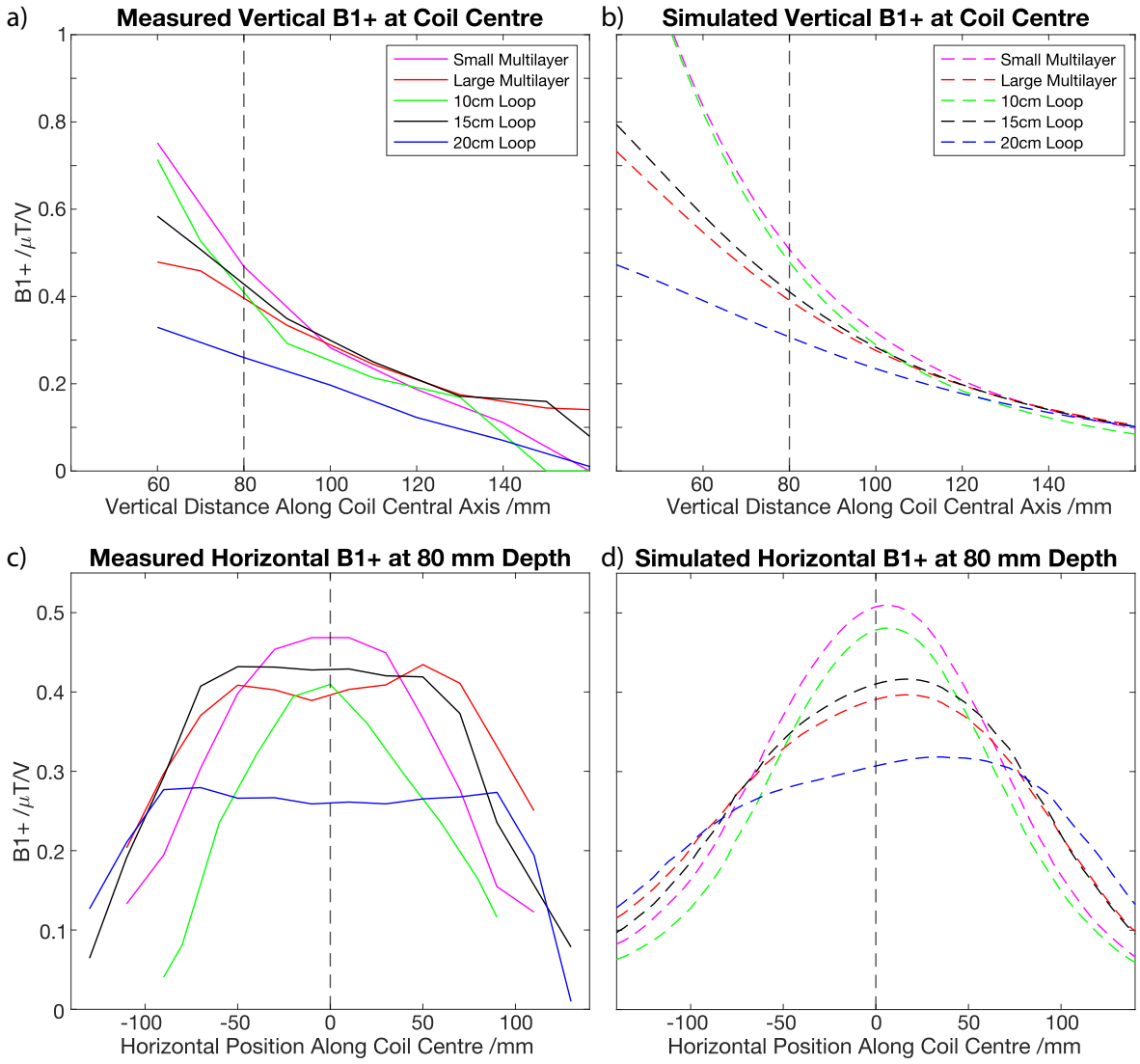

Figure G.1: On-axis 1D B_1^+ for two multi-layer and three conventional loop coils, vertically through the coil centre, and horizontally at 80 mm depth from coil.

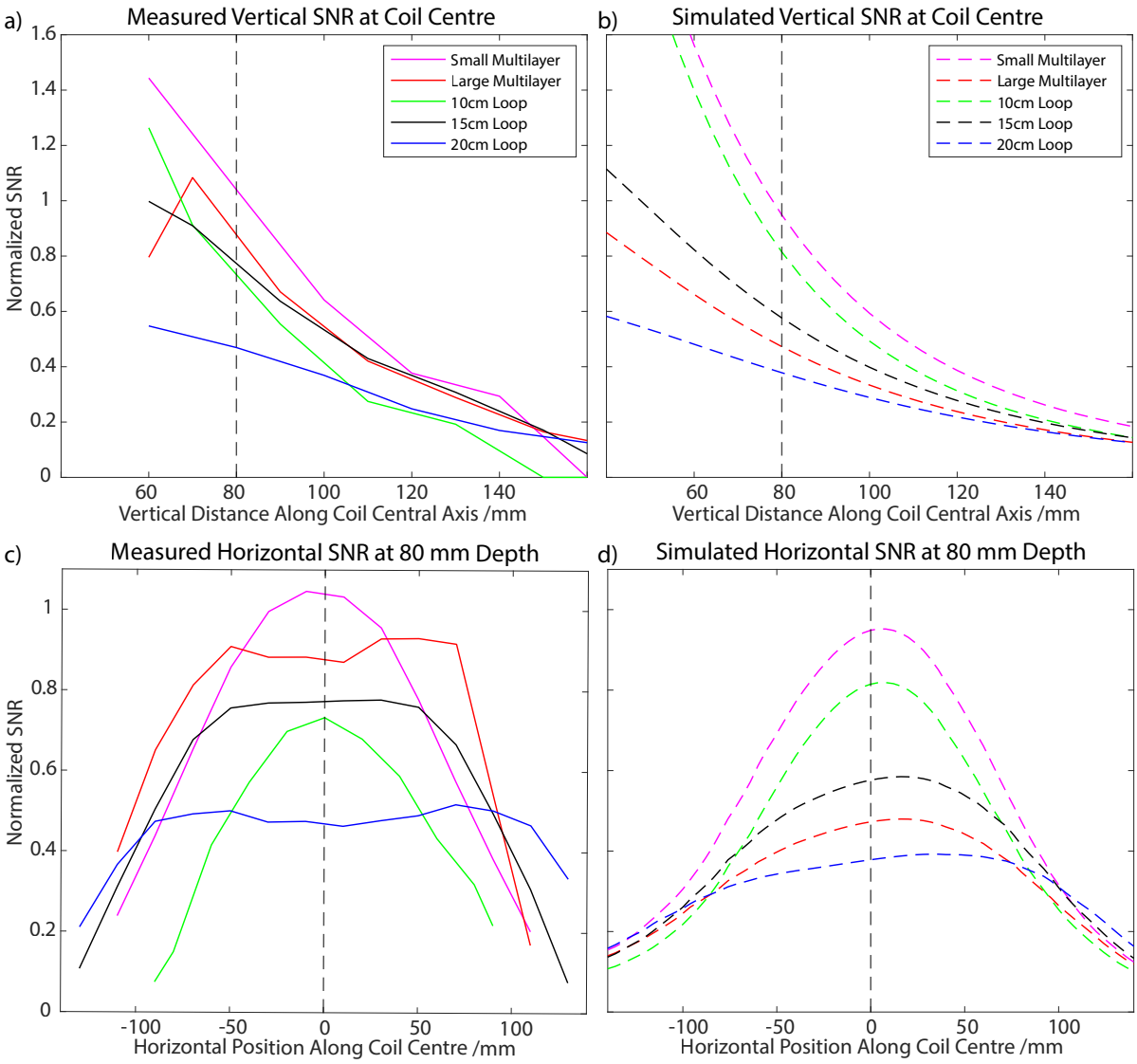

Figure G.2: On-axis 1D SNR for two multi-layer and three conventional loop coils, vertically through the coil centre, and horizontally at $80\,\mathrm{mm}$ depth from coil.

H | Four Element Transmit Array Optimisation Data

Following the work in section 6.3.1, the B_1^+ and S-parameter values for comparing four element transmit arrays and two element Helmholtz pairs for ^{13}C cardiac imaging, are presented here. The following tables present a summary of the simulated data through varying element dimension (Table H.1), and fillet radius, (Tables H.2 and H.3).

Table H.1: Element dimensions and horizontal element overlap separation for four element arrays with $10\,\mathrm{mm}$ fillet radius.

Element Dimension /mm		Element Separation /mm		0, 90, 180, 270° Phase Shift /°		Horizontal S-parameters /dB	
Width	Height	Horizontal	Vertical	B_1^+ Efficiency /μT V^{-1}	B_1^+ Uniformity	S_{21} (Upper)	S_{43} (Lower)
125	250	14.2	250	0.1475	0.7829	−9.23	−9.82
150	250	17.0	250	0.1322	0.8265	−11.28	−12.13
200	250	22.6	250	0.0978	0.8578	−12.93	−19.08
150	200	17.0	250	0.1054	0.8130	−6.24	−11.11
150	300	17.0	250	0.1447	0.8341	−8.01	−8.96

Table H.2: Fillet radius for four element arrays (of dimensions $150\,\mathrm{mm} \times 300\,\mathrm{mm}$).

Fillet Radius /mm	Element Separation /mm		0, 90, 180, 270° Phase Shift /°		Horizontal S-parameters /dB	
	Horizontal	Vertical	B_1^+ Efficiency /μT/V	B_1^+ Uniformity	S_{21} (Upper)	S_{43} (Lower)
10	17	250	0.1447	0.8341	−8.01	−8.96
20	17	250	0.1577	0.8393	−6.58	−8.54
30	17	250	0.1563	0.8545	−6.57	−8.50

Table H.3: Fillet radius for two element Helmholtz pairs (of dimensions $200\,\mathrm{mm} \times 200\,\mathrm{mm}$).

Fillet Radius /mm	Vertical Element Separation /mm	0, 180° Phase Shift /°		Vertical S-parameters /dB
		B_1^+ Efficiency /μT V^{-1}	B_1^+ Uniformity	S_{21} (Upper)
0	250	0.1086	0.8770	−6.52
10	250	0.1103	0.8721	−6.56
20	250	0.1116	0.8765	−6.56
30	250	0.1130	0.8745	−6.61

I | Array Design Performance Across Frequencies

Whilst discussion of the optimum transmit array design for other X-nuclei is outside the scope of this work, the array developed in section 6.3 may be used for different organs of the torso, and different nuclei. As such, the B_1^+ of the smaller four element array was simulated across a range of nuclei, and compared to the large Helmholtz pair used in clinical research (as initially described in section 6.1.1). The optimum element design will differ across frequencies, due to the dependence on the EM field depth penetration, EM coupling and other dielectric interactions. EM simulations were used to determine the B_1^+ efficiency and uniformity for the four element array and compared to a large Helmholtz pair from the lower bound frequency of $18.91\,\mathrm{MHz}$ (for deuterium MRI) to the upper bound frequency of $115.87\,\mathrm{MHz}$ (for fluorine MRI). The B_1^+ efficiency versus uniformity trade of curve is shown in figure I.1, the results for the four element array are shown in table I.1, and results for the large Helmholtz pair are shown in table I.2. It was found, that as the frequency was increased, the B_1^+ efficiency decreased, consistent with general observations on the difficulties associated with constructing RF coils for $7\,\mathrm{T}$ scanners. Additionally, as the frequency increases, the B_1^+ uniformity of the four element coil (in blue) increased, whilst the B_1^+ uniformity of the two element coil (in red) decreased. Therefore at higher frequencies (in this simualtion setup, past $49.86\,\mathrm{MHz}$ for ^{31}P), a greater number of array elements will achieve better uniformity.

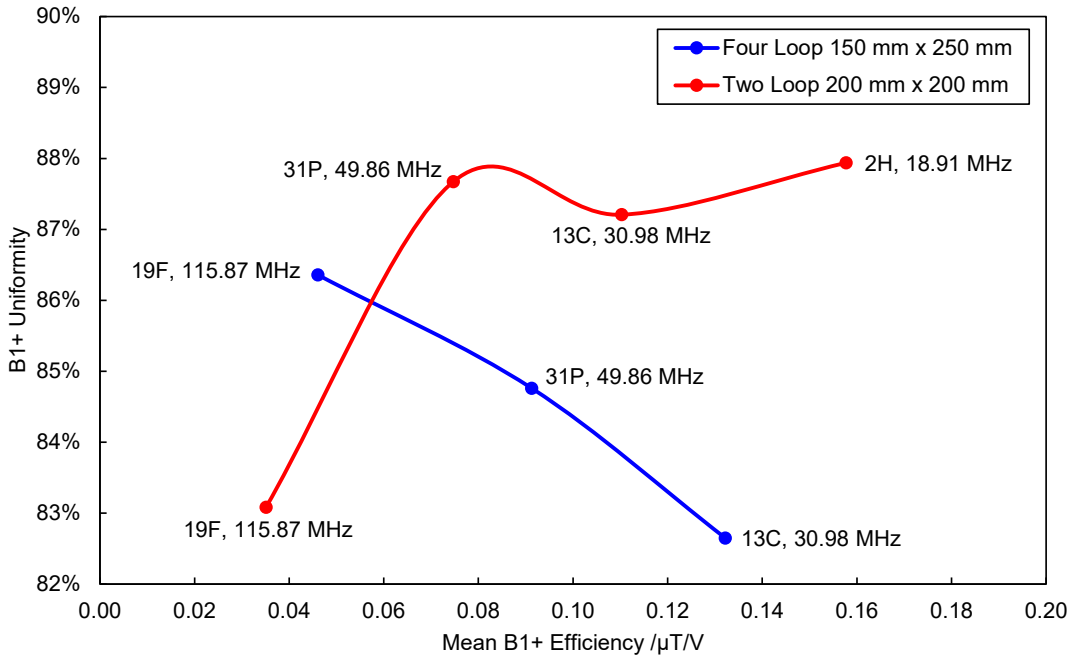

Figure I.1: Mean B_1^+ field efficiency versus B_1^+ field non-uniformity plot at $250\,\mathrm{mm}$ vertical separation. Performance of two and four loop arrays were compared over a range of frequencies, showing the benefit of numerous loops at higher frequencies.

Table I.1: B_1^+ for the four element array with $10\,\mathrm{mm}$ fillet radius and $250\,\mathrm{mm}$ vertical separation, across frequencies from $30.98\,\mathrm{MHz}$ to $115.87\,\mathrm{MHz}$

(Nuclei) Frequency /MHz	Element Separation /mm		0, 90, 180, 270° Phase Shift /°		Horizontal S-parameters /dB	
	Horizontal	Vertical	B_1^+ Efficiency /μT V^{-1}	B_1^+ Uniformity	S_{21} (Upper)	S_{43} (Lower)
(^{13}C) 30.98	17	250	0.1322	0.8265	−11.28	−12.13
(^{31}P) 49.86	17	250	0.0913	0.8476	−13.35	−15.08
(^{19}F) 115.87	15	250	0.0461	0.8636	−18.55	−21.75

Table I.2: B_1^+ for the Helmholtz pair with $10\,\mathrm{mm}$ fillet radius and $250\,\mathrm{mm}$ vertical separation, across frequencies from 18.91 to $115.87\,\mathrm{MHz}$

(Nuclei) Frequency /MHz	Vertical Element Separation /mm	0, 90, 180, 270° Phase Shift /°		Vertical S-parameters /dB
		B_1^+ Efficiency /μT V^{-1}	B_1^+ Uniformity	S_{21} (Upper)
(^{2}H) 18.91	250	0.1577	0.8794	−4.37
(^{13}C) 30.98	250	0.1103	0.8721	−6.56
(^{31}P) 49.86	250	0.0747	0.8767	−9.35
(^{19}F) 115.87	250	0.0351	0.8308	−16.20